

The Non-Destructive Measurement of the Radio Frequency Properties of Hard Rock Borehole Cores

Marc Rütschlin

Dissertation presented for the degree of Doctor of Philosophy in Engineering at the University of
Stellenbosch



Promoters:
Prof. Johannes H. Cloete
Prof. Keith D. Palmer

December 2005

Declaration

I, the undersigned, hereby declare that the work contained in this dissertation is my own original work, unless stated otherwise, and has not been previously, in its entirety or in part, submitted at any university for a degree.

Marc Rütschlin

28 June 2005

Abstract

The effective use of borehole radar in geophysical exploration requires accurate knowledge of the dielectric properties of the geological system in which it is employed. The attenuation and propagation velocity of pulses through rock must be known in order to plan and interpret experimental data. Conventional destructive methods for the measurement of hard rock cores require the careful preparation of samples. This firstly necessitates the selection of sampling position and the resulting estimation of rock properties based on sparse measurements, and secondly results in the loss of material and thus data.

The ready availability of cylindrical borehole core samples invites the use of a nondestructive means of measuring their properties. A novel design for a flexible guarded capacitor which conforms to a core's cylindrical surface is presented here. The proposed device has numerous advantages over previous methods. No material is lost to sample preparation and a detailed characterisation of the entire core, including inclusions and transitions between rock types, may be performed.

A detailed methodology for the rapid construction of a robust capacitor is given. Guidelines for its operation to achieve repeatable and accurate measurements of the complex dielectric constant of samples of varying homogeneity in the 1–25 MHz frequency range are presented.

The increased amount of data collected from complete core samples is analysed statistically, and amongst other things allows the estimation of the rock's homogeneity. Comparisons of the dielectric properties measured in the laboratory to propagation velocity estimates obtained from crosshole borehole shoots show that a more homogeneous sample is a better predictor of bulk propagating conditions. Detailed studies of the dielectric properties of economically important diamondiferous and platiniferous geological systems show that borehole radar is a feasible tool for the high resolution delineation of ore bodies and other geological targets.

Opsomming

Die effektiewe gebruik van boorgatradar in geofisiese eksplorاسie benodig akkurate kennis van die diëlektriese eienskappe van die geologiese sisteme waarin dit gebruik word. Kennis van die verswakking en voortplantingsnelheid van pulse deur die rots word benodig om eksperimente te beplan en gemete data te interpreteer. Vir konvensionele destruktiewe meetmetodes van harde rotskerne is noukeurige voorbereiding van monsters noodsaaklik. Hierdie proses vereis eerstens 'n keuse van meetposisies en die afskatting van rotseienskappe gebaseer op verspreide metings, en lei tweedens tot die verlies van materiaal en dus data.

Die beskikbaarheid van silindriese boorgat kernmonsters maak dit moontlik om die kerneienskappe op 'n nie-destruktiewe manier te meet. Die ontwerp van 'n nuwe buigbare afgeskermdde kapasitor wat op 'n silindriese kernoppervlak pas, word hier voorgestel. Die toestel het verskeie voordele bo huidige metodes. Geen materiaal word gedurende monstervoorbereiding verloor nie, en 'n volledige beskerming van die eienskappe van die hele kern, met insluitings en oorgange tussen rotstipes, kan verkry word.

'n Gedetailleerde prosedure vir die vinnige konstruksie van 'n robuuste kapasitor word gegee. Die gebruik van die toestel vir herhaalbare en akkurate metings van die komplekse dielektriese konstante van verskillend homogene monsters in die 1–25 MHz frekwensie bereik word beskryf.

Die groter hoeveelheid data wat deur middel van hierdie metode van hele kernmonsters verkry kan word, word statisties geanaliseer, en laat onder andere 'n skatting van die rots se homogeniteit toe. Vergelykings van laboratoriumgemete rotseienskappe met veldskattings van voortplantingsnelhede wys dat 'n meer homogene monster tot 'n beter afskatting van werklike voortplantingstoestande lei. Studies van die diëlektriese eienskappe van ekonomies belangrike diamanthoudende en platinumryk geologiese sisteme wys dat boorgatradar geskik is vir hōe resolusie uitkenning van ertsligame en ander geologiese teikens.

Acknowledgements

There are a number of people who have, in different ways and to varying degrees, helped this journey reach its end.

My first words are for my supervisors, Professors Johannes Cloete and Keith Palmer. I thank you for your unending enthusiasm and equally enduring patience. The breadth and depth of your knowledge have inspired me.

Without the technical staff at SED, who were always eager to help and willing to go out of their way to accommodate my ever changing requests, none of this would have been possible. For your technical know-how, the discussions and suggestions, thank you Wessel, Ulrich and Lincoln.

Without the constant and unquestioning support of my parents things would have been so much harder. Thank you for being there, for providing a stable and loving base, for making it easy to achieve.

It is my colleagues and friends at Stellenbosch that have made the years here ones I will cherish. To the E251 gang: without you it would certainly have been an infinitely duller time! Thomas, Werner, Chris, Martinette and Robert — thanks guys, we did it right. To the new guys, Marlize, Thomas, Nicola and Div — thank you for making the office what it was. A word of thanks also to Petrie for sustaining such a relaxed yet productive working environment.

John and Sue and Carl — what a good time we had, outdoors and in. Here's to many more cups of good strong coffee and brilliant routes to climb! You *can* have your cake and eat it.

Finally, to my Kate: as one chapter ends, so another begins. It was well worth the wait.

Contents

1	Introduction	1
2	Theory	8
2.1	Material Properties and Electromagnetic Wave Propagation	8
2.2	Dielectric Modelling	11
2.2.1	The Debye Model	11
2.2.2	The Lorentz Model	12
2.2.3	The Jonscher Power Law	13
2.2.4	The Analytic Continuation Model	14
2.3	Capacitance	15
2.4	Guarding	15
2.5	The Analysis of Measurement Uncertainty	16
2.5.1	A Statistical Approach	17
2.5.2	Sensitivity Analysis	18
2.5.3	Graphical Representation of Error Analysis	19
2.6	Measurement with the LCR Meter	20
2.6.1	Principle of Operation	20
2.6.2	Compensation and Calibration	21
3	The Parallel Plate Capacitor	24
3.1	Introduction	24
3.2	Electrode Design	24
3.2.1	Electrode Construction	26
3.3	Measurement Procedure	26
3.4	Measurement Accuracy	29
3.5	The Characterisation of Standard Materials	30
3.6	Conclusion	31
4	Cylinder Probe Design	32
4.1	Introduction	32
4.2	Analytic Solution	32
4.2.1	Potential Solution	33
4.2.2	Capacitance	36
4.2.3	Convergence	37
4.2.4	Discussion	38
4.3	Circuit Model	41
4.3.1	Component Value Estimation	44
4.4	Electrode Implementation	45

4.4.1	Electrode Geometry Design	45
4.4.2	Practical Considerations	46
4.5	Conclusion	49
5	Cylinder Probe Measurement	50
5.1	Introduction	50
5.2	Measurement with the LCR Meter	50
5.2.1	Measurement Procedure	50
5.2.2	Measurement Accuracy	51
5.3	Measurement of Transitions	58
5.4	Conclusion	65
6	Case Studies	67
6.1	Introduction	67
6.2	Representation of Measured Data	68
6.3	Bushveld Igneous Complex	70
6.3.1	Geological Background	70
6.3.2	Borehole Experiment Description and Local Geology	71
6.3.3	Electrode Design	71
6.3.4	Measurements of the Bleskop Marker	74
6.3.5	Measurement of the UG2 Reef and Triplets	79
6.3.6	Discussion	82
6.4	Diamond Geologies	87
6.4.1	Geological Background	87
6.4.2	Cullinan Mine	87
6.4.3	Snap Lake Mine	99
6.4.4	Conclusion	106
6.5	Conclusion	106
7	Conclusion	108
A	Electrode Construction and Operation	112
A.1	Electrode Construction	112
A.2	Measurement Procedure	118
B	Parallel Plate Sample Preparation	120
B.1	Hard Rock Samples	120
B.2	Plastic Samples	122
C	The Artificial Dielectric	123
D	MATLAB Scripts	126
D.1	<i>measure.m</i>	126
D.2	<i>cyl_calibrate.m</i>	130
D.3	<i>PP_calibrate.m</i>	132
D.4	<i>process_cyl_data.m</i>	133
D.5	<i>geometry.m</i>	134
	Bibliography	136

Chapter 1

Introduction

Geophysical exploration is driven by two motivating factors: economical and safety. Mining, especially at depth, is an expensive and hazardous undertaking. The need for prior knowledge of the structure of desirable targets like reefs or other ore bearing bodies, and the location of potentially dangerous disruptions to the reef such as faults, dykes, rolls, or water bearing inclusions, is well established [1]. Risks of potentially fatal slippage, rockburst and strainburst are greatly increased in the vicinity of these disruptions, as demonstrated in Figure 1.1 by the superimposition of fatalities onto a map displaying rolls on the Ventersdorp Contact Reef. The accurate delineation of ore bodies and disruptions to them (e.g. potholes interrupting the UG2 reef in the Bushveld Igneous Complex [2] — cf. Chapter 6.3) is of course also of substantial economical importance.

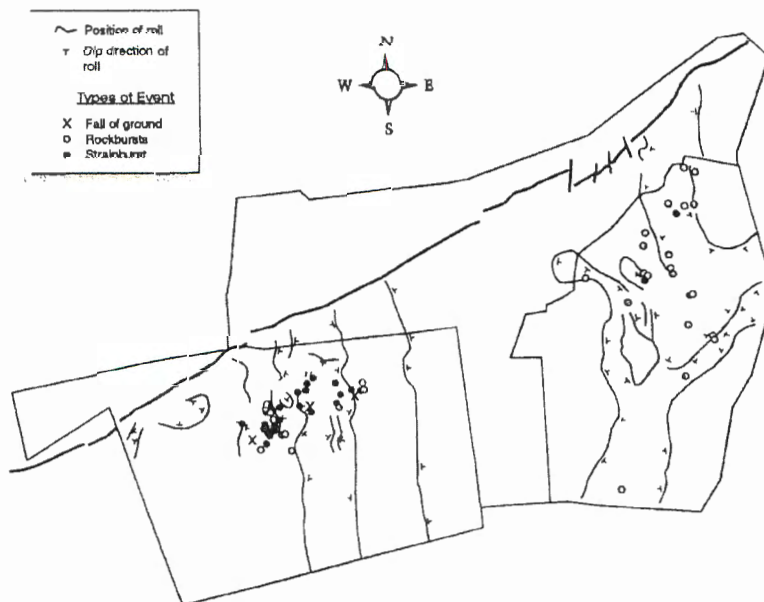


Figure 1.1: Superposition of fatalities on map showing occurrence of rolls at Western Deep Levels and Driefontein Gold Mines (1991-1995) [1].

Geophysical exploration has taken substantial strides thanks to the use of seismic and electromagnetic techniques in conjunction with core logging. The drilling of exploratory boreholes is however expensive and interpolations based on incomplete information are necessary to obtain a (hopefully) accurate picture of the geological scenarios to be encountered. Owing mainly to the rise of signal attenuation with frequency, most remote sensing methods are relatively low frequency and consequently only allow low

resolution estimation of the structure and position of ore bodies and other geological features. The price associated with drilling makes it desirable to maximise the information obtained from any one borehole.

The recent developments in borehole radar (BHR) technology (see for example [3, 4, 5]) have seen an increase in its use, particularly as a high resolution imaging tool [6]. The use of any radar technology underground is completely dependent on knowledge of how the electromagnetic wave will be altered by the rock it is propagating through. In particular, a propagating signal loses energy as it travels, and will be partially reflected from interfaces between materials with differing properties. The range of detection of such a contrasting rock type is determined by the energy lost during transit — this is related to the loss tangent of the material; the accurate calculation of the distance to a target is made possible by knowledge of the signal's propagation velocity, which is directly related to the rock's relative permittivity. Knowledge of the frequency characteristics of attenuation and signal velocity is critical for interpretation of radar data, and even potentially the design of the radar components themselves. If the attenuation constant changes with frequency, the dominant frequency of a propagating pulse will change with distance, as will the pulse shape and envelope and phase velocity.

In many South African mines, the diamond drilling of covering boreholes (typically of about 48 mm in diameter) for the detection of dykes and water fissures is a legal requirement [1]. This not only provides an ideal opportunity for the deployment of a BHR system, but also, in the form of the core samples, a ready supply of the rock immediately relevant to signal propagation. What's more, the samples come out of the diamond drilled boreholes pre-prepared. They are usually smoothly cylindrical, in lengths of up to about half a metre, inviting the application of an appropriately designed device to the measurement of their dielectric properties.

To place the following review of dielectric measurement techniques in perspective, it would at this point be useful to outline the requirements for a measuring device for these hard rock cores. First, the system should be nondestructive. The pre-prepared cores allow the avoidance of many negative factors relating to the preparation of samples — this must be taken advantage of. Second, the device should allow the *in situ* measurement of core samples, that is, it should be robust and portable enough to conduct measurements in a core yard. Finally, the device should measure the rock properties in a frequency range relevant to BHR (1–25 MHz in this case) with sufficient accuracy to enable meaningful predictions to be made regarding the feasibility of borehole radar experiments.

The Characterisation of Dielectric Material Properties

All measurement techniques have in common the desire to relate some measurable quantity to the complex dielectric constant ϵ^* . The measured capacitance in the case of a parallel plate capacitor or the shift in resonant frequency in the case of the resonant cavity method, for example, both depend on the permittivity of the material under test (MUT). A variety of techniques have been developed to determine the permittivity and loss tangent of dielectric materials. In addition to Von Hippel's seminal text [7], useful reviews have recently been conducted by, amongst others, Baker-Jarvis *et al.* [8], Afsar *et al.* [9], Bussey [10] and Roussy *et al.* [11, Ch. 5.7].

Measurement techniques can be broadly classified as destructive, that is, requiring the preparation of a sample of the material to be tested, and nondestructive. Different techniques have different areas of applicability in terms of frequency range, accuracy and convenience. There is often a trade-off between these aspects: resonant cavity techniques, for example, have extremely high accuracy but tend to be narrow band, while transmission line methods, on the other hand, can be used over a wide frequency band but are inconvenient since they require careful machining of samples. A comparison of various dielectric measurement categories is given with their respective advantages, disadvantages and typical measurement accuracies in Table 1.1. Also listed are a number of references in which different techniques were applied to the measurement of the dielectric properties of hard rock.

Technique	Advantages	Disadvantages	Typical Accuracy	Example
TL methods	Broadband	Sample preparation	$\pm 5\%$, ± 0.01	[12, 13]
Capacitor	Normal E-field	Air gap	$\pm 1\%$, $\pm 10^{-4}$	[14, 15, 16, 17, 18]
Cavity	Very accurate	Narrowband, low loss	$\pm 0.2\%$, $\pm 5 \times 10^{-5}$	[19, 13]
Resonator	Very accurate	Low loss region	$\pm 0.2\%$, $\pm 5 \times 10^{-5}$	
Open-ended probe	Nondestructive	Contact problem	$\pm 10\%$, ± 0.02	[19, 20, 21]
Surface waves	High frequency	Mode identification	$\pm 10\%$, $\pm 10^{-6}$	
Free-space	Nondestructive	Noisy	$\pm 5\%$, $\pm 10^{-2}$	

Table 1.1: Comparison of a number of dielectric measurement categories (modified from [8]). Typical accuracy is given in percentage of ϵ_r and absolute $\tan \delta$; the references listed are examples of the use of the respective techniques in the measurement of hard rock.

The focus here shall be on the nondestructive techniques, of which there appear to be a conspicuous dearth in Table 1.1, and particularly on those techniques applicable to the measurement of cylindrical samples. This perceived shortage is somewhat deceptive, since a number of other techniques may be adapted to be nondestructive if the sample geometry is suitable. For example, a slab of material with flat parallel sides may lend itself to measurement by a parallel plate capacitor or open ended coaxial probe.

A number of techniques hold promise for modification to the cylindrical geometry. The open ended coaxial line technique, shown schematically in Figure 1.2, is used for the measurement of smooth flat surfaces by placing it flush against the sample and measuring the reflection coefficient. The complex permittivity is then “extracted from the reflection coefficient by modelling the fringing fields at the discontinuity as an equivalent lumped admittance” [22]. Circuit parameters are inferred from measurements on known materials before being used to calculate the permittivity of the MUT. A more complete analysis taking into account higher order transverse magnetic modes in the coaxial line and the propagation of radiation into the sample was done by Mosig *et al.* [23]. The introduction of an air gap between the end of the coaxial line and the sample surface, whether from inexact probe construction or surface roughness, can reduce the sensitivity of the probe and result in errors in predicted permittivity. Theoretical calculations by Gershon *et al.* [24] show how increasing the gap width increases the reflection coefficient’s magnitude and phase to one and zero respectively. Especially at lower frequencies, the fringing fields penetrate very little from the end of the probe tip. An exact analytical analysis of the probe including ‘lift-off’, that is, the presence of an air gap, has been done by Baker-Jarvis *et al.* [25], who make the same observations as Gershon *et al.* but in addition investigate the effects of frequency. This technique does suffer from a large uncertainty in the measurement of the imaginary part of the permittivity, ϵ'' in low-loss materials. Gershon *et al.* recorded accuracies of 5 % for ϵ' but only 24 % for ϵ'' relative to standard measurements using an HP probe [24]. The coaxial line end may in principle be modified to fit onto a cylindrical sample’s curved surface, but no analytical solution to this problem is known. Further, the resulting probe would be extremely dependent on the core diameter and thus not very versatile.

The desire to non-destructively measure the permittivity of circuit boards, thin films, and substrates has led to open transmission line techniques. A microstrip, stripline, or coplanar fixture is formed on the material of interest, the system is operated in resonance, and measurements of the transmission and reflection responses are related to permittivity. The loss tangent can be obtained from a measurement of the quality factor. The complex dielectric constant depends on the fields in the sample and the fringing fields. Quite an extensive physical modelling of the system is required for ϵ^* to have any fundamental significance [8]. An example of such a multi-conductor coplanar system adapted to a cylindrical geometry was described by Karpuz *et al.* [26].

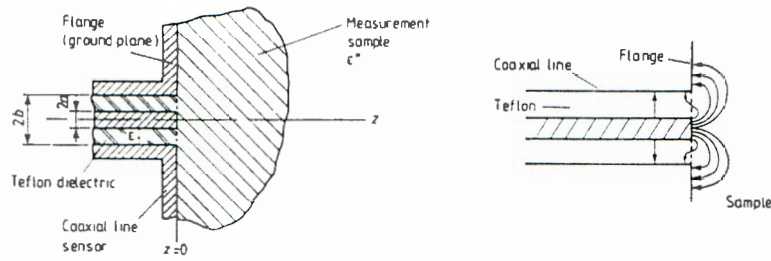


Figure 1.2: Geometry of and fields associated with the open-ended coaxial probe [22].

But the technique which holds the most promise for solving the problem at hand is dielectric profiling (DEP). This capacitive technique, generally ascribed to Moore and Paren [27], has been used to measure the permittivity and conductivity of ice cores. The following detailed discussion of this technique will trace its development from Moore and Paren's 1987 device to the more advanced electrode system and analytical solution described by Wilhelms [28] for his measurement of Antarctic ice core samples.

The capacitor of Moore and Paren [27] consisted of twenty 5 cm wide palladium coated brass segments — the measuring¹ electrodes — spanning an angle of 108°, with a 25 cm guard electrode at each end, and flat side guards of 140 mm width extending out from the core along the entire 1.5 metre capacitor length. The feed electrode was the same length and shape as the sensing and guard combination. The size and shape of the curved electrodes, which had the same radius of curvature as the cores being measured, were determined experimentally to address the compromise between measurement resolution and suitable impedance magnitude. The entire assembly was shielded from external electromagnetic interference by an aluminium case. During a measurement, two adjacent electrodes were switched 'on' as active capacitors, while the remainder were grounded, thus forming part of the guard. Measurements between 20 Hz and 300 kHz were conducted at an estimated accuracy of 0.5 % over "most of the measurement range". A schematic of this configuration is shown in Figure 1.3(a).

A subsequent article by Moore and Maeno [29] added a simplistic analytical treatment of the curved capacitor wherein an average value for plate separation was used in place of d in the standard $\epsilon A/d$ parallel plate capacitor equation. The resulting expression was in "satisfactory" agreement with experimental results for air capacitance.

A successor to the Moore and Paren system was described by Moore [30]. The capacitor geometry in this case, shown in Figure 1.3(b), was notably different in that one electrode was curved while the other was flat. The halved core sample rested in a curved cradle while a narrow guarded measuring electrode was passed along the core's flat upper surface. Arguably a step backwards, since sample preparation was now again required, the motivation was to increase the geometric capacitance by reducing the plate spacing, thus allowing a narrower measuring electrode (3 mm wide) to make higher resolution measurements. Measurements were conducted at millimetre resolution at 50 kHz.

The instrument described by Wilhelms in his thesis [31], and again in the paper by Wilhelms *et al.* [32], had two important geometric changes. First, the guard electrode was also curved, approaching the extended feed electrode to form only a small gap between the two. This geometry allowed Wilhelms to derive an analytical expression for the ideal geometric capacitance between the sensing and feed electrodes. Second, the guard was extended to enclose the sensing electrode, thereby shielding it and preventing stray fields from the rear of the sensing electrode from affecting the measurement. A schematic representation of the geometry is shown in Figure 1.4 [31]. The mechanical configuration in this case again had the

¹The 'measuring' electrode is the guarded electrode, while the 'feed' electrode is the unguarded opposing one. These concepts are discussed in more detail in Sections 2.3 and 2.4.

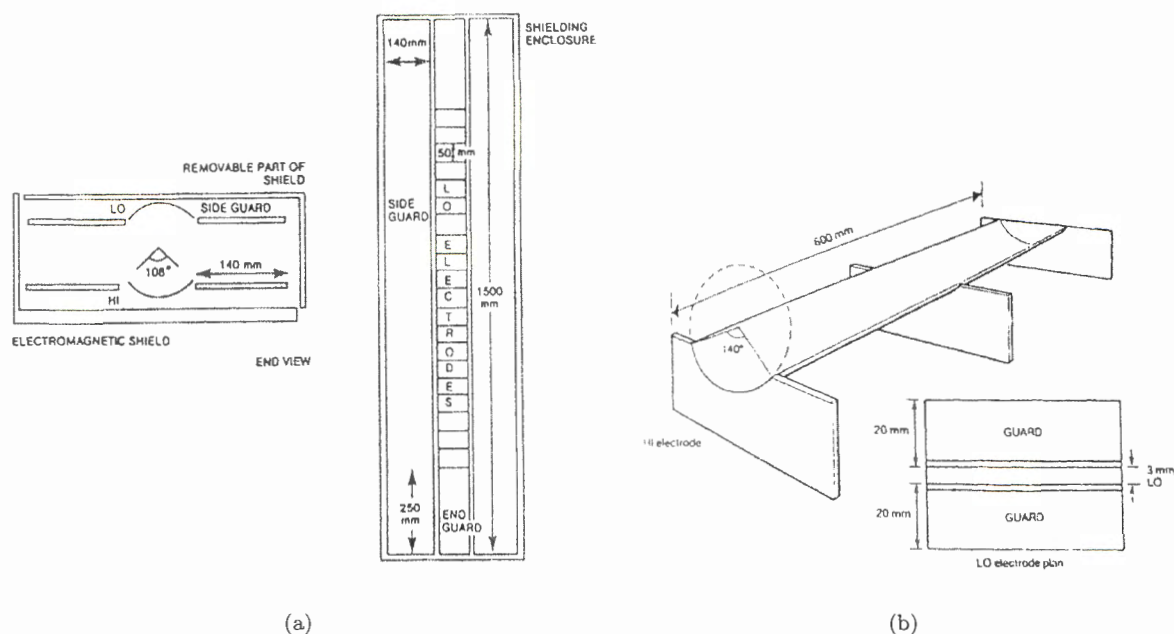


Figure 1.3: The electrode assemblies of (a) Moore and Paren [27] and (b) Moore [30].

core resting in a 3.5 metre long cradle formed by the aluminium feed electrode. The sensing electrode, with dimensions of 10 mm by 108° , was surrounded by a 70 cm long guard electrode; the sensor-guard combination was moved along the core sample by a stepper motor. Measurements to a frequency of 1 MHz were conducted to a claimed accuracy of 4.5 % in the case of permittivity and 8–15 % for conductivity [32]. The entire apparatus, with supporting equipment, weighed about 130 kg and was transported in three crates measuring $60 \times 80 \times 40$ cm.

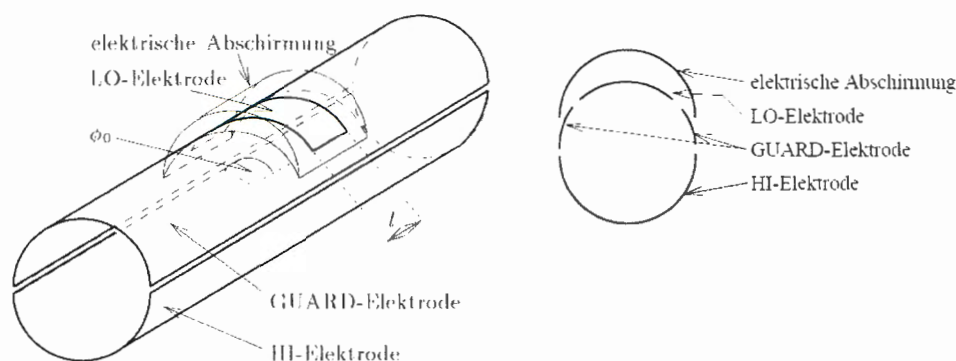


Figure 1.4: Three dimensional and end views of the electrode geometry of Wilhelms [31]. The 'LO' and 'HI' electrodes are the sensing and feed electrodes respectively.

Wilhelms' subsequent dissertation [28] expanded upon his previous work in a number of ways. The quasistatic analytical solution for the capacitance was extended to take into account the finite nature of the guard electrode. This necessitated that the sensor-guard and feed electrodes have the same dimensions, which in turn required that the core be transported through the electrode system rather than the electrode being moved. This was achieved by carefully suspending the sample — whose diameter was smaller than that of the cylinder cavity — in the centre of the cylinder volume using polyethylene foil before moving it with a stepping motor controlled sled. An analytical solution for the potential of the capacitor

containing a concentrically layered dielectric was formulated by Wilhelms for the extraction of the complex dielectric constant from measured data. Guidelines for the design of electrode geometries were given, and measurement resolution was estimated to be similar to the sensing electrode length. Calibration of this system was done in two stages: first the used impedance meter's standard open and short corrections were performed [33], then a number of cylindrical conductors of various diameter were placed in the centre of the cylinder to form lossless artificial dielectrics (as described in Appendix C). These were taken as a set of impedance values which were used as a calibration data set. The calculated accuracy of his measurements of the dielectric constant of ice cores was claimed to be about 2 % at a frequency of 250 kHz. The materials used in this last iteration were similar to Wilhelms' previous design [31], and the equipment had roughly the same packing dimensions and weight.

Outline of Dissertation

The measurement of hard rock cores holds some specific challenges not addressed by the methods described in the literature. The solution proposed in this study uses a novel flexible electrode geometry which conforms to the core. Where previous dielectric profiling applications were designed for the measurement of ice ($\epsilon_r \approx 4$ at 1 MHz [7]), it is the measurement of higher permittivity lossy materials at higher frequencies that is of interest here. This raises a number of challenges with regard to calibration: the standard open, short and load calibration method [33] is not possible with the design proposed, thus the use of materials with well known dielectric properties as calibration standards is required. The lack of sufficiently accurate data for most materials in the frequency range of interest in turn necessitated the development of a guarded parallel plate capacitor for the accurate characterisation of these materials.

A number of tools required during the rest of the thesis will be presented in Chapter 2. The central concepts of capacitance and guarding are discussed in Sections 2.3 and 2.4. The analysis of measurement uncertainty is likewise important for the work to follow; international conventions are followed in their calculation, and an intuitive graphical representation enhancing qualitative understanding of the 'error chain' is developed. The four-terminal pair measurement technique allows the accurate measurement of large impedances at these frequencies — its discussion is presented alongside the calibration techniques applicable in this dissertation.

The properties of reference materials are not listed adequately in the literature or by their manufacturers. When figures are given for the frequencies of interest in this study, they are not assigned any meaningful accuracy estimates — these are important for the calculation of the overall measurement uncertainty. The guarded parallel plate capacitor is a well understood device for the capacitance of which analytical solutions exist. With careful preparation of samples — a technique is described in Appendix B — accurate characterisation of reference materials and the uncertainties involved is possible. A simple yet robust design allowing such measurements is described in Chapter 3 along with the actual characterisation of the reference materials used in the cylindrical measurements.

The behaviour and design of the cylindrical capacitor is described in Chapter 4. The description of an analytical solution, as well as the development of a circuit model which adequately describes device behaviour in the frequency range of interest, serve to increase understanding of the capacitor's operation and as an aid for the design of an effective device. The design principles involved are described in this chapter, while a detailed procedure for the construction of these capacitors is presented in Appendix A.

The calibration procedure and uncertainty analysis are of great importance to any measurement. They are described in Chapter 5, along with techniques for making more repeatable measurements — repeatability is of major concern when accurate measurements are desired. The cylindrical capacitor allows the detailed measurement of rock cores containing different features; guidelines for sensible sampling rates and ways of approaching the measurement of transitions between two types of rock as well as inclusions of one rock type within another are also presented here.

Finally, the use of the cylindrical capacitor for the characterisation of rock core samples for BHR studies in three economically important case studies is described in Chapter 6. The Bushveld Igneous Complex (BIC) hosts about 75 % of the world's platinum group metals [34], and the accurate fine-scale delineation of its UG2 reef would greatly aid mine planning. Measurements of representative samples from the reef itself and the surrounding rock types are presented in Section 6.3. The feasibility of the BHR delineation of two different diamond bearing geological structures — the kimberlite pipe at the Cullinan mine in South Africa, and the kimberlite dyke at Snap Lake in Canada — is considered based on the results of the measurements in Section 6.4. The involvement of this study with actual BHR radar studies will allow the comparison of measurements done in the laboratory to results from cross borehole shoots in the field.

Novel Contributions

A number of original contributions are presented in this dissertation.

- A novel design and construction procedure for a flexible, guarded, shielded capacitor for the measurement of the complex dielectric properties of hard rock borehole cores is presented. The capacitor is able to accurately measure a useful range of material properties in the 1–25 MHz frequency range. The concept is of immediate use at lower frequencies and is extendable to frequencies of several hundred megahertz.
- A methodology for the accurate measurement of hard rock cores of differing condition is shown which accounts for repeatability problems and long term changes in measuring conditions.
- The new measurement technique provides far more comprehensive data regarding rock properties, necessitating a statistical approach to the analysis of results. Several parameters are proposed to quantify in particular the homogeneity of rock properties, allowing individual samples and rock types to be compared to each other.
- The measurement of whole cylindrical cores, without preparation, allows measurements of unprecedented detail to be carried out for rocks with an inhomogeneous structure. The measurement of transitions and inclusions becomes possible. The characterisation of rocks of inhomogeneous composition is enhanced since no decision need be made regarding where to sample a rock — the entire core is measurable. Further, no material is lost to sample preparation.
- It is shown that measurements of samples in the laboratory can be used to predict bulk propagating conditions, and propagation velocity in particular, with reasonable accuracy. The agreement between laboratory and field velocity estimates is better for more homogeneous samples; the homogeneity parameters described allow a threshold level of homogeneity above which accurate estimation is expected to be defined.
- The new dielectric characterisation of economically important geological systems in the borehole radar frequency range is performed. The results are directly applicable to BHR experiment planning, showing that the fine scale delineation of ore bodies is often feasible using an appropriate BHR system.

Chapter 2

Theory

This chapter provides some of the background theory, concepts and techniques which shall be of use in the chapters to come.

Of particular importance in the discussion of material properties and electromagnetic wave propagation presented in Section 2.1 are the various representations of a material's complex dielectric constant, ϵ^* , and how it relates to the parameters — propagation velocity and attenuation — governing wave travel through rock. A number of models for the frequency representation of ϵ^* are presented in Section 2.2. Though only the Jonscher characterisation is used in this dissertation, the others are provided for completeness, and since some may be more applicable to the modelling of rock types not described well by the Jonscher power law. The concepts of capacitance and guarding are central to this dissertation and are presented in Sections 2.3 and 2.4. A measurement without an estimate of its uncertainty is somewhat limiting. A statistical approach to the determination of measurement uncertainty following internationally accepted guidelines is presented in Section 2.5. The concept of sensitivity analysis is a useful qualitative evaluation tool; a numerical implementation is often required for the sort of evaluation performed in this study. Also presented in Section 2.5.3 is an intuitive way of representing an error network graphically. Finally, and importantly, the accurate four-terminal pair measurement configuration used in this study is described in Section 2.6. Calibration is an integral part of the measurement process — its definition and implementation in this dissertation are discussed in Section 2.6.2.

2.1 Material Properties and Electromagnetic Wave Propagation

Maxwell's equations describe the behaviour of electromagnetic fields. In free space, Faraday's law and Ampère's law can be written as

$$\nabla \times \mathbf{E} = -\frac{\partial \mathbf{B}}{\partial t} \quad (2.1)$$

$$\nabla \times \mathbf{H} = \mathbf{J} + \frac{\partial \epsilon_0 \mathbf{E}}{\partial t} \quad (2.2)$$

respectively. In a polarisable (but non-magnetic) medium, the current density in (2.2) gains a polarisation current term $\mathbf{J}_p = \frac{\partial \mathbf{P}}{\partial t}$, where \mathbf{P} is the polarisation density. Ampère's equation thus becomes

$$\begin{aligned} \nabla \times \mathbf{H} &= \mathbf{J}_u + \mathbf{J}_p + \frac{\partial \epsilon_0 \mathbf{E}}{\partial t} \\ &= \mathbf{J}_u + \frac{\partial (\epsilon_0 \mathbf{E} + \mathbf{P})}{\partial t} \end{aligned} \quad (2.3)$$

where the u subscript signifies the unpaired charges involved in the conduction current $\mathbf{J}_u = \sigma \mathbf{E}$, with σ the conductivity of the material. The displacement flux density is $\mathbf{D} = \epsilon_0 \mathbf{E} + \mathbf{P}$. With the introduction of complex permittivity, (2.3) may now be written as

$$\nabla \times \mathbf{H} = \epsilon^* j \omega \mathbf{E} \quad (2.4)$$

where $\epsilon^* = \epsilon' - j\epsilon''$ is the complex permittivity.

Taking the curl of (2.1) and (2.4), interchanging time and spatial derivatives, applying a vector identity, and substituting from (2.4) and (2.1) respectively, the electromagnetic wave equations follow:

$$\nabla^2 \mathbf{E} = -\epsilon^* \mu_0 \omega^2 \mathbf{E} \quad (2.5)$$

$$\nabla^2 \mathbf{H} = -\epsilon^* \mu_0 \omega^2 \mathbf{H} \quad (2.6)$$

For simplicity, consider the rectangular plane wave solutions in a homogeneous infinite medium (transverse components of uniform plane wave propagating in the z -direction):

$$E_z = E_0 e^{-jkz} \quad (2.7)$$

$$H_z = H_0 e^{-jkz} \quad (2.8)$$

where $H_0 = E_0/\eta$ contains the characteristic impedance of the medium, $\eta = (\mu_0/\epsilon^*)^{1/2}$. (The implicit $e^{j\omega t}$ time dependence has been omitted from (2.7) and (2.8).) The wave number¹ can be written as $k = k_0 n$, where $k_0 = \omega(\mu_0 \epsilon_0)^{1/2}$ is the wave number in free space and $n = (\epsilon^*)^{1/2}$ is the complex refractive index of the (non-magnetic) medium. An instructive way of writing the complex wave number is by separating its real and imaginary parts:

$$k = \beta - j\alpha = \omega(\epsilon^* \mu_0)^{1/2} \quad (2.9)$$

where α is the attenuation factor and β is the phase factor. The complex dielectric constant, ϵ^* , may be written as

$$\epsilon^* = \epsilon_0 \left(\epsilon_r - j \frac{\sigma}{\omega \epsilon_0} \right) = \epsilon_0 \epsilon_r (1 - j \tan \delta) \quad (2.10)$$

where ϵ_r is the specific permittivity of the material and $\tan \delta = \frac{\sigma}{\omega \epsilon_0 \epsilon_r}$ is its loss tangent. From (2.9) it follows, after equating real and imaginary parts and some manipulation, that the attenuation and phase factors become

$$\alpha = \frac{2\pi}{\lambda_0} \left[\frac{1}{2} \epsilon_r \left(\sqrt{1 + \tan^2 \delta} - 1 \right) \right]^{1/2} \quad (2.11)$$

$$\beta = \frac{2\pi}{\lambda_0} \left[\frac{1}{2} \epsilon_r \left(\sqrt{1 + \tan^2 \delta} + 1 \right) \right]^{1/2} \quad (2.12)$$

To summarise: an electromagnetic field propagates through a medium, giving rise to conduction and displacement currents related to the material's conductivity, σ , and (real) specific permittivity, ϵ_r . The field is attenuated as it passes through the medium, with different frequency components suffering different levels of attenuation and propagating at different speeds. The wave's rate of propagation is

¹The wave number is sometimes also referred to as the complex propagation factor, $\gamma = jk = \alpha + j\beta$. In this case, the electric field in (2.7) is $E_z = E_0 e^{-\gamma z}$ [35].

usually equated to its phase velocity. Using the wave number from (2.9) as well as the implicit time dependence in (2.7)

$$E_z = E_0 e^{-\alpha z} e^{j(\omega t - \beta z)} \quad (2.13)$$

one obtains the phase dependence of the wave

$$\phi = \omega t - \beta z \quad (2.14)$$

which results in a phase velocity of

$$v = \frac{dz}{dt} = \frac{\omega}{\beta} \quad (2.15)$$

The ratio of energy stored to energy dissipated in the material is proportional to its quality factor, which in turn is the inverse of the loss tangent

$$\begin{aligned} Q &= \frac{1}{\tan \delta} = \frac{\epsilon'}{\epsilon''} \\ &= 2\pi \frac{\text{average energy stored per half cycle}}{\text{energy dissipated per half cycle}} \end{aligned} \quad (2.16)$$

Thus, using (2.10), the above can be written as

$$\tan \delta = \frac{\sigma}{\omega \epsilon_0 \epsilon_r} \quad (2.17)$$

Now the wave number can be written as

$$\begin{aligned} k &= \omega \sqrt{\mu_0 \epsilon_0} \left(\epsilon_r - j \frac{\sigma}{\omega \epsilon_0} \right)^{1/2} \\ &= \frac{\omega}{c} \sqrt{\epsilon_r} \left(1 - j \frac{\sigma}{\omega \epsilon_0 \epsilon_r} \right)^{1/2} \\ &= \frac{\omega}{v} \left(1 - j \frac{1}{Q} \right)^{1/2} \end{aligned} \quad (2.18)$$

which, when subjected to a binomial expansion, can be approximated as

$$k \simeq \frac{\omega}{v} \left(1 - j \frac{1}{2Q} \right) \quad (2.19)$$

provided $Q \gg 1$. From (2.19), one obtains the following simple approximation for the attenuation factor

$$\alpha = \frac{\omega}{v} \frac{1}{2Q} \quad (2.20)$$

The equivalent phase factor approximation is seen in (2.15). (The same results for α and β can be derived directly from (2.11) and (2.12) by a binomial series expansion.)

The real and imaginary parts of the complex permittivity are related to each other by the Kramers-Kronig relations [36]:

$$\epsilon'(\omega) - \epsilon(\infty) = \frac{1}{\pi} P.V. \int_{-\infty}^{\infty} \frac{\epsilon''(\omega')}{\omega' - \omega} d\omega' \quad (2.21)$$

$$\epsilon''(\omega) = -\frac{1}{\pi} P.V. \int_{-\infty}^{\infty} \frac{\epsilon'(\omega') - \epsilon(\infty)}{\omega' - \omega} d\omega' \quad (2.22)$$

where $P.V.$ specifies the use of the principal value of the integral. This relation applies to the Fourier transform of any causal signal. Another form which avoids the singularity at ω is given by [37]

$$\epsilon'(\omega) - \epsilon(\infty) = -\frac{2}{\pi} P.V. \int_0^{\infty} \frac{\omega' \epsilon''(\omega') - \omega \epsilon''(\omega)}{\omega'^2 - \omega^2} d\omega' \quad (2.23)$$

$$\epsilon''(\omega) = \frac{2\omega}{\pi} P.V. \int_0^{\infty} \frac{\epsilon'(\omega') - \epsilon'(\omega)}{\omega'^2 - \omega^2} d\omega' \quad (2.24)$$

In closing, it can be seen from the above that a knowledge of ϵ_r and $\tan \delta$ is sufficient to characterise a non-magnetic material (such as the rock we are interested in). Propagation velocity and attenuation of the wave are what determine the range and dispersion of a radar signal in rock, and these can both be determined directly from the specific permittivity and loss tangent using equations (2.11), (2.12) and (2.15).

2.2 Dielectric Modelling

The analysis of electromagnetic wave propagation through any dielectric material, including rock, requires knowledge of the material's dielectric properties. This necessitates measurement, and, for numerical analysis at frequency points outside the discretely measured ones, the construction of a model. Various possibilities exist. The Debye, Lorentz and Jonscher models will be examined here along with the analytic continuation model.

The Debye equation describes dipolar mechanisms and may as such not be entirely suitable for dry rock ([38]), but the Cole-Cole function (as well as a power law (Jonscher) function) has been successfully fitted to data obtained from measurements of water-saturated rocks (carbonates and sandstone) by Taherian *et al.* [12] over a wide frequency range (10–1300 MHz). Hollender and Tillard obtained good results by fitting their Jonscher formalism to measured data from a variety of rock samples including saturated limestones, sandstone, shale, siltite, saturated and dry granites, and schists [38]. Knight and Nur found a power law dependence in the specific permittivity of sandstones at various levels of water saturation in the frequency range of 60 kHz to 4 MHz [14].

Only the Jonscher model has been fitted to the data measured in this study, with varying degrees of success. The other models are included for completeness and to provide possible alternatives for modelling rock properties, even though time constraints did not allow their application to the data obtained in the case studies described in Chapter 6.

2.2.1 The Debye Model

The Debye model sees the dielectric as consisting of freely rotating polar molecules in a dominating non-polar medium, that is, Mosotti's hypothesis² is assumed to hold [39]. The Debye equation for complex effective permittivity may be written as

²The model used by Clausius and Mosotti for determining the behaviour of a molecule in an electric field was that of a conductive sphere. Mosotti's hypothesis essentially considers the molecule to be a polarisable system, in which displacement of charge due to a force causes the moment [39].

$$\epsilon^* = \epsilon_\infty + \frac{\epsilon_s - \epsilon_\infty}{1 + j\omega\tau} \quad (2.25)$$

where ϵ_∞ and ϵ_s are the limiting high frequency and static values of the permittivity, and τ is the characteristic relaxation time of the molecule's dipole moment. The complex permittivity in (2.25) can be separated into its real and imaginary parts:

$$\epsilon' = \epsilon_\infty + \frac{\epsilon_s - \epsilon_\infty}{1 + \omega^2\tau^2} \quad (2.26)$$

$$\epsilon'' = \frac{\omega\tau(\epsilon_s - \epsilon_\infty)}{1 + \omega^2\tau^2} \quad (2.27)$$

Commonly used generalisations of (2.25) are the Cole-Cole [40] and Cole-Davidson functions [12]

$$\epsilon^* = \epsilon_\infty + \frac{\epsilon_s - \epsilon_\infty}{1 + (j\omega\tau)^{1-a}} \quad (2.28)$$

$$\epsilon^* = \epsilon_\infty + \frac{\epsilon_s - \epsilon_\infty}{1 + (j\omega\tau)^b} \quad (2.29)$$

The parameters a and b were introduced to account for the observation in many materials of a broader frequency range of dispersion and absorption and a smaller maximum value of ϵ'' than those predicted by the Debye model, and both values fall between zero and one. Both (2.28) and (2.29) reduce to the original Debye equation when $a = 0$ or $b = 1$.

The assumptions made in the development of Debye's theory are also its limiting factor: Mosotti's hypothesis is, by Debye's own admission, his theory's weakest point. It is far more applicable to the scenario of isolated polar molecules in a predominantly non-polar background [39].

2.2.2 The Lorentz Model

In the classical model of polarisation, a resonance is produced by the displacement of a charge cloud from its central ion and the resulting restoring force. The Lorentz model in addition takes into account the damping losses that result from radiation or interaction with other charges by the addition of a dr/dt term to the equation of motion for the displacement (cf. [41, pt. I, p. 23-3]). This results in a generalised expression for polarisability resulting from all electronic and ionic responses [42, pp. 680–682]

$$\alpha_j = \frac{F_j}{(\omega_j^2 - \omega^2) + j\omega\Gamma_j} \quad (2.30)$$

where the j subscript refers to the j th resonance occurring at ω_j , F_j is a measure of that j th resonance's strength and Γ_j is the damping constant. For example, the electronic polarisability is the ratio of the induced dipole moment and the local imposed field:

$$\alpha_e = \frac{(e^2/m)}{(\omega_0^2 - \omega^2) + j\omega\Gamma} \quad (2.31)$$

where e and m are the electron charge and mass respectively. The polarisability may be simply related to polarisation and thus to the dielectric properties by the general formulation [7, p. 19]

$$\mathbf{P} = (\epsilon_r^* - 1)\epsilon_0\mathbf{E} = N\alpha\mathbf{E}' \quad (2.32)$$

where α is the total polarisability of the material, consisting of an electronic polarisability, α_e , an atomic

polarisability, α_a , a dipole polarisability, α_d , and an interfacial polarisability, α_s ³. The local field is represented by \mathbf{E}' . Also note that ϵ_r is written as a complex number, ϵ_r^* , here. This accounts for α becoming complex due to the phase shift between the driving field and the resulting polarisation, and the resulting possible loss current [35].

2.2.3 The Jonscher Power Law

As stated previously, the Debye model has some shortcomings. Equation (2.25) is not obeyed directly except in some liquid dielectrics and loss actually departs seriously from the Debye predictions in most solids [43, 44]. This may be because the formula mainly describes dipolar mechanisms, and the effects of surrounding particles are assumed to cancel [35, p. 20]. An attempt at reconciling measured data with the Debye model was the introduction of a distribution of relaxation times, which were taken into account by integration over the distribution functions of loss frequencies. Although this seemed plausible in view of inhomogeneous materials, Jonscher argued that no independent way of confirming these functions' forms exists [44].

After examining measured data of numerous materials, he noted the general rule that the frequency dependence of the susceptibility of most materials followed the fractional power law

$$\chi''(\omega) \propto \omega^m \quad (2.33)$$

for the rising part of the curve, i.e. for frequencies below the loss peak frequency ω_p , and

$$\chi''(\omega) = \cot(n\pi/2)\chi'(\omega) \propto \omega^{n-1} \quad (2.34)$$

for the frequencies higher than ω_p where the exponents m and n fall in the range (0,1). Where the behaviour of the loss is more complex, it is possible to resolve frequency dependence into a superposition of two or at most three overlapping mechanisms of type (2.33) and (2.34). These empirical equations required a physical explanation, and a possible one was provided by Jonscher [43].

First, it is important to note that the Kramers-Kronig relations, (2.21) and (2.22), imply the same frequency dependence for χ' as for χ'' , so the ratio χ''/χ' is independent of frequency, as opposed to the Debye case where the ratio is equal to $\omega\tau$. The consequence is that the ratio

$$\frac{\chi''(\omega)}{\chi'(\omega)} = \frac{\text{energy lost per cycle}}{\text{energy stored per cycle}} = \cot\left(\frac{n\pi}{2}\right) \quad (2.35)$$

is constant with respect to frequency. It is suggested that this simple criterion is the universally applicable common feature of all dielectric materials obeying (2.33) and (2.34). Conversely, if (2.35) is applicable, then (2.33) and (2.34) display the only possible frequency dependence of loss.

The physical reasoning behind this is as follows: The general property of the dielectrics considered is that polarisation is due to discontinuously hopping charge carriers (electrons, ions or even dipoles). The concept of screening charges or dipoles adjusting slowly to the quickly hopping carriers is a result of many-body interactions. Jonscher contends that this 'dual' time scale leads to (2.35) and thus, through the Kramers-Kronig relations, to the universal frequency dependence [45].

Using (2.35), the effective dielectric permittivity can now be written as [38]

$$\epsilon^*(\omega) = \epsilon_0\chi_r \left(\frac{\omega}{\omega_r}\right)^{n-1} \left[1 - j \cot\left(\frac{n\pi}{2}\right)\right] + \epsilon_\infty \quad (2.36)$$

having the four real constant parameters ω_r , n , χ_r and ϵ_∞ .

³For a more detailed summary of these polarisation types, refer to [7, p. 19]

2.2.4 The Analytic Continuation Model

The classic derivation of the permittivity function as a link between the electric flux density (or displacement vector) and the applied electric field is based on a few basic physical assumptions, such as causality, and results in a description of the permittivity in the upper complex frequency half-plane and on the real frequency axis. The failure of the theories described in the previous sections to describe some phenomena such as the optical transparency of water led to a re-examination of dispersion by Díaz and Alexopoulos [46].

The work of Kramers and Kronig showed that dispersion is an analytic necessity of causality, independent of postulated physical mechanisms. Díaz and Alexopoulos contend that analyticity should imply completeness and that the failures experienced relate to limitations in the physical mechanisms proposed rather than in the incompleteness of our understanding of dispersion.

Using the existing upper half-plane properties of permittivity and the property of analytic functions that they can be extended beyond the domain in which they are known, the description of permittivity has been extended to include the lower frequency half-plane as well. Physical observations limit the allowable singularities in the lower half-plane to poles or zeros, eliminating essential singularities and branch points. The resulting rational meromorphic permittivity function can be expressed as

$$\epsilon(\omega) - 1 = \frac{(\omega - \zeta_1)(\omega - \zeta_2)(\dots)}{(\omega - \pi_1)(\omega - \pi_2)(\dots)} \quad (2.37)$$

The denominator of (2.37) must contain more terms than the numerator since $\epsilon(\omega) - 1$ decays as $1/\omega^2$ beyond the plasma frequency. In addition, causal symmetry, expressible as $\epsilon(-\omega^*) = \epsilon^*(\omega)$, results in a partial fraction expansion of (2.37) of the form

$$\epsilon(\omega) - 1 = \sum_{n=1}^N \frac{A_n}{(\omega - \pi_n)(\omega + \pi_n^*)} \quad (2.38)$$

Each element in the sum expressed in (2.38) is known as a complex Lorentzian. They become more significant when a pole of the form $\pi_n = a + jb$ is assigned the substitutions $a = (1/LC - R^2/4L^2)^{1/2}$ and $b = -R/2L$. Each term in (2.38) then reduces to

$$C_1 = \frac{A'_1}{1 - j\omega RC - \omega^2 LC} \quad (2.39)$$

which makes (2.38) a parallel combination of series inductor-capacitor-resistor (LRC) circuits, with the capacitance C and resistance R corresponding to the dc permittivity $\epsilon_0\epsilon_r$ and the bulk resistivity ρ respectively, and the inductance L representing natural resonances in the material. Thus far only poles in the lower half-plane have been considered. Should zeros be required they can be represented by the addition of another LRC path in parallel with R .

This approach, based solely on causality and the properties of analytic functions, results in a model which successfully describes the complex behaviour of water at optical frequencies. It is interesting that a pole with no inductive part reduces to a Debye term as described in Section 2.2.1. A complete LRC element closely relates to the Lorentz type effect described in Section 2.2.2. The addition of zeros can account for more complex behaviour.

2.3 Capacitance

The capacitance between two conductors is defined as the ratio of the total surface charge on the one and the potential difference between the two [42]. Using Gauss' law [47, p. 12], this can be written as

$$C_0 = \frac{\iint_S \epsilon_0 \mathbf{E} \cdot d\mathbf{a}}{\int \mathbf{E} \cdot d\mathbf{s}} \quad (2.40)$$

to elucidate the dependence of this 'vacuum' or 'geometric' capacitance on geometry and field distribution only.

The introduction into this space of a material with a permittivity of ϵ_r has the effect of increasing the amount of charge able to be stored in the system, resulting in a capacitance of $\epsilon_r C_0$ if the potential difference remains constant. Were the material to have complex dielectric constant $\epsilon^* = \epsilon_r(1 - j\omega \tan \delta)$ with its loss component, the definition of a 'lossy capacitor' is of use. The analogy with a parallel capacitor-resistor combination, with its admittance of $Y = G' + j\omega C'$, is evident when the admittance is written as $Y = j\omega \epsilon^* C_0$. This becomes

$$Y = \omega \epsilon_r C_0 \tan \delta + j\omega \epsilon_r C_0 \quad (2.41)$$

and it is seen that $C' = \epsilon_r C_0$, the capacitance with a lossless dielectric, and $G' = \omega \tan \delta \epsilon_r C_0$ is the loss component. Note that G' has the same geometric dependence as $\omega C'$ — they only differ in magnitude by $\tan \delta$.

2.4 Guarding

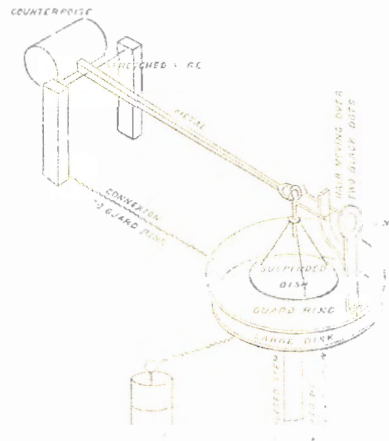


Figure 2.1: Thomson's guarded disc capacitor [48, Art. 217].

The principle of guarding may best be described by an example. Consider the case of two flat parallel conducting surfaces of infinite extent. One conductor is grounded, the other is held at some fixed potential. The capacitance between the surfaces is precisely calculable on a per area basis:

$$C/A = \epsilon/d \quad (2.42)$$

where ϵ and d are the dielectric constant of the material between the conductors and their separation respectively. Were one to only consider a finite disc-shaped area of, say, radius R , the capacitance of that disc and its corresponding area on the other electrode would be precisely $C = A\epsilon/d$.

As soon as the conductors are made finite — assume that they become circular discs — expression (2.42) is no longer valid (though it is a good approximation for large ratios of A/d). The difference is in the electric field distribution. In the infinite case, the field between the conductors was perfectly normal to the planes everywhere; in the finite case, fringing fields, not predicted by (2.42), make their appearance at the conductor edges. The resulting error in calculated capacitance increases as the ‘aspect ratio’ — defined in the disc case as the ratio of the disc radius and separation — is reduced. As shown, for example, by Nishiyama and Nakamura [49], the actual measured capacitance is over 30 % larger than that predicted by (2.42) for an aspect ratio of 0.2.

The removal of this fringing effect from a measurement would allow (2.42), for example, to be used as an accurate reference standard for the capacitance of the two parallel discs. The principle of guarding accomplishes precisely this: the enforcement of an analytically predictable field distribution in a region of interest.

This idea, originally used by Thomson in his measurements of capacitance ([50], cited in [48]), was elegantly described by Maxwell [48, Art. 217]: “In this way the force is measured only on that part of the disk where it is most regular, and the want of uniformity of the electrification near the edge is of no importance, as it occurs on the guard-ring and not on the suspended part of the disk. Besides this, by connecting the guard ring with a metal case surrounding the back of the attracted disk and all its suspending apparatus, the electrification of the back of the disk is rendered impossible, for it is part of the inner surface of a closed hollow conductor all at the same potential.”

The experimental configuration used by Thomson is shown in Figure 2.1. The idea of extending the guard to enclose the back of the sensing electrode is also mentioned in the above quote. For any physically realisable capacitor, (2.42) will of course never be perfectly valid. The small gap between the sensing and guard electrodes and the finite extent of the guard electrode prevent this.

The first of these, the finite guard-gap, results in a very slight fringing effect related to the gap width. It is usually accounted for by increasing the effective area of the sensing capacitor; for thin electrodes with small gaps, an increase corresponding to half the area of the gap is a very accurate approximation [51]. The second, the guard extent, is related to the separation between the sensor-guard combination and the opposing electrode. Again quoting Maxwell [48, Art. 201]: “...the radii of the large disk and of the guard-ring must exceed R by several multiples of A .” In this case, R and A refer to the sensing electrode diameter and the electrode separation respectively. It should be clear that this discussion is general. More detail is required for each particular type of electrode configuration, and will be presented when appropriate.

A final point is worth noting. It is usually supposed that the guard and sensing electrode must be kept at the same potential (see for example [52]), but, as Heerens points out in his review article [51], it does not matter whether the sensing or opposing electrode has a potential applied. It is the grounding of the guard electrode, and the virtual grounding of one other that is important. Despite a completely different field distribution, as shown in Figure 2.2, both configurations give exactly the same capacitance between the sensing and opposing electrodes.

2.5 The Analysis of Measurement Uncertainty

Every measurement has a degree of uncertainty, defined as “a parameter, associated with the result of a measurement, that characterises the dispersion of the values that could reasonably be attributed to the measurand.” [53]. For any measurement to be useful, the result must be given with an indication of this uncertainty. The method of evaluating uncertainty as presented by the relevant European Co-operation for Accreditation document [53] was found to be applicable to the work conducted in this study, and will be summarised in Section 2.5.1. Their approach is essentially identical to the guidelines described by the

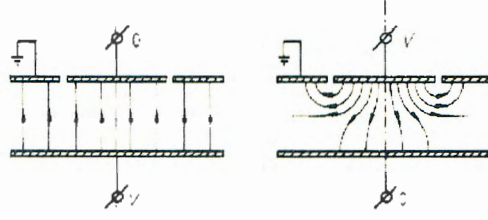


Figure 2.2: The electric field distributions found in a guarded parallel capacitor connected in two different ways. The configuration at left has the sensing electrode at the same potential as ground, while the right capacitor has the feed and ground electrodes at the same potential [51].

American National Institute of Standards and Technology [54]. The manner in which the uncertainties of the input quantities are determined makes this an essentially statistical approach. The concept of sensitivity analysis is often useful and will be introduced in Section 2.5.2, and an intuitive graphical flow-chart representation of the uncertainty analysis will be described in Section 2.5.3.

2.5.1 A Statistical Approach

The definition for ‘uncertainty’ was given above; the ‘measurand’ in this case refers to an output quantity Y , in this case for example ϵ_r or α , which is some function of a number of uncorrelated input quantities X : $Y = f(X_1, X_2, \dots, X_n)$. This function may be an analytical expression, or a more complicated relationship which is evaluated numerically, or, as in this case, a combination of the two. The input quantities X_i in all cases have an estimated value and an uncertainty associated with them. The manner in which the uncertainty is determined may be divided into two types: a ‘Type A’ evaluation relies on the statistical analysis of a series of observations, while a ‘Type B’ evaluation describes any other (non-statistical) method.

The estimated value of Y , denoted by y , is calculated using the input estimates x_i of X_i as $y = f(x_1, x_2, \dots, x_n)$. Since the quantities which are not known exactly may be treated as random variables, the variance or standard deviation may be used as a measure of their dispersion. The *standard deviation of measurement*, denoted by $u(y)$, is the standard deviation of Y , and is determined from x_i and the standard uncertainties $u(x_i)$ of X_i .

The Type A standard uncertainty of each input quantity is determined by the statistical analysis of a series of observations, which can be applied when a spread in the values has been obtained for that input quantity by several independent observations. The estimated value of an input quantity X_i may be obtained by the mean of the n individual observed values q_j :

$$x_i = \frac{1}{n} \sum_{j=1}^n q_j \quad (2.43)$$

The standard uncertainty $u(x_i)$ (also denoted by σ_{x_i} in this dissertation) is given by the experimental standard deviation of the mean, which is the positive square root of the experimental variance [53].

$$u(x_i) = \frac{1}{\sqrt{n}} \left(\frac{1}{n-1} \sum_{j=1}^n (q_j - x_i)^2 \right)^{\frac{1}{2}} \quad (2.44)$$

The Type B uncertainty evaluation is conducted by a “scientific judgement based on all available information on the possible variability of X_i ” [53]. In other words, it is an educated estimation. If care is taken, the reliability of a Type B evaluation may be equivalent to that of a Type A evaluation, especially if a relatively small number of observations was used for the latter.

Of particular use in this study is when only a lower (q_-) and upper (q_+) limit for X_i can be estimated. In this case, a probability distribution must be guessed at. If it is known that values of X_i are more likely to be near the centre of the interval, a triangular or normal (Gaussian) distribution may be a good model. In the absence of information apart from the limits of variability, a rectangular or constant distribution is a reasonable description in probability terms [53]. (This approach may for example be more valid when not enough samples are available for a Type A evaluation.) In this case, the estimated value is

$$x_i = \frac{1}{2}(q_+ + q_-) \quad (2.45)$$

and the square of the standard uncertainty can be calculated to be [55, p. 108]

$$u^2(x_i) = \frac{1}{12}(q_+ - q_-)^2 \quad (2.46)$$

The uncertainty of the output estimate y is given by the quadratic addition of the uncertainties associated with each input uncertainty,

$$u^2(y) = \sum_{i=1}^n u_i^2(y) \quad (2.47)$$

In (2.47), the contribution to the total uncertainty $u(y)$ by each input uncertainty $u(x_i)$ is determined by the sensitivity coefficient c_i : $u_i(y) = c_i u(x_i)$. This coefficient can be evaluated either analytically by taking the partial derivative of f with respect to X_i ,

$$c_i = \left. \frac{\partial f}{\partial X_i} \right|_{X_i=x_i} \quad (2.48)$$

or numerically by calculating the effect on the output y of a change in x_i of $\pm u(x_i)$:

$$c_i \approx \frac{f(x_i + u(x_i)) - f(x_i - u(x_i))}{2u(x_i)} \quad (2.49)$$

The measurand Y in this study is dependent on a number of independent variables, and will thus, according to the central limit theorem, have an approximately Gaussian distribution [56, p. 49] (according to [53], the conditions of the central limit theorem are met adequately if more than three components contribute to the output uncertainty). What this allows is the more accurate representation of the output uncertainty by multiplying $u(y)$ by a coverage factor k . If, for example, a coverage factor of 2 is used, then approximately 95.4 % of measurements will fall within $2u(y)$ of the estimation y [53]. This sort of estimation is also known as the ‘confidence level’ of the measurement [56]. Ten repeated measurements are usually taken as sufficient to reliably determine the uncertainty contributions of the inputs as calculated in (2.44) [53].

2.5.2 Sensitivity Analysis

Sensitivity analysis is frequently used in circuit analysis, for example to predict the sensitivity of a filter response to manufacturing tolerances in the capacitors used. It finds application beyond this whenever the effect on some function of small changes to its parameters is of interest. As an illustration, let the function P be dependent on a number of parameters x_i . A linear approximation of the effect of a small change in x_i can be obtained by calculating its partial derivative, resulting in the relative sensitivity [57]:

$$\begin{aligned}
 S_{x_i}^P &= \lim_{\Delta x_i \rightarrow 0} \frac{\Delta P/P}{\Delta x_i/x_i} \\
 &= \frac{x_i}{P} \frac{\partial P}{\partial x_i}
 \end{aligned}
 \tag{2.50}$$

This effectively amounts to saying that if, for example, $S_{x_1}^P = 2$, then a 1 % change in x_1 results in a 2 % change in P . For application in the uncertainty analyses conducted in this work, the unnormalised sensitivity is often more useful in that it gives the absolute change in P resulting from a small change in x_i [58]:

$$US_{x_i}^P = x_i \frac{\partial P}{\partial x_i} \tag{2.51}$$

In practice the uncertainty in P will always depend on a number of x_i . The individual changes due to n parameters are simply added to give the total measurement uncertainty:

$$\frac{\Delta P}{P} = \sum_{i=1}^n S_{x_i}^P \frac{\Delta x_i}{x_i} \tag{2.52}$$

Note also that, as mentioned, the sensitivity analysis is a linear approximation which is no longer necessarily valid if the total error is non-linearly dependent on a large individual error contribution — in this case it may be better to simply calculate the exact dependance. Since the uncertainty is mostly calculated numerically, this sort of exact calculation is usually what happens in any case.

2.5.3 Graphical Representation of Error Analysis

The graphical representation of errors discussed in this section makes for an intuitive view of what can quickly become quite an overwhelming analysis. Were P to be a function of five variables, and each of those again to depend on another five, there would be twenty-five dependencies.

An intuitive way of maintaining an overview of this potentially intricate network is shown in Figure 2.3. It is simply a graphical representation of all the dependencies at play. The dependencies of the function of interest, P , on x_i , are represented by the linking arrows; each parameter x_i is in turn dependent on a number of parameters a_i, b_i, c_i, \dots and also possibly on other x 's. The parameters a_i, b_i, c_i, \dots may, in the case shown in Figure 2.3, be seen as the final links in the network of chains (hence the double-line boundary): they are where an actual uncertainty is specified, for example of the error in measuring the thickness of sample. They do not have to be, of course — in general, any of the parameters may be the final link, or any may again depend on other parameters. Each connecting arrow represents a dependency which may be calculated either directly or by performing a sensitivity analysis using (2.50) or (2.51).

A typical error analysis using this graphical representation would perhaps be conducted as follows: Parameter a_1 is determined to have an uncertainty of 2% due to mechanical limitations. If $S_{a_1}^{x_1} = 0.5$, it would cause a 1% contribution to x_1 's uncertainty. In turn, $S_{x_1}^P = 1$, so a potential 1% error in P results from the original 2% uncertainty in a_1 . This procedure must be carried out for every path in the network, where a complete path is defined as running from the function of interest to the parameter for which an uncertainty can be specified independently. It can happen that some sensitivities may have opposite signs and cancel each other to some degree. The worst case uncertainty is of interest, thus the absolute of each potential error must be summed to obtain the total.

In addition to simply being used to calculate the measurement uncertainty, this graphical representation allows the quick pinpointing of major contributors to measurement error, which may aid in the design of a more robust and accurate measurement device.

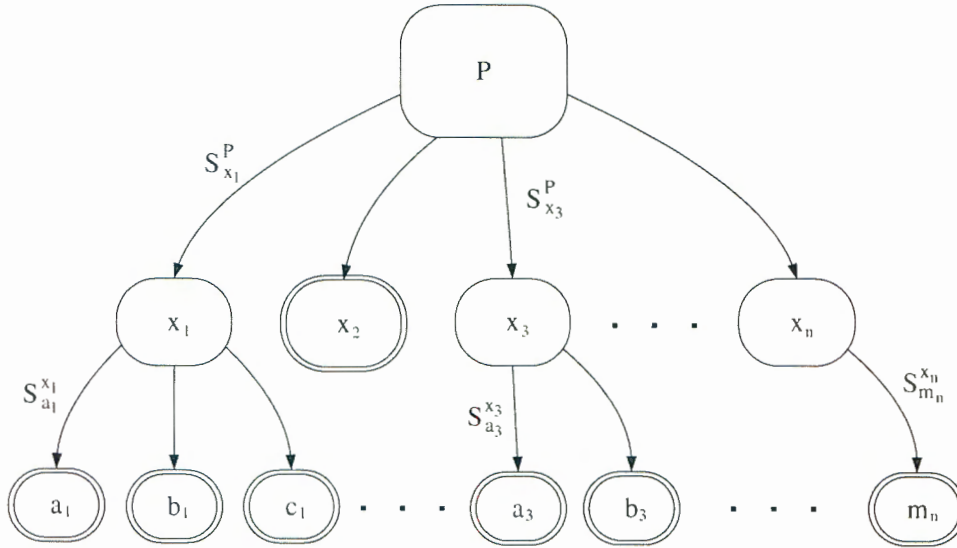


Figure 2.3: Graphical representation of how the uncertainty of a function P may be dependent on potential errors or uncertainties in a number of parameters x_i , which in turn may be dependent on other parameters $a_i, b_i, c_i, \dots m_n$. Each connecting arrow represents a dependency which may be calculated either directly or by performing a sensitivity analysis. A double-line denotes a final link at which an absolute uncertainty is specified.

2.6 Measurement with the LCR Meter

The auto-balancing bridge method of impedance measurement provides a good balance between accuracy and wide impedance measurement range, but suffers from a limited frequency range coverage [59]. Of particular interest to this work is its suitability to the measurement of guarded capacitor probes.

2.6.1 Principle of Operation

The device under test⁴ (DUT) is connected to the HP 4285A LCR meter [60] by a cabling method called the four-terminal pair configuration, the principle of which is shown in Figure 2.4. This configuration avoids the mutual coupling problems found in other configurations since the coaxial outer shield acts as the current return path, allowing no external magnetic fields to form. To realise the four-terminal pair circuit, the outer shields of the four terminals are connected to each other as close as possible to the DUT — the closer, the better the quality of the measurement [59].

The operation of the measurement configuration shown in Figure 2.4 may be described as follows. The aim is to accurately measure the voltage over and the current flowing through the DUT. The signal applied at the High Current (Hc) terminal is measured directly at the High Potential (Hp) terminal. To measure the current accurately at the Low Current (Lc) terminal, the Auto-Balancing-Bridge (ABB) is used to maintain the Low Potential (Lp) terminal at a virtual ground potential. The ABB can simplistically (but accurately, at low frequencies; at higher frequencies a more complex feedback system is necessary) be seen as using a simple operational amplifier to convert the current to a voltage. The feedback current is detected as a voltage over a range resistor. Both vector voltages are measured and separated into their quadrature components.

Some limitations of the ABB method necessitate a number of precautions when making accurate

⁴The ‘device under test’ (DUT) should not be confused with the ‘material under test’ (MUT) first referred to on p. 2 — the MUT refers only to the material being measured, perhaps in the DUT.

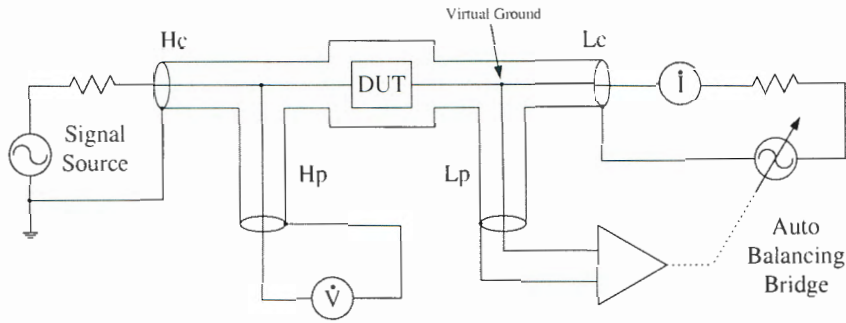


Figure 2.4: The four-terminal pair standard is defined by the ratio of open circuit voltage at the Hp port to the current at the Lc port when the current at Hp, and both the voltage and current at Lp, are zero. (Figure adapted from [60].)

measurements. As already mentioned, the signal path between the LCR meter and the DUT should be as short as possible. If it approaches a quarter of a wavelength, a standing wave may occur which does not allow the bridge to balance [61]. Additionally, the four-terminal pair construction should be extended to as close as possible to the DUT. This ensures that the measurement of the applied signal and feedback current are as accurate as possible.

2.6.2 Compensation and Calibration

According to Agilent's Impedance Meter Handbook [59], "Calibration is to define the 'calibration plane' at which the specified measurement accuracy can be obtained." Compensation, on the other hand, is a procedure whereby the errors created by the connection between the DUT and this 'calibration plane' are minimised, i.e. it is a characterisation of the test jig used. Calibration is performed by connecting a number of "standard devices" at the calibration plane, and adjusting the instrument so that the desired measurement output is obtained. However, a compensation is performed in the same way: in the LCR meter's case an open, short and load are recommended as compensation (sic) standards above 5 MHz.

While separating these definitions is undoubtedly useful to distinguish between the two concepts described in the case of Agilent's handbook, many definitions of 'calibration' are possible (see e.g. [62], [63]). According to Braudaway [64], "calibration includes establishment of all of the parameters affecting a measuring instrument." Individual definitions are necessary for differing measurement situations. The definition of two procedures is unnecessary when they together perform one function: the manipulation of a 'raw' output to give the desired result. 'Calibration' in this dissertation, at least for the measurement with the cylindrical capacitor, will be defined more broadly: a device will be regarded as calibrated when it delivers the expected results when a known DUT is measured.

The measurement strategy under consideration involves the use of the LCR meter's own compensation procedure for the parallel plate measurement of standard materials. In this case, the open, short and load measurements described below can be performed at the actual electrodes, allowing an accurate compensation. The pc-board design of the cylindrical electrodes, described in Chapter 4.4, does not allow direct open and short measurements, so the self-calibration technique described by Liu *et al.* [65] is proposed in this case. This method will rely on the standard materials measured with the parallel plate capacitor.

LCR Meter Internal Compensation

Various forms of what Agilent refers to as ‘compensation’ may be used to reduce the spurious effects of test fixture residuals. At low frequencies, a short and open compensation is sufficient to remove the effect of a feed circuit which is assumed to be adequately described by a simple series L-R impedance and parallel C-G admittance. By using a short circuit in place of the DUT, the L-R term may be obtained; an open circuit allows the series combination of the impedance and admittance to be measured.

The above assumption is only valid in very limited cases. If a custom test fixture is used [59, p. 4-4], or measurements are to be conducted at frequencies above 5 MHz [66], a load compensation should be performed in addition to the open and short compensations. The test fixture residuals may now generally be described by a two port network with transmission parameters. The DUT is successively replaced by a short, an open and an accurately known load. Measurements of each of these allows the correction of the measured DUT impedance to yield the actual material properties.

A number of sensible recommendations regarding the type of known load to be used are made in Agilent’s impedance measurement handbook [59]. The load should be 100 times smaller than the measured open impedance, and 100 times larger than the measured short, conditions easily satisfied in the measurements conducted in this study. Using a load of similar size and magnitude to the DUT results in a greater measurement accuracy; if a range of impedances are to be measured, selecting a load near the centre of this range is preferable.

In the case of capacitive measurement devices, the use of a known standard material as the capacitor dielectric suggests itself. The problem in this case is obtaining such a well-specified material — even a well known and supposedly very standard material such as Teflon is quoted in literature as having permittivities between 2.0 [67] and 2.1 [42], a 5 % uncertainty. The additional problem of procuring a material with a non-negligible well defined loss was also experienced by Wilhelms [28]. The permittivity of artificial (lossless) dielectrics can be increased by effectively adjusting the capacitor electrode spacing — this technique is described for the case of cylindrical dielectrics, used in the calibration of the cylindrical capacitor, in Appendix C.

Self-Calibration

The open, short and load compensation performed by the LCR meter is very similar to the one-reference calibration technique described by Liu *et al.* [65]. The ‘self-calibration’ methods described by Liu *et al.* for the improvement of impedance measurement accuracy are essentially the fitting of a first or second order Lagrange curve to the relation between actual and measured impedance values. This is usually sufficient, though the extension to higher order cases logically follows.

They describe two general cases: the linear and quadratic interpolation self-calibrations (LISC and QISC), which respectively rely on two and three known reference impedances. In the LISC case, if the reference impedances $\mathbf{Z}_r = [Z_{r1}, Z_{r2}]$ and measured impedances $\mathbf{Z}_m = [Z_{mx}, Z_{m1}, Z_{m2}]$ are known, then the unknown impedance Z_x may be calculated by interpolation as

$$Z_x = \mathbf{W}\mathbf{Z}_r^T \quad (2.53)$$

where the elements of the linear weighting matrix $\mathbf{W} = [W_{12}, W_{21}]$ are determined by

$$W_{ij} = \frac{Z_{mx} - Z_{mj}}{Z_{mi} - Z_{mj}} \quad (i, j = 1, 2) \quad (2.54)$$

For a non-linear measuring system, the QISC case is applicable. Three reference quantities are used, resulting in a reference matrix of $\mathbf{Z}_r = [Z_{r1}, Z_{r2}, Z_{r3}]$, measured impedances of $\mathbf{Z}_m = [Z_{mx}, Z_{m1}, Z_{m2}, Z_{m3}]$, and a quadratic weighting matrix $\mathbf{W} = [W_{123}, W_{231}, W_{312}]$ with elements determined by

$$W_{ijk} = \frac{(Z_{mx} - Z_{mj})(Z_{mx} - Z_{mk})}{(Z_{mi} - Z_{mj})(Z_{mi} - Z_{mk})} \quad (i, j, k = 1, 2, 3) \quad (2.55)$$

The calibrated impedance may be related to the reference quantities using the weighting factors explicitly as

$$Z_x = W_{123}Z_{r1} + W_{231}Z_{r2} + W_{312}Z_{r3} \quad (2.56)$$

In both cases, Liu *et al.* specify that the measured impedance value should lie between the reference impedances' measured values for accurate interpolation [63]. The choice of interpolation order depends on the system response, and in the case of a complex system its response is not easily determinable. Often the response is non-linear, and in such a case sufficient references, ideally spaced evenly throughout the measurement range, are required to adequately characterise the response and choose an interpolation. Clearly, more reference points allow a higher order interpolation. A number of test references may then be used to justify the choice and to estimate its accuracy.

As described above, the LCR meter's bridge measures real and imaginary impedance components. The fitting of theoretically determined reference impedance components to their measured counterparts thus suggests itself. The technicalities thereof and its appropriateness will be discussed in section 5.2.2. Other representations of the data may be used for the interpolation as well. For example, one could map measured capacitance to ϵ_r and measured dissipation factor to $\tan \delta$. The results will be slightly different in each case since the data points are differently spaced in their respective planes and thus the interpolation curves will differ. The most appropriate data representation will be the one in which the data points are most evenly spaced.

Chapter 3

The Parallel Plate Capacitor

3.1 Introduction

The parallel plate method of measuring material properties is well established and has already been discussed briefly in the literature review in Chapter 1. In the context of this dissertation, it provides a means of accurately characterising reference materials for the calibration of the newly developed cylindrical probe technique. The design of and measurement procedure for a simple yet robust guarded electrode configuration are presented here. The accuracy of this technique relies heavily on the ability to prepare samples with flat parallel surfaces. A relatively simple procedure for the preparation of such slices is described in Appendix B.

3.2 Electrode Design

The requirements for the design of this parallel plate electrode configuration are multiple: the mechanical construction should be simple, yet measurements should be accurate. The electrodes should interface with the four-terminal pair configuration of the HP4285 LCR meter. Importantly, the electrodes should be able to accommodate a reasonable range of sample geometries. This final requirement relates to sample thickness, which, as described below, determines the geometry of the guard electrode, and the core sample dependent diameter. The schematic description shown in Figure 3.1 will aid in the following discussion.

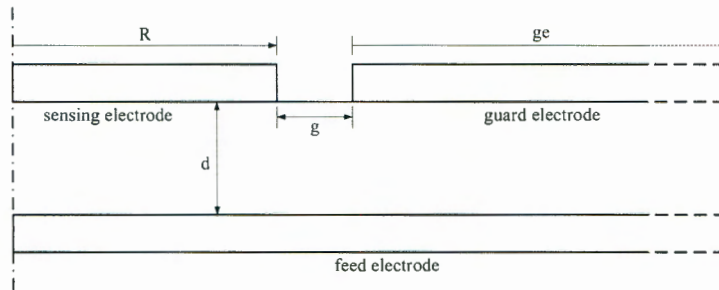


Figure 3.1: Schematic drawing of the guarded capacitor (without the cover), showing the dimensions relevant to this design discussion. The sample between the plates has a dielectric constant of ϵ^* , while the remainder of the space is filled with air. The dash-dotted line of symmetry at left marks the centre of the discs; the guard and feed electrodes extend out of view to the right.

It is sought to use the simple analytical expression for normal parallel plate capacitance as a standard reference value in the measurements. This is accomplished to a great degree by the use of the covered guard electrode configuration discussed in Section 2.4. The finite guard-gap and guard extent cause the field in the vicinity of the sensing electrode to not be strictly normal. They may respectively be compensated for and avoided to yield accurate measurements.

The gap between the sensing and guard electrodes results in a distortion of the ideal normal field distribution, and an increase to the effective sensor-feed capacitance. In general, the capacitance corresponding to half the gap width is added to the normal capacitance [68]. The normal and extra gap capacitance are given by

$$C_0 = \frac{\pi\epsilon^* R^2}{d} \quad (3.1)$$

$$C_g = \frac{\pi\epsilon^*}{d} \left[(R + g/2)^2 - R^2 \right] \quad (3.2)$$

Analytical and experimental results by Heerens *et al.* ([69], cited in [51]) show that this approximation is accurate to better than 1 ppm if, for thick electrodes, the gap depth, a , is at least five times larger than the gap width, g . The relative effect of the finite gap width on the approximation decreases exponentially with an increasing ratio a/g as $\exp(-\pi a/g)$. For thin electrodes, the guard gap should be smaller than one fifth of the sample thickness — in this case the relative effect is governed by $\exp(-\pi g/d)$. This is corroborated by the review of Goad & Wintle [68], although their focus is on thicker gaps.

The width of the guard electrode is the other design consideration which may have an effect on the ideal normal field distribution. If the guard does not extend far enough beyond the sensing electrode edge, the guard edge fringing effects may become apparent. Maxwell’s “several multiple” recommendation was quoted earlier in Section 2.4. Heerens discusses analytical calculations which show that the guard extent should be five times the sample thickness for the equations describing the normal capacitance to be accurate to within 1 ppm [70], and that the fringing fields have an exponentially decreasing effect according to $\exp(-\pi ge/d)$ as the extent is increased.

A numerical investigation into the guard extent for the limiting vacuum case was conducted using the MoM code FEKO¹ [71]. The guard extent was fixed while the plate separation d was varied to change the ratio ge/d from 2 to 20. In this range, the modelled feed-sensor capacitance changed by less than 0.5%, indicating that the guard-edge fringing fields hardly affect the normal capacitance, even when the guard is only twice the width of the sample thickness.

The reduction of these two uncertainties by appropriate geometry choices is also linked to measurable sample size. The guard extent and gap (for thin electrodes) requirements place an upper bound on the sample thickness, while, for thick electrodes, the electrode thickness to guard-gap ratio must be kept large enough. In general, the smaller the gap, the better, and the larger the guard extent, the better, but this becomes a mechanical consideration. Conversely, once constructed, the same rules can be used to determine what sample sizes are measurable.

Two general rules for a parallel plate guarded electrode design thus apply:

- The guard gap should be made as small as mechanically feasible — the resulting gap effect on uncertainty is smaller than 1 ppm if $a/g < 5$ for thick electrodes, or $g/d < 1/5$ for thin electrodes.
- Extending the guard beyond the sensing electrode by at least five times the sample thickness results in a less than 1 ppm uncertainty in the normal and gap capacitance expressions.

¹Numerical studies of small changes in geometry are difficult, but for this particular example the uncertainty caused by changes to the segmentation of the geometry was removed by keeping the same mesh and changing the ge/d ratio by moving the plates apart.

3.2.1 Electrode Construction

In specifying the electrode configuration design requirements for this application, the demands for an accurate yet simple solution were in competition. The ability to prepare samples with very flat and parallel surfaces — see Appendix B — allowed the proposal of the electrode geometry shown in Figure 3.2.

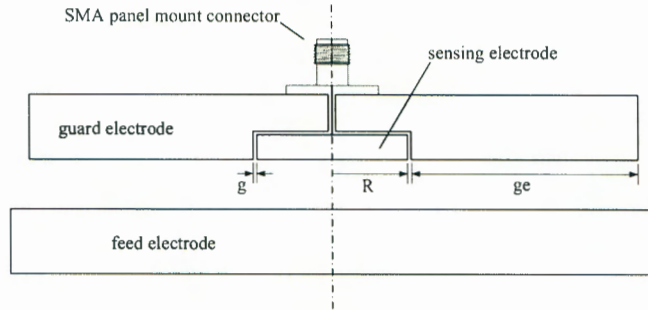


Figure 3.2: Schematic of the constructed guarded parallel plate electrode.

The lower ‘feed’ electrode is simply a disc, precision machined to have two parallel flat surfaces, with a side attachment point for a feed wire (not shown in Figure 3.2). Another disc is similarly prepared to be the guard and housing for the sensing electrode. This second disc (which can be smaller than the first disc as long as the guard extent remains sufficient) has a shallow cylindrical cavity machined out of it to house the sensing electrode. The cavity has an insulating film glued to its base with an epoxy, which in turn has the sensing electrode disc glued to it. The guard-sensor gap is filled in the same way. A staggered hole is now drilled centrally through the disc — a larger diameter from the top for the SMA connector’s insulated centre conductor to fit through, a smaller diameter from the bottom through the sensing disc to fit the centre conductor itself. Once the centre conductor is soldered to the sensing disc, the sensor-guard combination has its lower surface machined flat.

For accurate measurements, it is of critical importance that as many uncertainties and inaccuracies as possible are removed. The implication for the capacitor geometry is that it should be fixed in place for increased repeatability. It is important to keep the relative positions of the electrodes and external feed network identical throughout the measurement process (which includes the load compensation and measurement of the sample and its air comparison).

The holding jig designed to facilitate this is shown in Figure 3.3. The operation is simple. The lower feed electrode is fixed in place, while the guarded electrode combination’s movement is restricted to be vertical by the four thick rods marked ‘p’. After sample insertion, the sensing electrode is lowered until it rests on the sample. The three thin spacing rods (marked ‘s’) are now pushed down until they contact the bottom perspex support. The fasteners are tightened to keep the spacers in position once the sample is removed. Upon removal of the sample, the sensing electrode can be returned to its original position, maintaining the geometry of the structure for the air measurement.

3.3 Measurement Procedure

Measurements were made with the HP4285A LCR meter’s auto-balancing bridge [60], the principle of which was described in Section 2.6. The feed electrode is connected to the junction of the Hc and Hp terminals’ centre conductors, while the guard and sensing electrodes are connected to the joined Lc and Lp terminals’ ground and centre conductors respectively, allowing the ABB to force the centre conductor to the same potential as the grounded guard. The measurement configuration is shown photographically in Figure 3.3.

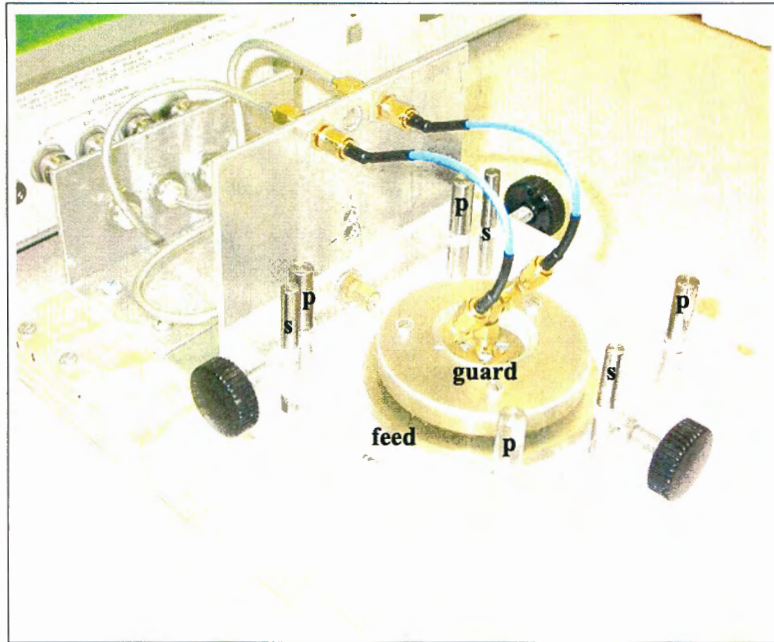


Figure 3.3: A photograph of the parallel plate capacitor designed for and used in this study. The positioning pins, marked 'p', hold the guarded sensing electrode in place, allowing only vertical movement. The spacing pins, marked 's', are used to set the air gap width to the same as that of the sample being measured.

The systematic errors due to the custom test fixture are eliminated by performing an open, short and load compensation (cf. Section 2.6.2). The open and short connections are made as described in Agilent's 16451B dielectric test fixture manual [66]. The open is created by surrounding the sensing electrode completely by the guard; this has the effect of surrounding the sensor completely with a conductor at the same potential as it, thus preventing any fields between the sensor and other conductors. The short is formed by simply connecting the sensing and feed electrodes. The custom connections created to fulfil these two requirements are shown in Figure 3.4. The aim here is to ensure repeatability, and the creation of high quality short and open circuits, by repeatedly positioning the shorting disc and opening enclosure centrally with regard to the sensing electrode. The perspex positioner shown in Figure 3.4 fulfils this function.

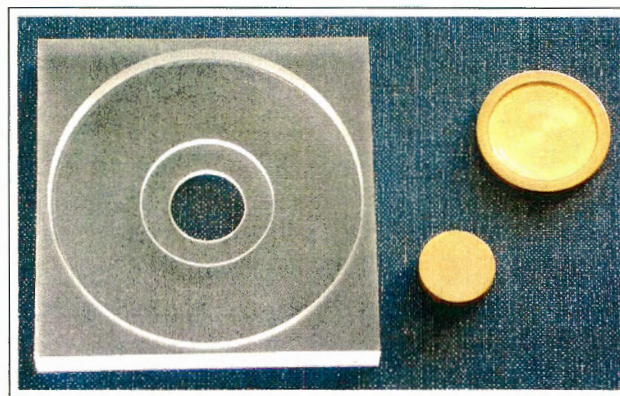


Figure 3.4: The open and short standards (right top and bottom respectively) constructed for use with the guarded parallel plate capacitor, are positioned repeatably using the perspex holder at left.

For calibration, the open, short and load (OSL) compensation described by Agilent [33] is used. The assumption is that the DUT — the guarded capacitor in this case — is connected to the bridge terminals by some network which can be described by a set of transmission parameters. These can be removed, effectively isolating the DUT, by the following calculation:

$$Z_{dut} = \frac{Z_{std}(Z_o - Z_{sm})(Z_{xm} - Z_s)}{(Z_{sm} - Z_s)(Z_o - Z_{xm})} \quad (3.3)$$

where the variables represent the following:

Z_{dut}	Corrected DUT impedance
Z_{xm}	Measured DUT impedance
Z_{std}	True value of the load standard
Z_{sm}	Measured impedance value of the load standard
Z_s	Measured value of the short circuit
Z_o	Measured value of the open circuit

The load standard consists simply of the capacitor with an air dielectric, the properties of which are assumed to be frequency independent. The plate separation is set to the same thickness as the sample to be measured, since this prevents geometric differences in the jig set-up from having an effect on the measurement.

During measurement, the only change being made to the system is thus the insertion of the sample. The impedance when the sample is inserted is only dependent on the capacitor geometry (which is the same as in the air capacitor case) and the properties of the inserted material. The extraction of the material properties relies on an adequate circuit model for the electromagnetic behaviour of the system. The need for the somewhat complex treatment of the edge fringing fields is removed by the use of the guarding principle, and the formation of the compensation open and short circuits directly at the electrodes removes the need for including an extra series impedance. As a result, a simple parallel resistor-capacitor combination fulfils this requirement in the 1–25 MHz frequency range. The resistor in parallel with the capacitor accounts for any potential loss a sample may have.

Conventionally, the true standard impedance Z_{std} in (3.3) would have been calculated from $Y_{std} = j\omega C_x \epsilon_{std}^*$, where C_x would be some reference capacitance, usually chosen as the analytical geometric capacitance ($C_0 + C_g$). Following correction by (3.3), the resulting Y_{dut} would then have been divided by C_x again to yield the measured ϵ^* . It is clear that the precise capacitance used in the calculation of the standard impedance does not affect the correction if the identical capacitance is used later in the extraction of the dielectric constant. For convenience, C_x may be chosen as 1, creating in effect a direct relation between the dielectric constant and the measured impedance.

Using this correction technique, the complex dielectric constant can thus be extracted in its constituent parts directly from Y_{dut} as

$$\epsilon_r = \frac{\text{Im}\{Y_{dut}\}}{\omega} \quad (3.4)$$

$$\tan \delta = \frac{\text{Re}\{Y_{dut}\}}{\text{Im}\{Y_{dut}\}} \quad (3.5)$$

The accuracy of the resulting measurement depends on a number of factors which will be discussed in the next section.

3.4 Measurement Accuracy

The procedure for the measurement of the complex dielectric constant of a material using the guarded parallel plate jig may be summarised as follows:

1. Conduct measurements of the various impedances required in (3.3).
2. Determine distribution of impedance values measured, i.e. their mean and standard deviation.
3. Calculate nominal dielectric constant from mean Z_{dut} .
4. Calculate the uncertainty in dielectric constant following the technique described in Section 2.5.

The uncertainty dependencies involved in this procedure may be represented graphically as shown in Figure 3.5. Both ϵ_r and $\tan \delta$ depend on the measurement repeatability of each impedance used in the calculation of Z_{dut} , as well as possible air gaps between the sample and electrode surfaces. Each of the double-line enclosed parameters shown in Figure 3.5 has an uncertainty assigned to it. Each connecting arrow represents some dependence, which is calculated as described in Section 2.5.

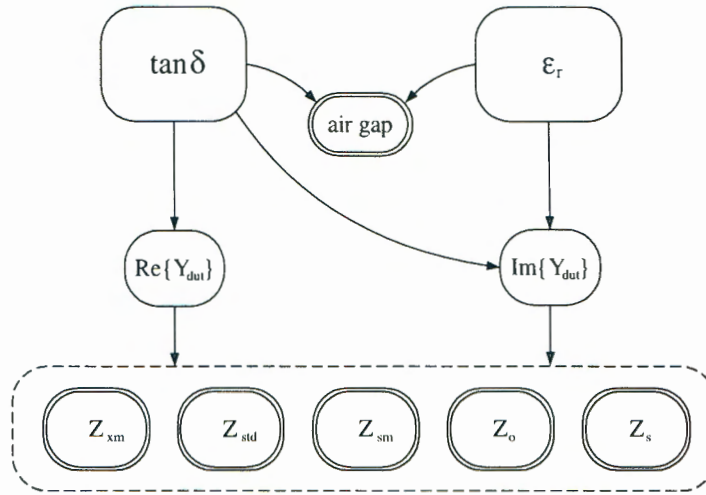


Figure 3.5: Graphical representation of the first order uncertainty dependencies in the calculation of ϵ_r and $\tan \delta$. Each Z_x in the dashed enclosure has its own associated measured repeatability.

The air gap deserves some more mention: it comes about because of the impossibility of preparing perfectly flat and smooth surfaces. The flatness and smoothness of a surface cannot easily be separated by measurement, but the measurement of the sample thickness at multiple points gives a very good indication of what sort of air gap can be expected. Half of the measured range of thicknesses may be used as a fairly good approximation for the air gap thickness. The calculation of its effect is simplified by using a circuit model approach. The impedance of an additional air capacitor, calculated using (3.1) and (3.2) with d replaced by the effective air gap thickness, is added in series to the nominal impedance calculated using $Y_{nom} = j\omega\epsilon_{nom}^*(C_0 + C_g)$, with C_0 and C_g calculated using the mean sample thickness, to form $Z_{tot} = Z_{nom} + Z_{ag}$. The effective permittivity and loss tangent for this case may be extracted by using this resulting total admittance in (3.4) and (3.5). A comparison of these values to the original nominal ones (from ϵ_{nom}^*) gives an indication of the uncertainty arising from the gap.

The effect on the measured capacitance of slight non-parallelism and surface roughness of the electrodes has been discussed by Brown & Bulleid [72]. The departures from linear behaviour were found to be very small: for an off-parallel angle between the polished electrodes of less than 0.18° , changes in the capacitance of the plates became practically undetectable when the electrodes were more than 500

μm apart. The effects of surface roughness (approximately $12\ \mu\text{m}$ surface undulation) were found to be even smaller than the effects of non-parallelism. The similarity of their capacitor dimensions to the ones in this study — their sensing electrode had a diameter of $30\ \text{mm}$ — suggests that plate non-parallelism and surface roughness leads to negligible error for small angles. As an example, an error of about $0.05\ \text{mm}$ in the preparation of a $4\ \text{mm}$ thick sample with $32\ \text{mm}$ diameter equates to a 0.09° non-parallelism, small compared even to Brown & Bulleid’s experiments. Surface undulations of a magnitude similar to those in their study are easily detected — there were none — and their effect can thus be discarded.

3.5 The Characterisation of Standard Materials

The aim here is the accurate characterisation of standard materials to be used in the calibration of the cylindrical capacitor probes. To facilitate this, a guarded parallel plate capacitor is constructed according to the guidelines described above. The capacitor was designed to comply with the additional demand that it be suitable for the measurement of prepared rock samples. The error analysis technique described in the previous section will be applied, and a brief discussion of the relationship between sample properties and measurement accuracy will be presented.

Since the standard materials used were plastic, machineable to any desired dimensions, the rock core diameters produced the main geometric design constraint. In this study, the rock slices to be measured were prepared from core samples with diameters ranging between about 32.5 and $55.6\ \text{mm}$. The sample thickness was flexible since they were prepared locally, but a thickness of about $3\text{--}4\ \text{mm}$ was easily achieved and thus chosen as the design basis since it kept the required guard extent conveniently small. Matters are eased if the sample diameter is somewhat larger than the sensing electrode diameter — it is not desirable for the sample edge to be in the vicinity of the guard-gap fringing fields². The sensing electrode diameter was thus chosen to be $20\ \text{mm}$, and actually constructed to be $19.9\ \text{mm}$. The guard gap width g was measured as $0.15\ \text{mm}$, comfortably satisfying the $a/g < 5$ requirement. The guard was extended by $24.9\ \text{mm}$ beyond the guard gap, allowing the accurate measurement of samples thinner than about $4.98\ \text{mm}$.

The reference standard materials used in this study were Teflon and Polyvinylidene Fluoride (PVDF), a specialised fluoroplastic quoted by the manufacturer as having a permittivity of 6.0 and a loss tangent of 0.165 at $1\ \text{MHz}$ [73]. Sample discs of these materials were machined by the method described in Appendix B, and measured as described above. The results for permittivity and loss tangent of Teflon and PVDF are shown in Figure 3.6.

The uncertainty in Teflon’s permittivity is between 0.8 and $0.9\ \%$ of the mean value; between 85 and $91\ \%$ of this error is contributed by the dominant air-gap uncertainty. A rise in the mean permittivity of about $0.7\ \%$ is experienced as the frequency rises from 1 to $25\ \text{MHz}$. This is indicative of an imperfect frequency compensation, since Teflon’s permittivity is generally accepted to be frequency constant in this range [7]. The uncertainty in the loss tangent of Teflon is smaller than about 0.0007 , with the air-gap contribution rising with frequency though remaining at less than $1.8\ \%$ of the total. An increase in the mean loss tangent of about 0.003 is also observed as the frequency is increased from 1 to $25\ \text{MHz}$. (The difference to the cylindrical calibration between using the rising properties of Teflon shown here or a flat frequency response is negligible.)

²This was not studied conclusively. Intuitively, if the sample edge is perpendicular to the electrode surfaces, i.e. parallel to the normal field lines, the result will simply be two capacitors in parallel: one containing the dielectric, the other vacuum. This should be valid whether the sample diameter is smaller or larger than the sensing electrode diameter. The non-normal gap fringing fields will then either be confined completely to the dielectric or air. The smaller the gap, the closer the edge can be to the gap without affecting measurement accuracy. Agilent’s HP 16451 guarded parallel plate probe manual discusses the applicable size of samples for two electrodes which have similar dimensions to the one studied here. For sensing electrode diameters of 5 and $38\ \text{mm}$ and guard gap widths of 0.13 and $0.2\ \text{mm}$, they recommend that the sample diameter be larger than or equal to 10 and $40\ \text{mm}$ respectively [66].

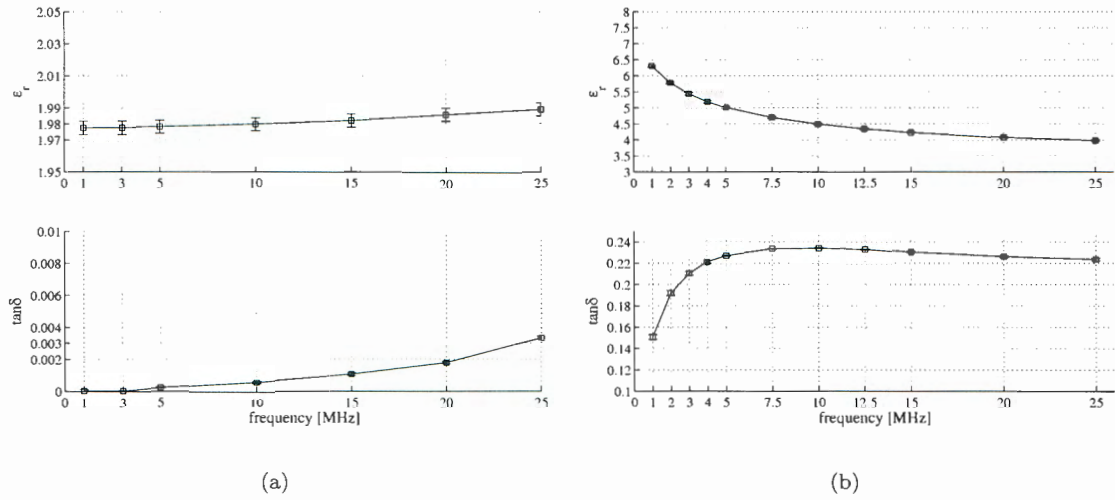


Figure 3.6: The permittivity and loss tangent of samples (a) Teflon and (b) PVDF.

In the case of PVDF, the permittivity uncertainty is between 0.5 and 0.7 %, with the air-gap contributing between 38 and 63 % of this. The loss tangent uncertainty is consistently smaller than about 0.0024, equating to a maximum of 1.5 % (at 1 MHz). The air gap contribution in this case is again low (less than 1 %) though also rising with frequency.

3.6 Conclusion

A parallel plate system has been developed for the accurate characterisation of the dielectric properties of a number of standard reference materials. One of the criteria for the electrode design was that it be able to measure prepared samples of typical rock core sizes should the need arise.

The properties of Teflon and PVDF have been measured accurately using an auto-balancing bridge with an open, short and load correction, with an estimated uncertainty of less than about 1.5 % in their permittivities, and better than 0.0025 in their loss tangents. This sort of accuracy is expected to be repeatable for any flat parallel samples larger than about 30 mm in diameter and smaller than 5 mm in thickness.

The contributing factors were the repeatability of the various impedance measurements and potential air gaps between the sample and the electrodes. The measurement repeatability was enhanced by the design of a custom jig for holding the electrodes, allowing only vertical movement of the measuring electrode. Air gaps were minimised by the careful preparation of sample; a simple technique allowing the preparation of plastic samples having a parallel flat surfaces to a tolerance of less than 0.02 mm was developed and is described in Appendix B.

Chapter 4

Cylinder Probe Design

4.1 Introduction

The aim of this study is to measure the dielectric properties of cylindrical hard rock cores non-destructively. This chapter describes the design of a guarded capacitor tailored to the unique challenges presented by the nature of the samples.

The drilling of boreholes and extraction of the cores inevitably results in small variations in the core diameter and complete breaks to core lengths. Depending on the type of rock, the breaks can be extremely irregular, not allowing the core pieces to be reassembled without substantial gaps in the material, or very ‘clean’. The electrode design should allow the measurement of such samples (to as great an accuracy as allowed by their condition), as well as the analysis of samples that are too brittle to be machined for destructive measurement techniques.

The design presented here is of a flexible guarded cylindrical capacitor based on the dielectric profiling techniques described by Moore and Paren [27], and Wilhelms [31, 28], amongst others. The flexibility of the electrodes allows them to conform to the potentially varying sample diameter (typically under about 0.2 mm along the length of a sample), as well as enabling a single constructed capacitor to host samples having a range of sizes.

The analytical solution for an ideal guarded cylindrical capacitor geometry is described in Section 4.2. It not only provides for a qualitative understanding of the electrode operation, but is also used in estimating the effect on the measurements of various non-ideal aspects of the geometry such as gaps between the electrodes. The development of a comprehensive circuit model of the proposed electrode configuration in Section 4.3 has the same objectives, but also has potential application in the extension of the device’s frequency range of operation and its use in a two port measurement system.

An important requirement for the device is that it be simple and quick to construct, yet that it be robust enough to allow repeatable measurement of core samples in the laboratory and the field. The creative implementation of a guarded shielded capacitor that allows the accurate measurement of hard rock cores of varying diameter in the 1–25 MHz frequency range will be explored in Section 4.4; detailed instructions for its construction are given in Appendix A. Limitations will be investigated and design guidelines proposed.

4.2 Analytic Solution

An analytical solution for the interior potential distribution, and resulting capacitance, of the guarded electrode configuration will be presented in this section. It follows in large part from the general treatment of the layered cylindrical problem by Wilhelms [28], whose aim was the use of an accurate calculation of

the electrode capacitance as a calibration standard for his rigid capacitor. Wilhelms used a full three-dimensional free-space approximation to motivate the sufficiency of the two-dimensional approach to the case in which the cylinder hosts concentrically layered dielectrics. These two cases adequately describe the electrode geometry in this dissertation.

The entire derivation is made under the assumption that the relatively small geometry allows an electroquasistatic approximation. According to Haus & Melcher [47], a quasistatic approximation is valid “if an electromagnetic wave can propagate a characteristic length of the system in a time that is short compared to times τ of interest”, that is $L/v \ll \tau^1$, where the electromagnetic wave propagation speed is $v = 1/\sqrt{\mu_0\epsilon_0\epsilon_r}$. Said differently, the structure’s dimensions should be small compared to the wavelength in question (always bearing in mind that the wavelength is inversely proportional to square root of permittivity — cf. (2.12)).

The frequency range of interest, 1–25 MHz, makes times on the order of about 6.4 nanoseconds relevant (in a vacuum). It is estimated, based on other studies reported in the literature (cf. references in Table 1.1), and previous measurements of rock slices [74], that the maximum expected permittivity of rock should not exceed $\epsilon_r \approx 15$ in the 1–25 MHz frequency range. Coupled with maximum dimensions of about 50 mm cylinder diameter and 50 mm sensing electrode length, this gives a system time constant of $L/v \approx 0.65$ ns. The electroquasistatic approximation is thus deemed valid.

A schematic representation of an ideal cylindrical electrode geometry is shown in Figure 4.1. The cylinder halves lie symmetrically about the plane formed by the z - and x -axes. The y -axis passes perpendicularly through the middle of the sensing electrode. The use of the cylindrical coordinate system is a logical choice, with the angle ϕ being measured positively from the x -axis.

The interior radius of the cylindrical elements is a . The sensing electrode spans an arc of ϕ_0 , centred on the y -axis, and has length l , centred on the x -axis. It is separated from the guard electrode by a small gap g . The guard electrode itself has a total length L , also centred on the x -axis, and extends azimuthally from Δ to $\pi - \Delta$, where the angle 2Δ is a measure of the small separation between the guard electrode and the feed electrode. The feed electrode has the same outer dimensions as the guard electrode, and extends azimuthally from $-\pi + \Delta$ to $-\Delta$. For the purpose of this discussion a potential of $+V/2$ is assigned to the measuring and guard electrodes, while the feed electrode is set at $-V/2$.

4.2.1 Potential Solution

Since this section assumes a vacuum filled geometry, the electroquasistatic approximation requires the solution of Laplace’s equation in the interior of the cylinder. In cylindrical coordinates [42, p. 365],

$$\nabla\Phi(r, \phi, z) = \frac{1}{r} \frac{\partial}{\partial r} \left(r \frac{\partial\Phi}{\partial r} \right) + \frac{1}{r^2} \frac{\partial^2\Phi}{\partial\phi^2} + \frac{\partial^2\Phi}{\partial z^2} = 0 \quad (4.1)$$

The solution to Laplace’s equation is uniquely determined by the boundary conditions. These can be either of the type Dirichlet, if the potential is specified on the surface, or of the type Neumann, if the first derivative of the potential, that is the charge distribution, is specified on the surface, or a combination of the two [75]. In our problem the bounding conductors are assigned potentials as specified above: the sensing and guard electrodes are at $+V/2$, the feed electrode at $-V/2$. The plane dividing the two electrode halves, i.e. $z = 0$, is also a plane of symmetry where $\partial\Phi/\partial n$ (Neumann) applies.

The potential at the boundaries where no conductor is present is somewhat more problematic. One may expect complicated field behaviour at the ends of the cylinder and the gaps between the guard and feed elements, where the potential moves from $+V/2$ through zero to $-V/2$ in some fashion. Wilhelms’ approach is to calculate the potential for the two extremes in potential transition: either all the gaps are made negligibly small, causing the potential to jump at $\phi = 0$ and $\phi = \pi$, and the cylinder is extended

¹This L should not be confused with the cylinder dimensions presented later.

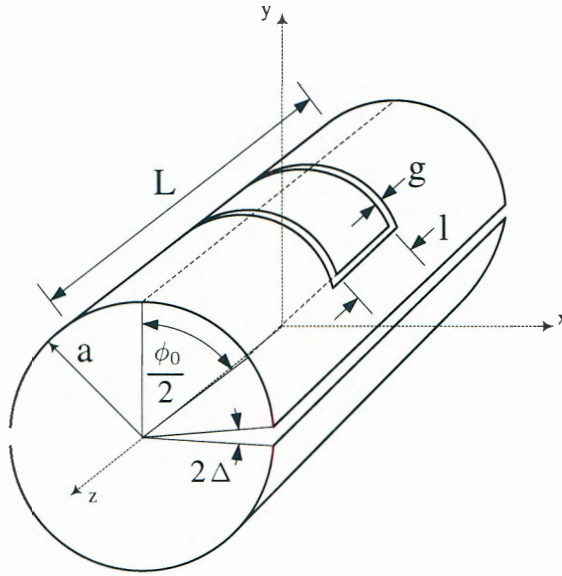


Figure 4.1: Schematic of the general cylindrical electrode geometry, showing the feed electrode at bottom and the sensing electrode surrounded by the guard electrode at top.

infinitely along the z -axis, or the potential jumps to zero at the gaps (at $\phi = \pm\Delta$ and $\phi = \pi \pm \Delta$) and the electrode ends at $z = \pm L/2$. These may be seen as the limiting cases, with the actual transitional behaviour lying somewhere between them.

Equations of the nature of (4.1) are commonly solved by the method of separation of variables. The potential is written as the product of three functions, each a function of one of the variables:

$$\Phi(r, \phi, z) = R(r)Q(\phi)Z(z) \quad (4.2)$$

Then (4.1) becomes

$$\frac{1}{r}R'QZ + R''QZ + \frac{1}{r^2}RQ''Z + RQZ'' = 0 \quad (4.3)$$

Dividing throughout by RQZ yields

$$\left(\frac{1}{r}\frac{R'}{R} + \frac{R''}{R}\right) + \frac{1}{r^2}\frac{Q''}{Q} + \frac{Z''}{Z} = 0 \quad (4.4)$$

This equation can be solved by assigning constants to the last two terms in (4.4) as follows:

$$\frac{Z''}{Z} = -k^2 \quad (4.5)$$

$$\frac{Q''}{Q} = -\nu^2 \quad (4.6)$$

Now, three ordinary differential equations result:

$$\frac{d^2 Z}{dz^2} + k^2 Z = 0 \quad (4.7)$$

$$\frac{d^2 Q}{d\phi^2} + \nu^2 Q = 0 \quad (4.8)$$

$$\frac{d^2 R}{dr^2} + \frac{1}{r} \frac{dR}{dr} - \left(k^2 + \frac{\nu^2}{r^2} \right) R = 0 \quad (4.9)$$

The solution to each of these is discussed separately below.

Axial Dependence

The general solution to (4.7) is a sum of terms of $\sin(kz)$ and $\cos(kz)$. It is known, however, that the potential must be symmetric with respect to the z -axis, thus the odd $\sin(kz)$ terms cannot form part of the solution. Further, the potential must fall to zero at $z = \pm L/2$, and so $\cos(kL/2) = 0$. A cosine term with this argument becomes zero when $kL/2 = (2n+1)\pi/2$, or $k = (2n+1)\pi/L$, where $n \in \mathbb{N}_0$. The solution for Z thus consists of terms of the form

$$\cos(2n+1)\frac{\pi z}{L} \quad (4.10)$$

Azimuthal Dependence

Similarly to the axial dependence case, the general solution to equation (4.8) is also a sum of terms in $\cos(\nu\phi)$ and $\sin(\nu\phi)$. This time, though, the potential must be zero for $\phi = 0$, this falling on the plane of symmetry between $+V/2$ and $-V/2$, and so the cosine terms are invalid. In addition, potential symmetry about the y -axis implies that only odd $\sin(\nu\phi)$ terms are allowed. A sine term becomes zero when the argument is an integer multiple of π , thus the solution for Q consists of terms of the form

$$\sin(2m+1)\phi \quad (4.11)$$

with $m \in \mathbb{N}_0$.

Radial Dependence

Equation (4.9) is a modified Bessel equation, the general solution of which is a linear combination of modified Bessel functions of the first, $I_\nu(kr)$, and second, $K_\nu(kr)$, kind [76]. Since the vacuum-filled interior of the cylinder is of interest to us, and $K_\nu(kr) \rightarrow \infty$ as $r \rightarrow 0$, only modified Bessel function terms of the first kind will occur in the solution². It has already been established that $k = (2n+1)\pi/L$ and $\nu = 2m+1$, thus the solution for R consists of terms of the form

$$I_{2m+1} \left((2n+1)\frac{\pi r}{L} \right) \quad (4.12)$$

Total Potential Solution

The total potential inside the cylinder is now given by combining the above functions linearly after (4.2), with some coefficients, resulting in a Fourier series. The general solutions for the z - and ϕ -dependences derived above are written as Fourier series expansions of 1. Thus (4.10) and (4.11) become [28]

$$1 = \frac{4}{\pi} \sum_{n=0}^{\infty} (-1)^n \frac{\cos(2n+1)\frac{\pi z}{L}}{2n+1} \quad \text{for} \quad |z| \leq \frac{L}{2} \quad (4.13)$$

²This assumption is not valid for the artificial dielectric described in Appendix C: in this case modified Bessel functions of the second kind will appear in the solution as well.

and

$$1 = \frac{4}{\pi} \sum_{m=0}^{\infty} \frac{\sin(2m+1)\phi}{2m+1} \quad \text{for} \quad 0 < \phi < \pi \quad (4.14)$$

The expansion in terms of the ϕ dependence, (4.14), is re-written as

$$\frac{2}{\pi} \sum_{m=0}^{\infty} \left(\frac{\sin(2m+1)(\phi - \Delta)}{2m+1} + \frac{\sin(2m+1)(\phi + \Delta)}{2m+1} \right) = \frac{4}{\pi} \sum_{m=0}^{\infty} \frac{\sin(2m+1)\phi \cos(2m+1)\Delta}{2m+1} \quad (4.15)$$

to take into account the finite side gaps of angle Δ . It can be seen that each term on the left of (4.15) is still an expansion of 1, and Wilhelms shows that (4.15) still satisfies the correct boundary conditions [28, p. 9]. In addition, the radial dependence, (4.12) is normalised to 1 on the boundary, $r = a$, as

$$\frac{I_{2m+1} \left((2n+1) \frac{\pi r}{L} \right)}{I_{2m+1} \left((2n+1) \frac{\pi a}{L} \right)} \quad (4.16)$$

Now the product of these three terms, (4.13), (4.15) and (4.16), with the potential of the measuring electrode, $+V/2$, to enforce the boundary condition, results in the general solution for the potential inside the cylinder:

$$\Phi(r, \phi, z) = \frac{8V}{\pi^2} \sum_{m=0}^{\infty} \sum_{n=0}^{\infty} (-1)^n \frac{\sin(2m+1)\phi \cos(2m+1)\Delta}{2m+1} \frac{\cos(2n+1) \frac{\pi z}{L}}{2n+1} \frac{I_{2m+1} \left((2n+1) \frac{\pi r}{L} \right)}{I_{2m+1} \left((2n+1) \frac{\pi a}{L} \right)} \quad (4.17)$$

4.2.2 Capacitance

With the guard electrode enforcing the desired field distribution in the region of the measuring electrode, the ideal normal interior capacitance between the feed and measuring electrodes is simple to calculate. Only the component of electric field, $E = -\nabla\Phi$, normal to the conductor surface contributes to the surface charge. By Gauss' continuity condition [47, p. 19],

$$\mathbf{n} \cdot (\epsilon_0 \mathbf{E}_a - \epsilon_0 \mathbf{E}_b) = \sigma_s \quad (4.18)$$

where region a is chosen to lie inside the conductor, region b lies inside the cylinder, and the normal \mathbf{n} points from region b to region a . The relation between the surface charge and the interior potential is then

$$Q = \int_{\xi}^{\pi-\xi} \int_{-\frac{l}{2}}^{\frac{l}{2}} \epsilon_0 \frac{\partial}{\partial r'} \Phi(r', \phi', z') \Big|_{r'=a} dz' a d\phi' \quad (4.19)$$

where Wilhelms' definition of $\xi = \frac{\pi}{2} - \frac{\phi_0}{2}$ is convenient to use.

Upon substitution of (4.17) in (4.19) and some mathematical manipulation, an expression for the free-space capacitance of the cylindrical capacitor of length l and arc coverage ϕ_0 (which takes into account the charge distribution on the finite guard beyond $z = \pm l/2$) emerges [28, p. 12]:

$$C_0 = \epsilon_0 \frac{l}{\pi} \ln \left(\cot \frac{\xi-\Delta}{2} \cot \frac{\xi+\Delta}{2} \right) + \frac{32a\epsilon_0}{\pi^2} \sum_{n=0}^{\infty} \frac{(-1)^n \sin \frac{(2n+1)\pi l}{2L}}{(2n+1)} \sum_{m=0}^{\infty} \frac{\cos(2m+1)\xi \cos(2m+1)\Delta}{(2m+1)^2} \frac{I_{2m+2} \left((2n+1) \frac{\pi a}{L} \right)}{I_{2m+1} \left((2n+1) \frac{\pi a}{L} \right)} \quad (4.20)$$

This equation has intuitively been divided into two terms as $C_0 = C_0^{\infty} + C_0^L$: the first is identical to

the free-space capacitance of the perfectly guarded sensing electrode, previously calculated by Wilhelms [31], while the second is a correction term to take into account the finite extent of the actual guard. The first term taken on its own, on the one hand, and the entire expression, on the other, correspond to the two extremes in potential transition discussed before. As $L \rightarrow \infty$, the second double summation term does indeed become zero.

The questions of convergence of the double summation, and after how many terms to terminate the summation, will be discussed in the following section.

4.2.3 Convergence

A summary of Wilhelms' discussion of the convergence of the double summation term in (4.20) will now be presented [28, Ch. 2.1.4].

Cauchy's convergence criterium can be summarised as follows: an infinite series $\sum_{v=0}^{\infty} a_v$ is convergent if, for every $\varepsilon > 0$, there exists a natural number $N(\varepsilon)$ such that $\sum_{v=n+1}^{\infty} a_v < \varepsilon$ for all $n > N(\varepsilon)$ [77]. Said simply: there must exist a value ε larger than the sum of any number of remaining terms after termination of the summation at the N th term. This ε is then the maximum allowable error of the sum. The generalisation of the Cauchy criterium to a double series requires the determination of summation limits N and M , such that any remaining sum is smaller than the error ε ([78], cited in [28]).

For a one-dimensional series with oscillating terms, like the individual components of (4.20), the summation is terminated if the oscillation magnitude remains below the specified error over a number of period lengths. In a two dimensional summation, the oscillations in both summation directions are observed. If the summation is terminated after N and M terms in the n and m directions respectively, one calculates the supremum³ of the function over a summation region bounded by N and M on the one hand, and $N + \mathcal{N}_n \mathcal{P}_n$ and $M + \mathcal{N}_m \mathcal{P}_m$ on the other. The number of period lengths, \mathcal{P}_n and \mathcal{P}_m , in the n and m direction are \mathcal{N}_n and \mathcal{N}_m respectively. The supremum of the sum over this region is an estimation of the error.

What is required now is the determination of appropriate summation boundaries N and M . This is achieved by calculating the longest period lengths in the second term of (4.20), which, to ease this task, can be rewritten as

$$C_0^L = \frac{8a\epsilon_0}{\pi^2} \sum_{n=0}^{\infty} \frac{\cos\left(\frac{(2n+1)}{2}\pi\left(1-\frac{l}{L}\right)\right) - \cos\left(\frac{(2n+1)}{2}\pi\left(1+\frac{l}{L}\right)\right)}{(2n+1)} \times \sum_{m=0}^{\infty} \frac{\cos((2m+1)(\xi-\Delta)) + \cos((2m+1)(\xi+\Delta))}{(2m+1)^2} \frac{I_{2m+2}\left(\frac{(2n+1)}{2}\frac{\pi a}{L}\right)}{I_{2m+1}\left(\frac{(2n+1)}{2}\frac{\pi a}{L}\right)} \quad (4.21)$$

The longest period in the n summation is obtained from the condition that $\mathcal{P}_n \frac{\pi}{2} \left(1 - \frac{l}{L}\right) = 2\pi$, that is $\mathcal{P}_n = 4L/(L - l)$, while the longest period in m results from $\mathcal{P}_m(\xi - \Delta) = 2\pi$, that is $\mathcal{P}_m = 2\pi/(\xi - \Delta)$. Wilhelms shows that the modified Bessel function part of (4.21) stays smaller than 1 [28, App. A.1], and, since the maximum area of a sinusoid is always smaller than its magnitude multiplied by half its period, the maximum error can be divided into [28, p. 14]:

$$\frac{32a\epsilon_0}{\pi^2} \frac{\mathcal{P}_n}{2} \frac{\mathcal{P}_m}{2} \frac{1}{2N+1} \leq \frac{\varepsilon}{2} \quad (4.22)$$

$$\frac{32a\epsilon_0}{\pi^2} \frac{\mathcal{P}_n}{2} \frac{\mathcal{P}_m}{2} \frac{1}{(2M+1)^2} \leq \frac{\varepsilon}{2} \quad (4.23)$$

³The supremum may be defined as "the least upper bound of a set S , defined as a quantity M such that no member of the set exceeds M , but if ϵ is any positive quantity, however small, there is a member that exceeds $M - \epsilon$." [79]. (Note that the symbols used in this footnote do not apply to the main text body.)

The required number of summation terms, N and M , to obtain a desired error ε can now be determined from (4.22) and (4.23). The actual value for the capacitance of the finite length cylinder will lie somewhere between the two bounds C_0^∞ and $C_0^\infty + C_0^L$. Wilhelms estimates halfway; the need for precise knowledge and further complicated analysis is reduced by keeping C_0^L small.

As an example, the capacitance is calculated for a typical geometry having $l = 30$ mm, $a = 16$ mm, $L = 50$ mm, $\phi_0 = 100^\circ$ and negligible side and sensor-guard gaps. Table 4.1 compares the number of summations in N and M , calculated from (4.22) and (4.23) respectively, required for C_0^L to converge to within the relevant error (which is stated as a percentage of C_0^∞). When a small error is specified, the large number of summations, in N particularly, quickly results in prohibitive computation times. An improvement in computational time with little loss in accuracy may be achieved by taking the mean of the last, say, 100, final elements in the (oscillating) cumulative sum of C_0^L . These sums are shown in the final column of Table 4.1; the mean value for an allowable error of 20% of C_0^∞ is within about 0.01 % of the mean value for an error of 1 %. Note that the mean does converge as the allowable error becomes smaller. The calculation of C_0^L in this way appears to lead to an error far smaller than that specified by ε .

ε (% of C_0^∞)	N	M	mean of last 100 terms of C_0^L ($\times 10^{-15}$)
20	302	12	3.52219
15	403	14	3.52237
10	605	17	3.52249
7.5	806	20	3.52252
5	1209	25	3.52254
2.5	2419	35	3.52256
1	6047	55	3.52256

Table 4.1: Comparison of the number of summation terms in N and M required to obtain the stated accuracy, ε . The mean of the last 100 terms of the cumulative sum is given in each case in the final column.

4.2.4 Discussion

The distribution and shape of those electric field lines originating or terminating on the sensing electrode is of primary importance in predicting the capacitance. In calculating C_0^∞ , certain assumptions are made regarding the geometric configuration of the guarded cylindrical capacitor:

1. The guard is assumed to be of infinite extent axially.
2. The side gaps are assumed to be infinitesimal, that is the potential goes from $+V$ to $-V$ at the x -axis.
3. The gaps between the guard and measuring electrodes are assumed to be infinitesimal.

The effect of the finite cylinder length and non-zero side gaps has been taken into account in the calculation of the correction term C_0^L . Thus two bounds to the actual capacitance value: C_0^∞ and $C_0^\infty + C_0^L$, exist. The effect of various geometric variations can be predicted using C_0^L .

Guard Length

As the guard's extent beyond the sensing electrode is reduced in length, the field lines originating on the sensing electrode are increasingly no longer forced to remain straight (in the $y-z$ plane, that is), but start spreading slightly. The question arises of how large the guard electrode extent must be for C_0^L to be sufficiently small relative to C_0^∞ , that is, for the electric field in the sensing electrode region not to be affected noticeably by the outside field distribution. It would for instance be expected that a cylinder with a smaller diameter would require a shorter guard electrode, but some quantitative analysis, in the form of a design rule relating required L to other electrode parameters, is required.

The correction term for finite length, C_0^L in (4.20), has been calculated for various combinations of a and l , chosen to cover the projected range of required geometries. Of interest is the guard length at which $C_0^L = 0.01 \times C_0^\infty$. For each length of sensing electrode, a linear relationship between L and a is found. Defining the extent of the guard electrode beyond the sensing electrode as $L_{ge} = \frac{1}{2}(L - l)$ yields the equations in Table 4.2. The dependence of L_{ge} on a decreases as the measuring electrode becomes longer because of the increase of C_0^∞ with l — the relative size of C_0^L thus decreases. A decrease in the dependence on a is also seen for increasing ϕ_0 for the same reason.

l	$\phi_0 = 100^\circ$	$\phi_0 = 120^\circ$
0.01	$L_{ge} = 1.30a - 0.004$	$L_{ge} = 1.25a - 0.004$
0.03	$L_{ge} = 1.20a - 0.007$	$L_{ge} = 1.15a - 0.007$
0.05	$L_{ge} = 1.10a - 0.007$	$L_{ge} = 1.05a - 0.008$
0.07	$L_{ge} = 1.05a - 0.008$	$L_{ge} = 1.00a - 0.008$
0.09	$L_{ge} = 0.95a - 0.008$	$L_{ge} = 0.90a - 0.007$

Table 4.2: Equations relating guard extent, $L_{ge} = \frac{1}{2}(L-l)$, at which $C_0^L = 0.01C_0^\infty$, to cylinder radius, a , were derived for various measuring electrode lengths. The measuring electrode covered arcs of $\phi_0 = 100^\circ$ and $\phi_0 = 120^\circ$; the gaps between the sensing and guard electrodes, and between the guard and feed electrodes, were taken as zero. All dimensions are in metres.

Based on these equations, a simple, if somewhat arbitrary, design rule can be proposed: For C_0^L to be smaller than 1 % of C_0^∞ :

$$L_{ge} > 1.5a \quad \text{or} \quad L > 3a + l \quad (4.24)$$

This recommendation is applicable in the range of electrode geometries which would be of interest to us. The guard extent may have to be longer than $1.5a$ for very short sensing electrodes. Longer electrode lengths would present no problem since the a -dependent term in L_{ge} is decreasing as l increases. Once designed, the exact ratio of C_0^L to C_0^∞ can be calculated for use in the estimation of the guard length's effect on predicting C_0 accurately.

Side Gap Width

As the side gap increases, the ϕ -dependence of the electric field changes. Again, the field lines originating or terminating on the sensing electrode are no longer forced to remain in the central region of the cylinder, but are allowed to spread.

Wilhelms conducted a brief analysis in which he calculated C_0^∞ while increasing the side gap Δ from 0 to 36° . He found that the capacitance increased with an increasing side gap and concluded that the gap should be kept small — a gap of about 3° was considered quite acceptable [28, p. 17].

However, the equation for C_0^∞ , identical to the first term in (4.20), was derived under the assumption of a certain electric field distribution in the $y-z$ plane, only present in its ideal form when the side gap

is negligible [31]. This assumption clearly becomes increasingly invalid as Δ is increased. Whereas a correction term, C_0^L , was added to account for the changing z -dependent field as the guard is shortened, no correction term for increasing Δ was derived.

Equation (4.20) is thus not suitable for analysis of the side gap effect, but a numerical investigation may cast some light on the problem. The results of such a simulation using the method of moments code FEKO [71] are shown in Figure 4.2. Surprisingly, it seems that opening the gap may not have as large an effect as suspected. For a larger ϕ_0 , the change in capacitance as one increases Δ does become relatively larger, as expected, since the fields originating on the outer edges of the sensing electrode will be closer to the gap, and thus more susceptible to the small changes in field distribution. To quantify: as Δ increases from 1° to 25° , the capacitance changes by about 2.9 % from its initial value for $\phi_0 = 80^\circ$, by 3.4 % for $\phi_0 = 100^\circ$, and by 4.6 % for $\phi_0 = 120^\circ$.

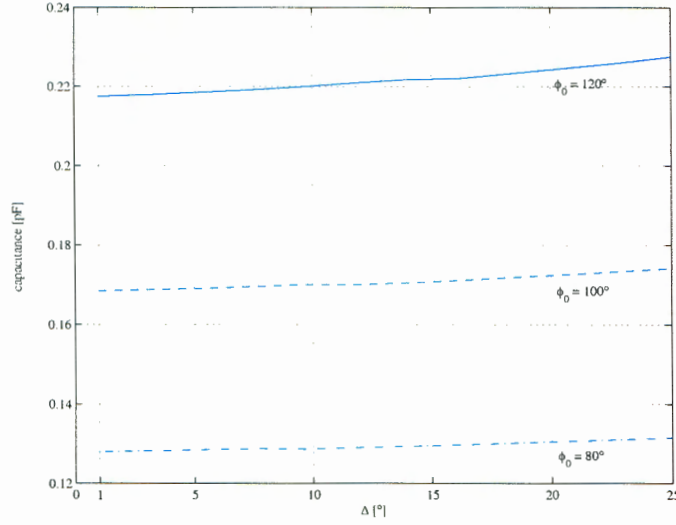


Figure 4.2: The effect on the capacitance of varying Δ from 1° to 25° has been determined numerically for a capacitor geometry with $l = 30$ mm, $L = 120$ mm and $a = 15$ mm, and $\phi_0 = 80, 100$, and 120° .

But what of a guideline for how narrow to keep the gap? To keep the capacitance within 1% of its initial, $\Delta = 1^\circ$, value, the gap must be kept below about 8° for $\phi_0 = 120^\circ$. Since this is the most stringent case, this limit is sensible for the other arc coverages as well. An 8° gap angle translates to a gap width of about 2 mm for a cylinder with $a = 15$ mm. Since this presents no mechanical problem, it is recommended simply that the gap be kept as small as mechanically comfortable, but certainly below 8° .

Guard-Sensor Gap Width

A non-infinitesimal gap between the guard and sensing electrode results in an effective area increase in the measuring electrode, provided its base area remains unchanged. This effect has been studied for parallel plate guarded capacitors, and the results obtained are applicable to the cylindrical geometry as well.

Corrections for this finite gap for the case of a guarded parallel plate have been summarised for various electrode types [68]. In general, the extra capacitance due to the gap can be written as

$$C_g = \frac{\epsilon_0 \epsilon_r P g}{2t} \quad (4.25)$$

where P and g are the total electrode perimeter and width of the gap, and t is the electrode separation.

Constructing the gap to be much smaller than the cylinder radius results in a geometry for which Heerens' thin electrode rule [51], described previously in Section 3.2, is valid: the approximation of adding a capacitance corresponding to half the gap width is accurate to better than 1 ppm if the gap width is less than one fifth the feed-sensor electrode spacing.

For the cylindrical geometry under consideration, the gap can be divided into two categories: the lateral gap, parallel to the core axis, and the perpendicular transverse gap. In the transverse gap, the electric field does not vary across the gap, so the fields will split evenly between the guard and sensing electrode, as in the parallel plate case. For the lateral gap, however, the field strength increases as the side gap between the guard and feed electrode is approached, that is as $\phi \rightarrow \pi/2$. In this case one would thus expect an increase in the normal capacitance of slightly less than half of the gap capacitance. In both cases, a maximum estimate of the capacitance increase is that of half the gap capacitance.

The extra vacuum capacitance due to the gap can be estimated using the first term of (4.20) with $\Delta = 0^\circ$:

$$C_{g0}(l', \xi') = 2\epsilon_0 \frac{l'}{\pi} \ln \left(\cot \frac{\xi'}{2} \right) \quad (4.26)$$

For the lateral and transverse gaps respectively, the total additional gap capacitance will be

$$C_{gl} = 2 \times [C_{g0}(l + 2g, \xi - \gamma/2) - C_{g0}(l + 2g, \xi)] \quad (4.27)$$

$$C_{gt} = 2 \times C_{g0}(g/2, \xi) \quad (4.28)$$

where γ is the gap's arc coverage. The gap corners have been included in the expression for lateral gap capacitance. A maximum estimate of the total capacitance due to the gap to be added is now simply the sum

$$C_g = C_{gl} + C_{gt} \quad (4.29)$$

Correction curves for the finite gap may be calculated by (4.29) for specific sensing electrode geometries. Shown in Figure 4.3 is the effect of increasing the gap for some typical configurations. The fringing capacitance increases less quickly relative to C_0 for larger sensing electrode areas. Not shown in Figure 4.3, but also of interest, is that an increase in ϕ_0 will affect C_g more than the same increase in l^4 . This is again due to the increasing electric field intensity as the cylinder sides are approached.

Guard-sensor gaps of smaller than 0.2 mm are easily realisable with the etched substrate electrodes construction proposed in Section 4.4. Since the expressions given above are an approximation, it is recommended to keep the guard-sensor gap as small as possible to minimise uncertainty.

4.3 Circuit Model

A circuit model of the guarded, shielded capacitor aids understanding of its operation and measurement, and can be useful in the design of capacitors. A model can be made valid for any arbitrary frequency range by increasing its complexity to account for non-quasistatic effects and the inevitable resonances caused by various inductor-capacitor combinations. Of interest in this case, however, is a certain frequency range, so the least complex model which adequately describes the electromagnetic phenomena in this band is sought. The model developed here applies to the electrode configuration described in Section 4.4.

First consider a two-dimensional view of proposed electrode configuration as shown in Figure 4.4. The capacitor is accessed via the two ports shown. The wires connecting the ports to the shield represent

⁴No quantitative analysis of the relative effects of these two geometric changes was done.

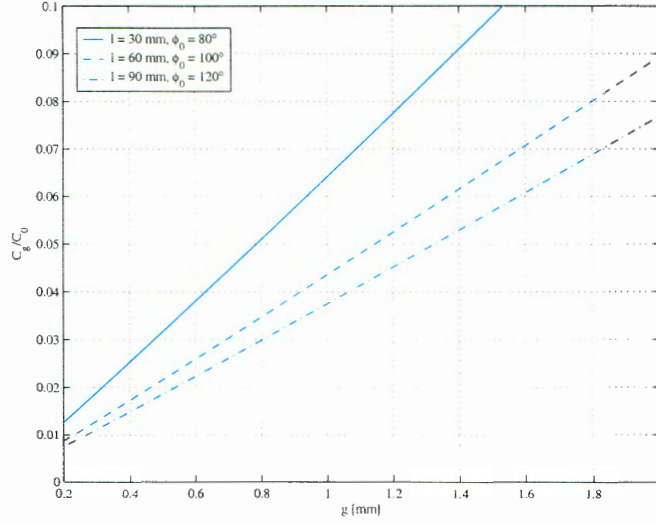


Figure 4.3: The relative gap correction capacitance increases as the gap is widened.

the outer conductors of the coaxial feeds, while the shorter wires connecting the ports to the sensing and feed electrodes represent the sensing conductors. Defining a specific ground point is difficult, since the two feed points are removed from each other and may have a potential difference between them, but the outside of the shield can be regarded as being at one potential in the frequency range of interest, and is thus the best choice.

The geometry shown in Figure 4.4 has the advantage that the capacitance can either be extracted from a full two-port S -parameter measurement, or by connecting the electrodes in the classical guarded capacitor configuration described in Section 2.4. Note that these two measurements are essentially equivalent if the two-port admittance parameters Y_{21} or Y_{12} are extracted from the two-port measurements: $Y_{12} = I_1/V_2|_{V_1=0}$, that is, the transfer admittance is the ratio of the current at one port to the voltage feed at the other. Since this device is passive, and will not contain any nonreciprocal media, $Y_{21} = Y_{12}$ and $Z_{21} = Z_{12}$ [80, p. 193]. This also reinforces Heerens' statement concerning the connection of guard electrodes [51], mentioned previously in Section 2.4.

The most intuitive way to construct the circuit model shown in Figure 4.5 is perhaps to ascribe relevant circuit elements to each part of the geometry shown in Figure 4.4, starting with an equivalent parallel resistor and capacitor, R_{dut} and C_{dut} , representing that part of the core sample penetrated by the electric fields between the sensing and feed electrodes in region a . The two capacitors on either side of the DUT RC combination, C_s , represent the additional capacitance of the thin layers of substrate on which the electrodes are etched. The internal electric fringing fields between the guard and feed electrodes in region b can be represented by a similar element containing R_{gf} and C_{gf} , as can the internal fields between the guard and sensing electrodes, by $R_{gc,int}$ and $C_{gc,int}$. Regions c and d contain no dielectric and thus their fringing fields are represented by single capacitors C_{fs} and C_{cs} respectively. Finally, the current paths in chambers c and d are accounted for by the inductors L_1 and L_2 , with the feed wires connecting to the respective electrodes being dominant.

This relatively simple model adequately describes the device in the frequency range of 1–25 MHz. The inductances associated with current flow through the ground conductor at bottom have been included in L_1 and L_2 as appropriate. The capacitors C_{fs} and C_{cs} combine the external sensor-guard and sensor-shield, and external feed-guard and feed-shield capacitances respectively.

A qualitative analysis of this equivalent circuit reveals a number of properties interesting to the design process and measurement. The first point of interest is the interaction between the feed inductors and

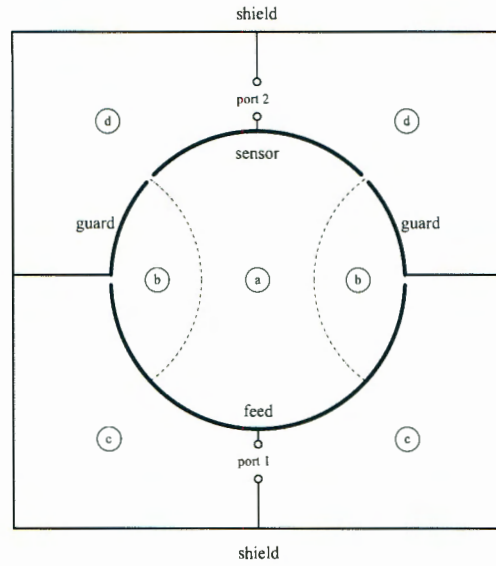


Figure 4.4: An x - y plane cut through the centre of the device clarifies the construction of the circuit model. The core is contained in regions a and b , with region a hosting the field lines of interest in the measurement and b being the internal fringing region, while the external fringing occurs in regions c and d .

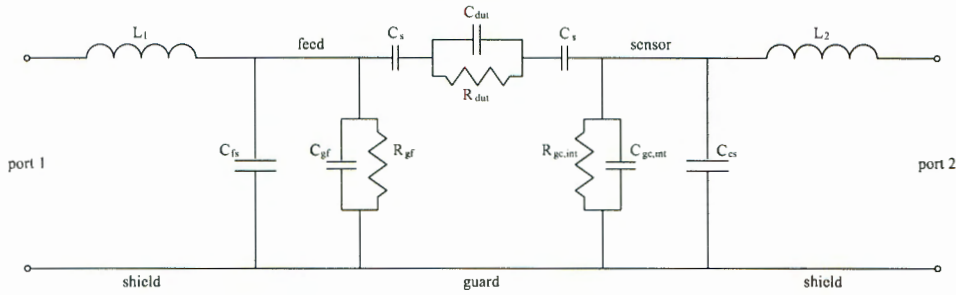


Figure 4.5: This circuit model describes the device shown in Figure 4.4 electrically. The nodes corresponding to the various electrodes are marked. The inductors combine the respective shield and wire inductance paths, while C_{fs} and C_{cs} combine the respective electrode-guard and electrode-shield capacitances.

the various capacitor combinations — the resulting resonances limit the measurable frequency range of the device. The two lowest frequency resonances are formed by the interaction of L_1 with the parallel combination of $C_{fr,1}$ and $C_{dut} + C_{fr,2}$, and the interaction of L_2 with the parallel combination of $C_{fr,2}$ and $C_{dut} + C_{fr,1}$. Here, $C_{fr,1} = C_{fs} \parallel C_{gf}$ and $C_{fr,2} = C_{cs} \parallel C_{gc,int}$. The effect of the DUT properties on the capacitance values of C_{dut} , C_{gf} and C_{gc} is to lower these resonant frequencies (of the form $1/\sqrt{LC}$).

Another pertinent question is how the relationship between $Z_{dut} = 1/j\omega C_{dut}^*$ and Z_{tot} , the total impedance between ports 1 and 2, is affected by the various fringing components. Of interest to us is the potential over and the current through the DUT, so it is important to understand how the measured impedance differs from the actual impedance. Consider a signal source applied to port 1. The total current drawn by the device, related to the total impedance observed at this port, causes a potential drop over L_1 . The current divides between the first fringing capacitance, $C_{fr,1}$, and the DUT branch. This latter DUT current then flows mostly through L_2 — which also causes a (much smaller) potential drop — into port 2, where it is measured. The portion of the current through Z_{dut} diverted to ground through $C_{fr,2}$ is minimal when the auto-balancing bridge measurement technique described in Section 2.6

is used, since there is then essentially no potential difference between the sensing and guard electrodes. Were the source to be placed at port 2, a similar scenario would unfold, with a dominant potential drop in L_2 and the major current diversion by $C_{fr,1}$.

The major effect on measurement accuracy is thus caused by the potential drops over the two feed inductors and the substrate capacitors. These effects on the measurement are controllable by appropriate design of, in particular, the shield and feed geometry of the capacitor. It is clearly desirable to increase the measurable frequency range and decrease the potential drop and current diversion effects described. These can all be accomplished in principle by reducing the inductance and capacitance values.

4.3.1 Component Value Estimation

A good estimate of the various component values may be obtained by numerical simulation using, for example, FEKO [71], and by two-port measurement using a network analyser. These may be used as a starting point from which other techniques may be used to refine the values to fit actual measurements of the constructed device. This sort of parameter determination only has to be conducted once for each electrode configuration, since the various geometric capacitance values are purely dependent on the device geometry.

Two adjustments to the geometry provide almost all the information required for the determination of the inductive and capacitive component values: a) the feed is short-circuited to the guard electrode, and b) the sensor is short-circuited to the guard electrode. The geometries shown in Figure 4.6 result.

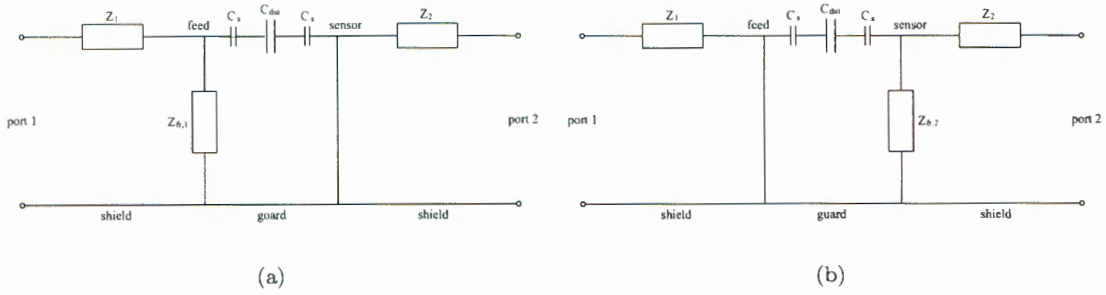


Figure 4.6: (a) Short-circuiting the sensing and guard electrodes allows the determination of Z_2 from the two-port parameter Z_{22} , and with knowledge of Z_1 , gives a value for $Z_{fr,1}$. (b) Similarly, short-circuiting the feed and guard electrodes allows the determination of Z_1 and $Z_{fr,2}$.

In the first case, Figure 4.6(a), the two-port parameter $Z_{22} = V_2/I_2|_{I_1=0}$ yields a value for Z_2 . The phase in the frequency range of interest is equal to $+90^\circ$ to within a negligible amount, suggesting that Z_2 is almost purely inductive. The extraction of a value for $L_2 = |Z_{22}|/\omega$ follows directly. Similarly, the second case, Figure 4.6(b), leads to a value for $L_1 = |Z_{11}|/\omega$.

Once values for the inductors have been obtained, the fringing components $Z_{fr,1}$ and $Z_{fr,2}$ can be calculated. In the case of Figure 4.6(a), the phase of Z_{11} is about -90° , suggesting a dominant capacitive behaviour⁵. A value for $Z_{fr,1}$ can be determined from the total value of Z_{11} , which in this case is

$$Z_{11} = Z_1 + Z_{fr,1} || Z_{dut} \quad (4.30)$$

where $Z_1 = j\omega L_1$, and $Z_{dut} = 1/j\omega C_{dut} + 2/j\omega C_s$; C_{dut} is given theoretically by (4.20) and C_s may be estimated analytically as described in Section 4.4. Now the total fringing capacitance on the side of

⁵The inductances L_1 and L_2 are typically on the order of a few nH, while the capacitances $C_{fr,1}$ and $C_{fr,2}$ are a few pF in size. The total impedance $Z = j\omega L + 1/j\omega C$ is thus completely dominated by the capacitive term in the frequency range of interest.

port 1, incorporating C_{fs} and C_{gf} , can be calculated as $C_{fr,1} = 1/\omega |Z_{fr,1}|$. In the same way, a value for $C_{fr,2}$, incorporating $C_{gc,int}$ and C_{cs} can be determined from

$$Z_{22} = Z_2 + Z_{fr,2} || Z_{dut} \quad (4.31)$$

The separation of $C_{fr,1}$ and $C_{fr,2}$ into their respective internal and external (with respect to the core) components requires some more work. The proportionality between the internal capacitances C_{gf} and $C_{gc,int}$ and the core permittivity can be used to estimate their values separately from C_{fs} and C_{gc} , which do not depend on the core material. A lossless artificial dielectric can be implemented by placing a conducting cylinder centrally in the core cavity, as described in Appendix C. By varying the ratio between this cylinder's radius and the electrode radius a , a range of effective permittivities can be obtained. Using the vacuum capacitance and a capacitor containing such an artificial dielectric, the capacitances can be separated:

$$C_{fr,1,\epsilon_r} = \epsilon_r C_{gf} + C_{fs} \quad (4.32)$$

$$C_{fr,1,0} = C_{gf} + C_{fs} \quad (4.33)$$

where the additional subscripts ϵ_r and 0 denote the results for the core containing the artificial dielectric and vacuum respectively. Subtracting (4.33) from (4.32) results in

$$C_{gf} = \frac{C_{fr,1,\epsilon_r} - C_{fr,1,0}}{\epsilon_r - 1} \quad (4.34)$$

and thus immediately also $C_{fs} = C_{fr,1,0} - C_{gf}$. An identical procedure using $C_{fr,2}$ also leads to the separation of C_{cs} and $C_{gc,int}$.

4.4 Electrode Implementation

The aim in this section is to review the requirements for an electrode system to accurately measure rock core samples, then to propose and discuss a design. The discussion will be kept fairly general. It is not the aim here to give a detailed design procedure — a detailed construction procedure for the electrodes is presented in Appendix A — but rather to introduce some of the concepts and compromises involved.

4.4.1 Electrode Geometry Design

The qualitative discussion of electrode geometry design presented here is intended to highlight some of the compromises involved. Beyond the rules described previously for constructing the guard to minimise uncertainty in the analytical capacitance expression, it should be said at the outset that there is no ‘correct’ or ‘optimal’ electrode geometry. Certain geometries may be more suitable for certain measurement situations, but the use of the LCR meter’s bridge system ensures that a large range of capacitances, and certainly any capacitor typically constructed for the measurement of rock cores, may be measured accurately.

The one fixed dimension is the diameter of the core. This has no bearing on the calculation of C_0 , but does impact on the guard electrode dimensions. The choice of sensing electrode dimensions l and ϕ_0 is subject to a number of considerations. A longer and wider (where by ‘wider’ a larger arc coverage is meant) electrode results in a larger, arguably more easily measurable, capacitance, as well as exposing a larger region of the core to the measuring field. A wider sensing electrode arc coverage will make the measurement more susceptible to the effects of side gap field disturbances. The resolution of a longer electrode, its ability to measure rapid transitions and small inclusions, will be diminished but it will give

a better average indication of the rock's properties, particularly if it is quite complex geologically (like the pegmatoidal feldspathic pyroxenite measured in Section 6.3). Wilhelms suggests that the resolution of such an electrode is of the order of the electrode length [28, p. 45]. The measurement of small inclusions depends on whether the change in averaged properties of the host and inclusion can be distinguished by the method described in Section 5.3. A shorter electrode will be more sensitive to the measurement of fine variations in the rock and the characterisation of the properties of narrow inclusions.

The guard surrounding the sensing electrode is required to enforce a field distribution which allows the use of the derived analytical expressions. Deviations from the ideal caused by finite extent of the guard and the gaps between it and the other electrodes need to be considered. Design equations for guard length derived earlier (see Table 4.2) allow the choice of an adequate axial guard extent. The effect of finite side gaps on the sensor-feed capacitance is small if the gaps are not too large. The guard-sensor gaps are taken into account by adding the correction calculated by (4.29) for the additional gap capacitance to C_0 . It should be noted that the generally accepted practice of minimising air gaps also has the detrimental effect of increasing fringing capacitances, although the effect is negligible if the electrodes are used by feeding port 1 and measuring at port 2 in Figure 4.5. A compromise between an accurately known field distribution and not too excessive fringing component values is required, particularly if using a two port measurement technique.

The extension of the guard electrode around the back of the sensing electrode is required to eliminate fringing fields between the feed and the back of the sensing electrode. Enlarging this extension to stretch along the entire length of the guard electrode, as well as to enclose the feed electrode, has certain construction advantages which shall be discussed presently. The extension of the guard in this way effectively isolates the region inside the shield from the outside. The sensing electrode in particular is far removed from any external field influences. The shield's interior is divided into three, essentially separate, parts. The inside of the cylinder, the measuring region, is not affected by the areas between the electrodes and shield, provided the inter-electrode gaps are kept reasonably small. This allows substantial flexibility in the precise geometry of the shield: standard shield dimensions despite differing core diameters simplify the design of a jig for holding the shielded capacitor in place. A detailed design for such a holding jig, necessary for making repeatable measurements, is presented in Appendix A.

4.4.2 Practical Considerations

A primary goal for the electrode construction is to provide a well-defined field distribution in the central cylindrical region. The critical design area is thus the sensing electrode: it and the immediately adjacent guard must be carefully constructed if the field is to be described as precisely as possible by the analytical solution presented in this work. The requirements for the further removed guard regions and the shield are less stringent, provided certain requirements are met.

Of interest is the measurement of hard rock core samples. An unavoidable consequence of the drilling operation is that the diameters of cores from boreholes of the same size designation, and even from the same borehole, may differ. The differences are often of the order of a few tenths of a millimetre. The avoidance of air gaps between the electrodes and core is of paramount importance: their dimensions would not be quantifiable with any sort of reasonable accuracy and their effect would thus not be removable. It is also undesirable to construct an entire new electrode set for every slight variation in core diameter.

Both of these problems can be addressed by the use of flexible electrodes which are pressed against the core. The careful etching of the electrodes onto a thin flexible single sided pc-board substrate allows this flexibility, and a very precise dimensioning of the sensing electrode and guard gap. Another advantage of this manner of electrode construction is its speed. A single electrode can be adjusted for small variations in core diameter by taking advantage of its flexibility, but a core whose diameter differs by more than a few tenths of a millimetre from the intended design diameter requires a different set of electrodes to

be constructed to ensure elimination of the air gap. This becomes an easy process if one can simply etch a new electrode set. Wrapping the electrodes around the core with the substrate side touching the rock holds the advantages of allowing easy access to the electrodes from the ports, and protecting the electrodes from scratching by the core and the associated changes to the electrode geometry.

Further requirements for the construction are that it be quick and simple to construct, yet that it provide adequately accurate measurements. As can be concluded from the calibration procedure described in Section 2.6.2, the measurement accuracy is to a large degree dependent on the ability to make repeatable measurements. These can only be ensured if the device is robust enough to withstand the mechanical strain of having samples passed through the cylinder cavity. The conflict between having a flexible set of electrodes and a rigid unmoving remainder of the system is apparent.

The only strain on the device during measurement, and thus the largest factor influencing measurement repeatability, is the movement of the cores through the capacitor. Two design choices, both related to the substrate, can reduce the strain considerably. Firstly, the use of a smooth substrate material with a low friction coefficient will allow easier passage of the core. Secondly, a thinner more flexible substrate will require less pressure to close snugly around the core. In combination, these allow easier sample movement and thus less system deformation.

The use of a flexible electrode does not affect the calibration procedure but does necessitate some additional steps to extract the correct core properties. Two effects must be compensated for: the presence of the substrate layer between the core and the electrodes, and the slight changes in electrode geometry due to the changing core diameter.

Substrate Effect

The substrate used was chosen for several reasons: its flexibility allows it to be formed around the MUT core with very little mechanical effort, while the smooth laminate surface allows samples to be passed through the cylinder with a minimum of pressure, thus lowering the mechanical strain on the entire device and increasing measurement repeatability and measurement accuracy.

The presence of the substrate naturally does have an effect on the measurement, though. This effect is expected to differ for varying geometric and dielectric properties of the MUT. Wilhelms addresses the problem of concentrically cylindrically layered dielectrics [28] by an iterative approach, but a simpler approximation is adequately accurate and more instructive when only a thin outer layer is to be added to the core, as is the case here.

The addition of this thin additional layer can be modelled accurately by adding another capacitor, labeled C_s , in series to the original core capacitance predicted by (4.20). The effect of such a thin layer — the substrate used in this study typically has a thickness of $d_s \approx 50 \mu\text{m}$ — on the electric field distribution is not noticeable. Two approximations for the description of this extra capacitance suggest themselves: those of a coaxial cylinder or of a parallel plate capacitor. (In both cases, the effect on the geometric capacitance is under consideration.)

The capacitor C_s in fact consists of two parts, one each corresponding to the area of substrate layer immediately bordering the sensing electrode and the corresponding region of the feed electrode. If the ratio of outer and inner radii of the substrate layer is defined as $v = b/a$ (where a corresponds to the core radius, and $b = a + d_s$), then, in the coaxial case (using [42, p. 196]),

$$C_{s,c} = \frac{1}{4} \frac{\phi_0}{\pi} \frac{2\pi l \epsilon_0}{\ln(b/a)} = \frac{\phi_0 l \epsilon_0}{2 \ln(v)} \quad (4.35)$$

where the quarter multiplier arises from the consideration of two half-coaxial capacitors in series, and the sensing electrode region is demarcated by the ϕ_0/π factor. The second approach sees the series addition of two rectangular parallel capacitors with plate spacing $(b - a)$ and width of $\phi_0(b + a)/2$:

$$C_{s,pp} = \frac{1}{2} \frac{(b+a)\phi_0 l \epsilon_0}{2(b-a)} = \frac{\phi_0 l \epsilon_0}{4 \frac{v-1}{v+1}} \quad (4.36)$$

The substrate capacitance may thus be written as

$$C_s = \frac{\phi_0 l \epsilon_0}{2V_f} \quad (4.37)$$

where V_f assumes either $\ln(v)$ or $2 \frac{v-1}{v+1}$, depending on which approximation is used. It is simple to show that the two in fact approach each other as $v \rightarrow 1$, that is, as $d_s \rightarrow 0$. The agreement between the two, to better than the fifth decimal when $v < 1.05$, demonstrates that practically no field spreading occurs in the substrate.

The impedance takes into account the complex dielectric constant of the substrate, ϵ_s^* , measured using the parallel plate capacitor described in Chapter 3. The substrate effect may be removed by the subtraction of the two substrate capacitors' impedances Z_s from all measured impedances before the calibration is carried out.

$$Z_s = \frac{1}{j\omega\epsilon_s^*C_s} \quad (4.38)$$

Changing Diameter Effect

A specific electrode is designed for a nominal core diameter, and to be able to accommodate smaller and larger cores providing the side gaps remain small enough so that the guidelines described in Section 2.4 are enforced. Since the sensing electrode has a fixed width corresponding to the nominal ϕ_0 , any change in the core diameter will result in an effective change to the arc coverage angle.

This effect may be simply compensated for. The nominal electrode width, given by $\phi_0 R_0$, does not change and is thus also equal to the new core radius, given by $\phi_x R_x$. The new core angle is thus trivially written as

$$\phi_x = \frac{R_0}{R_x} \phi_0 \quad (4.39)$$

Since the complex dielectric constant may in general be related to the measured impedance by the vacuum capacitance as $Z = 1/j\omega\epsilon^*C_0$, the effect of the change in the sensing electrode arc may be approximated by simply calculating the ratio of $C_0(\phi_0)$ to $C_0(\phi_x)$. The adjustment to the dielectric constant is thus

$$\epsilon_{eff}^* = \epsilon_{dut}^* \frac{C_0(\phi_0)}{C_0(\phi_x)} \quad (4.40)$$

where ϵ_{dut}^* is the calibrated measured value for ϵ^* before the diameter effect is accounted for.

Another effect of the changing core diameter is the relative change in the side gap angles. As with the sensing electrode arc coverage, the one side gap width remains fixed and thus its angle changes. This effect is small. The other gap changes more substantially. One of the design criteria in deciding what range of core diameters to accommodate was that this gap stay larger than about 0.5° and smaller than about 8° (cf. Section 4.2.4). So not only do the side gaps' angles change, but they become asymmetric as well.

A careful numerical investigation into the effects of asymmetric gaps on the sensor capacitance was conducted using FEKO. Since fine differences in capacitance are being investigated, all influence due to gridding of the geometry were removed. By keeping the sensing and guard electrodes constant, and gridding the feed electrode identically while rotating it slightly from its symmetrical position to either side, the effect of the changing gap may be isolated.

In this way, the side gaps were changed from a symmetric 4.5° to being 1° and 8° respectively. The difference between these two configurations was found to be less than 0.11 % for core diameters between 30 and 52 mm. Another test, where the gaps were initially asymmetric (4.5° and 1°) before the feed electrode was rotated until the gaps were inverted, also showed a small effect (smaller than 0.04 %).

4.5 Conclusion

A guarded, shielded, cylindrical capacitor design has been proposed for the non-destructive measurement of hard rock samples in the 1–25 MHz frequency range. Rock cores from the same borehole often have slightly varying diameters because of drill bit wear and the hardness of different rock types. The flexible nature of the electrodes allows measurement of cores of various sizes, and even one core of varying size, using a single electrode. The enclosure of the electrodes in a rigid housing allows repeatable measurements and shields the measurement system from external electrical field interference.

A flexible electrode with rigid outer shield makes for an interesting construction problem which is addressed in more detail in Appendix A. Some consequences of the flexible electrode are the changing effective electrode arc coverage and gap width. The effect of these was investigated and respectively compensated for and found not to have a significant influence on the analytical solution. The choice of using a flexible laminate substrate for etching the electrodes onto has the advantage of allowing simple yet precise electrode construction. The effect of the substrate may be removed by consideration of two substrate capacitors in series with the DUT capacitance. Once the properties of the substrate have been determined using the parallel plate capacitor described in Chapter 3, a sufficiently accurate parallel plate or coaxial approximation of the capacitance of these capacitors allows them to simply be subtracted from the measurement before calibration.

The analytical solution for the capacitance of the cylindrical capacitor presented in Section 4.2.2 provides insight into the capacitor's behaviour. Knowledge of the field distribution itself suggests techniques for the measurement of rock samples — measurement in different orientations, for example, allows a better evaluation of rock properties. The effect of the sensing electrode dimensions allows investigation of the effect of finite guard and gaps. The presentation follows Wilhelms' solution closely, adding observations regarding the effects of the side gaps and guard-sensor gap. The former were investigated numerically using a MoM code called FEKO [71]. Gaps of $\Delta \lesssim 8^\circ$ affect the analytical solution by less than 1 %; the difference between equal and asymmetric gaps resulting from changing electrode sizes was smaller than about 0.15 %. The guard-sensor gap is approached in the same way as guarded parallel plates.

Design guidelines for constructing the electrode are given so that its analytical capacitance is known to within a quantifiable uncertainty. The effects of a finite shield and gaps are taken into account by assuming two boundary condition limits — it can not be known precisely where within the limits the actual solution lies, so the difference between the limits is minimised to reduce uncertainty.

A circuit model adequate in the frequency range of interest was constructed for the proposed shielded geometry. Apart from increasing understanding of the device behaviour while being measured, the model shows that the electrode is in principle useable to much higher frequencies. The limiting factors are the resonances resulting from interactions between inductors and capacitors. The frequency response of the circuit model can be confirmed by measurement with an ANA. A method for the estimation of circuit model component values was presented.

The implementation of the electrode design was discussed generally here, and a detailed technical electrode design and construction procedure is presented in Appendix A. The methodology for producing accurate measurement results is discussed in Chapter 5.

Chapter 5

Cylinder Probe Measurement

5.1 Introduction

The HP 4285A LCR meter [60] was chosen to conduct the measurements described in this dissertation due to its suitability to the accurate measurement of a large range of impedance values. This chapter describes a methodology for the accurate measurement of rock core samples using the electrodes designed in Chapter 4. Essentially, a calibrated measurement involves the processing of raw data to obtain the unknown material properties of the samples in question. This calibration makes use of a map which has been established between the measured properties of a number of known reference materials and their actual properties.

The accuracy of measurements is affected largely by accurate knowledge of the reference materials, repeatability of measurements, and the establishment of a ‘correct’ map. The reference materials in this study are characterised accurately using the parallel plate capacitor described in Chapter 3. Methods for and the limitations involved in making repeatable measurements and the creation of an appropriate map are described in this chapter. A number of electrode devices were designed and constructed for the case studies presented in Chapter 6; their calibrations are evaluated using a nylon sample.

Rock samples occurring naturally are seldom homogeneous, and may often contain transitions between rock types or narrow inclusions of one rock type within another. The cylindrical electrodes developed in this study are ideal for their measurement, allowing a far more complete characterisation of the rock’s dielectric properties than other methods. The measurement of narrow inclusions is investigated thoroughly. Naturally occurring inclusions are seldom geometrically regular structures, but can be approximated by the general cases of a straight disc shaped inclusion and an angled inclusion. A method for the reasonably accurate estimation of the material properties of a narrow inclusion is presented in Section 5.3.

5.2 Measurement with the LCR Meter

5.2.1 Measurement Procedure

In the same way as for the parallel plate capacitor, the Hp and Hc terminals’ centre conductors are connected to the feed electrode, while the Lp and Lc terminals’ centre conductors are connected to the sensing electrode. The outer shield of the jig is connected to the ground of the four-terminal pair configuration. Again, the connections between the Hp and Hc, and Lp and Lc, centre conductors should be made as close as possible to the measuring electrodes.

Whereas an open, short and load *compensation* was performed before measurement with the parallel plate capacitor, the construction of the cylindrical electrodes as an etched pc-board, while providing

distinct advantages, does not allow a short or open circuit to be created easily. The creation of standard samples for each individual measurement jig is required. Air is a tempting standard but must be discarded since the flexible pc-board used, though extremely advantageous in the elimination of air-gaps between the electrode substrate and the sample during measurement, tends to deform in the complete absence of a sample. A low-loss standard with low permittivity is easily implemented by forming a cylinder of Teflon. PVDF was chosen as a standard material precisely for its relatively high loss tangent (see Figure 3.6(b)). On its own, it is useful as a reference point in the mid dielectric constant range expected; when its effective permittivity is raised by inserting a conducting centre (as described in Appendix C) it becomes a valuable high permittivity standard (a permittivity increase of a factor of about 3 is easily achieved). The availability of reference materials with properties covering a permittivity range of about 2 to 15 and a loss tangent of between 0.001 and 0.2 in the frequency range of interest, and the means with which to measure these properties accurately (described in Chapter 3), allowed the use of the technique described in Section 2.6.2 for the calibration of the cylindrical capacitor to measure material properties in these ranges.

The self-calibration described in Section 2.6.2 essentially amounts to establishing a map between reference points and the corresponding measured response at those points. The representation of a lossy material by a parallel RC circuit model is adequate in the frequency range used. The representation of data in terms of the real and imaginary components of its impedance (or admittance) is desirable since the reference points are better spaced and allow a more accurate mapping. Following the calculation of a theoretical impedance value from the RC equivalent model of the reference materials, a second order Lagrange mapping between the real and imaginary components of this theoretical and the measured reference impedance is performed as described by (2.55) and (2.56). The established map may be used to calculate the actual impedances of unknown materials. The interpolation accuracy will clearly be highest when the DUT's properties lies within the range covered by the standards. The further they are outside the range, the lower the accuracy is expected to be.

Using the three materials described above (Teflon, PVDF, and the artificial dielectric) as reference standards, the effective material properties may be extracted from the calibrated admittance as

$$\epsilon_r = \frac{\text{Im}\{Y_{dut}\}}{\omega} \quad (5.1)$$

$$\tan \delta = \frac{\text{Re}\{Y_{dut}\}}{\text{Im}\{Y_{dut}\}} \quad (5.2)$$

Note that the effect of the substrate must be removed from each measured impedance as described in Section 4.4 before the calibration is performed.

A detailed methodology for making accurate and repeatable measurements is discussed in Appendix A.

5.2.2 Measurement Accuracy

The graphical error analysis technique introduced in Section 2.5.3 is applied again here as shown in Figure 5.1. The accuracy of the measured complex dielectric constant depends on two things: the measurement repeatability and the calibration accuracy. Though both are critical for the absolute evaluation of material properties, a valuable and legitimate comparison of materials is possible with a less accurate calibration if the measurements are repeatable.

A good estimation of the measurement repeatability of the reference standards, Z_{ori} , and the unknown measured value, Z_{ox} , may be obtained by the following technique. The three reference material cores and a number of rock cores form the repeatability standard set. The rock samples should be chosen to

be representative of the diameter and surface condition of all the core to be measured — one or two will usually suffice — and should be carefully returned to the same position relative to the sensing electrode for each measurement. The aim is to measure the entire repeatability set a number of times (N) in succession before the measurement of all the rock cores — the pre-characterisation — then another N times after the measurement of all the rock cores — the post-characterisation. During each of these repeatability measurement sequences, the repeatability samples should be measured in random order. The pre- and post-characterisation measurements should be conducted immediately before and after the rock measurements. In this way long term changes in the measuring conditions may be avoided.

The characterisation of the device before and after the sample measurements accounts for any geometric or electrical changes the device may undergo due to the mechanical strain of the measurement procedure. The use of rock cores simulates this strain better since the plastic reference samples used usually have a lower friction coefficient, and also simulates the errors due to inaccurate sample positioning. Note that the properties of the rock sample chosen play a role here: a more homogeneous rock will clearly be more tolerant to slight positioning errors than a sample with a rapidly varying high dielectric constant. The dominant positioning error in such a case will not be distinguishable from the repeatability error.

There will usually (but not always) be a decrease in the repeatability between the pre-characterisation and the post-characterisation. It may also occur that the mean of the post-characterisation measurements changes but the variation remains similar. In this case the device response has not degraded but simply changed slightly. In any event, the total $2N$ measurements are taken as a single set from which mean values of and variations in the reference sample impedances are calculated. The maximum variation in the properties of the rock repeatability samples measured is taken as a good approximation of the contribution of measurement repeatability to the total uncertainty likely to be experienced in the actual measurement of a sample.

As alluded to already, the repeatability measurements amount to a characterisation of the measuring device used, and must be repeated for every device. In fact, it is recommended that a pre- and post-characterisation is carried out for every set of measurements conducted, and preferably regularly during a long measurement sequence. A form of redundancy is created by these repeated characterisation measurements: if problems did arise, the accuracy of less data would be placed in question if the previous characterisation were recent. In general, the change in device response increases with the number of samples measured.

The relative complexity of the defining equations makes it more convenient to directly calculate the uncertainty in the capacitance components due to geometric uncertainties. This essentially amounts to implementing the sensitivity defined in (2.52) numerically, as described in Section 2.5.1.

Calibration Accuracy

As discussed in Section 2.6.2, the choice of reference materials is important to obtain the correct calibration curve, while another set of known materials is required for confirmation of the calibration. The limitations in acquiring materials with suitable accurately known properties, i.e. with properties spaced evenly throughout the range of interest, has been discussed. Whereas artificial dielectrics with a range of permittivities may be constructed as described in Appendix C, materials with a spread of loss tangents are far more problematic to find. This problem is counteracted to some degree by treating data in the complex impedance plane. Using a parallel RC circuit model representation of the capacitor (with geometric capacitance C_0) containing a dielectric (with complex dielectric constant ϵ^*), the real and imaginary parts of the equivalent admittance and impedance of the model may be written as

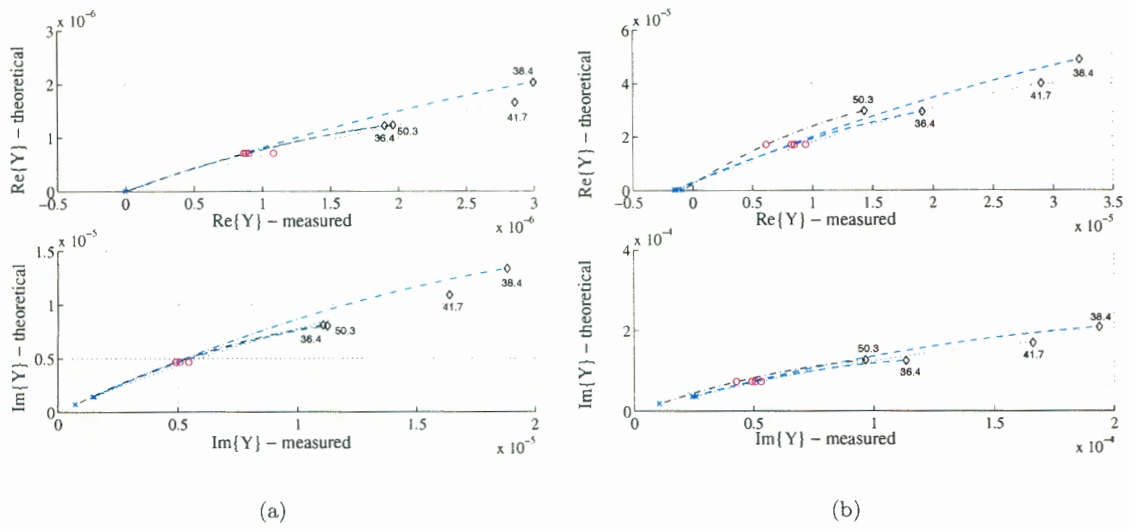


Figure 5.2: A comparison of raw measured and actual real and imaginary parts of the admittance at (a) 1 MHz and (b) 25 MHz. The crosses correspond to Teflon, the circles to PVDF, and the diamonds to the artificial dielectric. The nominal capacitor core diameter is written next to the curves, which have been determined by a second order Lagrange interpolation.

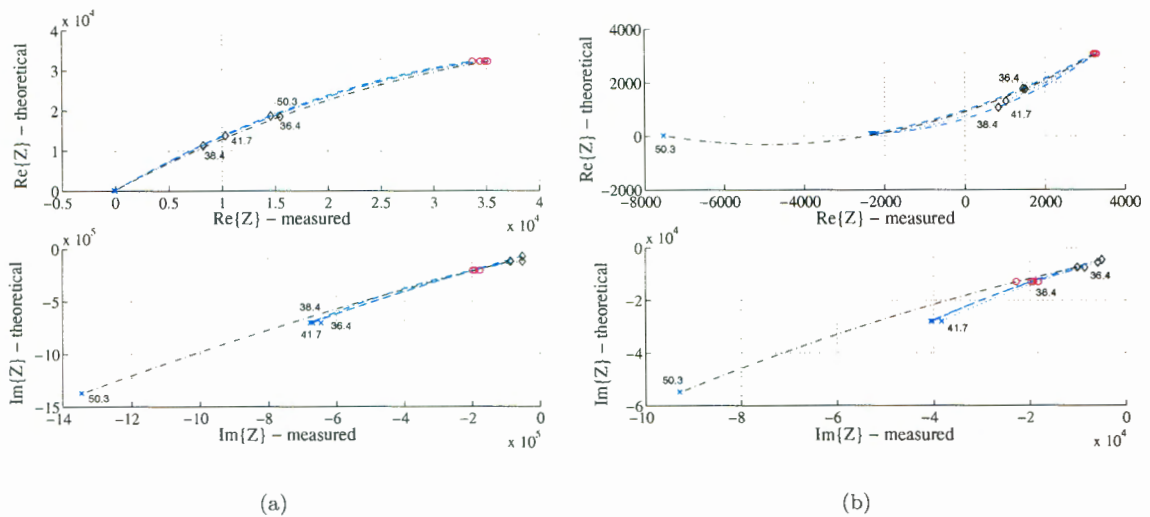


Figure 5.3: A comparison of raw measured and actual real and imaginary parts of the impedance at (a) 1 MHz and (b) 25 MHz. The crosses correspond to Teflon, the circles to PVDF, and the diamonds to the artificial dielectric. The nominal capacitor core diameter is written next to the curves, which have been determined by a second order Lagrange interpolation.

with a large measured Cp can result in a real part of Y which is larger negative than that of a material with smaller Cp and D , i.e. a material's real admittance, and thus extracted parameters, are perceived as smaller than they actually are. For example, a nylon sample with measured $Cp \approx 2.6$ pF and $D \approx -0.036$ (typical values) has a smaller (i.e. larger negative) $Y_r = \omega CpD$ than a piece of Teflon with measured values of $Cp \approx 0.16$ and $D \approx -0.056$, even though Teflon's individual values are clearly smaller. This property of the device limits the measurement range somewhat for materials whose raw D measure negatively if an admittance curve fitting is carried out. This problem is not manifested in the impedance calibration which is thus preferable in such a case.

Though not an ideal reference material, a nylon rod was machined into cylindrical samples as tests for the 36.4, 38.4 and 41.7 mm electrodes. A slice of the material was also prepared as described in Appendix B for measurement with the parallel plate capacitor. The slice used was about 4.3 mm thick with a thickness variation of less than 0.02 mm and thus less than a quarter of a percent uncertainty due to the air gap. The parallel plate measured values are compared to the measured properties, obtained by calibration of data measured using the three electrodes, in Table 5.2. The properties of the nylon sample measured with the parallel plate capacitor are about $\epsilon_r \approx 3.1 - 3.2$ and $\tan \delta \approx 0.019 - 0.021$, with both dropping in frequency (between 1 and 25 MHz) from the high value mentioned to the low value. The agreement in calibrated ϵ_r for the 36.4 and 38.4 mm electrodes is within 4.5 % of the parallel plate measurement, but slightly worse for the 41.7 mm capacitor. The loss tangent agreement is also consistently within 0.01 at frequencies to 20 MHz for all the electrodes. At 25 MHz the agreement is slightly worse — presumably due to the properties of nylon causing the measurement problem described above — but still within 0.017. Interpolation in the Z and Y planes yielded similar results, as would be expected from investigation of Figures 5.3 and 5.2.

Electrode	Calibration Type	$\Delta \epsilon_r$	$\Delta \tan \delta$
36.4 mm	Z	$< 3.5\%$	< 0.010
	Y	$< 2.9\%$	$< 0.009^1$
38.4 mm	Z	$< 4.4\%$	$< 0.007^1$
	Y	$< 2.5\%$	$< 0.008^1$
41.7 mm	Z	$< 9.1\%$	$< 0.008^1$
	Y	$< 8.2\%$	$< 0.011^1$

Table 5.2: The 1–25 MHz maximum differences between parallel plate measured permittivity and loss tangent values are compared for calibration in the Z and Y domains. No reference material was available for the 51.3 mm electrode set.

Careful selection of reference materials is the primary concern in making an accurate calibration. The materials should be homogeneous, temperature-stable, and should have the same properties from batch to batch. Further, the materials should be accurately machineable, i.e. their dielectric properties should not change when heated. Of equal concern is the plane in which the calibration should be carried out. This is partly related to the response of the measuring device, as described above.

It can be seen how measurement accuracy depends on both the measurement repeatability and on the accurate knowledge of material properties. If either are compromised, the interpolation curve will be incorrectly determined and predictions of properties using the curve likewise.

¹The stated $\Delta \tan \delta$ is applicable to 20 MHz. At 25 MHz the agreement is slightly worse but always within 0.017.

Substrate Effect

The effect of the substrate on which the electrodes are etched is taken into account in Figure 5.1 by the ‘ Z_{subs} ’ component. The effect of adding this very thin extra layer of material between the core and capacitor electrodes can be approximated very well as the addition of another capacitance in series with C_0 . Since the electric field in the immediate vicinity of the capacitor electrodes is essentially normal to them, and thus practically perpendicular to both boundaries of the layer, this second capacitor can be approximated with high accuracy by a coaxial capacitor with $C = 2\pi\epsilon^*/\ln(b/a)$, as described in Section 4.4.2. Even a parallel plate capacitor approximation will be accurate for very thin layers. The substrate effect is removed by the subtraction of the two substrate capacitors’ impedances from all measured impedances prior to calibration. The uncertainty due to this removal stems from the uncertainty in knowledge of the substrate’s dielectric constant, which was determined by stacking 12 small sheets of the substrate and measuring their properties with the parallel plate capacitor described in Chapter 3. In addition, the geometric capacitance of the substrate capacitor depends on the precise dimensions of the core being measured.

The relative effect of the substrate capacitance on the measured impedance may be estimated by considering the upper row of elements between ports 1 and 2 in the circuit model shown in Figure 4.5. The question to be asked is how large the combined impedance of the substrate capacitors is relative to that of the DUT capacitor. The series impedances of these two capacitors may be written as

$$Z_s = \frac{2}{j\omega C_s^*} = \frac{2}{j\omega\epsilon_0\epsilon_s^* \frac{\phi_0 R l}{d_s}} \quad (5.7)$$

$$Z_{dut} = \frac{1}{j\omega C_{dut}^*} = \frac{1}{j\omega\epsilon_0\epsilon_{dut}^* \frac{l}{\pi} \ln \Theta} \quad (5.8)$$

$$(5.9)$$

where the parallel plate approximation is used for C_s and the perfectly guarded cylindrical capacitance C_0^∞ , given by the first term of (4.20), is used for C_{dut} . The argument of the natural logarithm is $\Theta = \left(\cot\left(\frac{\xi-\Delta}{2}\right)\cot\left(\frac{\xi+\Delta}{2}\right)\right)$. The ratio of the two impedances is given by

$$\frac{Z_s}{Z_{dut}} = \frac{2}{\pi} \cdot \frac{\epsilon_{dut}^*}{\epsilon_s^*} \cdot \frac{\ln \Theta}{\phi_0} \cdot \frac{d_s}{R} \quad (5.10)$$

The expression in (5.10) has been divided into four parts. The first ratio is $2/\pi \approx 0.64$. The relative permittivity of the substrate is approximately equal to 4, thus the magnitude of the second component of (5.10) is smaller than one in the case of all the rocks measured in this study, and is certainly smaller than 4, regardless of $|\epsilon_{dut}^*|$. The magnitude of the third component, calculated for $80^\circ \leq \phi_0 \leq 120^\circ$, lies between 1 and 1.3. This leaves the fourth component: d_s/R is always smaller than 0.003 for a substrate thickness of 50 μm and core radii ranging between 18.4 and 25.7 mm. Thus it can be said with confidence that the magnitude of the substrate capacitor’s impedance will be below about 0.5 % of the DUT impedance for all the situations encountered in this study. The uncertainty in this 0.5 % contribution will be the effect on the total measurement uncertainty, thus even a 10 % error in the determination of Z_s will result in a negligible contribution to the total uncertainty. The exact effect is calculated explicitly during the calibration procedure.

Geometric Effects

Another effect of measuring a range of core diameters is that the effective arc coverage ϕ_0 changes depending on the core size. This change can be compensated for quite simply when it is recognised

that the physical width $w = \phi_{0,nom} R_{nom}$ of the sensing electrode remains constant (nominal dimensions designated by the ‘nom’ subscript). If a core of radius R is measured, the change in core radius translates linearly to a change in ϕ_0 , and we can thus write:

$$\frac{R}{R_{nom}} = \frac{\phi_{0,nom}}{\phi_0} \quad (5.11)$$

This change is compensated for by calculating the change in the capacitance predicted by (4.20) corresponding to the change in ϕ_0 .

Air Gaps

Air gaps can be a limiting factor in decreasing measurement uncertainty, and they were an important consideration in the design of the electrodes. The problem is not so much the presence of the air gap itself as the unpredictability of the gap thickness when cores of different diameters are to be measured. The quantification of this gap thickness with any reasonable accuracy would be impossible. The thin flexible laminate used for the etching of the electrodes was chosen precisely for its ability to conform very closely to cores having a range of diameters. When pressed against the core by simple elastic bands, no air gap at all was observed by optical inspection² in the upper chamber or in the vicinity of the sensing electrode in the lower chamber. A slight air gap is sometimes present immediately adjacent to where the support struts connect with the guard electrode; it is not unexpected as this is the only rigid section of the laminate. This is an artifact of the electrode construction, and varies negligibly (i.e. not measurably) for the small range of core diameters for which a specific electrode has been designed. Considering this constancy, and that the gaps are not in the vicinity of the more important field region adjacent to the sensing electrode, the air gap may be seen as a systematic error and is thus removed during the calibration procedure. Its effect is thus deemed to be negligible and it is not taken into consideration in the uncertainty analysis.

5.3 Measurement of Transitions

One of the reasons for the development of the cylindrical capacitor was its ability to increase the limited ability (if not total inability) of other techniques to characterise variations occurring along typical rock cores. Of particular interest is the measurement of narrow, usually irregular, inclusions in the host rock. This is something destructive techniques do not allow with reasonable accuracy, if at all.

It should immediately be noted that measurements of transitions need not and cannot be approached blindly, where by ‘blindly’ is meant interpretation based purely on the measured dielectric constant. Extensive, often complete, knowledge of the core structure is available through visual inspection. A search for inclusions or changes in the rock is not required — their existence and position is known. What is of interest here is the determination of the dielectric properties of the various rock types encountered from the limited sample available. Each section of core needs to be considered individually, with more attention being paid to ‘interesting’ features like inclusions or variations in the rock. This does not preclude the need for measuring the entire core — variation in optical appearance and dielectric constant are not necessarily correlated. Thus an initial low-resolution measurement of the entire core is recommended, followed by closer inspection of any interesting dielectric features (which were either known or discovered during the initial sweep).

The aim of this section is to present guidelines for the accurate measurement of varying core sections, and in particular of narrow inclusions. The three variables relevant to an accurate measurement interpretation are the geometries of the inclusion and the measuring electrode, and the sampling rate, which will

²No light was seen to pass between the core and electrode substrate.

here refer to how often a measurement is performed (in millimetres per sample (mmps)). The question of how to extract an inclusion's dielectric constant is followed immediately by the following pertinent questions:

1. How long should the sensing electrode be?
2. How often should one sample along the length of the core?

With regard to measuring transitions, it should be noted that the relation between the electrode length l and inclusion length s is important, as is the relative sampling rate.

The measurement of the core moving past the sensing electrode of length l is (to a good approximation) analogous to the convolution of a rectangular window function, representing the measured field, with some arbitrary yet finite function, representing the dielectric properties of the rock core. Of use here is the distributive property of the convolution integral, stated simply as [81, p. 85]

$$h(z) * [f_1(z) + f_2(z)] = h(z) * f_1(z) + h(z) * f_2(z) \quad (5.12)$$

where $h(z)$ is the rectangular windowing function, and $f_1(z)$ and $f_2(z)$ are two z -dependent functions describing the core's dielectric constant. What this allows is the construction of a general model of the dielectric variation along a core. Inclusions of a different rock type in a host are seldom of an easily describable shape, but their general form could be seen to fall between two extremes: a 'straight' disc-shaped inclusion whose boundaries are perpendicular to the core axis, and an 'angled' inclusion, obtained by slicing the core at some angle ϕ , separating the two segments, and inserting another material. The two inclusion types are shown schematically in Figure 5.4.

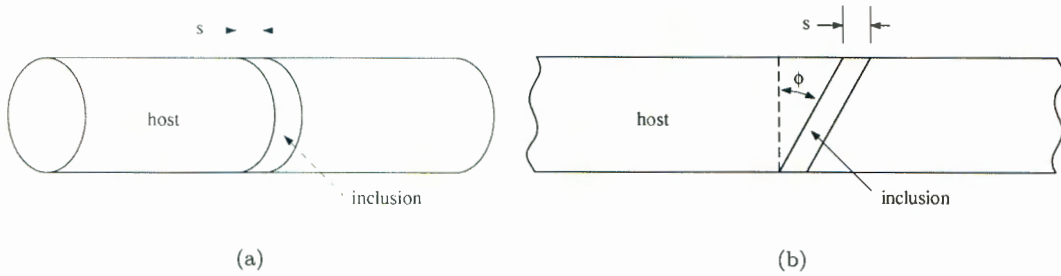


Figure 5.4: (a) The geometry of a 'straight' inclusion. (b) A side view of an 'angled' inclusion, having an angle ϕ with the vertical.

It is aimed to show that a prediction by the convolution approach compares well to measurement for straight samples, and to establish a relation between measurements of straight and angled inclusions of similar thickness. Then, by comparison to these controlled test cases, the dielectric constant of actual inclusions will be extractable with reasonable accuracy from measured data.

Consider first the case of a host with complex dielectric constant ϵ_h^* containing a homogeneous straight inclusion of length s with dielectric constant ϵ_i^* . Two cases distinguish themselves: $s \geq l$ and $s < l$. Both convolutions are trivial to perform graphically — the derivations are not explained in detail here, but the predictions are shown graphically (while being compared to measured results) in Figure 5.6. In each case, the rectangular window function $h(z)$, normalised to have a unit area by assigning it a height of $1/l$, is convolved with another rectangular function having a width of s and height ϵ_i^* . The surrounding host rock is assumed to be of infinite extent in the z -direction.

The 'rise-distance' of the resulting waveform is dictated by the shorter of s and l , while the duration of the measurement plateau is equal to the larger of the two. For a long inclusion, the maximum

value of the measured dielectric constant is equal to the inclusion's properties, while the averaging of the short inclusion with its surrounding host's properties is evident in the lower maximum value of $\epsilon_t^* = \epsilon_h^* + (s/l)(\epsilon_i^* - \epsilon_h^*)$. If the inclusion and the electrode have the same length, there will be one sharp peak without any plateau. This immediately suggests a criterium for how fine an inclusion a certain electrode length is capable of measuring: the measured $(s/l)(\epsilon_i^* - \epsilon_h^*)$ must be larger than the measurement uncertainty in the dielectric constant of the host rock. If the inclusion is detectable, its actual properties can be estimated using the circuit model approach discussed below.

The derived figures also lead to some suggestions regarding the sampling rate for short inclusions. The measured rise-distance cannot be shorter than the sample spacing if this spacing is larger than the inclusion width s . Obtaining a precise characterisation of the transition is less important than measuring the plateau height accurately. The more measurements are taken while the inclusion is completely within the sensing electrode boundaries for a short electrode, or while the inclusion completely covers the electrode for a long inclusion, the more accurately its properties may be estimated. If the inclusion and sensing electrode have the same length, a measurement should be conducted when the boundaries of the inclusion and electrode coincide for an accurate estimate. It is recommended that the sampling spacing be at least three times larger than the larger of s and l (which corresponds to the maximum plateau width).

The above argument shows that, for a short pulse, the measured complex admittance (and dielectric constant) is, to a good approximation, a proportional averaging of the host rock and the inclusion. A circuit element view is again intuitive and eases the calculation of the inclusion's properties. We again consider the simple case of a single inclusion: the total of the two parallel complex admittances Y_h and Y_i is simply

$$\begin{aligned} Y_t &= j\omega\epsilon_t^*C_0 = j\omega\epsilon_{r,t}(1 - j\tan\delta)C_0 \\ &= Y_h + Y_i = G_h + G_i + j(B_h + B_i) \\ &= \omega[\epsilon_{r,h}\tan\delta_h C_{0,h} + \epsilon_{r,i}\tan\delta_i C_{0,i}] + j\omega[\epsilon_{r,h}C_{0,h} + \epsilon_{r,i}C_{0,i}] \end{aligned} \quad (5.13)$$

where $C_{0,h} = ((l-s)/l)C_0$ and $C_{0,i} = (s/l)C_0$, and the subscripts 'h' and 'i' refer to the host and inclusion respectively. The total measured permittivity and loss tangent can now be written as follows:

$$\epsilon_{r,t} = \epsilon_{r,h} \left(\frac{l-s}{l} \right) + \epsilon_{r,i} \left(\frac{s}{l} \right) \quad (5.14)$$

$$\tan\delta_t = \frac{\epsilon_{r,h}\tan\delta_h \left(\frac{l-s}{l} \right) + \epsilon_{r,i}\tan\delta_i \left(\frac{s}{l} \right)}{\epsilon_{r,h} \left(\frac{l-s}{l} \right) + \epsilon_{r,i} \left(\frac{s}{l} \right)} \quad (5.15)$$

With the total measured properties and knowledge of the host material's properties, (5.14) and (5.15) easily yield the dielectric properties of the inclusion. The results obtained here are identical to the convolution approach. Again, this is an approximation based on the assumption that the field distribution has no z -component and does not take into account the concentration of field in regions with a higher dielectric constant. As will be seen when comparing these predictions to experimental results, this approximation is quite good.

Given measured values of measured permittivity and loss tangent, the properties of an inclusion may be estimated by an inversion of (5.14) and (5.15) using the known host properties:

$$\epsilon_{r,i} = \epsilon_{r,t} \left(\frac{l}{s} \right) - \epsilon_{r,h} \left(\frac{l-s}{s} \right) \quad (5.16)$$

$$\tan \delta_i = \frac{\epsilon_{r,h}}{\epsilon_{r,i}} \left(\frac{l-s}{s} \right) (\tan \delta_t - \tan \delta_h) + \tan \delta_t \quad (5.17)$$

Inclusions found naturally in rock samples are seldom geometrically ‘neat’, but their properties may be estimated by considering a range of possible thicknesses.

The question of multiple narrow inclusions may again be treated by the convolution approach. If the distance d between inclusions, measured from the trailing edge of the first to the leading of the second, is greater than the electrode width l , they may be treated simply as successive single pulses. If the spacing is shorter, overlap occurs, but two distinct peaks will still be distinguishable if the electrode length is shorter than the sum of the gap and the shorter of the two inclusions. When the electrode width is larger than the total inclusion train width, the measured graph assumes the form of a staggered peak, shown for two short inclusions in Figure 5.5, the side-plateaus of which represent the two individual inclusions. As the ratio of the electrode length to pulse train width increases, these side-plateaus become narrower, necessitating a higher sampling rate if they are to be detected. This is where the additional visually obtained information about the core structure is useful: if it is known that numerous inclusions exist, the sampling frequency can be adjusted in this region to increase the measurement accuracy.

When more than two intrusions follow closely upon one another, it becomes extremely difficult to distinguish between them if the electrode width is not very short. In this case an accurate characterisation would necessitate a narrow electrode — of the same order of size as the inclusion lengths — sampling very finely across the set of disturbances.

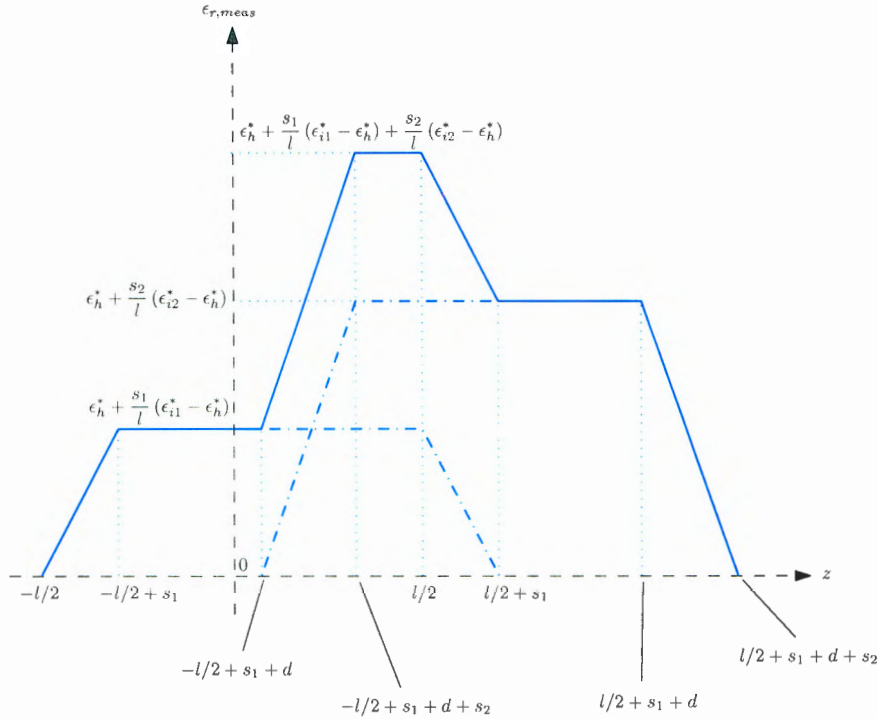


Figure 5.5: Two successive short ($s < l$) inclusions with spacing $d < l$ are perceived in a measurement as shown.

Measured Results

A set of measurements was carried out using the 36.4 mm diameter electrode set constructed for the case study described in Section 6.3. Several PVDF discs of different thickness, straight and angled, were placed between two thick layers of a Teflon host, and the resulting system was measured, starting at 10 mm before the leading inclusion edge first encountered the sensing electrode, and ending 10 mm after the falling edge had left it. Since the thinnest disc had a thickness of 2.05 mm, a sampling rate of 2 mm/ps was used to allow adequate resolution.

Measurements of the straight PVDF discs in a Teflon host are shown in Figure 5.6. The permittivity results match the predictions by (5.16) and (5.17) closely (to within 10 % throughout at 1 MHz, and within 3 % at 25 MHz), but the loss tangent measurements correspond less well to the predictions, worsening for small inclusions as the frequency increases (up to 0.045 absolute difference in $\tan \delta$). The $\tan \delta$ match is good for wider inclusions throughout. It is interesting to note the shape of the measured results. The permittivity curves consistently have the same form as the predictions and match the peak plateau value most closely for the widest inclusion. The loss tangent's curve is wider for larger inclusions, indicating that a material with a high $\tan \delta$ is perceived before it is actually in contact with the sensing electrode. The 'bulging' narrows at higher frequencies.

Three PVDF angled inclusions were measured in two different hosts. Inclusions with thicknesses of 2.22 and 10 mm, inclined at 30° were placed in a nylon host ($\epsilon_r \approx 2.15$, $\tan \delta \approx 0.001$), while another 4 mm thick PVDF slice angled at about 45° was inserted into a different nylon host ($\epsilon_r \approx 3$, $\tan \delta \approx 0.005$). The first two cases were measured at 5 different orientations as shown in Figures 5.7 and 5.8, while the third, shown in 5.9 was only measured in three. For the first two angled inclusions, the 180° orientation corresponds to the inclusion being angled so that the leading edge meets the sensing electrode first, and the 0° to when the trailing edge leaves the electrode last. (The orientations are switched for the 45° angled inclusion. A symmetry is observed in each case around the 90°. In general the peak perceived magnitude of the properties is also largest for the 90° case, dropping similarly to the 0° and 180° measurements.

In the case of the 2.22 mm insertion, the peak predicted values for a straight 2.22 mm inclusion (using (5.16) and (5.17)) would be $\epsilon_r = 2.58$ and $\tan \delta = 0.04$ at 1 MHz and $\epsilon_r = 2.39$ and $\tan \delta = 0.44$ at 20 MHz. The measured permittivity values for the 90° orientation is the closest to this peak (always within about 3 %), while all the orientations are within about 7 % of the peak. In the case of the loss tangent, the peak value of the 90° measurement is almost equal to the peak prediction at 1 MHz but shows a substantial difference (about 0.03 absolute) from the straight inclusion prediction at 20 MHz. The 10 mm inclusion shows similar tendencies: the permittivity comparison is slightly worse than for the 2 mm slice, but the peak values of the 90° components are always within 10 % of the straight peak.

The 4 mm thick 45° angled slice was placed between two lengths of a different sample of nylon, and only measured in the 0, 90 and 180° orientations. The measured results in Figure 5.9 are again fairly symmetric about the 90° measurement (the slight asymmetry is due to the orientation not being set precisely), and agreement between the prediction (again for a straight inclusion) and measured peak permittivity is within 3 % throughout. The measured loss tangent is again less close, particularly at high frequency where the difference is up to about 0.025.

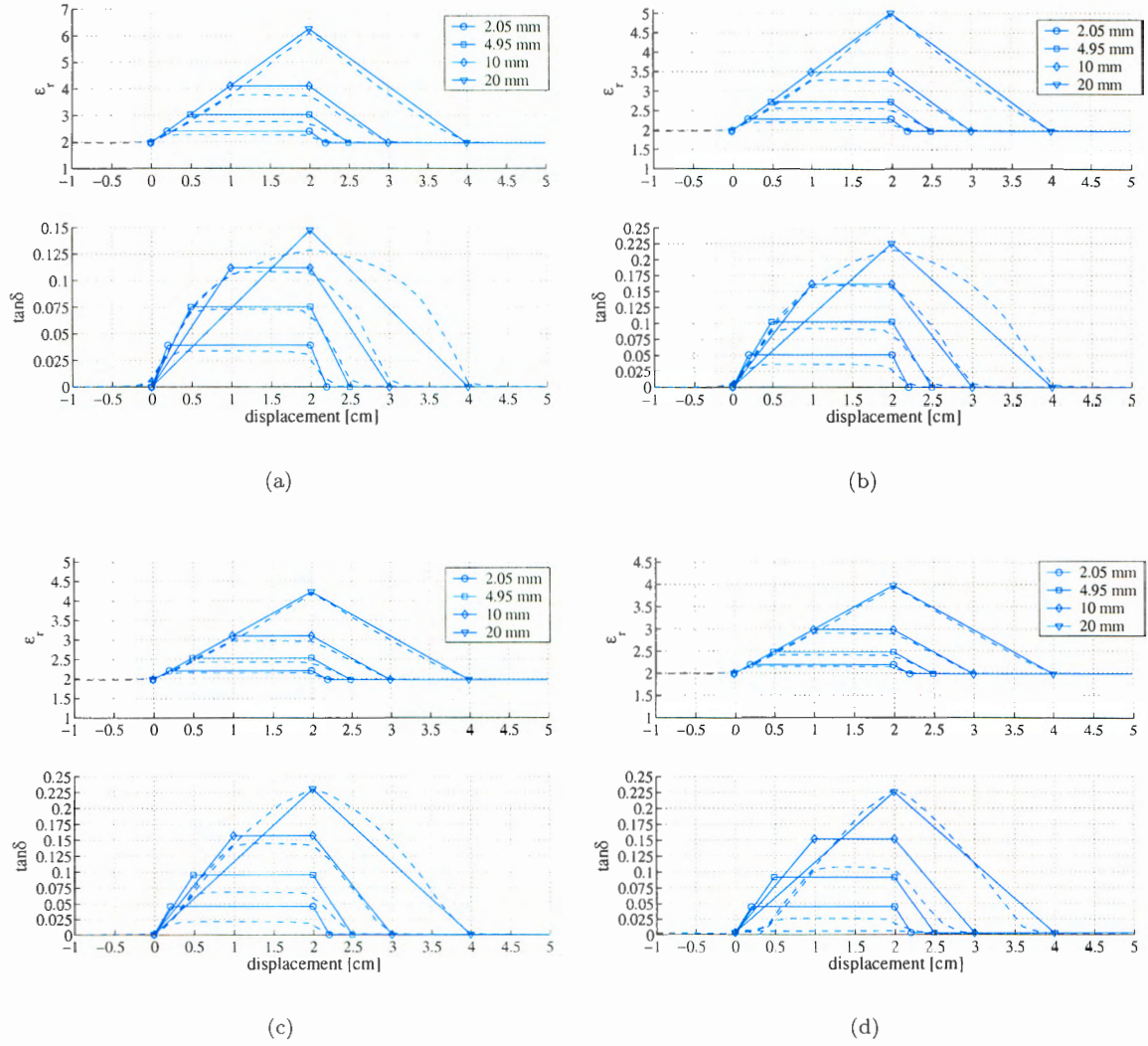


Figure 5.6: The measured permittivity and loss tangent of straight narrow PVDF inclusions in a Teflon host at (a) 1 MHz, (b) 5 MHz, (c) 15 MHz and (d) 25 MHz. The measured values are depicted by the dashed lines, while the solid lines represent the predictions according to (5.16) and (5.17).

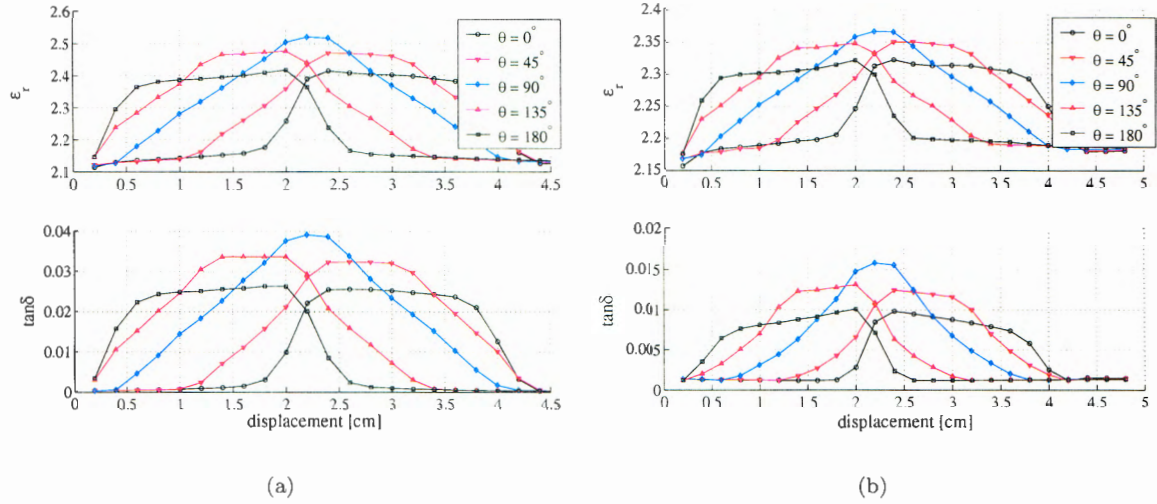


Figure 5.7: The measured permittivity and loss tangent of the 2.22 mm PVDF inclusion angled at about 30° in a nylon host at (a) 1 MHz, (b) 20 MHz. The peak predicted values for a 2.22 mm straight inclusion would be $\epsilon_r \approx 2.52$ and $\tan \delta \approx 0.04$ at 1 MHz and $\epsilon_r \approx 2.39$ and $\tan \delta \approx 0.02$ at 20 MHz.

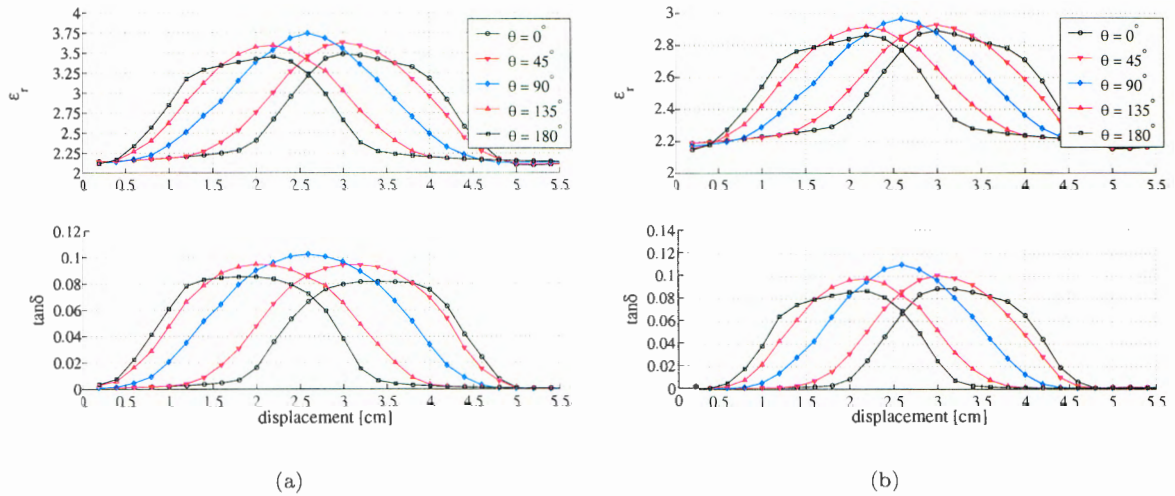


Figure 5.8: The measured permittivity and loss tangent of the 10 mm PVDF inclusion angled at about 30° in a nylon host at (a) 1 MHz, (b) 20 MHz. The peak predicted values for a 10 mm straight inclusion would be $\epsilon_r \approx 4.2$ and $\tan \delta \approx 0.11$ at 1 MHz and $\epsilon_r \approx 3.13$ and $\tan \delta \approx 0.15$ at 20 MHz.

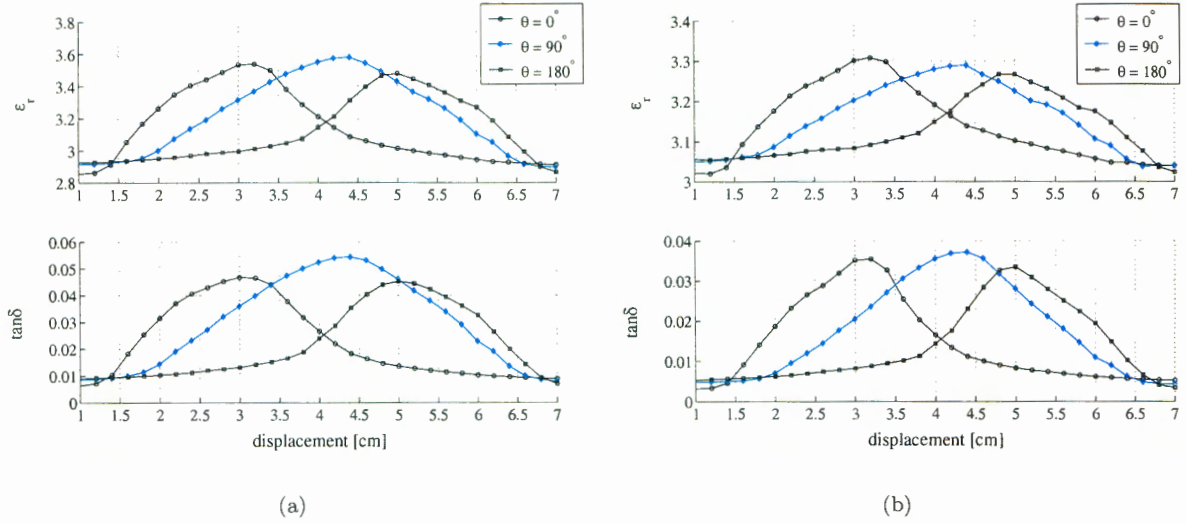


Figure 5.9: The measured permittivity and loss tangent of the 4 mm PVDF inclusion angled at about 45° in a nylon host at (a) 1 MHz, (b) 20 MHz. The peak predicted values for a 4 mm straight inclusion in this host would be $\epsilon_r \approx 3.57$ and $\tan \delta \approx 0.056$ at 1 MHz and $\epsilon_r \approx 3.25$ and $\tan \delta \approx 0.06$ at 20 MHz.

5.4 Conclusion

This chapter has presented methodologies for the measurement of rock samples in the 1–25 MHz frequency range. The basic principle is the comparison of raw data obtained from the measuring device (which in this study is defined as the combination of instrument and test fixture) and equivalent data calculated from accurately known reference material properties. Techniques for making repeatable measurements and at the same time quantifying that repeatability are essential for an accurate calibration.

Various aspects of the calibration procedure and its limitations are described. The appropriate selection of reference materials, evenly spread throughout the range of materials to be measured, as well as the use of appropriate checking materials, is necessary to obtain and confirm the correct calibration curve. Representing the data in the appropriate format is essential, although scant difference was found in this study between calibrations done in the admittance or impedance planes. Though not ideal a nylon test sample was used to check the calibration curves of three of the four electrodes used in this study. Cylinder measurements of the permittivity of nylon were consistently within 10 % of parallel plate measurements, and loss tangent to within about 0.01 up to a frequency of 20 MHz, allowing the electrodes to be used with reasonable confidence in the case studies described in Chapter 6. It is speculated that accuracy estimates based on the measurement of nylon are conservative. The properties of nylon were not known with sufficient certainty, and the samples were not ideally prepared; it was also not known how they may have responded to the machining process. Unfortunately no other more suitable materials were available.

A number of other influences on measurement accuracy were presented. The electrode substrate has an effect on the measurement which can be removed using the circuit model developed in Section 4.3. Further, compensation for the effects of geometric changes to the capacitor due to the flexible electrodes' response to core diameter variations was discussed, along with the uncertainty arising from possible air gaps.

The measurement of relatively gradual variations in the material properties along a core presents no problems. What has been shown here is that a simple circuit model approach may be used to estimate the properties of inclusions narrower than the measuring electrode's width with good accuracy if they can be

approximated as straight inclusions, and with reasonable accuracy otherwise by comparing their measured properties to those of the constructed angled inclusions discussed above. The measurements of loss tangent in particular were in general less accurate in the prediction of the plateau maxima, particularly at the higher frequencies. Time constraints did not allow the cause for the larger discrepancies to be determined — this is the subject of further study. The measurements worst affected were for inclusions of small loss tangents at high frequency. The permittivity agreement was good throughout, allowing accurate estimates of inclusions' ϵ_r . As shall be discussed in more detail in the conclusion of Chapter 6, this is arguably more important for the planning and analysis of borehole radar experiments. The good agreement between the model and theory at low frequencies provides an alternative avenue for the estimation of high frequency properties in some cases: if the properties of a bulk sample of a similar material are known (e.g. chromitite, which is known to change in properties [82] but is expected to behave similarly in frequency), the low frequency properties can be used as a basis for estimating the inclusion's properties at higher frequencies.

Chapter 6

Case Studies

6.1 Introduction

The application of the developed measurement system to the measurement of materials in three actual borehole radar (BHR) studies of economically important geological systems is discussed in this chapter. The aims in all the case studies are two-fold. First, the specific questions posed by a case study must be answered. This will in general entail the characterisation of the RF propagating conditions of a certain geological environment. The quantity and detail of data obtainable with this device necessitated the development of techniques for the analysis of the collected data. Thus part of the discussion will always be general in nature, with an eye toward applicability to other studies.

It is important to determine the properties, or range of properties, of the various rock types encountered. Although they may appear optically homogeneous, the properties of each separate type of rock actually vary within a certain range. As more samples are obtained, this range can be extended or narrowed down (a statistical approach is useful — the one used is described in Section 6.2), with the final aim being the establishment of a database of rock properties. (This is beyond the scope of this study.) When different local geological geometries are encountered, the previously established range of material properties can again be employed in analysis. The expected material properties of various rocks may clearly be estimated with greater certainty as more samples are obtained. In the case of narrow inclusions, a single sample might not result in very accurate material property prediction, though the presence and rough size of a contrast will be obvious.

Regardless of the exact experiment background or details, planning and interpretation of data is eased substantially by having as complete as possible a knowledge of the dielectric properties of the geological materials and systems likely to be encountered. Important for radar wave propagation are to consider the effect on the pulse of passage through and reflection from ‘homogeneous’ rock and planar layered ‘structures’ like the Bleskop Marker (discussed in Section 6.3.4).

The case studies considered were undertaken as part of BHR studies in three relevant and economically important mines. The delineation of the platinum bearing UG1 and UG2 reefs in the layered Bushveld Igneous complex is discussed in Section 6.3. This study is divided into the investigation of a single interesting feature found in the UG1 unit — this demonstrates the capability of the capacitor to measure complex layered systems on a fine scale — and a broader investigation of the entire unit structure. The delineation of two diamondiferous kimberlite structures necessitated the studies described in Sections 6.4.2 and 6.4.3. In a number of cases, laboratory predictions of the pulse propagation velocity are compared to bulk estimates from cross-hole BHR shoots [83].

6.2 Representation of Measured Data

The objective of the measurement of rock samples is always the prediction of how a radar signal will be affected by the medium it is travelling through. The aim is for the translation between a limited set of laboratory measurements and macroscopic rock properties to be as accurate as possible. The continuous measurement along a sample is already a great improvement over the extremely localised measurement of prepared samples with, for example, a parallel plate capacitor. The standard approach for the measurement of a single sample in this study is to measure it at some fixed resolution, for example every 10 mm, commencing and ceasing measurement while an unbroken section of the core covers the sensing electrode, before measuring ‘interesting’ features in more detail. Additional data may be obtained by measuring the core in different orientations.

Each individual measurement can be described by a mean expected value and the Measurement Uncertainty (MU) (in fact a variance, quantifying the accuracy of an individual measurement, as described in Section 2.5.1). The aim is the estimation of the bulk properties of the rock from numerous laboratory measurements. No rock is perfectly homogeneous, but it is still desirable to represent its properties by a single number if appropriate.

The further analysis of the rock properties may be aided by the division of the measurements into groups. If it is assumed that each measurement in a group is of the same quantity, then the uncertainty of the properties of the group as a whole may be estimated using a statistical method called the analysis of variance [84]. Further, if each group is assumed to be a gross measurement of the same quantity, then a total estimate of aspects of the rock’s dielectric behaviour may be obtained. The uncertainty of a group consists of two components added in quadrature: the first is an estimate of the MU, s_{wit}^2 , taken as the mean of the individual MU’s, the second is the variation between the group’s expected values, s_{bet}^2 . Clearly the group analysis loses meaning if the MU is larger than the variation between groups — in such a case no statement regarding the consistency of the rock can be made.

The group uncertainties (GU’s) may be sub-divided into the rotational GU (RGU) and linear GU (LGU). The total group uncertainty (TGU) and total group mean (TGM) (also called the *grand mean* [84]) are also occasionally appropriate to describe the properties of an entire core with a single distribution. There is no ‘correct’ way of defining these — it is sought to quantify the characteristics of the core’s properties in some way, and the definitions to follow serve that purpose.

The rotational group uncertainty (RGU) is intended to quantify the difference between the measurements in the four orientations. Though tempting to ascribe any differences between these measurements to anisotropy of the material, it is not possible to distinguish this effect from that of small-scale inhomogeneities. Although constituents of a rock may display anisotropy on a microscopic level, the rock’s essentially random composition precludes such effects at the scale of the measurement. The dielectric constant’s components, permittivity and loss tangent, are represented by single scalar values, and the RGU’s are taken as measures of the small-scale inhomogeneity of the measured material.

Consider the division of the core into N discs, each corresponding to a set of four orientational measurement points at a single lateral position along the core. An estimation of the rock property uncertainty of each disc consists of two components: one due to the MU’s of each individual measurement point (the intra-group uncertainty, s_{wit}^2), the other due to the variation between the individual measurements’ expected values (the inter-group uncertainty, s_{bet}^2). Again, for the purposes of this analysis, each of the four measurements is assumed to be of the same quantity. Then the first component may be estimated by averaging the four MU’s [85]. The second is taken as the standard deviation of the individual expected values, and is added in quadrature to the first:

$$E(RGU_i) = s_{wit,i}^2 + s_{bet,i}^2 \quad (6.1)$$

If it is now assumed, again for the purposes of this argument, that each RGU_i is an estimation of the same quantity, then the total RGU may be estimated by

$$E(RGU) = \overline{RGU}_i = \frac{1}{N} \sum_{i=1}^N RGU_i \quad (6.2)$$

The linear group uncertainty is calculated in a similar way to the RGU. In this case the variation of the properties along the core is of interest. The LGU is also a measure of the rock's inhomogeneity, but on a slightly larger scale than the RGU (depending on the length of the sample). The core is divided into M linear groups (M corresponding to the number of orientations measured, i.e. usually 4), each containing N individual measurements. The uncertainty of each group is again the square addition of the averaged MU's and the inter-group variation:

$$E(LGU_k) = s_{wit,k}^2 + s_{bet,k}^2 \quad (6.3)$$

The total LGU may in this case be estimated by

$$E(LGU) = \overline{LGU}_i = \frac{1}{M} \sum_{k=1}^M LGU_k \quad (6.4)$$

The total group uncertainty is a measure of the total variation among all the measurements taken of a core, and is estimated by treating all the (i.e. MN) measurements as if they were of the same quantity [84]. In the same way as for the RGU and LGU, the TGU's estimation is calculated by combining the average of all the MU's and the variation between all the measurements' expected values. The total group uncertainty will usually be very close to the larger of the RGU and LGU.

Two further parameters prove useful for the analysis of the measured data:

1. The coefficient of variation (CV) is defined as the ratio of standard deviation to mean of a particular sample set [86], and gives an idea of the relative dispersion of the sample values. In this case, it gives an idea of the relative homogeneity of an individual sample's properties. If the total group CV is small, the sample is fairly homogeneous and it may be possible that the measured properties can be taken as a good indicator of the bulk properties. A number of phenomena may lead to a significant CV, and a closer investigation into the likely cause would be required.
2. The intra-material spread (IMS) of a material type (for example, granite or norite) is defined as the ratio of the maximum to minimum value of any of that material type's properties. The IMS of the mean of a number of norite samples' permittivities, for example, gives an indication of how different the permittivities of norite as a rock type are. Applying this parameter to the standard deviation of a property is less intuitive, but useful nonetheless in that it tells us something about how the composition of the various samples of one rock type differ. For example, a high IMS in the standard deviation of the permittivities of a number of quartzite samples would imply that some samples are quite homogeneous while others may have a permittivity which varies rapidly on a small scale.

The CVs of the rotational, linear and total group uncertainties are of interest, and are in each case calculated by the relation of the relevant uncertainty to the grand mean. In all of the above definitions, the use of terms like 'small' and 'large' cannot be absolute. The magnitude of parameters must always be seen in relation to those of other rock types. In the case of a certain sample displaying a relatively large CV or a material type having a large IMS, the cause should be investigated and the applicability of the measured properties to bulk properties evaluated.

Note that this sort of group analysis of the material properties is not invalidated by the uncertainty due to calibration interpolation. Individual measurement repeatability is the key here: individual measurements of similar rock properties measured with the same device may be compared with confidence if they are repeatable.

The material properties at 25 MHz are most relevant to analysis of BHR data and are thus the only ones tabulated explicitly in this chapter. But knowledge of the properties' frequency dependence is important and the complex dielectric constant may often be represented fairly accurately with the Jonscher model discussed in Section 2.2.3. As will be seen, the models can usually be fitted to the measured permittivity points to within about 5 %, but the loss tangent fit is often less good. Further, the form of the resulting Jonscher curve is sometimes not the same as that of the actual properties, making extrapolation in frequency suspect.

6.3 Bushveld Igneous Complex

6.3.1 Geological Background

The Bushveld Igneous Complex (BIC) is one of eight known layered igneous complexes in the world, and is the only one mined for platinum [34]. This with some success, since it hosts about 75 % of the world's known platinum group metals (PGM) resources, and produces about 75 % of the world's platinum, and 35 and 75 % of its palladium and rhodium respectively.

The BIC is estimated to be about 2050 mega-years in age, and covers an area of approximately 65 000 square kilometres in north-western South Africa, with the town of Rustenberg roughly at its western edge. It has the typical inverted funnel shape of layered complexes [34], with its rim exposed at the surface at a number of locations, and its centre deep underground. Capped by overlying Bushveld granites, amongst others, the BIC itself is a composite body consisting of four sill-like intrusives which together form a mafic/ultramafic layered series (also known as the Rustenberg Layered Suite (RLS) [82]) in which all the chromite and platinum producing ore horizons lie [34].

The stratigraphy in various parts of the BIC differs substantially in terms of thickness and lithological variations [82]. In general, however, it may be divided into four zones (corresponding to the intrusives): the basal (or lower) zone, consisting of interlayered periodite and pyroxenite, is separated from the overlying critical zone (CZ) by a continuous chromitite layer. The CZ consists of a succession of dunite, pyroxenite, anorthosite and chromite layers, and is host to large deposits of chromium and platinum. The most important of these deposits occur within the UG2 chromitite layer and the Merensky reef, which also marks the transition from the CZ to the overlying main and upper zones.

Since its initial exploitation in the 1970's, the economic importance of the UG2 chromitite layer increased to the point that it produced 42 % of ore processed in 1999 ([87], cited in [83]). Its economic importance in terms of PGM concentration has come to rival that of the Merensky reef [82].

Its high-resolution delineation by borehole radar is the focus of a number of current explorations (see e.g. [83]); accurate knowledge of its own and the various surrounding layers' dielectric properties is critical for experiment planning and interpretation of measured data.

Of primary importance to the planned and conducted borehole studies is the CZ region between the UG1 and UG2 chromitite layers [83], also known as the UG1 unit. The stratigraphy of the unit can vary substantially in terms of the thickness and occurrence of individual layers. A detailed local description of the relevant stratigraphy is required in the planning and evaluation of any individual experiment. For this reason, no general description of its geology will be given. Rather, the local environments encountered in the borehole experiments conducted will be described in detail in Section 6.3.2.

The UG1 unit presents us with an ideal opportunity to demonstrate the abilities of the developed

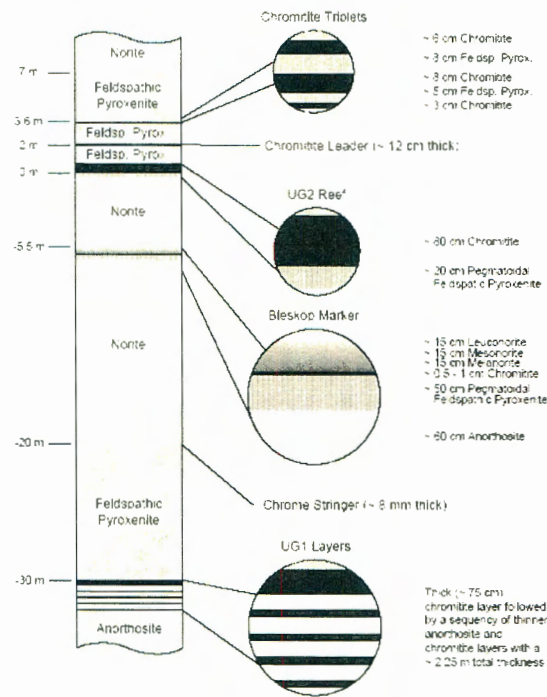


Figure 6.1: Herselman's generalisation of the stratigraphy between the UG1 and UG2 reefs [83].

of the device due to measurement stresses.

For the measurement of the Bleskop Marker, three repeatability measurement sets were conducted: one before and after both BKM measurements, and one between the measurements of the whole core and the chromitite stringer. The worst-case repeatability data are summarised in Tables 6.1 and 6.2. The variation in uncalibrated measured impedance data is presented: the magnitude uncertainty is listed as a percentage of the mean of the measured values, while the phase uncertainty is absolute. A comparison of these two tables is interesting. In the first characterisation, the 'before' and 'after' values are similar, but the total repeatability is worse, implying that the device response has changed during the measurement of the BKM but not worsened. The second characterisation again has similar before and after values, but this time the total repeatability is not worse than the individual ones. In this case the device response has not changed or worsened noticeably. It appears that repeatability is better and measurement uncertainty is reduced if device characterisation is carried out at shorter intervals, particularly if many cores are to be measured with a single capacitor.

Another three repeatability measurements were done during the measurement of UG2 cores: characterisations were done before and after the measurement of samples 2, 4, 5, 6, 7 and 10 (Table 6.3), before and after the measurement of samples 3, 9 and 11 (Table 6.4), and before and after the measurement of the transitions in samples 3 and 9, shown in Figure 6.6 (Table 6.5).

In all cases repeatability of the total CV_Z was smaller than about 1.4 %, and the measured phase angle was stable within 0.3° . The magnitude of Z is proportional to ϵ_r while the phase angle is directly related to the loss tangent, thus the repeatabilities in Tables 6.1 to 6.5 are direct estimates of the influence on these properties' measurement accuracy.

Sample	before		after		total	
	CV_Z [%]	σ_θ [°]	CV_Z [%]	σ_θ [°]	CV_Z [%]	σ_θ [°]
Teflon	0.06 ₃	0.03 ₂₅	0.05 ₂₅	0.01 ₂₅	0.08 ₂₅	0.02 ₂₅
PVDF	0.31 ₅	0.07 ₂₅	0.22 ₅	0.05 ₂₅	1.14 ₅	0.22 ₁
Art. Diel.	0.37 ₅	0.08 ₁	0.52 ₂₅	0.10 ₂₅	1.09 ₅	0.24 ₁
BKM-2	0.26 ₁	0.08 ₂₅	0.29 ₂₅	0.06 ₁	0.41 ₁	0.16 ₁

Table 6.1: The measurement repeatability of the 36.4 mm probe used for the Bleskop Marker sample was determined by 5 pre- and 5 post-characterisation measurements, done immediately before and after measurement of the total core. (The subscript in each case denotes the frequency (in MHz) at which the repeatability was worst.)

Sample	before		after		total	
	CV_Z [%]	σ_θ [°]	CV_Z [%]	σ_θ [°]	CV_Z [%]	σ_θ [°]
Teflon	0.05 ₂₅	0.01 ₂₅	0.16 ₂₅	0.02 ₂₅	0.11 ₂₅	0.01 ₂₅
PVDF	0.22 ₅	0.05 ₂₅	0.15 ₂₅	0.03 ₂₅	0.25 ₅	0.07 ₁
Art. Diel.	0.52 ₂₅	0.10 ₂₅	0.24 ₂₅	0.04 ₁	0.42 ₂₅	0.10 ₂₅
BKM-2	0.29 ₂₅	0.06 ₁	0.30 ₂₅	0.06 ₂₅	0.28 ₂₅	0.08 ₁

Table 6.2: The repeatability of the 36.4 mm probe used for the measurement of the BKM's chromitite stringer was determined again, using the post-characterisation measurements from Table 6.1 as the pre-characterisation values in this case, and performing another 5 post-characterisation measurements following measurement of the stringer. (The subscript in each case denotes the frequency (in MHz) at which the repeatability was worst.)

Sample	before		after		total	
	CV_Z [%]	σ_θ [°]	CV_Z [%]	σ_θ [°]	CV_Z [%]	σ_θ [°]
Teflon	0.04 ₃	0.01 ₂₅	0.12 ₂₅	0.02 ₁₅	0.09 ₂₅	0.02 ₂₅
PVDF	0.29 ₅	0.06 ₂₅	0.32 ₂₅	0.07 ₂₀	1.39 ₅	0.30 ₁
Art. Diel.	0.28 ₅	0.07 ₁	0.25 ₂₅	0.04 ₂₅	1.29 ₅	0.29 ₁
UG2-5	0.25 ₁	0.07 ₁	0.22 ₁	0.07 ₂₅	0.41 ₂₅	0.09 ₁

Table 6.3: The repeatability measurements of the 36.4 mm probe used for the measurement of the UG2 samples 2, 4, 5, 6, 7 and 10. (The subscript in each case denotes the frequency (in MHz) at which the repeatability was worst.)

Sample	before		after		total	
	CV_Z [%]	σ_θ [°]	CV_Z [%]	σ_θ [°]	CV_Z [%]	σ_θ [°]
Teflon	0.06 ₂₅	0.02 ₂₅	0.05 ₂₅	0.02 ₁₅	0.08 ₃	0.01 ₁₅
PVDF	0.26 ₅	0.06 ₂₅	0.18 ₅	0.11 ₂₅	0.95 ₅	0.20 ₁
Art. Diel.	0.33 ₅	0.09 ₂₅	0.35 ₅	0.07 ₂₀	0.74 ₂₅	0.16 ₁
UG2-5	0.28 ₂₅	0.11 ₁	0.27 ₂₅	0.12 ₂₅	0.49 ₂₅	0.09 ₂₅

Table 6.4: The repeatability measurements of the 36.4 mm probe used for the measurement of the UG2 samples 3, 9 and 11. (The subscript in each case denotes the frequency (in MHz) at which the repeatability was worst.)

Sample	before		after		total	
	CV_Z [%]	σ_θ [°]	CV_Z [%]	σ_θ [°]	CV_Z [%]	σ_θ [°]
Teflon	0.05 ₂₅	0.02 ₁₅	0.05 ₂₅	0.01 ₁₀	0.07 ₂₅	0.01 ₁₀
PVDF	0.18 ₅	0.11 ₂₅	0.34 ₂₅	0.06 ₁₅	0.81 ₅	0.18 ₁
Art. Diel.	0.35 ₅	0.07 ₂₀	0.27 ₂₅	0.06 ₂₅	0.91 ₅	0.19 ₁
UG2-5	0.27 ₂₅	0.12 ₂₅	0.37 ₂₅	0.06 ₂₅	0.39 ₂₅	0.10 ₂₅

Table 6.5: The repeatability measurements of the 36.4 mm probe used for the measurement of some of the UG2 samples’ transitions. (The subscript in each case denotes the frequency (in MHz) at which the repeatability was worst.)

6.3.4 Measurements of the Bleskop Marker

The detailed analysis of the Bleskop Marker structure allows the demonstration of the ability of the guarded capacitor to measure fine-scale changes in dielectric constant of a sample, as well as providing additional data on the properties of rock types commonly found in the UG1 unit. It should again be noted that the precise structure of the Bleskop marker is highly variable. The sample at our disposal was taken from a borehole in Bleskop mine used for delineation experiments, and knowledge of its precise dielectric property sequence was thus useful in interpretation of the data obtained in those experiments [83].

Sample Descriptions

The sample shown photographically in Figure 6.2 shall now be described geologically from top to bottom. From left to right, the first 18.5 cm consists of noritic rock: the initial light leuconorite, having a 90 % anorthosite content, changes through mesonorite to the darker melanorite, which is 80 % pyroxenite. Following this is an irregular oblique chromitite inclusion (also referred to as a ‘stringer’) of about 25 mm thickness. The next 51 cm is a partially broken section of rock containing mottled pegmatoidal feldspathic pyroxenite (PFP), which is a dominantly darkish rock with irregular lighter inclusions. A 60 cm anorthosite layer is followed by a gradual transition to norite (lightly speckled with pyroxenite), which extends to the end of the sample [88].

The sample consists of eight parts of varying length, described in detail in Table 6.6. The quality of the breaks between samples varies: some are clean, allowing a tight fit with minimal impact on measurement accuracy, while others, in particular those between sections 2, 3, 4 and 5, have disintegrated quite badly. The measurements in the region of these breaks will be affected by the breaks, but the section of core affected is relatively short (about 18 cm).

Measurement Results

The mean of four orientational measurements of the dielectric properties of the entire core, measured at 1 cm intervals, is shown below a photograph of the core in Figure 6.2. This view shows clearly how the dielectric properties change with material. As expected, the chromitite stringer is conspicuously different from its host. Less expected is the dramatic variation in the properties of the PFP section between the stringer and the transition to anorthosite at the 72 cm mark. The dielectric constant of this PFP layer, while not quite as large as the chromitite’s, contrasts dramatically with the anorthosite and norite properties, and may thus constitute a substantial local radar reflector.

An interesting feature of the BKM is the chromitite stringer found between 18.5 and 21 cm along the core. As shown in the close-up photographic views in Figure 6.3, the stringer is quite irregular but roughly

Section	Section End [cm]	Description
1	28.3	Norite transition starting at 3.0 cm; chromitite stringer between 18.5 and 21.0 cm; pegmatoidal feldspathic pyroxenite to end.
2	51.0	Pegmatoidal feldspathic pyroxenite
3	56.5	Pegmatoidal feldspathic pyroxenite
4	59.7	Pegmatoidal feldspathic pyroxenite
5	67.6	Pegmatoidal feldspathic pyroxenite
6	96.0	Pegmatoidal feldspathic pyroxenite, changing to anorthosite between 72.0 and 73.0 cm.
7	107.8	Anorthosite
8	149.0	Anorthosite, changing gradually to norite between 133.0 and 135.0 cm; <i>oblique sample end.</i>

Table 6.6: Description of the various core sample pieces constituting the Bleskop Marker.

oblique. Its width, were it to be measured by enclosing it with two planes perpendicular to the core axis, is about 25 mm. Measurements of the dielectric constant in the four orientations, displayed in Figure 6.4, show how the magnitude, shape and precise axial position of the peaks change depending on which orientation the stringer is measured in. The curves and the photographs should be used in conjunction: the 90° curve corresponds to the stringer encountering the measuring electrode in the position shown in Figure 6.3(b). The stringer contacts the sensing electrode latest in the 270° measurement, and in Figure 6.3(d) the chromitite edge is indeed furthest from the top. Further, the slightly lower maximum peak value of the 180° measurement corresponds to the break in the stringer seen in Figure 6.3(c).

The discussion of the measurement of inclusions from Section 5.3 finds application here: the properties of the chromitite stringer may best be estimated by measuring it with a relatively narrow electrode at different orientations. Comparison with the transition measurements shown in Figure 5.6(a) is revealing. An estimate of the actual properties at 25 MHz can be made by approximating the stringer as an angled (about 30 degrees) inclusion of approximately 10 mm width. Since the maximum values for permittivity and loss tangent in the graphs in Figure 5.8 agree to within about 10 % (apart from the loss tangent at 20 MHz) to the maximum values for a straight inclusion, an estimation of the stringer's properties if were approximated as a straight inclusion of between 10 and 20 mm will be conducted. Using (5.16) and (5.17), with $l = 20$ mm, the maximum orientational $\epsilon_{r,t} \approx 14.5$ and $\tan \delta_t \approx 0.23$, the host properties $\epsilon_{r,h} \approx 7.6$ and $\tan \delta_h \approx 0.04$, the permittivity and loss tangent of the chromitite found in the stringer may be estimated to be $\epsilon_{r,i} \approx 28.9$ and $\tan \delta_{r,i} \approx 0.33$ when $s = 10$ mm, and of course as $\epsilon_{r,i} \approx 14.5$ and $\tan \delta_{r,i} \approx 0.23$ when $s = 20$ mm. It would be reasonable to expect the actual values to lie somewhere between these estimates.

Apart from seeing the BKM as a single unit, it is instructive to look at each material type found in the BKM separately as well. The material properties of the four material sections found in the sample — two norite sections from 1–16 and 135–145 cm, pegmatoidal feldspathic pyroxenite from 22–50 cm, anorthosite from 75–130 cm and another norite section from 135–145 cm — are listed in Table 6.7 after the manner described in Section 6.2. The rotational and linear variation in these materials' measurements are shown in Table 6.9. The maximum predicted individual measurement uncertainties listed in Table 6.8 are all substantially lower than any of the group uncertainties.

The Jonscher parameters of the samples, given in Table 6.10, give an adequate representation of ϵ_r but not of $\tan \delta$. Extrapolation in frequency based on these models would not be recommended.

Sample	x [cm]	Permittivity		Loss Tangent		Atten. [dB/m]		Velocity [m/ μ s]	
		$\bar{\epsilon}_r$	CV_{ϵ_r}	$\overline{\tan \delta}$	$CV_{\tan \delta}$	$\bar{\alpha}$	CV_{α}	\bar{v}	CV_v
norite	1–16	7.59	1.27	0.04	13.57	0.28	13.87	108.80	0.64
	135–145	7.45	0.90	0.04	6.69	0.24	6.89	109.79	0.45
PFP	22–50	7.75	8.39	0.06	41.70	0.40	45.86	107.94	4.24
anorthosite	75–130	7.37	1.17	0.04	8.13	0.26	8.20	110.39	0.59

Table 6.7: Material properties of the individual BKM materials at 25 MHz.

Sample	x [cm]	Permittivity	Loss Tangent	Atten. [dB/m]	Velocity [m/ μ s]
norite	1–16	0.016	0.001	0.005	0.108
	135–145	0.015	0.001	0.005	0.108
PFP	22–50	0.023	0.001	0.007	0.119
anorthosite	75–130	0.015	0.001	0.005	0.109

Table 6.8: Maximum predicted individual measurement uncertainty, calculated as described in Section 2.5.1, of the BKM material sections at 25 MHz.

Sample	x [cm]	Permittivity		Loss Tangent		Atten. [dB/m]		Velocity [m/ μ s]	
		CV_{RG}	CV_{LG}	CV_{RG}	CV_{LG}	CV_{RG}	CV_{LG}	CV_{RG}	CV_{LG}
norite	1–16	1.19	1.10	2.81	13.88	2.97	14.20	0.60	0.56
	135–145	0.92	0.81	4.87	6.33	5.17	6.45	0.46	0.40
PFP	22–50	5.27	8.44	11.57	42.14	14.01	46.36	2.67	4.53
anorthosite	75–130	0.97	1.11	3.81	8.08	4.08	8.13	0.49	0.56

Table 6.9: Coefficients of variation of the individual BKM materials at 25 MHz, calculated as described in Section 6.2.

Sample	x [cm]	n	χ_r	ϵ_{∞}	max. $ \Delta \epsilon_r $ [%]	max. $ \Delta \tan \delta $
norite	1–16	0.26	0.04	7.28	4.31 ₂₅	0.040 ₂₀
	135–145	2.52	0.32	7.06	0.33 ₂₅	0.045 ₁
PFP	22–50	0.43	0.26	7.20	4.23 ₂₅	0.028 ₂₀
anorthosite	75–130	0.29	0.04	7.03	4.47 ₂₅	0.038 ₂₀

Table 6.10: Jonscher parameters of the mean dielectric properties of the Bleskop Marker rock types. The maximum difference between the permittivity and loss tangent predicted by the Jonscher model and the actual value are shown, along with the frequency at which the maximum difference occurs (subscripts).

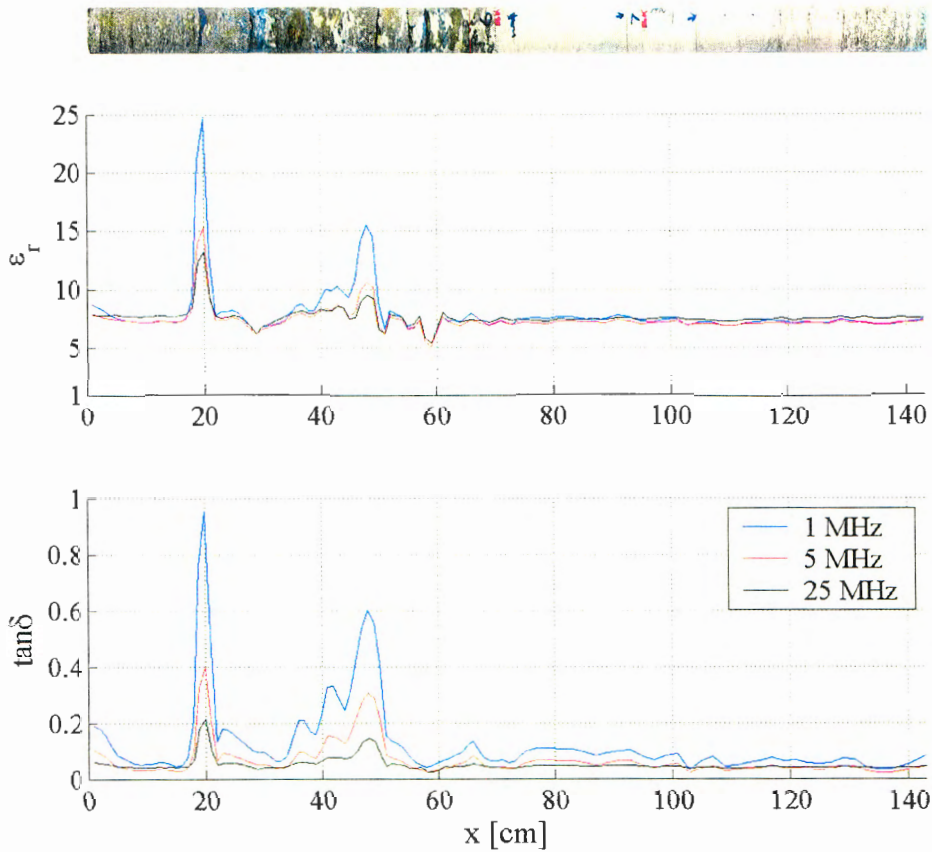


Figure 6.2: The mean measured dielectric properties of the entire Bleskop Marker, at 1, 5 and 25 MHz, are shown below a photograph of the core. The properties of the norite and anorthosite sections of the core are fairly homogeneous, as presented in Table 6.7, with the notable exception of a number of features: the chromitite stringer at about 20 cm results in a sharp ‘spike’ in the properties; the variation in PFP properties can be related to a change in material composition, culminating in the peak at about 50 cm; the broken up section of core between 50 and 60 cm results in the rough behaviour of both properties in that region. Measurements were conducted at 10 mm intervals using a sensing electrode with $l = 20$ mm.

The properties of norite and anorthosite are very similar: both are relatively homogeneous rocks with low attenuation factors ($\alpha < 0.3$ dB/m) and radar propagation velocities above about 108 m/ μ s. In both cases, the linear group uncertainty is somewhat larger than the rotational group uncertainty, indicating that these are quite homogeneous materials on a fine scale. The 1–16 cm norite sample’s LGU is somewhat higher than that of the later norite and the anorthosite. The higher dielectric constant in the first 3 cm of the core is due to the core sampling the end of another material. This calls attention to the unavoidable restrictions of measuring limited samples, as the small available section of this ‘other’ material is not sufficient to quantify its properties with any sort of confidence.

The pegmatoidal feldspathic pyroxenite has very similar mean properties to the surrounding rock at 25 MHz, but displays much higher group uncertainties. These may be explained by observing the close-up photographic view of the PFP section shown in Figure 6.5. It is clear that this rock is quite irregular, appearing almost like a conglomerate. Its properties vary considerably, exhibiting a permittivity range of about 6.25 to 15.5 and 6.25 to 9.5 at 1 and 25 MHz respectively, and a loss tangent range of about 0.06 to 0.6 at 1 MHz and 0.035 to 0.15 at 25 MHz. Some sections of its behaviour could not be determined due

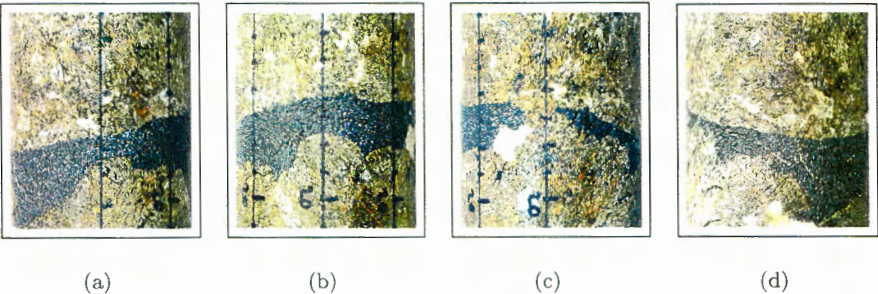


Figure 6.3: Close-up views of the BKM’s chromitite stringer in the four orientations corresponding to the curves in Figure 6.4: (a) 0°, (b) 90°, (c) 180° and (d) 270°. The core is measured from top to bottom, i.e. the top of the stringer encounters the sensing electrode first.

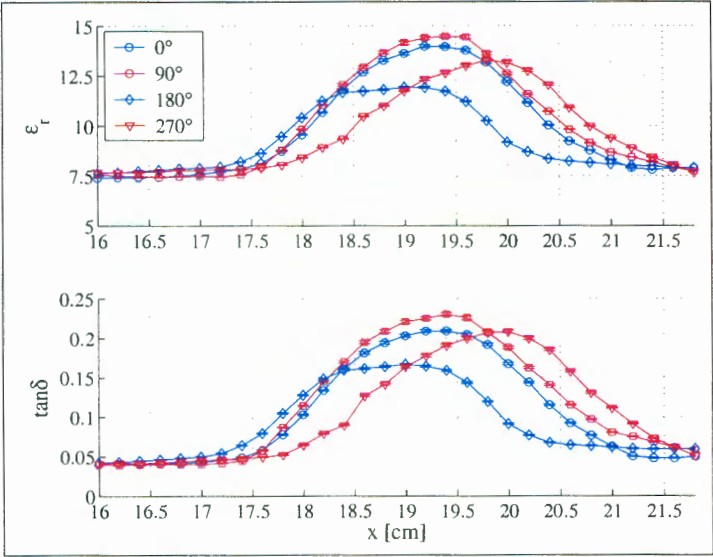


Figure 6.4: Close-up measurements of the chromitite stringer found at about 20 cm were conducted in all four orientations at 2 mm intervals, at 25 MHz, using a sensing electrode with $l = 20$ mm.

to damage to the core. These effects are particularly evident in the permittivity plot between 50 and 60 cm in Figure 6.2; the dip at about 29 cm is presumably also due to the break between samples 1 and 2. The behaviour of the loss tangent in comparison to the permittivity is noteworthy: the breaks between the samples affects its measurement far less.

The 50 cm PFP sample length available is very limiting. The properties change substantially from the PFP immediately adjacent to the chromitite stringer to the peak found at about 48 cm. These peak properties are substantially larger than the noritic and anorthositic expanses below and above the marker, and it is thus reasonable to expect that it will result in quite a clear reflection.

The question of whether the property curves seen here are similar in regions adjacent to the borehole from which this sample was extracted cannot be answered without further samples. The possibility that the thicker PFP layers found adjacent to the UG1 and UG2 reefs [89] may also have greatly varying properties cannot be ignored. If high-resolution imaging of these reefs is desired, a better idea of the properties of these layers is required.



Figure 6.5: Photograph of the pegmatoidal feldspathic pyroxenite section of the BKM between 22 and 71 cm. The rough breaks between sections 2, 3, 4 and 5 are visible toward the right of the image, as are the slightly better fitting breaks between sections 1 and 2 toward the left, and 5 and 6 at the far right. The variation in the complex rock structure is clearly visible.

6.3.5 Measurement of the UG2 Reef and Triplets

Sample Descriptions

Ten samples were obtained from borehole WV171 in the Rustenberg Section's Waterval mine. The samples were chosen to represent the UG2 and the immediately surrounding rock types. Geological and photographic descriptions are shown in Table 6.11. These samples present an opportunity to obtain good estimates of the dielectric properties all the host rock types surrounding the UG2, as well as of the major chromitite layers, the triplets, the leader and the main reef.

Measurement Results

The samples were measured over their entire length at 1 cm intervals. Sample 1's condition only allowed it to be measured in a single orientation, but the other samples were all measured in the standard four orientations. The measurements of regions of homogeneous rock were extracted to provide estimates of their bulk propagating characteristics, while some transitions were investigated in more detail to investigate the properties of thin layers and to gain a further understanding of the electrode's operation. Six material types were found in the cores measured; their measured dielectric properties at 25 MHz are listed in Table 6.12. The predicted individual measurement accuracy, shown in Table 6.13, is always smaller than the group uncertainties in Table 6.14, allowing statements to be made regarding material consistency.

The intra-material spreads of feldspathic pyroxenite and chromitite at 25 MHz, given in Table 6.15, show both materials to be fairly homogeneous (compare these IMS's to those of the Premier and Snap Lake materials in Tables 6.24 and 6.34). The fitting of Jonscher models to the frequency response of mean

material properties is shown in Table 6.16. As for the BKM materials, the permittivity fit is reasonable but large differences are apparent between the modelled and measured loss tangents.

It is clear that the chromitite layers' properties are all similar ($11.67 \leq \overline{\epsilon_r} \leq 12.16$, $0.09 \leq \overline{\tan \delta} \leq 0.11$) and differ as a group from all the host rocks', both in terms of permittivity and loss tangent. An exception is melanorite's mean loss tangent of about 0.08, which is only slightly below that of chromitite. While chromitite has a relatively high attenuation constant of between about 0.7 and 0.9 dB/m, the other rock types (again with the exception of melanorite) provide adequate propagating conditions. With the exception of pegmatoidal feldspathic pyroxenite, all rock types are fairly homogeneous on a local scale.

The properties of PFP ($\epsilon_r \approx 7.8$, $\tan \delta \approx 0.06$) and anorthosite ($\epsilon_r \approx 7.4$, $\tan \delta \approx 0.04$) are very close to the equivalent BKM samples' properties (PFP: $\epsilon_r \approx 8.3$ and $\tan \delta \approx 0.06$; anorthosite: $\epsilon_r \approx 7.4$, $\tan \delta \approx 0.05$), but melanorite is clearly different from the BKM norite, having a substantially higher loss tangent (0.08 vs. 0.04) and attenuation constant (0.52 vs. 0.26 dB/m). The inhomogeneity of PFP is also evident in both samples — the rock shown in Table 6.11 seems finer grained than the BKM PFP and accordingly displays a smaller TGU than the BKM sample.

Most of the materials have rotational group uncertainties that are either similar to or smaller than their linear group uncertainties, implying that they are relatively homogeneous on a centimetre scale. The chromitite found in samples 6 and 7, and particularly in sample 9, on the other hand, has larger rotational group uncertainties. The suggestion is that chromitite displays a fine scale variation but is quite homogeneous on the scale of the layer thickness. The small variation in sample 3's chromitite is likely due to the layer's short extent. The complex geology of PFP (sample 10) again results in an LGU substantially larger than that of any of the other materials.

Two interesting transitions are found in samples 3 and 9. Sample 3 contains a 3 cm section of pegmatoidal feldspathic pyroxenite between the feldspathic pyroxenite hangingwall and the third UG2 triplet. This transitional layer can be seen between the 18 and 21 cm marks in Figure 6.6(a): both the permittivity and loss tangent of the PFP section are noticeably higher than of the feldspathic pyroxenite. The PFP properties correspond closely to those of the PFP in sample 10 at 25 MHz, showing that small sections of rock may at least provide an indication of expected rock properties if no other samples are available.

Sample 9's main UG2 chromitite layer is interrupted near its top edge by an intrusion of feldspathic pyroxenite. The effect on the dielectric properties is clearly visible in Figure 6.6(b), which shows 5 mm resolution measurements starting from 18 cm along the core. The peak permittivity of the removed chromitite section matches that of the main body closely, as does the permittivity of the feldspathic pyroxenite that of the main hangingwall. The loss tangent also displays the same tendencies (particularly clearly at 25 MHz). Again, small sections of rock show promise in giving a reasonable estimation of bulk properties.

The anorthosite properties are only an estimate since the condition of sample 1 prevented accurate measurement. Only a single orientation was measured, and the continual presence of airgaps due to the 'corkscrewing' drill action places those results in question. Another estimate of the properties of anorthosite may be obtained from the top few cm of sample 2, which were measured with a resolution of 2 mm. Figure 6.7 shows the measured permittivity and loss tangent of the first few centimetres of this sample at 1, 5 and 25 MHz. Anorthosite's permittivity and loss tangent are estimated from the first centimetre of these measurements as $\epsilon_r \approx 7.95$ and $\tan \delta \approx 0.08$ respectively, slightly higher than sample 1's properties. The air gap present during the measurement of sample 1 would tend to decrease the effective measured properties, but sample 1's properties do match the properties of BKM anorthosite closely. More samples would be required for a conclusive statement on the properties of anorthosite.

The presence of the chromitite stringer in sample 2 is clearly detected, and its properties may be estimated using the work done on the measurement of inclusions in section 5.3.

The measurement of the two chromitite ends of sample 4 may be used to estimate the properties of the first and second triplets. The first triplet's permittivity and loss tangent are approximately 12.5 and 0.14 respectively at 25 MHz, while the second triplet has corresponding properties of $\epsilon_r \approx 10.7$ and $\tan \delta \approx 0.11$. These values fall in the same range as those observed in the larger chromitite samples (shown in Table 6.12).

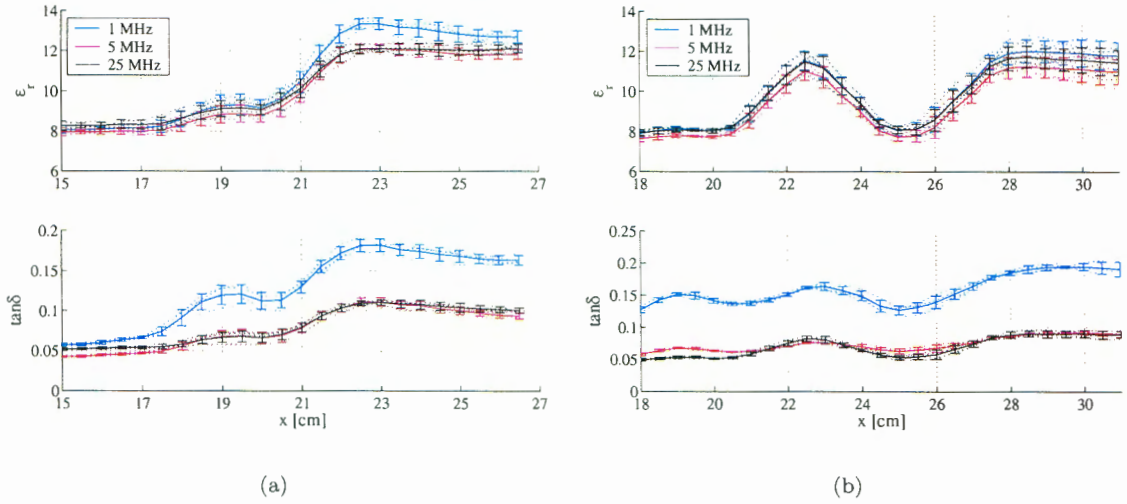


Figure 6.6: Two interesting transitions between materials are found in samples 3 and 9.

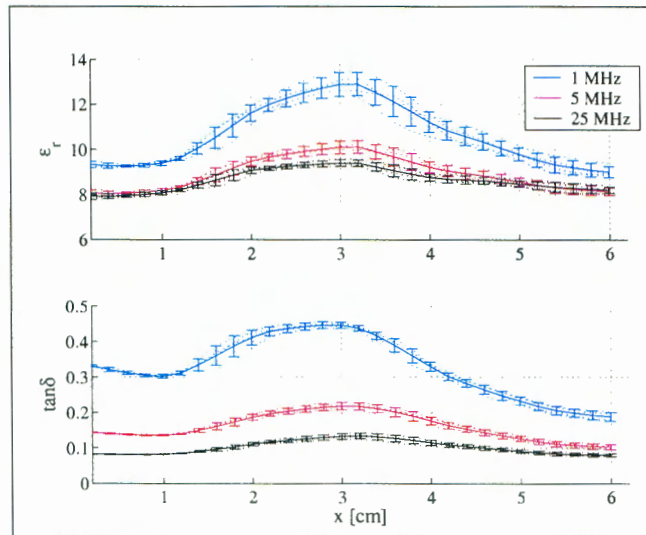


Figure 6.7: The dielectric properties of the top 6 cm of sample 2 allow an estimation of the properties of anorthosite ($\epsilon_r \approx 7.95$ and $\tan \delta \approx 0.08$ at 25 MHz), and clearly show the effect of the chromitite stringer. The error bars shown are the RGU at each linear measurement point.

6.3.6 Discussion

The measurement of a collection of samples from within and around the economically important UG2 reef, representing all the major material types found, has been described. The ability of the capacitor to accurately predict bulk propagation speeds as well as measure small-scale transitions in core sample properties was demonstrated.

Measurements of the same rock types from the UG2 layers and Bleskop Marker, spaced some 6 metres apart, yielded similar results. Various similarly spaced samples described in the UG2 measurement (Section 6.3.5) also had properties which were in close agreement. The argument for using the measured results of localised samples in the prediction of bulk material properties is thus strengthened. Comparison of the propagation velocities calculated in Tables 6.7 and 6.12 to velocities estimated from a cross-hole radar shoot in the field support this further.

Two propagation velocity estimates were performed by Herselman following cross-hole BHR experiments in different sections of the UG1 unit. The first was made from data obtained from a radar trial at Bleskop mine where the transmitter and receiver were deployed in the rock immediately below the UG2 main chromitite reef. Three different surveys were used to estimate a peak pulse velocity of $104 \text{ m}/\mu\text{s}$ [83]. The laboratory prediction for the propagation velocity of the melanorite found immediately below the UG2 reef (Table 6.12) is $104.7 \text{ m}/\mu\text{s}$, which is within 1 % of the bulk estimate.

The second experiment was conducted at the RPM Bleskop mine in June 2002. In this case the boreholes' collars are just below the Bleskop Marker. The boreholes extend for about 90 metres, mainly staying in the norites found between the BKM and the UG1 reef. A velocity estimate was again made from cross-hole pulse arrival times along 90 m of the cores. Herselman's velocity estimate of $110 \text{ m}/\mu\text{s}$ [83] is very close to the laboratory measurements of the norites and anorthosite found in the lower section of the BKM core sample (between 108.8 and $110.4 \text{ m}/\mu\text{s}$ at 25 MHz), again an agreement of within 1 %. It would appear that laboratory measurements of fairly homogeneous rock samples provide a good estimate of propagation velocities found in similar rock types in the field.

Some conclusions about the expected bulk propagating conditions and the feasibility of radar detection of the UG2 may be drawn. The permittivity and loss tangent of the various chromitite layers at 25 MHz are consistently higher than the other rock types found (arguably with the exception of certain sections of pegmatoidal feldspathic pyroxenite and the loss tangent of melanorite). This noticeable contrast in the properties should (and does [83]) result in noticeable radar reflections. Attenuation of all the host rock types is below about 0.5 dB/m and propagation velocities are consistently above $104 \text{ m}/\mu\text{s}$, making for good propagating conditions. Most of the rock types are fairly homogeneous. Pegmatoidal feldspathic pyroxenite is geologically and dielectrically less homogeneous — local knowledge of the occurrence of this rock type in particular is important for interpretation of radar data.






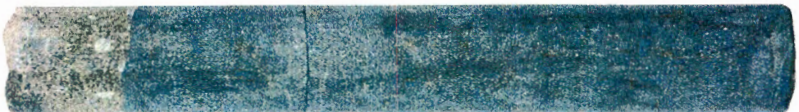
Sample	Diameter [mm]	Sample Description
UG2-1	36.10	
		Homogeneous sample of coarse poikilitic anorthosite taken from the hangingwall of the UG2 above the triplets. This sample exhibited severe 'cork-screwing': its diameter varied continually, presumably due to gyration of the bit during drilling.
UG2-2	36.15	
		This sample straddles the intersection at 55.85 m between the coarse poikilitic anorthosite and underlying medium textured feldspathic pyroxenite. The change is marked by a very narrow (2 mm) oblique chromitite stringer.
UG2-3	36.10	
		This feldspathic pyroxenite host contains the uppermost chromitite triplet (UG2 Triplet 3); the 3 cm section above (to the left of) the chromitite consists of pegmatoidal feldspathic pyroxenite.
UG2-4	36.13	
		This sample's ends lie in the second and first triplets respectively, while the central region is feldspathic pyroxenite.
UG2-5	36.10	
		Fairly homogeneous feldspathic pyroxenite.
UG2-6,7	36.07	
		Samples 6 and 7 fit together snugly and cover the transition from the overlying feldspathic pyroxenite into the UG2 main leader, a 29 cm thick chromitite layer lying about 1.5 m above the main UG2 reef.

Table 6.11: Geological descriptions of the samples of UG2 and surrounding rocks obtained from Waterval borehole WV171 [90].



UG2-9 36.07 This sample covers the transition from a fine feldspathic pyroxenite to the main UG2 chromitite layer. A 3 cm wide intrusion of feldspathic pyroxenite removes a 2 cm section of chromitite from the main body.



UG2-10 36.10 Sample 10 starts at the very bottom edge of the UG2 chromitite layer but consists mainly of pegmatoidal feldspathic pyroxenite.



UG2-11 36.10 Homogeneous sample of medium grained melanorite, which forms the immediate footwall of the UG2.

Table 6.11 (cont.): Geological descriptions of the samples of UG2 and surrounding rocks obtained from Waterval borehole WV171 [90].

Material	Sample	Permittivity		Loss Tangent		Atten. [dB/m]		Velocity [m/ μ s]	
		$\overline{\epsilon_r}$	CV_{ϵ_r}	$\overline{\tan \delta}$	$CV_{\tan \delta}$	$\overline{\alpha}$	CV_{α}	\overline{v}	CV_v
anorthosite	1	7.43	3.20	0.05	9.09	0.33	10.42	109.98	1.61
	2	8.26	2.08	0.06	7.76	0.42	8.66	104.30	1.03
	3	8.31	2.06	0.05	5.01	0.33	5.44	104.00	1.03
feldspathic pyroxenite	4	8.21	5.38	0.05	11.65	0.33	14.20	104.70	2.65
	5	8.00	3.49	0.05	12.37	0.34	13.63	105.98	1.75
	9	7.75	2.24	0.04	10.60	0.27	11.51	107.70	1.13
chromitite	3	12.16	2.92	0.10	5.95	0.83	7.00	85.88	1.49
	6,7	11.67	2.57	0.11	5.03	0.86	5.51	87.65	1.29
	9	11.70	4.36	0.09	4.93	0.72	6.76	87.62	2.23
PFP	10	8.28	5.89	0.06	29.69	0.38	32.21	104.29	2.76
melanorite	11	8.19	1.23	0.08	4.27	0.52	4.67	104.68	0.62

Table 6.12: Material properties of the individual UG2 materials at 25 MHz.

Sample	Permittivity	Loss Tangent	Atten. [dB/m]	Velocity [m/ μ s]
anorthosite	1	0.013	0.001	0.097
	2	0.037	0.002	0.212
	3	0.020	0.001	0.114
feldspathic pyroxenite	4	0.042	0.002	0.222
	5	0.035	0.001	0.213
	9	0.017	0.001	0.108
	3	0.057	0.001	0.190
chromitite	6,7	0.102	0.003	0.348
	9	0.057	0.001	0.190
PFP	10	0.058	0.003	0.260
melanorite	11	0.018	0.001	0.110

Table 6.13: Maximum predicted individual measurement uncertainty, calculated as described in Section 2.5.1, of the UG2 material sections at 25 MHz.

Material	Sample	Permittivity		Loss Tangent		Atten. [dB/m]		Velocity [m/ μ s]	
		CV_{RG}	CV_{LG}	CV_{RG}	CV_{LG}	CV_{RG}	CV_{LG}	CV_{RG}	CV_{LG}
anorthosite	1	—	3.20	—	9.09	—	10.42	—	1.61
	2	1.36	2.11	4.44	7.50	4.83	8.44	0.68	1.04
	3	2.10	2.09	3.69	5.06	4.51	5.52	1.05	1.04
feldspathic pyroxenite	4	3.72	4.69	4.93	11.67	6.33	14.02	1.86	2.30
	5	2.22	3.45	5.02	12.55	5.74	13.82	1.12	1.73
	9	1.90	2.22	3.41	10.79	4.17	11.70	0.96	1.12
	3	2.82	3.04	4.66	6.03	5.87	7.10	1.44	1.56
chromitite	6,7	2.74	2.59	3.94	5.00	4.66	5.54	1.37	1.30
	9	4.77	3.04	5.36	3.62	7.50	4.65	2.44	1.57
PFP	10	3.52	5.87	8.71	29.88	9.76	32.40	1.69	2.74
melanorite	11	1.29	1.18	4.37	3.04	4.81	3.42	0.64	0.59

Table 6.14: Coefficients of variation of the individual UG2 materials at 25 MHz, calculated as described in Section 6.2.

Material	Permittivity		Loss Tangent		Atten. [dB/m]		Velocity [m/ μ s]	
	$\overline{\epsilon_r}$	CV_{ϵ_r}	$\overline{\tan \delta}$	$CV_{\tan \delta}$	$\overline{\alpha}$	CV_{α}	\overline{v}	CV_v
feldspathic pyroxenite	1.07	2.61	1.06	1.02	1.56	2.61	1.03	2.57
chromitite	1.04	1.70	1.21	2.47	1.19	1.27	1.02	1.73

Table 6.15: IMS parameters of the UG2 materials at 25 MHz, calculated as defined in Section 6.2: the IMS's are simply the ratio of the maximum to minimum value of each parameter in a material type.

Sample		n	χ_r	ϵ_{∞}	max. $ \Delta \epsilon_r $ [%]	max. $ \Delta \tan \delta $
anorthosite	1	0.57	0.21	6.86	4.34 ₂₅	0.032 ₂₀
	2	0.45	0.23	7.59	4.10 ₂₅	0.038 ₂₀
	3	2.36	0.27	7.81	0.92 ₂₅	0.045 ₁
feldspathic pyroxenite	4	0.36	0.07	7.67	4.44 ₂₅	0.044 ₂₀
	9	2.42	0.27	7.25	0.78 ₂₅	0.069 ₁
chromitite	3	0.65	1.15	10.48	4.92 ₂₅	0.048 ₂₀
	6,7	0.40	0.53	10.53	4.07 ₂₅	0.051 ₂₀
	3	0.65	1.15	10.48	4.92 ₂₅	0.048 ₂₀
	10	0.49	0.19	7.58	4.52 ₂₅	0.039 ₂₀
	11	0.43	0.41	7.51	3.36 ₂₅	0.028 ₂₀

Table 6.16: Jonscher parameters of the mean dielectric properties of the UG2 rock samples. The maximum difference between the permittivity and loss tangent predicted by the Jonscher model and the actual value are shown, along with the frequency at which the maximum difference occurs (subscripts).

6.4 Diamond Geologies

This section will host the study of two diamond geologies: one found at Cullinan mine in South Africa and the other at Snap Lake in Canada. The studies are similar in that they all involve the delineation of a diamond-hosting kimberlite structure in the surrounding host rock, but the host rocks differ. The primary interest is thus in the bulk propagating properties of the host rock types in general, but also of the kimberlite itself since it must be determined whether a radar contrast exists between it and the host. The Cullinan mine study involves the detection of a kimberlite pipe, while the Snap Lake kimberlite occurs in the form of a dyke.

The format of this Section will be as follows. A brief introduction to the origin and geology of kimberlite structures will be followed by the individual case studies, each of which will contain a discussion of the local geology, a description of the available samples, and a presentation and discussion of the measurement results. In the Cullinan study, estimates of the propagation velocity in the field were available from the cross-hole BHR measurements described by Herselman [83]. Finally, results from the three separate investigations will be consolidated into a single statement on the general applicability of borehole radar in the delineation of kimberlite structures.

6.4.1 Geological Background

Diamonds form in what is called the diamond stability field, a region of the earth's outer mantle where an acceptable combination of temperature and pressure allows their formation and preservation. The pressures required only occur at depths of over 120 km, but the temperature at these depths is usually too high for diamonds to form. Below certain old regions of the earth underlain by what is termed the Archaean craton, however, the temperature is relatively cool and diamonds may form [91].

Volcanic eruptions of kimberlite through Archaean cratons sometimes sample this diamond field, transporting diamonds to the surface. Upon cooling, the remaining kimberlite pipes or dykes, should they contain diamonds, become what are termed 'primary' diamond deposits. These kimberlite occurrences contain a clear majority of the world's diamond deposits, and are the structures of interest in the case studies described below. Water erosion of kimberlite pipes may result in alluvial and marine 'secondary' diamond deposits.

The physical structure of kimberlite pipes may be divided, from top to bottom, into three vertical zones: the crater, diatreme, and root zones. The presence and condition of the zones depends on the nature of the eruption and the host rock (see e.g. [92]), and the level of erosion. The crater and diatreme zones generally have fairly regular boundaries (the Premier mine exploits the diatreme zone of its pipe), while a distinguishing feature of the root zone is its irregular shape and complex internal geology in which several types of kimberlite may be present [93]. The mining difficulties experienced in the exploitation of the root zones [91] makes the potential use of borehole radar in their delineation very attractive.

6.4.2 Cullinan Mine

Introduction and Geological Background

The kimberlite pipe found at Cullinan originally measured 32 hectares at its surface; its conical sides have a 64 degree from vertical slope, different from the 82 degrees classic for South African volcanos [94]. The diatreme grades into the root zone below about 550 m depth, and it is these lower regions of the pipe that have become interesting for subterranean exploitation.

A number of exploratory NQ sized boreholes were drilled in various positions around the pipe; four are shown in Figure 6.8. From their collars, generally situated about 60 to 70 metres from the pipe edge, they extend between about 220 and 480 metres into the country rock below 763 m level. Samples were

obtained from borehole PM551, which has an initial dip of about -67.6 degrees, and extended for 420 metres into the country rock next to the pipe before it caved in to its current depth of about 300 metres.

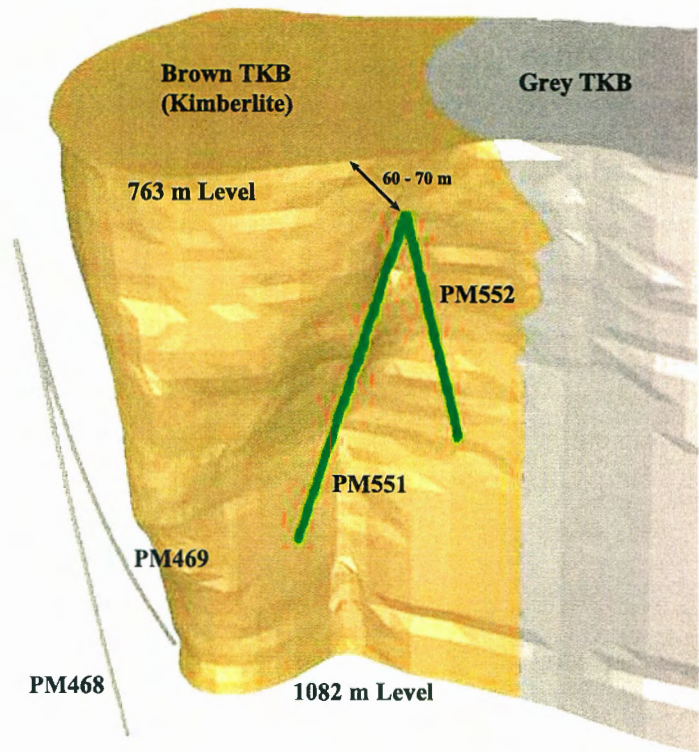


Figure 6.8: The Cullinan kimberlite pipe (brown TKB) with surrounding exploratory boreholes. The collars of boreholes PM551 and PM552 are co-located within about 2 metres, and are about 60-70 metres from the pipe.

Determining the feasibility of the use of BHR in this delineation would involve two components: firstly, to determine how far a radar wave in the frequency band of the available BHR would propagate through the host media, and secondly, to predict whether the dielectric contrast between the kimberlite pipe and the host media would be sufficient to allow the detection of its boundaries. As shown in the rough core log of borehole PM551 in Figure 6.9, the host has a complex layered stratigraphy, consisting essentially of three rock types: norite, quartzites, and ‘metasediments’. The term ‘metasediment’ is actually a broad term used to classify a whole host of metamorphosed sedimentary rocks, as evidenced by the dramatically different appearance of the various samples seen in Table 6.19. Any attempt to answer the questions posed must involve a quite thorough selection of samples, covering the majority of rock types encountered.

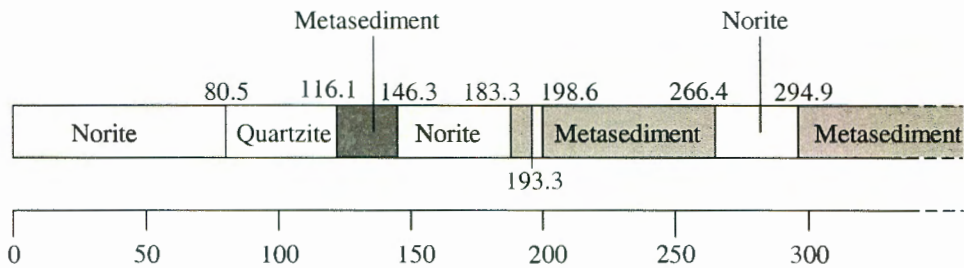


Figure 6.9: The core log of borehole PM551 (based on [95]).

Sample Descriptions

Thirteen samples, representative of the various host layers and rock types found, were taken from borehole PM551 and were suitable for study using the cylindrical capacitor. They are shown photographically and described briefly in Tables 6.17–6.19.

In each case, a sample will be described by the combination of its initial letter (Q for quartzite, N for norite and MS for metasediment) with its rounded down integer depth, so, for example, the quartzite sample from 92.5 metres will be designated by ‘Q92’. All the samples’ diameters were between 50.0 and 50.7 mm, with the harder quartzites generally having a larger diameter and the softer norites being thinner. (Note that the sample thickness is not related to depth and is thus not thought to be attributable to drill bit wear.)

The norite and quartzite bands are fairly homogeneous in appearance but the metasediment samples shown in Table 6.19 differ substantially. The upper metasediment band (116.1–146.3 m) is described as ‘a fine-grained, pale grey to black, hard, laminated metasediment, interbedded with small zones of hard white quartzite’ [95]. Samples Q120 and Q143 are examples of this interbedded quartzite. The lower metasediment bands (183.3–193.3 m and 198.6–266.4 m) are described as ‘variable’ and ‘highly variable’ respectively, and also contain thinly laminated zones of ‘calceous’ quartzite.

Electrode Design

A set of electrodes was designed for a nominal sample diameter of 50.35 mm, and to be able to accommodate samples within 0.5 mm of that. Considering the substrate thickness of 0.05 mm, the implication was that the side gaps be 1.98 mm ($\Delta = 4.5^\circ$) nominally, with an allowed range of between 0.39 and 3.53 mm, translating to about 0.9 and 7.9 degrees for the respective minimum and maximum sample diameters. Note that the 7.9° maximum falls just within the 8° rule discussed earlier in Section 4.2.4, which limits the inaccuracy of the defining equation for C_0^∞ to within about 1 % for $\phi_0 = 120^\circ$. Further, according to the design criterion for the guard length, also described in Section 4.2.4 as $L > 3a + l$, the guard length L need be at least 96.43 mm for the maximum 50.85 mm core diameter and a $l = 20$ mm sensing electrode length. The chosen guard length of $L = 122$ mm (chosen according to $L > 4a + l$) easily satisfies this rule, resulting in an uncertainty in C_0 of about 0.22 % due to the guard length. Sensing electrode dimensions of $l = 20$ mm and $\phi_0 = 100^\circ$ (nominal) were chosen. A 20 mm sensing electrode length was deemed sufficient for the cores under investigation; the 100 degree arc coverage was chosen to reduce side gap influences.

The substrate used was again the GTS7600 Ultraflex copper polyimide laminate [96] with a 50 micron polyimide film and 70 micron copper foil coating. The various dimensions for the etching of the electrodes onto the laminate can be calculated using the MATLAB script *geometry.m*, listed in Appendix D.5.

To accommodate the electrode set, the outer shield box was designed to have a width of 100 mm and a height of 80 mm. The larger size of this device results in lower mechanical rigidity and thus suggests that the measurement repeatability may be slightly lower than that of the smaller device used in the Bleskop Marker study.

The measurement repeatability was again determined by the repeated insertion, measurement and extraction of a number of representative samples. An artificial dielectric was constructed from PVDF and brass, following the theory discussed in Appendix C, to have an effective permittivity increase of a factor of about 2.32 over PVDF. The three reference materials — polystyrene, PVDF and the artificial dielectric — and two rock samples were measured in random order, with the order being changed for each measurement iteration. Samples Q92 and MS221 were chosen as representative of the rock cores: they cover a fair range of sample diameter (50.3 to 50.6 mm), and MS221’s surface was quite rough due to drilling damage.

The repeatability of raw measured impedance data is shown in Table 6.20 as the percentage variation in impedance and absolute standard deviation in phase. Ten measurements were taken: the first five before the whole series of rock sample measurements, and the second five after. One would have expected some degradation of the device to have occurred during the measurement process, but this was not strictly the case. The first five measurements were not consistently more repeatable than the second five. In the case of the second five measurements of the artificial dielectric, for example, the repeatability improved. The total repeatability was worse than that of the individual sets, but not dramatically. The exact source of this change is impossible to specify with certainty, but a change in the geometry of the device as a whole (that is, including the feed system) was likely the reason.

Measurement Results

All the samples from PM551 were measured at 1 cm intervals along their intact lengths. The measured properties of all the samples are shown at 25 MHz in Table 6.21. The coefficients of variation and intra-material spreads of the PM551 samples at 25 MHz are shown in Tables 6.23 and 6.24 respectively. The predicted individual measurement uncertainties shown in Table 6.22 are small in comparison to the group uncertainties. As mentioned in Section 6.2, the use of the terms ‘small’ and ‘large’ when applied to the CV and IMS is not absolute; figures should be seen in relation to others, and perceived anomalies related to their causes.

As an example, consider the samples MS201 and Q360. These two samples both exhibit high permittivity CV’s, but the cause in each case is different. A comparison of the permittivity and loss tangent along each core’s length is shown in Figure 6.10. The high CV of the heavily layered MS201 is due to the continual variation in its properties along the entire core, while in Q360’s case the presence in the sample of two distinct regions is responsible. The higher permittivity and loss tangent in the rightmost region of Q360 coincides with the darker sample colouration visible in Table 6.17.

The dotted lines in Figure 6.10(a) are plots of the individual orientation measurements of MS201, and highlight the measurements’ dependance on sample orientation. Owing to the angle of the dark inclusions, they are visible sooner or later depending on the orientation in which they first make contact with the sensing electrode. This effect is seen most strikingly in the 1 MHz loss tangent between 12 and 14 cm, and on the very left of the 1 MHz permittivity curve. (Confer with the angled inclusion discussion in Section 5.3.)

The relevance of particular samples’ properties should always be borne in mind. For example, the properties of Q143 differ quite substantially from the other quartzite samples and will increase the IMS of quartzite as a group somewhat. But it does not come from a known quartzite band and will thus probably not be relevant to propagation characteristics in those bands.

The frequency behaviour of the various properties at 25 MHz may be described by the Jonscher parameters in Table 6.25. The model matches the measured permittivity values quite well (to within 5 % in all cases but one) but consistently struggles with loss tangent. The model fits homogeneous samples’ measured data better (cf. the norites) but extrapolation using the model, one of the aims of using it, is not really feasible if the largest differences are at the highest frequency. Often the form of the measured data does not match the form of the model’s defining equation (see (2.36)): the measured data will increase again at high frequency after dropping at first, while the Jonscher model decreases asymptotically to ϵ_∞ . Whether this is caused by measurement problems or inappropriateness of the model to the rock types measured — the model does fit the frequency response forms of other rocks measured in this study better — remained unresolved at the time of going to press .

All the rocks measured display the same trend of dielectric constant and both properties’ spreading parameters (CV and IMS) decreasing with frequency. The latter observation may imply that the microscopic measurement results translate more readily to bulk properties as the frequency increases.

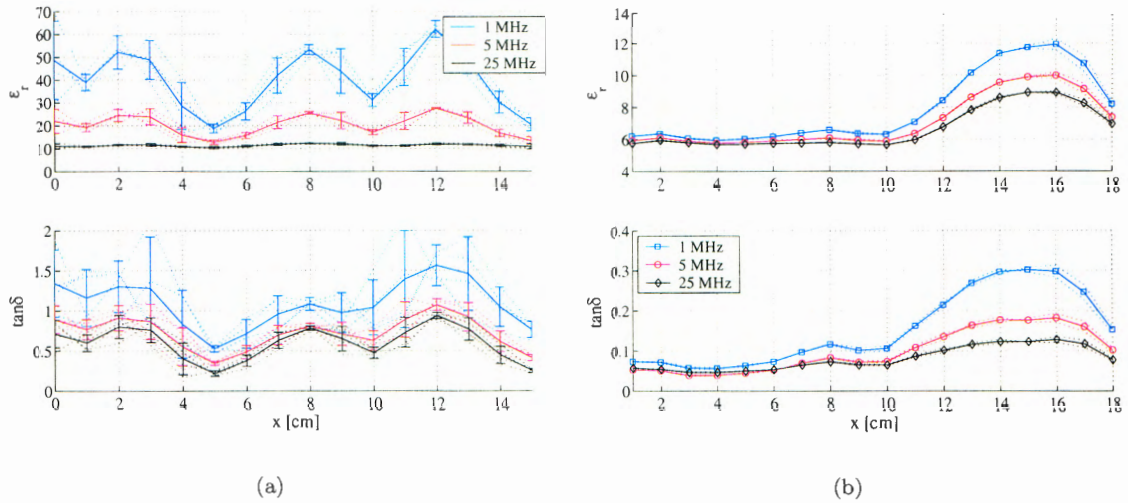


Figure 6.10: The permittivity and loss tangent of samples (a) MS201 and (b) Q360. The dotted lines indicate the individual measurements at each orientation, while the solid line is the mean at each frequency. The error bars represent the RGU at each linear point.

Norite occurs in a number of bands, two of which are represented here. The norites display the lowest group uncertainties throughout in each individual sample. They also are the most similar as a group, having the lowest IMS. Samples N60 and N70 are from the upper band, and would indicate that this band is consistently a moderately good material for radar propagation. These samples' properties have the smallest spreads by a substantial margin, and also in general have the lowest attenuation factors (between 0.8 and 1.1 dB/m). Predicted propagation velocities of between 98.5 and 100.0 m/ μ s at this depth compare very well to a cross-hole field estimation of about 102 m/s (within about 3.6 % and 2 % respectively). Sample N269 displays similar properties.

The quartzite occurring in the band between 80 and 120 metres seems to be a good propagator based on the two samples Q89 and Q92. Both are quite homogeneous at 25 MHz, and have relatively small permittivity GU's. Their propagation velocities are fairly similar (105.3 and 114.2 m/s), and both have relatively small attenuation factors (1.16 and 0.48 dB/m). Comparison of these results with cross-hole propagation measurements confirmed that these two samples were a good indicator of propagation velocity, which was estimated to be about 116 m/s between depths of 88 and 108 metres. This compares very well to the laboratory predictions (to within 10.2 % and 1.6 % respectively), and particularly to sample Q92. A look at sample Q89's 1 MHz figures reveals that its properties actually vary quite substantially. This may be the cause of the poorer agreement to crosshole measurements. Sample Q92, though shorter, was more homogeneous and thus, in retrospect, perhaps a better indicator of bulk properties.

Sample Q120 comes from the very bottom edge of the quartzite band, and differs markedly in appearance and substance from Q89 and Q92. It is a far lighter rock, and, as described in Table 6.17, contains a number of irregular inclusions, the dielectric effect of which are most pronounced at 1 MHz. Though approaching the edge of the radar range, the trend of the crosshole measurements is that the velocity is decreasing from the 106 m/s estimated at 118 metres depth to about 91 m/s at 120 metres — the laboratory prediction of 87.7 m/s again compares well (to within 3.8 %).

Sample Q143 differs the most from the other quartzite samples, and has noticeably worse propagation characteristics ($\alpha \approx 6.2$ dB/m; $v \approx 75$ m/s). No quartzite layer is mentioned at this depth in the core

log, and the sample is in fact marked as an ‘interbedding’. Sample Q360 has properties similar to those of Q92, but is not relevant to radar experiments since borehole PM551 has caved in beyond a depth of 300 metres.

As mentioned previously, metasediment refers less to one type of rock than to an entire class of metamorphosed sedimentary rock. The MS samples, with the notable exception of MS201, are all fairly homogeneous at 25 MHz. The loss tangent of MS234 also varies gradually between about 0.05 in the sample centre and 0.2 at either end, despite the homogeneous optical appearance of the sample — hence the high loss tangent and attenuation LGUs. However, the properties of the available samples differ quite a lot from each other. This makes accurate prediction of bulk properties difficult. The estimated bulk propagation velocity of about 94 m/s at a depth of 123 m matches the laboratory prediction of MS123’s 95.5 m/s quite well (within about 1.6 %). But the predicted velocity of MS134, which is in the same layer according to the core log, is about 108.5 m/s, which does not agree with the bulk estimation of about 95 m/s very well.

Sample MS201 is unusual optically as well as in its dielectric properties. As evident in the photograph in Table 6.19, it is densely layered. The dielectric properties behave accordingly, as shown in Figure 6.10(a). The calculated mean value is clearly less relevant here than, for example, that of the norite samples. The deeper samples MS221 and MS234 are again quite similar to MS123 and MS134 and promise good propagation conditions. No comparison to bulk cross-hole measurements was possible since the boreholes had diverged excessively at this depth.

Discussion

Variable radar propagation conditions exist in the host surrounding the kimberlite pipe at Cullinan diamond mine. There are obvious differences between samples of the same designation: the quartzites and metasedimental samples generally exhibit relatively large IMS’s, particularly in their loss tangents and attenuation factors. A major hinderance in making reasonable bulk propagation predictions for the entire region surrounding the pipe is the lack of knowledge of the frequency of occurrence of the different rock types.

It would appear from the favourable agreement between the bulk propagation velocities, estimated from a cross-hole shoot, and the laboratory measurement of samples at 25 MHz, that a more homogeneous sample is usually a better predictor of bulk properties. The propagation velocities obtained from the measured properties of samples N60, N70, Q92 and MS123, all fairly homogeneous, corresponded to field estimations to within about 4 %. These four samples also had the lowest CVs in their respective material groupings.

On the whole, the prospects for BHR detection of the kimberlite pipe from the country rock over large reaches of its depth are positive. Propagation conditions in the host rock are good, and while no samples of the Cullinan kimberlite pipe itself were available, a good contrast between it and the host is expected based on the properties of kimberlite samples from Snap Lake (see Section 6.4.3). Certain ‘blind-spots’ with poor radar propagation can be expected, as the high attenuation factors of samples Q120, Q143 and MS201 show.

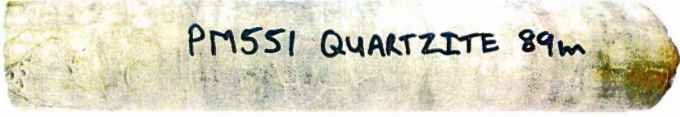
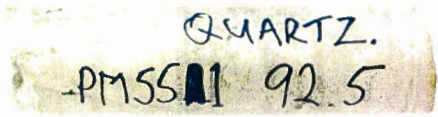
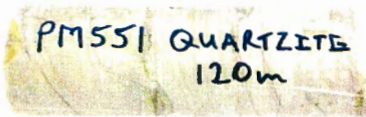

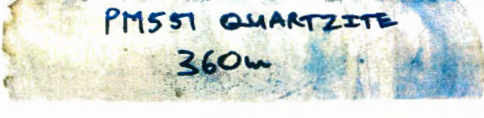
Sample	Diameter [mm]	Sample Description
89	50.5	 <p>Fine-grained hard white quartzite host containing a number of slightly darker irregular inclusions.</p>
92.5	50.6	 <p>Fairly homogeneous fine-grained hard white quartzite sample containing a number of cracks but no inclusions.</p>
120	50.2	 <p>Hard white quartzite sample containing a number of irregular localised inclusions which do not transect the entire core.</p>
143	50.3	 <p>Fairly homogeneous sample with some dark faults running through it. Some surface damage is evident.</p>
360	50.7	 <p>Fairly homogeneous sample in two parts: the rock becomes noticeably darker about 50 mm from the right sample end.</p>

Table 6.17: Geometric descriptions of the quartzite samples from borehole PM551, listed by depth. The diameter of an individual sample is always constant to within about 0.05 mm; the actual size of the samples is just over three times larger than shown.

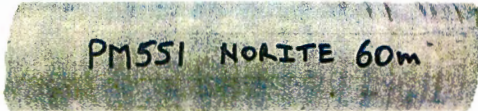

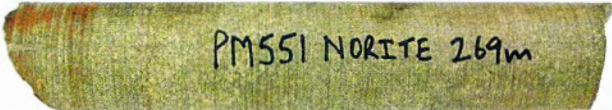
Sample	Diameter [mm]	Sample Description
60	50.0	 Homogeneous medium-grained hard grey norite sample, lighter in colour than sample N70.
70	50.2	 Homogeneous medium-grained grey norite.
269	50.0	 Fairly homogeneous medium-grained grey norite sample with some slight discolouration.

Table 6.18: Geometric descriptions of the norite samples from borehole PM551, listed by depth. The diameter of an individual sample is always constant to within about 0.05 mm; the actual size of the samples is just over three times larger than shown.






Sample	Diameter [mm]	Sample Description
123	50.3	 Very dark sample, becoming gradually lighter toward one end.
134	50.3	 Predominantly dark rock containing many irregularly spaced yet parallel lighter grayish inclusions which intersect the entire core.
201	50.05	 Heavily striated sample containing alternating, sometimes irregular but mostly parallel, dark and light layers. The interfaces generally form an angle of about 70° with the perpendicular bisector of the sample.
221	50.3	 Darkish, fairly homogeneous though subtly layered sample. Its surface has been damaged during drilling.
234	50.3	 Fairly uniform grayish sample.

Table 6.19: Geometric descriptions of the metasediment samples from borehole PM551, listed by depth. The diameter of an individual sample is always constant to within about 0.05 mm; the actual size of the samples is just over three times larger than shown.

Sample	first 5		second 5		total	
	CV_Z [%]	σ_θ [°]	CV_Z [%]	σ_θ [°]	CV_Z [%]	σ_θ [°]
Polystyrene	0.07 ₂₅	0.08 ₂₅	0.15 ₂₀	0.13 ₂₅	0.32 ₅	0.11 ₂₅
PVDF	0.22 ₅	0.08 ₂₅	0.26 ₁₅	0.07 ₂₅	0.26 ₁₅	0.08 ₂₅
Art. Diel.	0.47 ₅	0.11 ₂₅	0.20 ₁₀	0.05 ₁	0.50 ₅	0.15 ₂₅
MS221	0.30 ₁	0.08 ₂₅	0.39 ₁	0.11 ₂₀	0.33 ₁	0.12 ₂₅
Q92	0.10 ₁	0.08 ₁	0.18 ₁	0.06 ₁₅	0.28 ₁	0.13 ₁

Table 6.20: The measurement repeatability of the probe used for the Cullinan samples was determined by 5 pre- and 5 post-characterisation measurements. The separate as well as total repeatabilities are shown in polar form as the CV of the impedance magnitude and the standard deviation of the phase. (The subscript in each case denotes the frequency (in MHz) at which the repeatability was worst.)

Sample		Permittivity		Loss Tangent		Atten. [dB/m]		Velocity [m/ μ s]	
		$\bar{\epsilon}_r$	CV_{ϵ_r}	$\overline{\tan \delta}$	$CV_{\tan \delta}$	$\bar{\alpha}$	CV_α	\bar{v}	CV_v
quartzite	89	8.05	4.74	0.18	33.61	1.16	35.13	105.30	2.65
	92.5	6.89	4.02	0.08	21.92	0.48	23.10	114.18	2.07
	120	11.28	2.96	0.38	34.30	2.85	32.66	87.68	2.16
	143	14.21	10.77	0.77	20.04	6.21	22.07	75.08	6.48
	360	6.91	17.96	0.09	33.15	0.54	42.37	115.19	8.21
norite	60	9.22	1.28	0.15	6.21	1.06	6.09	98.45	0.64
	70	8.96	1.55	0.12	3.81	0.81	3.90	99.96	0.78
	269	9.29	3.15	0.23	12.82	1.57	13.73	97.75	1.72
metasediment	123	9.68	2.42	0.27	6.92	1.90	7.61	95.51	1.28
	134	7.64	2.82	0.06	11.41	0.40	11.97	108.48	1.39
	201	11.42	6.10	0.60	38.98	4.37	38.33	85.20	5.13
	221	9.82	5.24	0.20	26.04	1.40	28.52	95.26	2.69
	234	7.64	3.45	0.10	50.32	0.63	51.78	108.32	1.84

Table 6.21: Material properties of the individual Cullinan samples at 25 MHz. Total CVs are given as a percentage.

Sample		Permittivity	Loss Tangent	Atten. [dB/m]	Velocity [m/ μ s]
quartzite	89	0.019	0.002	0.013	0.102
	92.5	0.013	0.002	0.010	0.113
	120	0.050	0.010	0.063	0.211
	143	0.127	0.026	0.181	0.333
	360	0.020	0.002	0.014	0.117
norite	60	0.021	0.002	0.014	0.109
	70	0.022	0.002	0.014	0.111
	269	0.027	0.002	0.015	0.121
metasediment	123	0.026	0.002	0.016	0.118
	134	0.017	0.001	0.008	0.106
	201	0.055	0.012	0.076	0.234
	221	0.042	0.003	0.023	0.148
	234	0.015	0.002	0.011	0.099

Table 6.22: Maximum predicted individual measurement uncertainty, calculated as described in Section 2.5.1, of the Cullinan samples.

Sample		Permittivity		Loss Tangent		Atten. [dB/m]		Velocity [m/ μ s]	
		CV_{RG}	CV_{LG}	CV_{RG}	CV_{LG}	CV_{RG}	CV_{LG}	CV_{RG}	CV_{LG}
quartzite	89	2.27	4.78	13.60	33.95	14.16	35.50	1.16	2.68
	92.5	2.72	4.06	19.07	20.05	19.53	21.85	1.42	2.10
	120	3.08	2.60	21.36	34.65	20.44	32.97	2.01	2.04
	143	9.20	10.20	20.04	18.56	17.72	19.67	5.40	5.95
	360	1.34	18.22	16.96	100.03	17.72	106.30	0.54	8.33
norite	60	1.28	1.22	2.53	6.26	2.62	6.26	0.61	0.59
	70	1.68	1.52	3.71	3.34	3.90	3.52	0.84	0.77
	269	2.35	3.12	4.24	13.03	4.58	13.96	1.20	1.71
metasediment	123	1.90	2.42	6.34	5.76	6.74	6.65	1.00	1.29
	134	2.07	2.87	7.53	11.21	7.53	11.85	1.02	1.41
	201	4.77	6.05	20.44	39.80	19.89	39.18	3.22	5.23
	221	3.56	5.23	7.96	26.67	9.45	29.16	1.70	2.70
	234	1.02	3.50	16.92	50.63	17.29	52.12	1.84	1.87

Table 6.23: Coefficients of variation of the individual Cullinan samples at 25 MHz, calculated as described in Section 6.2.

Material	Permittivity		Loss Tangent		Atten. [dB/m]		Velocity [m/ μ s]	
	$\overline{\epsilon_r}$	CV_{ϵ_r}	$\overline{\tan \delta}$	$CV_{\tan \delta}$	$\overline{\alpha}$	CV_{α}	\overline{v}	CV_v
quartzite	2.06	6.07	9.63	1.71	12.94	1.92	1.53	3.97
norite	1.04	2.46	1.92	3.36	1.94	3.52	1.02	2.69
metasediment	1.50	2.52	10.00	7.27	10.93	6.80	1.27	4.01

Table 6.24: IMS parameters of the Cullinan materials at 25 MHz, calculated as defined in Section 6.2: the IMS's are simply the ratio of maximum to minimum value of each parameter in a material type.

Sample		n	χ_r	ϵ_{∞}	max. $ \Delta\epsilon_r $ [%]	max. $ \Delta \tan \delta $
quartzite	89	0.71	2.94	5.10	2.47 ₂₅	0.014 ₂₀
	92.5	0.67	1.18	5.58	3.20 ₂₅	0.023 ₁₅
	120	0.32	2.11	9.99	2.20 ₃	0.100 ₂₅
	143	0.29	5.13	12.92	6.71 ₃	0.260 ₂₅
	360	0.67	0.81	5.94	3.36 ₂₅	0.025 ₂₅
norite	60	0.71	3.42	5.94	3.36 ₂₅	0.025 ₂₅
	70	0.71	2.63	5.76	2.87 ₂₅	0.019 ₂₅
	269	0.67	3.77	6.20	3.47 ₂₅	0.022 ₂₅
metasediment	123	0.64	3.89	5.98	1.22 ₂₅	0.031 ₂₅
	134	0.75	0.98	6.42	4.03 ₂₅	0.036 ₂₅
	201	0.39	4.92	8.54	2.88 ₁	0.125 ₂₅
	221	0.74	4.56	5.28	2.50 ₂₅	0.011 ₂₀
	234	0.68	1.83	5.72	2.94 ₂₅	0.025 ₂₅

Table 6.25: Jonscher parameters of the mean dielectric properties of the Cullinan mine rock samples. The maximum difference between the permittivity and loss tangent predicted by the Jonscher model and the actual value are shown, along with the frequency at which the maximum difference occurs (subscripts).

6.4.3 Snap Lake Mine

Introduction and Geological Background

The Snap Lake kimberlite dyke is situated in the Archaean Slave Province craton in the Northwest Territories in Canada. It has an average thickness of about 2.8 metres and can be seen roughly as a mostly continuous sheet, spread out over at least 25 square km, gently dipping at approximately 15 degrees to depths of 1500 metres or more [97], with some offsets but no complete breaks. On a local scale, the dyke exhibits some undulation, and even some step-like behaviour in the more brittle sections of the host [98].

The aim of these measurements is again to determine the feasibility of delineating the dyke boundaries by borehole radar shoots from the host rock, which is predominantly an intrusive granitoid. Parts of the dyke are also emplaced within metavolcanic and metasedimentary rock [98]. No detailed knowledge regarding the boreholes was available at the time of publication.

Sample Descriptions

Nine samples were obtained from Snap Lake mine, three each of the kimberlite dyke, shown in Table 6.26, the granitic host (Table 6.28) and the metavolcanic host (Table 6.27). Their condition varied — some samples were fractured — but they were all suitable for nondestructive evaluation to a degree sufficient to obtain meaningful data, that is, to allow a statement regarding the existence of a contrast between the host and dyke. The sample designations are used as provided by the Snap Lake geologists: SL-80301–3 are kimberlite samples, SL-80304–6 and SL-80307–9 are metavolcanic and granitic host rock respectively [99].

Electrode Design

The samples' diameters fell within two distinct ranges, necessitating the design and construction of two capacitor sets. The granite samples' diameters were very close together, ranging between 41.67 and 41.73 mm, while the remaining samples had diameters of between 38.25 and 38.5 mm.

The larger electrode was designed to accommodate a nominal sample diameter of 41.7 mm (with a nominal side gap of $\Delta = 4^\circ$), and to be able to handle samples between 41.4 and 42.23 mm in diameter. This range was again determined by the physical minimum and 8° side-gap maximum. The guard length L was set to 105 mm, more than satisfying the $4a + l$ requirement used previously, and causing a 0.016 % uncertainty in the calculation of C_0 . The smaller electrode was to accommodate samples between 38.1 and 38.9 mm diameter (38.4 mm nominally with $\Delta = 4.5^\circ$), and had a total guard length of $L = 100$ mm, resulting in a 0.013 % uncertainty in C_0 . Both sensing electrodes had dimensions of $l = 20$ mm and $\phi_c = 100^\circ$ (nominal). The shield boxes for the large and small capacitors had dimensions of 100×80 mm and 80×60 mm respectively.

The measurement repeatability of the two probes used was determined as described in Section 5.2.2 and Appendix A. The five pre- and five post-characterisation measurements are tabulated along with the total uncertainty in Tables 6.29 (38.4 mm probe) and 6.30 (41.7 mm probe). The phase uncertainty is similar in all cases, staying below a standard deviation of about 0.3° . The impedance variation of the 38.4 mm probe is slightly worse than that of the 41.7 mm probe, particularly in the case of the PVDF. This particular material's repeatability is unusual because the individual pre- and post-characterisation measurement sets are tightly grouped but the total CV is only about 1.4 %, signifying a shift in behaviour of the probe during the measurement process. The relatively high repeatability CV's seen in the measurement of SL-80302 are largely due to errors incurred by inaccurate positioning of this high permittivity sample.




Sample	Diameter [mm]	Sample Description
80301	38.25	 “Main” hypabyssal kimberlite with coarse macrocrysts and calcite veining at 5–8 cm spacing. The sample is slightly fractured but fits together well.
80302	38.40	 Intact hypabyssal kimberlite sample with coarse macrocrysts; minor calcite veining.
80303	38.28	 Kimberlite from near-contact margin containing thin closely spaced calcite veinlets. This sample is again fractured but the pieces fit together tightly.

Table 6.26: A summary of the geometric descriptions of the kimberlite samples from the Snap Lake dyke [99].

Measurement Results

The measured data of all three rock types at 25 MHz are summarised in Table 6.31; the rotational and linear variations in the rock types appear as their coefficients of variation in Table 6.33. The individual predicted measurement uncertainties, shown in Table 6.32, are in all cases substantially smaller than the property means or any of the group uncertainties, thus not invalidating the group analyses. The sample condition, on the other hand, does play a role in limiting the appropriateness of the group parameters in a number of cases: a number of samples only allowed the measurement of a few points while others were broken, as described in Tables 6.26 and 6.27.

The intra-material spreads in Table 6.34 are quite low for the permittivity of all the materials, but higher for the loss tangent of granite and the metavolcanic host. The relatively low absolute values of granite’s $\tan \delta$ ’s are the cause in its case while the metavolcanic host group analysis parameters in particular should be seen in the context of the limited nature of those samples. The Jonscher models shown in Table 6.35 represent kimberlite ($\Delta \epsilon_r < 1.2 \%$, $\Delta \tan \delta < 15 \%$) and the metavolcanic host ($\Delta \epsilon_r < 3.5 \%$, $\Delta \tan \delta < 18 \%$) very well, but struggle again with the loss tangent of granite. Extrapolation is again risky as the largest differences between the model and measured values occur at high frequency.

The three available samples of kimberlite were all in fairly good condition. Although SL-80301 and SL-80303 were broken in places, the parts fitted together well enough to allow 15 and 18 axial measurement positions respectively. Sample SL-80302, though not broken, was shorter and thus only 9 measurements were possible in each orientation. Though the appearance and geological composition of all three samples




Sample	Diameter [mm]	Sample Description
80304	38.30	 Massive non-foliated metavolcanic host rock. This sample has a change in size about halfway along it, presumably due to a drilling problem, that greatly reduces its measurable section.
80305	38.50	 Metavolcanic host with some felsic banding indicating foliation direction. The sample is broken at four places along the band edges, but again the pieces fit together cleanly. The measurable area is decreased due to the core being incomplete at one end.
80306	38.30	 Metavolcanic host rock with narrow thin crinkled felsic bands indicating foliation direction. This sample's measurable area is very small due to a drilling error — as seen in the Figure a large part of the core has been removed in a cylindrical fashion.

Table 6.27: A summary of the geometric descriptions of the metavolcanic host rock samples from the Snap Lake dyke [99].

differ, their dielectric properties are fairly similar. SL-80303's permittivity is slightly higher than that of the other two, but the loss tangent of all the samples is relatively high (in the range of about 0.3–0.4). The variation in all the kimberlite samples' dielectric constants is quite low (consistently smaller than about 8 %), indicating that kimberlite is in general relatively homogeneous on a centimetre scale. The attenuation constant of all the samples is above about 2 dB/m, while the signal propagation velocity is consistently below about 100 m/ μ s. The RGUs and LGUs of kimberlite's properties are quite similar, implying that the inhomogeneity found is on a fairly small scale.

The samples of metavolcanic host were all in poor condition for measurement by this (or any) technique. SL-80304 appears to have originated from an area of the borehole at which the drilling tips were exchanged — its diameter varies slightly along the upper half of the core before experiencing a large change — only four axial measurement positions were possible. SL-80305 was broken into four pieces but allowed 11 measurements. This sample comes from the intersection of two boreholes and is missing a large piece; only four measurements along the core were possible. Although the CVs were all small, the variation parameters of SL-80304 and SL-80306 are based on only four samples and are thus of limited value. The loss tangent TGUs are all relatively high (larger than about 15 %), but this is partly due to the relation of the uncertainties to small mean values ($\tan \delta$'s all below 0.1). That said, the mean data is nevertheless valuable: the permittivity and loss tangent of the metavolcanic host samples are consistently




Sample	Diameter [mm]	Sample Description
80307	41.73	 Grey medium grained granitic host rock.
80308	41.70	 Medium grained Fe-rich reddish grey granitic host rock. (The sample was not noticeably magnetic.)
80309	41.67	 Fine grained grey granitic host rock.

Table 6.28: A summary of the geometric descriptions of the granitic host rock samples from the Snap Lake dyke [99].

below about 9.2 and 0.01 respectively. The attenuation is also quite low (below about 0.63 dB/m) while the propagation velocity is above about 100 m/ μ s throughout. The metavolcanic RGUs are mostly larger than their LGUs, presumably because of the few axial points measured.

The samples of granitic host rock are all in near perfect condition for non-destructive measurement: they are unbroken with smooth surfaces, their diameters are constant, and they are long enough to allow sufficient axial measurement positions. Despite having different appearances, the dielectric constant of the three samples is quite similar. Their permittivities are all between 5.8 and 6.6 and their loss tangents are all below 0.1 (sample SL-80309 has a particularly low mean loss tangent of 0.01). Similarly to the metavolcanic samples, the relatively high loss tangent TGU's may be attributed to the small absolute values of $\tan \delta$. The samples are all relatively homogeneous with regard to their permittivity. Granite seems to have quite a high propagation velocity (consistently above 117 m/ μ s) and low signal attenuation of smaller than about 0.55 dB/m. Similar to kimberlite, the RGUs here are also not substantially different from the LGUs.

Sample	first 5		second 5		total	
	$CV_Z[\%]$	$\sigma_\theta[^\circ]$	$CV_Z[\%]$	$\sigma_\theta[^\circ]$	$CV_Z[\%]$	$\sigma_\theta[^\circ]$
Teflon	0.05 ₂₅	0.03 ₂₅	0.34 ₂₅	0.01 ₂₅	0.15 ₂₅	0.06 ₂₅
PVDF	0.34 ₅	0.09 ₂₅	0.18 ₂₅	0.05 ₂₅	1.40 ₅	0.30 ₁
Art. Diel.	0.13 ₂₅	0.04 ₂₅	0.42 ₂₅	0.08 ₁	0.68 ₁₀	0.17 ₁
SL-80302	0.56 ₁	0.11 ₁	0.68 ₂₅	0.06 ₁	0.92 ₁	0.16 ₂₅

Table 6.29: The measurement repeatability of the 38.4 mm probe used for the Snap Lake sample was determined by 5 pre- and 5 post-characterisation measurements. The separate as well as total repeatabilities are shown in polar form as the CV of the impedance magnitude and the standard deviation of the phase. (The subscript in each case denotes the frequency (in MHz) at which the repeatability was worst.)

Sample	first 5		second 5		total	
	$CV_Z[\%]$	$\sigma_\theta[^\circ]$	$CV_Z[\%]$	$\sigma_\theta[^\circ]$	$CV_Z[\%]$	$\sigma_\theta[^\circ]$
Teflon	0.05 ₃	0.02 ₂₅	0.06 ₂₅	0.04 ₂₀	0.07 ₂₅	0.07 ₂₅
PVDF	0.09 ₂₀	0.03 ₂₅	0.13 ₂₅	0.09 ₁₅	0.18 ₅	0.11 ₂₅
Art. Diel.	0.19 ₂₀	0.09 ₂₅	0.10 ₅	0.05 ₁₀	0.25 ₅	0.09 ₂₅
SL-80307	0.11 ₁	0.08 ₁	0.27 ₂₅	0.07 ₂₅	0.19 ₂₅	0.17 ₁

Table 6.30: The measurement repeatability of the 41.7 mm probe used for the Snap Lake sample was determined by 5 pre- and 5 post-characterisation measurements. The separate as well as total repeatabilities are shown in polar form as the CV of the impedance magnitude and the standard deviation of the phase. (The subscript in each case denotes the frequency (in MHz) at which the repeatability was worst.)

Sample		Permittivity		Loss Tangent		Atten. [dB/m]		Velocity [m/ μ s]	
		$\bar{\epsilon}_r$	CV_{ϵ_r}	$\overline{\tan \delta}$	$CV_{\tan \delta}$	$\bar{\alpha}$	CV_α	\bar{v}	CV_v
kimberlite	80301	10.18	7.07	0.34	7.63	2.42	9.99	92.89	4.25
	80302	9.01	3.30	0.29	4.05	1.98	4.33	98.86	1.65
	80303	13.06	6.07	0.40	7.75	3.22	10.25	81.52	3.25
metavolcanic	80304	6.77	4.47	0.08	14.78	0.45	15.98	115.24	2.27
	80305	9.16	8.46	0.09	15.49	0.63	16.70	99.24	4.39
	80306	8.18	3.94	0.09	18.35	0.62	17.28	104.74	1.99
granite	80307	6.27	3.03	0.04	13.97	0.24	14.71	119.74	1.50
	80308	6.55	2.41	0.09	10.54	0.55	11.11	117.01	1.22
	80309	5.82	1.38	0.01	25.93	0.06	26.20	124.25	0.69

Table 6.31: Material properties of the individual Snap Lake materials at 25 MHz. Total CV's are given as a percentage.

Sample		Permittivity	Loss Tangent	Atten. [dB/m]	Velocity [m/ μ s]
kimberlite	80301	0.047	0.002	0.017	0.269
	80302	0.042	0.002	0.011	0.237
	80303	0.053	0.004	0.033	0.174
metavolcanic	80304	0.036	0.001	0.009	0.300
	80305	0.047	0.001	0.011	0.271
	80306	0.041	0.001	0.010	0.268
granite	80307	0.015	0.001	0.007	0.135
	80308	0.014	0.001	0.006	0.130
	80309	0.013	0.001	0.006	0.139

Table 6.32: Maximum individual measurement uncertainty, calculated as described in Section 2.5.1, of the Snap Lake samples.

Sample		Permittivity		Loss Tangent		Atten. [dB/m]		Velocity [m/ μ s]	
		CV_{RG}	CV_{LG}	CV_{RG}	CV_{LG}	CV_{RG}	CV_{LG}	CV_{RG}	CV_{LG}
kimberlite	80301	7.60	6.34	5.22	7.38	8.49	9.33	4.53	3.87
	80302	3.37	2.81	3.30	3.64	3.65	4.38	1.68	1.44
	80303	6.09	4.42	6.15	6.88	8.93	8.67	3.21	2.40
metavolcanic	80304	4.89	2.70	11.45	12.72	15.98	12.90	2.48	1.35
	80305	8.53	7.70	14.80	12.53	18.22	15.47	4.36	4.00
	80306	3.85	3.21	18.35	7.59	19.04	8.42	1.94	1.61
granite	80307	3.23	2.50	12.31	10.40	13.31	10.60	1.59	1.23
	80308	1.68	2.38	7.32	9.37	7.66	9.93	0.85	1.21
	80309	1.33	1.39	21.42	23.67	21.56	24.00	0.66	0.69

Table 6.33: Coefficients of variation of the individual Snap Lake samples at 25 MHz, calculated as described in Section 6.2.

Material	Permittivity		Loss Tangent		Atten. [dB/m]		Velocity [m/ μ s]	
	$\bar{\epsilon}_r$	CV_{ϵ_r}	$\overline{\tan \delta}$	$CV_{\tan \delta}$	$\bar{\alpha}$	CV_{α}	\bar{v}	CV_v
kimberlite	1.45	5.48	1.38	6.48	1.63	8.19	1.21	3.05
metavolcanic	1.35	5.62	1.13	16.21	1.40	16.65	1.16	2.88
granite	1.13	2.27	9.00	16.81	9.17	17.34	1.06	1.14

Table 6.34: IMS parameters of the Snap Lake materials at 25 MHz, calculated as defined in Section 6.2: the IMS's of the means are simply the ratio of maximum to minimum value of each property in a material type; the variations' IMS's are calculated as the mean of the CV's.

Sample		n	χ_r	ϵ_∞	max. $ \Delta\epsilon_r $ [%]	max. $ \Delta \tan \delta $
kimberlite	80301	0.45	2.74	7.76	1.07 ₁	0.047 ₂₅
	80302	0.49	2.53	6.76	1.18 ₁	0.020 ₂₅
	80303	0.55	5.90	7.75	1.07 ₁	0.050 ₂₅
metavolcanic	80304	0.49	0.45	6.23	2.98 ₂₅	0.010 ₃
	80305	0.55	0.81	8.20	3.40 ₂₅	0.016 ₂₀
	80306	0.51	0.74	7.39	2.99 ₂₅	0.008 ₃
granite	80307	0.46	0.24	5.87	4.08 ₂₅	0.015 ₂₀
	80308	0.59	0.74	5.71	3.39 ₂₅	0.015 ₂₀
	80309	0.35	0.05	5.56	4.80 ₂₅	0.023 ₂₀

Table 6.35: Jonscher parameters of the mean dielectric properties of the Snap Lake rock samples. The maximum difference between the permittivity and loss tangent predicted by the Jonscher model and the actual value are shown, along with the frequency at which the maximum difference occurs (subscripts).

Discussion

A comparison of the various materials' properties reveals a contrast between kimberlite and its host rocks at 25 MHz. The loss tangents of both host materials is substantially lower than kimberlite's; the host permittivities are also lower in general, with granite's being markedly less than the ϵ_r of kimberlite. A good radar contrast is thus expected in those regions where the kimberlite pipe is found in a granitic host. There should also usually be a detectable contrast when it is in a metavolcanic host, but an unfortunate combination of local kimberlite and host rock types could cause 'blind spots' for the BHR. Both hosts do exhibit favourable conditions for radar propagation at 25 MHz: signal attenuation is below 0.65 dB/m and v is above 99 m/ μ s in all cases.

The limited quality of the metavolcanic samples in particular leaves some room for doubt as to the behaviour of these rocks in terms of radar propagation. The measurement of samples of better quality would be required to increase certainty in the conclusions drawn.

6.4.4 Conclusion

The use of the developed system in characterising diamondiferous geological systems has been demonstrated. In general, a reasonable radar contrast is to be expected between kimberlite and its host. That said, the number of kimberlite types in existence is far greater than the limited samples available for this study. Even in a single structure, a number of different kimberlite types are often found [93]. This is confirmed by the Snap Lake samples, which display geological and dielectric differences. This, combined with a lack of kimberlite from the Premier pipe, makes it difficult to generalise based on the Snap Lake results alone. Although Agashev makes mention of the geochemical similarities between Snap Lake and South African kimberlites [100], a more extensive sampling of local kimberlite would be required for greater certainty in the Premier case.

The host rock is generally a reasonable medium for radar propagation. All the Snap Lake samples have attenuation below 1 dB/m. The complex layered Premier country rock is variable but still appears to offer reasonable propagation conditions in large sections. This is confirmed by the cross-hole shoot conducted at that mine [83]. As mentioned previously, the large number of rock types encountered in the Premier case in particular would require a more detailed classification and core log.

Some of the Snap Lake samples were of limited quality, but it was still possible to collect useful data from the intact sections. The ability of the capacitor to measure broken samples is extremely useful, and a distinct improvement over previous methods.

6.5 Conclusion

The characterising of rock core samples always has the same basic aim: the estimation of radar propagating conditions in a host and the likelihood of reflection from some target. This study was done in conjunction with a number of borehole radar shoots using the GeoMole borehole radar, with spectral content in the 10–80 MHz frequency range [83]. The discussions in this section have thus focussed on the 25 MHz frequency component, which falls roughly in the centre of this band in terms of energy content of the spectrum.

The cylindrical capacitor developed in Chapter 4 proves ideal for this task, being able to accurately measure cores of different commonly available diameters and differing condition. Reasonable measurements are possible even if the core is brittle or broken into pieces. A brittle core which would not ordinarily allow the careful preparation of the small samples generally required for destructive measurement techniques is able to be measured using this system. Provided the breaks between pieces are smooth and the outer surface is complete, broken cores may be measured with little loss of accuracy. (This assertion was not proved explicitly.)

The capacitor has shown promise in measuring core samples from a wide range of commonly used borehole types (diameters from 36.4 to 51.3 mm). Further, material properties in a large range are distinguishable with a reasonable degree of accuracy. Permittivities measured ranged between about 5.8 and 15 at 25 MHz; loss tangents of between 0.01 and 0.8 were measured at 25 MHz.

The accuracy estimate is dominated by the calibration accuracy. It is impossible to assign a good accuracy estimate to properties outside the ranges of reference materials. Fortunately the permittivity often lies in an easily achievable range — the propagation speed and range of targets can thus be estimated with good accuracy, allowing detailed mapping of, for example, ore horizons. The measurement accuracy of loss tangent is lower and thus makes estimation of detection range more problematic. It is however possible to compare different materials to each other with reasonable certainty, particularly if they are measured with the same device. This allows prediction of contrasts between materials even if the exact magnitude thereof is uncertain.

A limited evaluation of the uncertainty due to calibration was described in Section 5.2.2. Measurements of a nylon sample with three of the electrodes used in the case studies described compared reasonably well to the parallel plate measured properties of a carefully prepared slice of the same nylon sample. None of the rock samples measured have permittivities as low as nylon, but the ‘good’ behaviour of the calibration curves shown in Figures 5.2 and 5.3 would suggest that the sort of accuracy obtained for the nylon sample may apply to the rock samples measured as well, at least those that have properties between those of Teflon and the artificial dielectric. The BIC measurements are thus estimated to be accurate to within about 4 % in permittivity and within 0.01 in loss tangent. The Snap Lake samples were measured using two electrodes: the kimberlite and metavolcanic samples are estimated to have accuracies of better than about 5 % for permittivity and 0.01 for loss tangent, but the granite samples, though homogeneous and in good condition, may only be accurate to within about 10 % for ϵ_r . Confirmation materials with properties similar to those of the rocks measured would be required to confirm this.

Estimates of propagation velocity from three field experiments compare favourably with properties measured in the laboratory. It would appear that the measurement of homogeneous samples from well known geological systems like the UG1 unit can provide very accurate estimates of conditions in the field: a better than 1 % agreement was found in two separate cases. Even for a more complex system like that found at Premier diamond mine, reasonable predictions may be made. The limitation in the Premier case is really a lack of knowledge of the precise stratification — a number of different Premier samples were obtained but little knowledge of their abundance in the field was available. Nevertheless, propagation velocity predictions were within about 5 % of estimations from field data. On a quantitative level, it is conspicuous that all agreements of better than about 4 % were for materials with $CV_v \lesssim 2$ (cf. Tables 6.7, 6.12 and 6.21).

The aim of most borehole experiments is the delineation of some target. Estimation of its distance from the transmitter and receiver require accurate interpretation of pulse travel time and thus accurate knowledge of propagation velocities. Comparison of the results obtained in this dissertation to field experiments would indicate that laboratory measurements can indeed result in accurate predictions. Accurate knowledge of the loss experienced by a wave as it travels through the rock is also important, but arguably less so. There is flexibility in the positioning of a borehole relative to where the target is suspected to be. With rough knowledge of the loss tangent, the borehole can be drilled in such a position that adequate reflections are guaranteed. It is accurate knowledge of the propagation velocity that will allow the prediction of small scale variations in the target geometry, and it is precisely this sort of knowledge that allows more detailed mine planning and decreased danger to miners.

The frequency behaviour of the various samples was modelled by the least squares fitting of a Jonscher model with varying success. The diamond samples were in general more amenable to the model, having the same form as (2.36), while the samples from the Bushveld Igneous Complex were in general less suitable. Although the model may often be used adequately in the 1–25 MHz frequency range studied, extrapolation of the material properties in the frequency domain based on the model is not recommended if $\Delta\epsilon_r$ and $\Delta\tan\delta$ are worst at high frequency.

Chapter 7

Conclusion

The device design and measurement methodology presented in the preceding chapters are a significant advance in the measurement and interpretation of the radio frequency dielectric properties of hard rock borehole core samples. The non-destructive measurement technique allows for the thorough investigation of the complete core sample. This allows a more detailed interpretation of results since the sampling is less sparse, and the confident relation of microscopic laboratory measurements to bulk propagating characteristics of a host.

The design in Chapter 4 incorporates some of the established principles of dielectric profiling, but extends and improves upon these to result in a device particularly well suited to the problem at hand: the measurement of hard cylindrical rock borehole core samples in the 1–25 MHz frequency range. Indeed, the improvements over previous methods for the measurement of hard rock samples — all destructive, as far as is known — are considerable.

An example will serve to illustrate the new capabilities that this device offers. Consider once again the Bleskop Marker (BKM) sample discussed in Section 6.3.4 and shown photographically along with its measured dielectric properties in Figure 6.2. This single sample contains many of the feature types one would want to be able to measure: large sections of relatively homogeneous and inhomogeneous rock, narrow inclusions in a host, as well as transitions between different rock types. In addition, the sample contains breaks between its constituent pieces, some clean (i.e. there is a tight fit between adjacent parts) and others rough.

A traditional (destructive) measurement approach would immediately raise the question of where to sample the core. For the homogeneous half metre section of anorthosite (96–133 cm), the answer to this question would not critically affect the interpretation of measurement results, but it becomes extremely difficult to justify the use of any particular section in the pegmatoidal feldspathic pyroxenite (PFP) region (51–96 cm) in quantifying the materials' properties. The cylindrical capacitor obviates the need for this question, instead posing a much simpler query regarding the ideal sampling density. The measurement of a narrow inclusion like the chromitite stringer in particular would be virtually impossible using conventional measurements. With the continuous measurement technique introduced in Chapter 5, a relatively detailed, accurate, and certainly more instructive measurement of such features is possible. A variable sampling rate can be employed to investigate such fine inclusions while not unnecessarily over-sampling homogeneous features like the anorthosite.

There has traditionally been a problem in relating laboratory measurements to propagation velocities observed in the field because crystal sizes in some conglomerates are comparable to the dimensions of samples [101] measured with parallel plate capacitors. This problem may be reduced by measuring the larger volume of rock in the cylinder cavity.

A further negative yet unavoidable side effect of a sample's preparation is the loss of material and

The range within which dielectric properties can be measured to a specified accuracy is determined by the properties of the reference materials used — the Lagrange map described in Section 2.6.2 is valid for materials with properties between those of the outermost reference samples. The creation of artificial dielectrics, as described in Appendix C, may extend the permittivity range, but suitable materials with stable and known loss tangents remain difficult to find, let alone obtain. Calibration beyond the reference material range by extrapolation is possible but does not guarantee absolute accuracy, only the estimation of materials' properties relative to each other.

Confirmation of the calibration and predicted measurement accuracy is possible using further samples with known dielectric properties. An attempt to confirm that measurements actually lie within the uncertainty prediction was made using nylon. Cylindrical measurements of its properties were within about 10 % and 0.01 of parallel plate measurements of a nylon sample for permittivity and loss tangent respectively. These values are substantially larger than typical predicted uncertainties of about 5 % in either case. It should be said that nylon is hardly an ideal sample since its properties are not very well known and its reaction to machining is uncertain; further, the nylon samples were not prepared to the degree of accuracy that the calibration samples had. It was however the only option available at the time of measurement. The values listed should thus be seen as an upper limit on the accuracy. Indeed, the generally excellent agreement between the laboratory and bulk propagation velocity estimates for homogeneous samples would appear to confirm this. Even at these upper limits, the accuracy is still comparable to the majority of destructive methods listed in Table 1.1. It is thought that more appropriate test materials would provide a better estimation of the measurement accuracy.

The detail of information regarding the dielectric properties of a number of economically important geological systems that has been obtained in this study is unprecedented. Further, the position of this study as part of a larger project has allowed for remarkably accurate comparisons between microscopically and macroscopically predicted propagating conditions. The positive consequences for the mining industry, both in terms of safety and economically, are large. The improvement in the application of laboratory measurements to the planning and interpretation of borehole radar shoots will accelerate the entire measurement process and reduce its cost.

Recommendations

The device presented in this work is a prototype that will see improvement in future design iterations. Recommendations can be divided into two broad categories: the improvement of measurement quality using the current electrode design, and mechanical design enhancements or increases in the capability of the device.

The range and accuracy of measurable dielectric properties are both largely dependent on the reference materials used. Obtaining reference materials with larger permittivities and particularly loss tangents will relate directly to an extended measurement range, as well as the ability to confirm the calibration in that range. The difficulty in obtaining lossy samples has been mentioned repeatedly. One possible solution would be the use of lossy liquids with well known properties, like ethanol ($\epsilon_r \approx 25$, $\tan \delta \approx 0.03$ at 25 MHz) or methanol ($\epsilon_r \approx 33$, $\tan \delta \approx 0.01$ at 25 MHz) [102] contained in custom-made holders. Wilhelms' potential solution for concentrically layered cylinders could then be used to calculate the effective reference material properties.

In addition to aiding analysis in the work presented here, the circuit model developed in Chapter 4.3 will be a valuable tool in extending the measurable frequency range. The key frequency range limitations result from resonant frequencies associated with the interaction of the various capacitor-inductor pairs shown in Figure 4.5. Careful design of the shield geometry and its connection to the guard electrode, as well as the feed structures, to lower capacitance and inductance values, can shift the resonances up in frequency, thus extending the measurement range. All resonances will be affected in the same way,

but the dominant ones (i.e. those at the lowest frequencies) are best lowered by decreasing the feed inductances and guard-shield capacitance. The seemingly contradictory requirements of shortening (or widening) the feed conductor — to lower inductance — and increasing the distance between the guard and the shield — thus lowering capacitance — provide the opportunity for some creative design.

The frequency range under consideration in this study included the centre frequency of a specific borehole radar [83] and thus allowed the use of the accurate LCR meter in the 1–25 MHz range. The auto-balancing bridge method in general currently allows measurements to frequencies of roughly 110 MHz [61]. One of the attractions of the electrode design presented here is its versatility: it can be used to make two-port measurements using an automatic network analyser, something which could, with careful electrode design, conceivably extend the frequency range to hundreds of megahertz. (Analysis of the circuit described in Figure 4.5, using typical capacitance and inductor values, shows that the lowest resonant frequencies for the current device designs are above about 200 MHz.)

At lower frequencies the design of dedicated measurement electronics would result in an extremely portable device that could ostensibly be used to conduct *in situ* measurements in core yards, greatly accelerating the BHR measurement and analysis process. (Note that using the current system in this way is quite feasible, simply requiring the transportation of the measuring equipment.)

A mechanism for automating the movement of the core through the cylinder cavity, perhaps similar to the system used in Wilhelms' devices [31, 28], would also accelerate the measurement process. A measurement of all four orientations of a 20 cm length of core at a 1 cm resolution (i.e. 80 measurements) typically takes about an hour using the current method. A faster measurement rate would allow more detailed (read: higher resolution) measurements to be performed. This would clearly be problematic with samples that are in poor condition, since great care is required in such cases to avoid further irreversible damage to the cores.

Another possibility would be the use of multiple sensing electrodes, acting either as the sensing electrode or part of the guard, similar to the design used by Moore [27]. The method used in this work for etching electrodes on a flexible substrate would allow the precise construction of such a system. This multiple electrode solution would be beneficial for the measurement of broken or brittle cores. In addition, the measurement repeatability would be greater since less movement of the core would result in less mechanical strain on the system as a whole, and thus a lower possibility of damage to the electrodes or slight changes in the geometry.

To summarise finally, the creative implementation of a novel electrode design has greatly enhanced the capabilities for measuring the complex dielectric properties of hard rock cores. The robust shielded capacitor, easily constructed in a standard laboratory, allows the rapid, repeatable and accurate measurement of borehole cores without requiring any sample preparation. The advantages over conventional measurement systems are numerous, and extensive scope exists for further improvement.

Appendix A

Electrode Construction and Operation

A.1 Electrode Construction

This section is intended to be a technical document presenting detailed instructions for the construction of the cylindrical capacitors designed and presented in Chapter 4. It is an appendix and not a section in the main dissertation body because this is one implementation resulting in a prototype device, which, though functioning well, is by no means the final product. Improvement is possible and necessary. Rather, this document describes a functional and robust construction procedure, containing practical suggestions gleaned from the device's long development process.

The format used will be a listing of and motivation for the materials used, followed by a photographically supported step-by-step construction procedure. The design of the jig¹ to hold the shielded capacitor in place is also of critical importance in ensuring accurate measurements. Again, a relatively simple yet robust design will be presented.

Material Requirements

The implementation discussed in Section 4.4 was deliberately general and will be elaborated upon here. The components of the shielded capacitor can be divided into the flexible electrode, the rigid enclosing shield, and the structure supporting the electrodes (which also partly serves as the connection between the electrode and the shield). The rigidity of the shielding box is critical for good measurement repeatability.

The flexible electrode is the heart of the system and as such also demands the most important design choices. The requirements for extreme flexibility and a smooth substrate surface were mentioned in Section 4.4: the material chosen and used in this implementation is the GTS7600 series of copper polyimide laminates by GTS Flexible Materials [96]. This material is available in a range of substrate and copper deposit thicknesses; a laminate of about 100 μm thickness was used in the construction of the electrodes for this study. The pressure exerted by a small number of evenly spaced ordinary elastic bands was sufficient to keep the electrodes pressed against the core. The laminate surface was smooth enough for the core samples to pass through the electrodes with a minimum of applied pressure.

The rigid enclosing shield mentioned above is the outer box through which the measuring device must access the capacitor. Two issues are important here. First, the rigidity of the box must be sufficient to not deform under the mechanical strain of measurement. Second, the material used must allow for rapid construction — this was one of the original design requirements. The use of a fairly thick (1.4 mm

¹The 'jig' spoken of here refers to the actual mechanical holding device as well as the interface between the capacitor and the measurement instrumentation.

thickness was adequate) double sided pc-board for the side, top, and bottom sides of the box gave this rigidity while allowing simple manufacture. One advantage which should not be underestimated is that the conducting surfaces are easily connected to each other by a solder joint. The two conducting sides of the pc-board should be connected to each other to form a single conducting unit. The use of adhesive Aluminium tape provides an adequate Ohmic contact.

The box ends are the connection points for the shield conductors and provide the access holes for the core to the capacitor. Rigidity and ease of construction are again requirements which are met by the use of perspex sheeting. The construction of a suitably sized hole does not weaken the support given to the shield, while the inherent transparency of the material lends some aesthetic appeal to the construction. The shield may be attached solidly to the perspex end-sheets by narrow diameter screws.

The flexible capacitor and rigid shield have been discussed, but it is the link between the two which provides the greatest constructional challenge. This link acts firstly as a connection between the guard electrode and the shield, but must also support the core's weight as it is passed through the capacitor. Rigid single sided pc-board strips are again easily shaped to the correct dimensions and provide adequate stiffness to be used as support struts.

Finally, the connection of measuring instrument ports to the centre and feed electrodes again requires the connection to the flexible electrode. The coaxial cable from the instrument is connected to a bulkhead receptacle — the outer conductors connect straight to the shield, while the inner conductors are connected to their respective electrodes by narrow conducting strips which are bent to form a sort of spring as shown in Figure A.2. The advantages of this connection are two-fold: the flexibility of the electrode is not impaired by the sprung centre conductor extension, and the larger surface area used in the solder join provides a more durable connection.

Construction Procedure

What follows is a step-by-step procedure for the construction of the shielded capacitors described in this study. The most time-consuming aspects are the etching of the electrodes and the machining of the perspex end plates. Once these are done, the assembly time for a single device is estimated to be about two hours.

1. Once the electrodes have been laid out and etched on the laminate, they should be cut out so that the electrode edges bordering the side gaps have as little excess cleared laminate as possible adjacent to them. It is advisable to leave slightly more excess laminate at the guard ends, as this protects the guard conductor from physical damage due to sample insertion to some extent. The electrodes should now be formed around a sample of nominal design diameter, and held in place by evenly spaced elastic bands. The sample used should be heat resistant as soldering will be conducted in its immediate vicinity.
2. The perspex end plates should have their holes machined to lie centrally and to be large enough to accommodate the largest expected sample (with the electrode wrapped around it). The length of the shield plates should be slightly shorter than the guard electrode's total length to allow the perspex end plates to act as additional restraints for the electrodes. The end plates are placed over the ends of the cylinder, then secured to the shield side walls. Care must be taken to secure the electrodes and core centrally in the end holes using some form of temporary spacer, since the placing of the support struts will tend to push the core off-centre.
3. The struts are formed from single sided rigid pc-board, including indentations for the elastic electrode shapers, and placed in such a fashion as to support the core when it is inserted. This prevents the relatively heavy core from being able to move sideways and thus lie eccentrically in the cylinder

(also causing an air gap on its one side). The struts are soldered to the guard electrode as shown in Figure A.1. Great care must be taken in this step, as an incorrect fit may result in unpredictable air gaps in the vicinity of the struts' connecting points to the electrode. Soldering should be done at a low heat and as quickly as possible to prevent damage to the laminate surface. Filing the strut edges away at an appropriate angle eases their insertion and the soldering to the shield and guard electrode. When the capacitor is designed to accommodate large heavy cores, it may be beneficial to further support the struts. A third perspex plane with a slightly larger hole, cut in half and shaped to fit between the bottom plate and the struts, is perfect for this task. The two halves should be spaced evenly and the hole should be slightly bigger than the end plates' holes to not interfere with the electrodes. Screws from the bottom and sides hold these perspex supports in place, as seen in Figure A.2.

4. The top and bottom plates have central holes to accommodate the bulkhead connectors drilled through them; the bottom plate also the plastic spacer required for positioning in the holding jig secured to it, as shown in Figure A.3. The ends of the sprung conducting strips are soldered to the middle of the appropriate electrodes (again quickly, using low heat, to prevent damage to the substrate), and the bulkhead connectors are placed through the holes in the plates. The plates are now secured to the perspex end plates.
5. The shield is turned into a single conductor, at essentially a single potential, by connecting each top/bottom-side plate pair with conducting Aluminium tape.

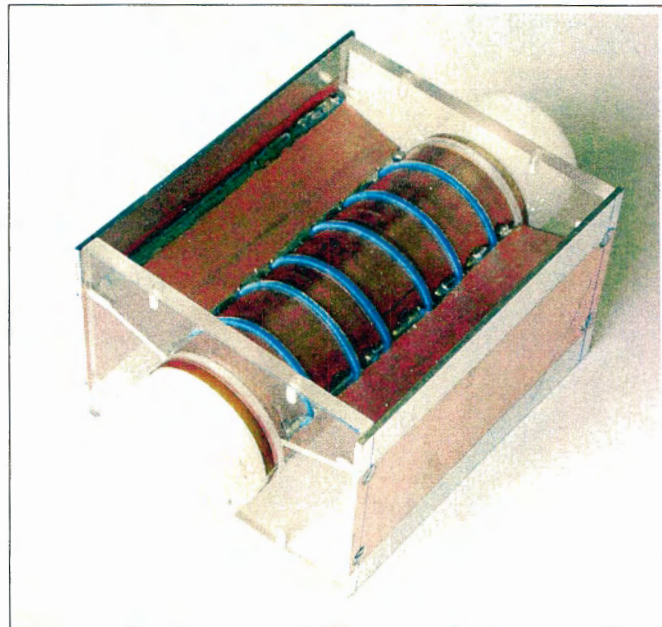


Figure A.1: View of the electrode during the construction process just after the struts have been placed and soldered to the guard electrode.

Holding Jig

To ensure measurement repeatability, it is critical that the capacitor be held rigidly in place for the duration of the measurement process. Of particular importance are the connectors: even small changes in their position can result in unacceptable changes to the measured phase. The mechanical strain placed

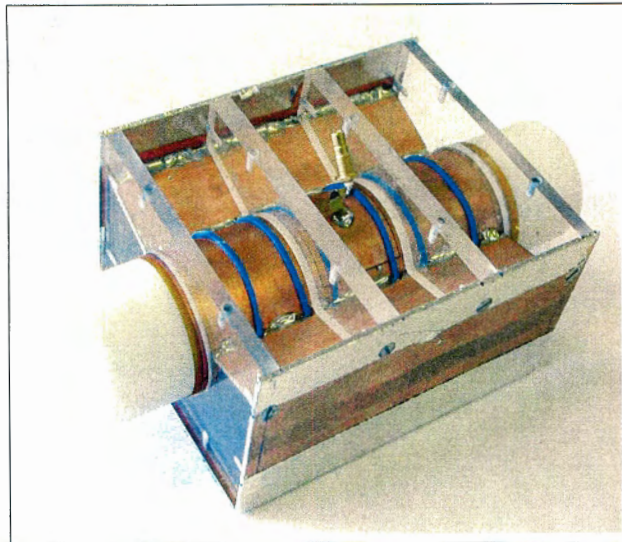


Figure A.2: View of the electrode during the construction process. The flexible feed has been soldered to the sensing electrode and the perspex supports have been inserted to stabilise the bottom cavity.

on the capacitor box (and thus the connectors) during movement of the samples necessitates some form of jig to hold the device firmly in position.

The holding device is shown with the capacitor box in place and removed in Figures A.4 and A.5. In principle the box is to be secured from the sides, since it is the effect of lateral movement of the samples that it is desired to counteract. The left and right side restrainers are labelled as 'L' and 'R' in Figures A.4 and A.5. The box is positioned centrally in the base marked 'H', shown in detail in Figure A.6, by way of a plastic spacer which is secured to the bottom plate of the box, as shown in Figure A.6. The bottom bulkhead connector must be positioned centrally in the spacer's centre opening — this ensures that it aligns correctly with the jack in the base. The natural inclination of the side restrainers is to push the box up when they press against it. This is problematic since it changes the fit and geometry of the bottom connection, but can be counteracted effectively by holding the box down with the top restrainer (marked 'T').

After placing the box in its holder, the top restrainer is lowered and fastened. The right restrainer is then pushed against the side of the box and secured. Finally the left restrainer may be pushed against the box, locking it in place. The connection of the H ports to the feed electrode is now made with the flexible blue cables, as shown in A.4. Note how the connection between the Hc and Hp terminals is made as close to the electrode as possible by the T-connector shown. The connection of the LCR meter's L ports is made similarly through the base. SMB connectors are used throughout to allow simple connection.

The pressure exerted on the capacitor box by the various restrainers (and particularly by the top one) requires the shield to be constructed accurately. The perspex end plates in particular should be carefully aligned — any problem with their positioning can result in the holes being pushed out of alignment and the sample not being able to pass through the cylinder any longer.

Provided the box is constructed carefully and secured properly using the jig described here, extremely repeatable measurements can be made.

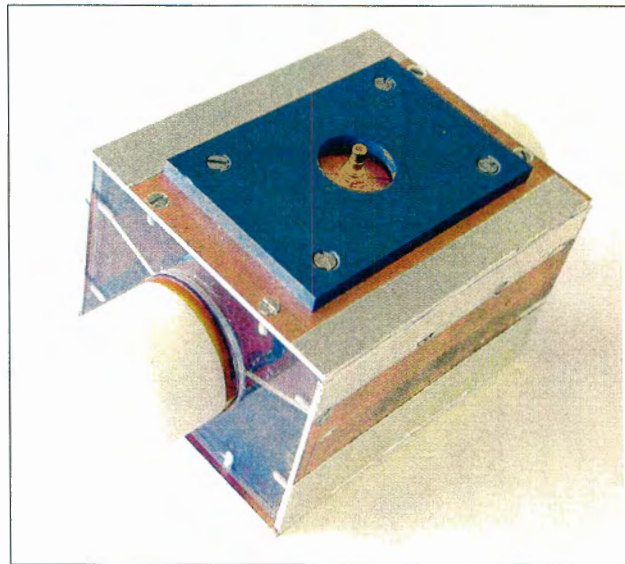


Figure A.3: View of the electrode after construction. The plastic spacer and SMB bulkhead connectors are clearly visible.

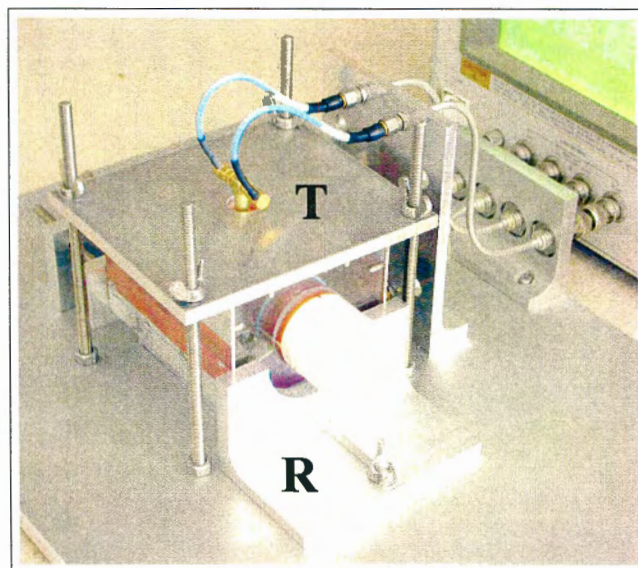


Figure A.4: View of the device holder with the capacitor box in place. The top restrainer (T) is fastened tightly and prevents the box from being pushed up by the side restrainers.

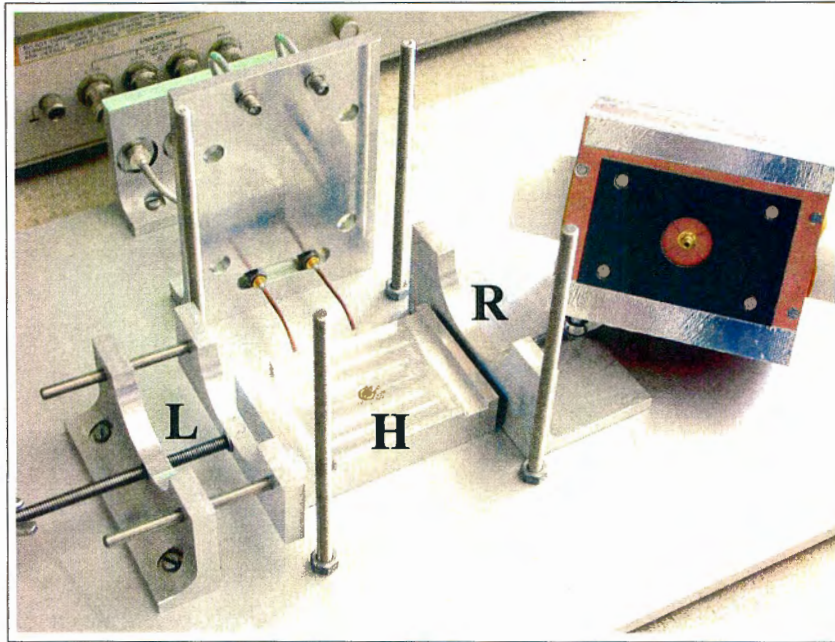


Figure A.5: View of the open device holder (H) and an electrode set with the plastic spacer shown. The side restrainers are marked 'L' and 'R', and the Lp and Lc feed cables are visible. They are connected to each other using an SMB T-connector, the third terminal of which is visible in the centre of the holder.

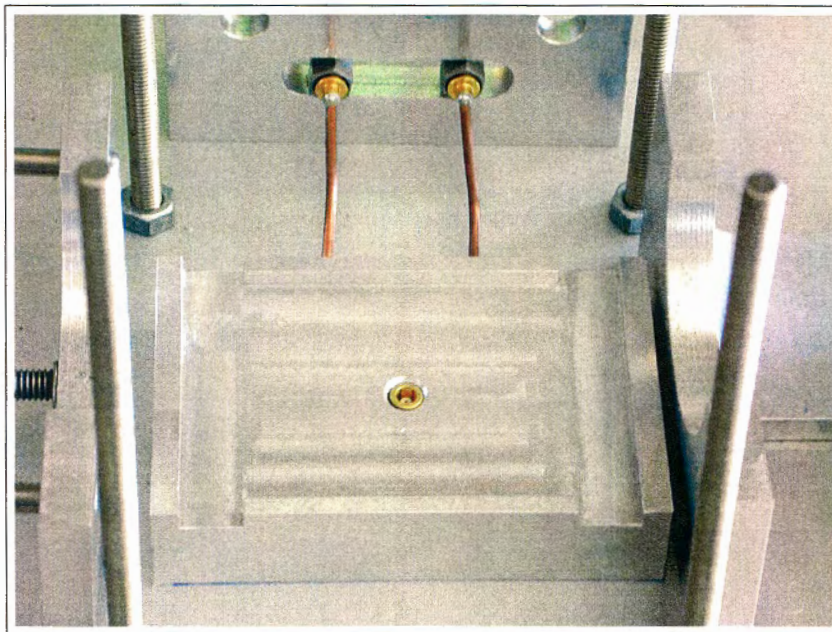


Figure A.6: Close-up view of the device holder.

A.2 Measurement Procedure

This section is intended as a practical guide toward making measurements with the cylindrical capacitor designed in this study. The information contained here is meant as a practical supplement to the measurement description in Chapter 5. As such, a brief summary of the procedure employed will be followed immediately by a detailed point form routine for measurements using the HP 4285 LCR meter [60]. Reference will be made throughout to the appropriate MATLAB scripts listed in Appendix D.

Measurement Procedure

The aim is to make the most accurate measurements possible. A calibration procedure has been developed which essentially maps the measured impedance to a complex dielectric constant using a mapping function determined by the response of the device to a number of standard materials. This response will differ to some degree for each device constructed; the mapping will also differ depending on the exact properties of the standard materials used. It is thus important that the measurement procedure avoids the influence of these possible differences: each experiment must be treated individually, even to the extent of characterising the particular batch of a certain reference material used in a particular measurement sequence. For example, two samples of Teflon obtained separately cannot be assumed to have exactly the same properties — they may differ by up to a few percent. This sort of difference will translate directly to an increased uncertainty in the measurements.

On occasion the reader will be referred to the MATLAB scripts used in the measurements and calibration. The operation of these scripts can be fairly complex, involving the setting of a number of variables. Describing the internal workings of the scripts would be superfluous here. The reader is thus rather referred to the detailed commentary in each script.

1. The first step in the measurement process is the accurate determination of the material properties of the reference standards used. The use of two materials is advocated, one with a low permittivity and loss tangent, the other with a high permittivity and loss tangent to cover as wide a range of rock sample properties as possible. In this study, a third artificial material is created by the insertion of a conducting centre into the high loss material, as discussed in Appendix C.

The parallel plate capacitor described in Chapter 3 is used to carefully measure prepared samples of the two materials. A technique for the preparation of such samples is described in Appendix B — the samples should have sides which are as flat and parallel as possible to reduce potential air gaps, the largest contributing factor to measurement uncertainty in this case.

A repeated measurement of the open and short compensation standards need only be conducted once if a number of samples are measured in the same session. They should be remeasured if a long break occurs between measurements. Each sample is also measured repeatedly so that a Type A evaluation of the measurement uncertainty may be conducted (refer to Section 2.5.1). Between each repetition of a measurement, the sample should be completely removed from and reintroduced to the capacitor. This helps to compensate for possible errors caused by the positioning of the sample.

The MATLAB script *measure.m* is used to conduct the measurement and calibration. Precise instructions are given in this script.

2. The first step in the measurement of the core sample is the characterisation of the device prior to the sample measurements. Again, the aim is a Type A characterisation of the uncertainties of the inputs to the calibration. In addition to the three reference samples, a representative selection of rock samples is measured repeatedly to obtain an estimate of the uncertainty involved in each rock core measurement. The number of rock samples required depends on the size and condition of the

cores to be measured: if all the cores have the same diameter and surface condition, one sample may suffice; otherwise a number of samples representing the extremes in diameter and surface condition should be chosen.

The MATLAB script *measure.m* is again used for this process. After the first measurement sequence of the three standards and specified number of rock repeatability samples, the order is randomised for the remaining repeatability measurement sequences. It is recommended that at least five such sequences are conducted for both the pre- and post-characterisation, so that the total of ten measurements may comply with the reliability criterion mentioned in Section 2.5.1.

3. The measurement of the rock cores should commence immediately following the pre-characterisation of the device. A random point on each core is chosen as the 0° orientation, and the core is marked along that axis at the desired measurement intervals. The first point to be measured should be marked to coincide with when a section of the core with intact surface just covers the sensing electrode completely.

It is important to minimise the altering of the device response due to geometric changes. The implication for the accurate measurement of a number of samples is that they should all be fed through the capacitor in as similar a fashion as possible, that is, they should be inserted from the same side, they should be pushed gently without forcing them, and any section of the core far from the box should be supported from below to prevent torque from distorting the cylindrical shape of the electrode. Also, one of the reference samples should be used as a spacer between measurements of cores to prevent the electrodes from collapsing (and possibly becoming damaged). Teflon is recommended for this purpose due to its extremely low friction coefficient.

The MATLAB script *measure.m* may be used repeatedly for the measurement of all the rock cores to be characterised.

4. Immediately after the measurement of the rock cores, the post-characterisation of the device should take place. The procedure followed is identical to the pre-characterisation described in Point 3. The data from the two characterisations is combined to estimate the uncertainty of the relevant input arguments for the calibration.
5. Once all the data has been gathered, and each input argument for the calibration can be assigned an expected value and an uncertainty, the calibration may be conducted. The MATLAB script *measure.m* may be used for the calibration of an individual measurement, but, since the four orientation measurements are often combined, the user-modified script *process_data.m* is perhaps more suitable in most cases. This script simply automates the calibration of the four orientations' data sets, combining them and presenting the relevant output data in an easily digestible form. The analysis of the data must of course always be done on an individual basis, taking into account the geological scenario and core sample set available.

Appendix B

Parallel Plate Sample Preparation

The need exists for a simple method of preparing samples for accurate measurement with the parallel plate capacitor developed as part of this dissertation. The dominant criteria for a suitable sample are that it be of a suitable thickness and have flat and parallel sides. A method for preparing hard rock slices, with thicknesses above about 2 mm and a variation of less than 20 micrometres in that thickness, is described here. The preparation of plastic slices is also discussed.

B.1 Hard Rock Samples

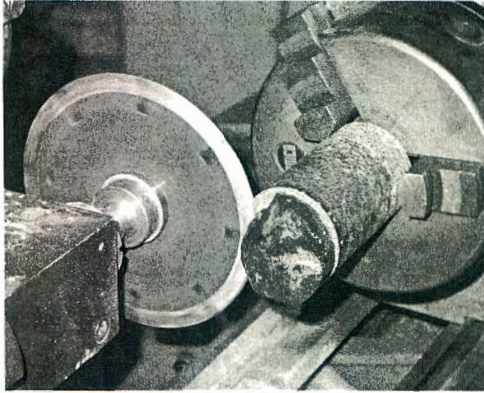
The stages involved in the preparation of an accurate sample are shown photographically in Figure B.1. A lathe with an angle grinder attachment is used to cut and smooth the rock slices with a diamond blade. The first step, shown in Figure B.1(a), is the removal of the inevitably rough core sample end to create the first smooth surface. The core sample is gripped tightly by the lathe's chuck — if it is too long to be held stably, a supporting attachment which allows free rotation of the sample may be used. Should it be necessary, the freshly exposed end can then be smoothed further as shown in Figure B.1(b): the blade is held at the same angle relative to the core, and it is passed along the surface. Particularly in the smoothing steps, rotating the lathe chuck fairly slowly in a direction counter to the diamond blade's much faster rotation yields the best results.

The next step is to cut off the slice, as shown in Figure B.1(c). The slice should initially be cut slightly too thick, since some more rock is lost in the smoothing of the second surface. The slight raised section in the slice centre must now be removed. A special holder for the slices may easily be fashioned from brass or aluminium¹. It is essentially a short staggered tube, cut along one side so that gap in the circle is formed. The already smoothed side of the slice is placed flush against the narrower section of the holder, and the tightening of the lathe chuck holds the sample in place by closing the slight longitudinal gap and thus pressing against the edges of the slice.

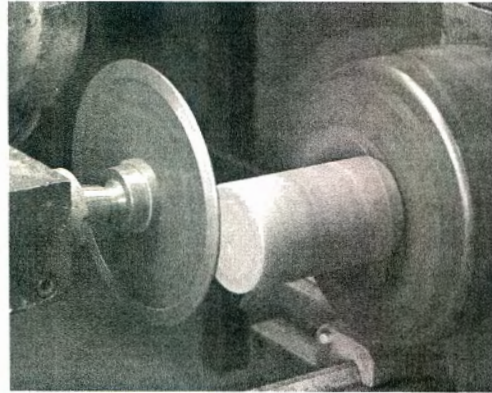
Once the sample is held in this way the second side may be smoothed similarly to the first, as shown in Figure B.1(d). If required, the sample may be inverted and smoothed on the other side again.

The relaying of some practical experiences in the construction and use of the holder may be beneficial. After initial machining of the sample holder, a longitudinal cut is made to facilitate the gripping of the slice. This cut may lead to a slight deformation of the holder, necessitating a re-machining of the surfaces against which the sample rests in particular. It was also found that aligning the holder in the chuck identically when smoothing the opposing sides led to better results.

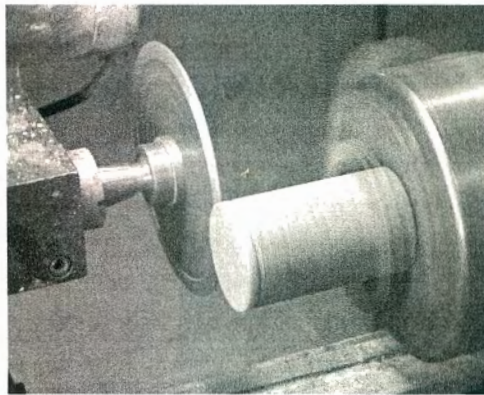
¹The use of plastic is not recommended since it is more easily damaged, leading to the slice not being held equally parallel to the blade in the smoothing process.



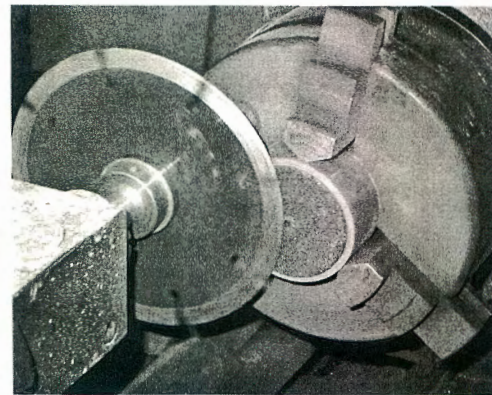
(a)



(b)



(c)



(d)

Figure B.1: Four stages are involved in the accurate preparation of hard rock slices for measurement with a parallel plate capacitor. (a) The rough end of the core sample is removed. (b) If necessary, the exposed end is smoothed. (c) A slice is cut. (d) The slice is inverted, placed in a custom holder, and the other side is smoothed.

B.2 Plastic Samples

A slightly different approach is required in the preparation of plastic samples. The preparing of the first surface and cutting of the slice is similar to the hard rock case, the difference being that a simple machining bit replaces the angle grinder. If the plastic slice is pressed by the sample holder, though, it deforms slightly. If smoothed in this state, a noticeable concavity results upon release of the slice from the holder: the slice is thinner in the centre than at the edges. A satisfactory way of avoiding this problem is to first smooth the first surface and cut the slice, as before, then to re-prepare the surface of the plastic rod still held in the lathe. Using double-sided adhesive tape, the slice is now stuck tightly to this new surface by its already smooth surface. The slice's second surface may now be prepared. This method yields samples with a tolerance similar to the rock samples, typically of better than a 20 micrometre variation in the sample thickness.

Appendix C

The Artificial Dielectric

The calibration of the cylindrical capacitor by the method described in Section 5.2.1 involves the use of three reference standards with known dielectric properties. The materials should be chosen so that their property range corresponds as well as possible to the projected range of properties of the rock samples to be measured. Two factors constrain one's choices: firstly, a limited selection of suitable standard materials (lossy materials in particular are difficult to obtain — this problem was also experienced by Wilhelms [28, p. 82]) is available, and, secondly, the range of rock properties is difficult to predict due to the general lack of measurement results available in the frequency range of interest.

Ideal for this study would be three materials having a low, medium and high combinations of ϵ_r and $\tan \delta$ respectively. The terms ‘medium’ and ‘high’ are relative to the projected rock property range, which is taken here as $1 \lesssim \epsilon_r \lesssim 25$ and $0.001 \lesssim \tan \delta \lesssim 0.5$. Well-characterised lossy materials are particularly difficult to acquire, but PVDF [73], having a permittivity of about 6 and a loss tangent of about 0.2 in the frequency range of interest, proves useful. While having a reasonably ‘high’ loss tangent, its permittivity is decidedly ‘medium’ in relation to the projected property range. The problems associated with finding suitable materials make the option of an artificial dielectric very attractive.

The aim of increasing the effective (perceived) dielectric constant may be accomplished by the concentric layering of different materials. This was discussed by Wilhelms, who used conducting cylinders of differing diameters centred in his air-filled capacitor to provide a range of predictable capacitance values which can otherwise be seen as effective dielectric constants [28]¹.

The analytical solution for the capacitance of a cylindrical capacitor, of the type discussed in this dissertation, containing concentrically layered dielectrics was solved formally by Wilhelms [28]. The relatively simple two-layer approach is a subset of the complete solution which finds application here. Consider a cylindrical capacitor containing two concentrically layered materials having outer radii b and a as shown in Figure C.1. The total effective dielectric constant may be altered by varying the relation of the radii $v = b/a$ or by changing the individual materials’ properties. Implementation of Wilhelms’ two-layer solution allows the investigation of the range of effective dielectric constants achievable using available materials like Teflon and PVDF. The result is that it is possible to simulate a material with a high permittivity or with a high loss tangent, but not both. Combining Teflon and PVDF does not give much of an improvement over plain PVDF.

Another option is available if the loss tangent of PVDF is deemed acceptable: the perceived permittivity may be increased by inserting a conducting centre cylinder. Practically attainable ratios of b to a allow an increase in ϵ_r of a factor of about 2–3. In this conducting centre case, a coaxial capacitor approximation yields acceptable results for the capacitance for quite a large range of v . This more intuitive approach is described here for its ease of implementation.

Again consider the configuration shown in Figure C.1, but this time with a conducting centre cylinder.

¹This is analogue to the parallel plate artificial dielectric consisting of a cubic array of conducting spheres [47].

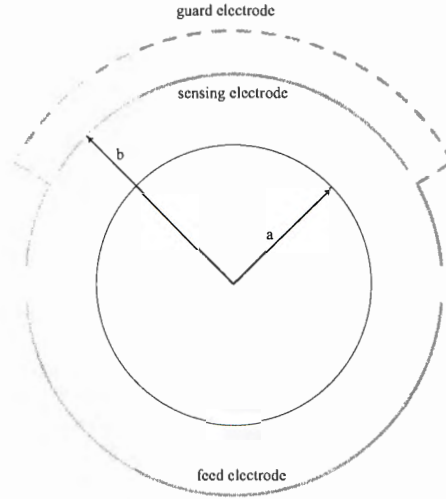


Figure C.1: Schematic plane view of the cylindrical capacitor containing a centred conducting core.

The upper and lower electrodes are given equal yet opposite potentials. The assumption that all gaps are infinitesimal is a valid one for ratios of $v \approx 1$, since the field region adjacent to the sensing electrode is not influenced by the side gap fields. The smaller the arc of the sensing electrode, the further v can be from 1 while the approximation remains valid. A plane of electrical symmetry exists in the plane separating the feed and guard electrodes. Each half-cylindrical capacitor can be approximated as half of a full coaxial capacitor having a capacitance of $C = \frac{1}{2} \frac{2\pi\epsilon^*}{\ln(v)} \frac{\phi_0}{\pi}$ [F/m] [42]. The total capacitance of the two capacitors in series is half again of this capacitance. Assuming an even normal field distribution in the entire gap, the proportion of the field in the sensing electrode region results in a total capacitance (per metre) of

$$C = \frac{1}{4} \frac{2\pi\epsilon^*}{\ln(b/a)} \frac{\phi_0}{\pi} \quad (\text{C.1})$$

This expression matches Wilhelms' full solution and a numerical method of moments solution for a vacuum filled capacitor extremely well over a large range of v .

The effective permittivity is increased but the loss tangent remains constant. This is to be expected as the actual properties of materials used remain the same, only the geometry and thus the vacuum capacitance is changed. If the total capacitance is written as $C = C_0\epsilon_r(1 - j \tan \delta)$, and its admittance as $Y = j\omega C$, it is clear that the loss tangent, $\tan \delta = -\text{Im}\{Y\}/\text{Re}\{Y\}$ cannot change if only C_0 is altered. The effective permittivity, though, becomes $C_0\epsilon_r$ and thus appears different.

A number of the artificial dielectrics, constructed using PVDF and brass centre conductors, are shown in Figure C.2.

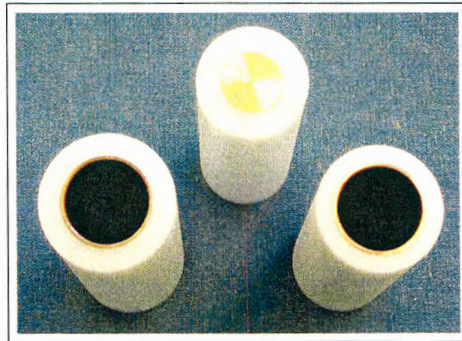


Figure C.2: Some artificial dielectrics.

Appendix D

MATLAB Scripts

This Appendix contains the MATLAB scripts created during the study. All scripts are fully documented to facilitate ease of use. The script *measure.m*, starting on page 126, is used to conduct all the measurements described in this dissertation. For the calibration of cylindrical and parallel plate measurements, it calls *cyl_calibrate.m* (page 130) and *pp_calibrate.m* (page 132). The script *process_cyl_data.m* (page 133) is used to process the measured data — it calls the cylindrical calibration in *measure.m*. Finally, *geometry.m* (page 134) is used for the electrode layout. Many of the smaller function files called by the scripts listed here are not included explicitly. They are available on request from the author.

D.1 *measure.m*

```
% ----- %
% ---- Introduction ---- %
% ----- %
%
% This script is used to conduct the measurement of a rock sample using the
% cylindrical probe and LCR meter. The layout is designed to guide the user
% through the entire measurement process in five steps:
%
% 1. Characterisation of the standard materials using the parallel plate
%    capacitor.
% 2. Pre-characterisation of the cylindrical capacitor.
% 3. Measurement of the MUT.
% 4. Post-characterisation of the cylindrical capacitor.
% 5. Calibration of the measured data to yield the rock properties of
%    interest: complex dielectric constant, attenuation and propagation
%    velocity.
%
% The commenting in the script is thorough, and is intended as a form of
% documentation for the measurement process, complementary to the
% measurement procedure description in Appendix X.
%
% Marc Ruetschlin, 29 February 2004

% ----- %
% ---- Action Setup ---- %
% ----- %
%
% The five possible actions described above are now (de)activated by
% setting their respective enabling variables to (0) 1. They must
% be done in order, although step 3, the MUT measurement, may be conducted
% repeatedly before continuing to steps 4 and 5 should the measurement
% of a number of materials be required.

do_parallel_plate_measurement = 0;
do_pre_characterisation       = 0;
do_measurement               = 0;
do_post_characterisation      = 0;
do_calibration               = 0;

% The user may specify the filenames used in the calibration externally by
% setting this variable to 1.
external_filename_specification = 0;

% Some of the measurement types require certain actions to have been
% completed or specific files to exist. Should a check for these be
% negative, the user will be prompted to perform the necessary steps. The
% precise details can be found in the introductory commentary to each
% section.
%
% Some settings may require manual (de)selection in the relevant
% section - the user should familiarise her/himself with them before
% performing the measurement.

% ----- %
% ---- Miscellaneous Setup ---- %
% ----- %

% ----- %
% Frequency points at which measurements are to be conducted. If the
% variable already exists, it won't be modified.
if exist('freq')
    freq = [1 3 5 10 15 20 25]*1e6;
end

% FILENAMES - these are important as they are used in the calibration.
if 'external_filename_specification'
    % Parallel plate data files. If the substrate is being measured, label it
    % as 'subs' when prompted for a descriptor - it will then be saved in the
    % reference file for the cylindrical calibration.

    % Data from single parallel plate measurement.
    pp_save_fname = ['pp_data_' date '.mat'];
    % Reference material properties for calibration.
    ref_save_fname = 'ref_save.mat';

    % Repeatability data for cylinder characterisation. The filename must
    % contain either 'before' or 'after', and have the same format otherwise.
    save_fname_rep = 'repdata_before.mat';

    % Cylindrical measured data
    % cyl_save_fname = ['cyl_data_' date '.mat'];
    cyl_save_fname = 'cyldata.mat';

% ----- Initialise Files ----- %
% Initialize all the files if they don't exist:
if exist('backup.mat', 'file') ~= 2
    save backup freq;
end
if exist(aval('cyl_save_fname'), 'file') ~= 2
    eval(['save ' cyl_save_fname ' freq;']);
end
% ----- %

% ----- %
% Calibrated material properties
% cal_matprop_fname = ['matprop_' date '.mat'];
% cal_matprop_fname = 'caldata.mat';

% STRING designation of MATERIAL to be calibrated - the variable
% Z_cal_mat_str must be in the file cyl_save_fname.
if do_calibration
    cal_mat_str = mat_str;
end

% ----- %
% ----- Parallel Plate Measurement ----- %
% ----- %

if do_parallel_plate_measurement
```

```

% This section can be used either for the measurement of any prepared
% MUT sample, but is also specifically designed for the characterisation of
% the standard materials used in the cylindrical capacitor characterisation
% and calibration. The difference in the latter case is that the user is
% prompted for the two reference materials used as standards in the
% cylindrical calibration. These materials' properties are then saved in a
% .mat file used in the cylindrical calibration.

measure_single = 1;
measure_standards = 0;
only_calibrate = 0; % If calibration with existing data is desired...

% In either case, the measurement sequence is initiated by the measurement
% of an OPEN and SHORT standard. This should be done once per measuring
% session - if the variables 'Z_open' and 'Z_short' are not present, it will
% be assumed that these measurements have not been performed yet and they
% will be.

% The number of repetitions for each measurement can be changed by setting
% 'num_reps'. The default is 5; using less is not recommended but using
% more may result in a more accurate measurement.

num_reps = 5;

if ~only_calibrate

    % For display purposes:
    if num_reps > 1
        meas_str = 'measurements'; else meas_str = 'measurement';
    end

    % ----- %
    % First, open LCR meter link and adjust its settings if required.
    lcr = openlcr; % opens link
    if ~exist('settings_done')
        LCR_setup(lcr); % performs setup - see 'LCR_setup.m' for options
        settings_done = 1;
    end

    % ----- %
    % Now, conduct OPEN and SHORT measurement sequences.
    if ~exist('Z_open')
        disp('-----');
        disp(['Conducting ' num2str(num_reps) ' OPEN ' meas_str '.']);
        % Conduct measurement - for options consult 'LCR_measure.m'.
        [Cp_open, D_open] = LCR_measure(lcr, 'meas_rep', 'multier',...
            'num_meas', num_reps);
        Z_open = cpd2z(Cp_open, D_open, freq);
        save backup freq Z_open -append; % backup save
    end

    if ~exist('Z_short')
        disp('-----');
        disp(['Conducting ' num2str(num_reps) ' SHORT ' meas_str '.']);
        % Conduct measurement - for options consult 'LCR_measure.m'.
        [Cp_short, D_short] = LCR_measure(lcr, 'meas_rep', 'multier',...
            'num_meas', num_reps);
        Z_short = cpd2z(Cp_short, D_short, freq);
        save backup freq Z_short -append; % backup save
    end

    % ----- %
    % Now we must either conduct a single measurement or measure all the
    % standards.

    if measure_single
        disp('-----');
        disp('Conducting single material measurement. ');
        disp('-----');
        mat_str = input('Please enter material descriptor: ');
        d_dut(1) = input('Please enter maximum thickness of sample [mm]: ');
        d_dut(2) = input('Please enter minimum thickness of sample [mm]: ');
        eval(['d_dut.' mat_str ' = d_dut/1e3;']); % convert from mm to m
        disp('-----');
        disp(['Conducting ' num2str(num_reps) ' ' meas_str ' of ' ' ...
            mat_str ' ' ' ']);
        % conduct measurement
        [Cp, D] = LCR_measure(lcr, 'meas_rep', 'multier',...
            'num_meas', num_reps);
        eval(['Z.' mat_str ' = cpd2z(Cp, D, freq);']);
        eval(['save backup Z.' mat_str ' -append;']); % backup save

        % air measurement
        disp('-----');
        disp('Please set spacers and remove sample. ');
        disp(['Conducting ' num2str(num_reps) ' air ' meas_str '.']);
        [Cp, D] = LCR_measure(lcr, 'meas_rep', 'multier',...
            'num_meas', num_reps);
        eval(['Z_air.' mat_str ' = cpd2z(Cp, D, freq);']);
        eval(['save backup Z_air.' mat_str ' -append;']); % backup save
        clear Cp D d_dut;

    elseif measure_standards
        disp('-----');
        disp('Conducting reference material measurements. ');
        disp('-----');
        % --- 1st reference material --- %
        disp('-----');
        disp('Please insert 1st reference material. ');
        d_dut(1) = input('Please enter maximum thickness of sample [mm]: ');
        d_dut(2) = input('Please enter minimum thickness of sample [mm]: ');
        d_dut_ref1 = d_dut/1e3; % convert from mm to m
        disp('-----');
        disp(['Conducting ' num2str(num_reps) ' ' meas_str ' ...
            ' of 1st reference material.']);
        % conduct measurement
        [Cp, D] = LCR_measure(lcr, 'meas_rep', 'multier',...
            'num_meas', num_reps);
        Z_pp_ref1 = cpd2z(Cp, D, freq);
        save backup Z_pp_ref1 d_dut_ref1 -append; % backup save

        % air measurement
        disp('-----');
        disp('Please set spacers and remove sample. ');
        disp(['Conducting ' num2str(num_reps) ' air ' meas_str '.']);

        [Cp, D] = LCR_measure(lcr, 'meas_rep', 'multier',...
            'num_meas', num_reps);
        Z_pp_ref2 = cpd2z(Cp, D, freq);
        save backup Z_pp_ref2 d_dut_ref2 -append; % backup save
        clear Cp D d_dut;

        % --- 2nd reference material --- %
        disp('-----');
        disp('Please insert 2nd reference material. ');
        d_dut(1) = input('Please enter maximum thickness of sample [mm]: ');
        d_dut(2) = input('Please enter minimum thickness of sample [mm]: ');
        d_dut_ref2 = d_dut/1e3; % convert from mm to m
        disp('-----');
        disp(['Conducting ' num2str(num_reps) ' ' meas_str ' ...
            ' of 1st reference material.']);
        % conduct measurement
        [Cp, D] = LCR_measure(lcr, 'meas_rep', 'multier',...
            'num_meas', num_reps);
        Z_pp_ref2 = cpd2z(Cp, D, freq);
        save backup Z_pp_ref2 d_dut_ref2 -append; % backup save

        % air measurement
        disp('-----');
        disp('Please set spacers and remove sample. ');
        disp(['Conducting ' num2str(num_reps) ' air ' meas_str '.']);
        [Cp, D] = LCR_measure(lcr, 'meas_rep', 'multier',...
            'num_meas', num_reps);
        Z_pp_ref2 = cpd2z(Cp, D, freq);
        save backup Z_pp_ref2 d_dut_ref2 -append; % backup save
        clear Cp D d_dut;

    end

    % ----- %
    % Close the link to the LCR meter:
    closelcr(lcr);

    % ----- %
    % Finally, the CALIBRATION to obtain the material properties of the
    % measured materials is performed using the function 'PP_calibrate.m'.
    % Again, either the material properties of the single material are
    % calculated if measure_single = 1, or those of the reference
    % materials. In either case, the properties are saved in the filename
    % specified above.
    %
    % A figure of the resulting properties with errorbars denoting the
    % standard deviations of the measurements is produced. Make sure that
    % the variables exist in the workspace!

    if exist('Z_short') & exist('Z_open')
        if measure_single % in this case Z_mat_str must exist
            eval(['' save ' pp_save_fname ' *eper_err* *tand_err* mat_str ...
                ' , eper_err.' mat_str ' , tand_err.' mat_str ' ' ' ...
                ' PP_calibrate(Z_open, Z_short, Z.' mat_str ...
                ' , Z_air.' mat_str ' , d_dut.' mat_str ' , freq);']);
            % If substrate is being measured, store data in correct format.
            if mat_str(1:4) == 'subs'
                deper_subs = eper_err_subs; dtand_subs = tand_err_subs;
                eval(['save ' ref_save_fname ' Z* *eper_subs *tand_subs' ...
                    ' -append;']);
            end
            % Save that data:
            eval(['save ' pp_save_fname ' *eper* *tand* -append;']);
        elseif measure_standards % in this case Zref1 and Zref2 exist
            [eper1, tand1, deper1, dtand1] = ...
                PP_calibrate(Z_open, Z_short, Z_pp_ref1, Z_air_pp_ref1, ...
                    d_dut_ref1, freq);
            [eper2, tand2, deper2, dtand2] = ...
                PP_calibrate(Z_open, Z_short, Z_pp_ref2, Z_air_pp_ref2, ...
                    d_dut_ref2, freq);
            % Save that data:
            eval(['save ' ref_save_fname ' Z* *eper* *tand* -append;']);
        end

        % ----- %
        % And plot the results...

        if measure_single % in this case Z_mat_str must exist
            figure;
            subplot(2,1,1); hold on; grid;
            eval(['errorbar(freq/1e6, eper.' mat_str ...
                ' , eper_err.' mat_str ' , eper_err.' mat_str ' , 'k-s');']);
            ylabel('epsilon_r');
            title(['Measured properties of ' num2str(num_reps) ...
                ' samples of ' ' strrep(mat_str, ' ', '-') ' ' date]);
            subplot(2,1,2); hold on; grid on;
            eval(['errorbar(freq/1e6, tand.' mat_str ...
                ' , tand_err.' mat_str ' , tand_err.' mat_str ' , 'k-s');']);
            ylabel('tan/delta'); xlabel('frequency [MHz]');

        elseif measure_standards % in this case Zref1 and Zref2 exist
            figure; % 1st reference material
            subplot(2,1,1); hold on; grid;
            errorbar(freq/1e6, eper1, deper1, 'k-s');
            ylabel('epsilon_r');
            title(['Measured properties of ' num2str(num_reps) ...
                ' samples of 1st reference material - ' date]);
            subplot(2,1,2); hold on; grid on;
            errorbar(freq/1e6, tand1, dtand1, 'k-s');
            ylabel('tan/delta'); xlabel('frequency [MHz]');

            figure; % 2nd reference material
            subplot(2,1,1); hold on; grid;
            errorbar(freq/1e6, eper2, deper2, 'k-s');
            ylabel('epsilon_r');
            title(['Measured properties of ' num2str(num_reps) ...
                ' samples of 2nd reference material - ' date]);
            subplot(2,1,2); hold on; grid on;
            errorbar(freq/1e6, tand2, dtand2, 'k-s');
            ylabel('tan/delta');
            xlabel('frequency [MHz]');
        end

    end
end

```



```

% -----
% ----- Pre-characterisation -----
% -----
if do_pre_characterisation

% This section performs the pre-characterisation measurement of the
% cylindrical probe. This involves the measurement of the three
% reference samples, consisting of the two materials measured by the
% parallel plate and an artificial dielectric constructed from the 2nd
% reference material, and a specifiable number of rock samples.
% Measurements are conducted using 'LCR_measure.m', and the
% pre-characterisation data is saved in the specified file so that it
% can be loaded later when the calibration is done.

num_rock_samples = 2; % no. of rock samples used as repeatability tests
num_reps = 5; % default number of repetitions -
% again, don't use less than 5

% The geometry of the device must be entered manually here as well:

geometry.l = 20e-3; % centre electrode length
geometry.phi0 = 100; % nominal centre electrode arc coverage
geometry.g = 0.15e-3; % guard-centre gap
geometry.d_sub = 0.05e-3; % thickness of substrate
geometry.R_nom = 41.7e-3/2; % nominal radius of standards
geometry.R_core = 41.7e-3/2; % actual radius of core being measured

% Artificial dielectric dimensions.
geometry.b_artdiel = 41.7e-3/2; % outer radius
geometry.a_artdiel = 27.8e-3/2; % inner (conductor) radius

% Check that filename is correct - it must contain 'after':
if isempty(findstr(save_fname_rep, 'before'))
    save_fname_rep = strrep(save_fname_rep, 'after', 'before');
end

% For display purposes:
if num_reps > 1
    meas_str = 'measurements'; else meas_str = 'measurement';
end

% -----
% First, open LCR meter link and adjust its settings if required.
lcr = openlcr; % opens link
if ~exist('settings_done')
    LCR_setup(lcr); % performs setup - consult 'LCR_setup.m' for options
    settings_done = 1;
end

% -----
% Perform the pre-characterisation measurements. The first set is done
% in order, first using the 3 reference materials, then the rock
% samples. For the remaining sets, the measurement order is randomised.

% add the three references to the rock samples
num_rep_samples = num_rock_samples + 3;

rep_order = 1:num_rep_samples;
% loop for cycles of rep. measurements
disp('-----');
disp(['Will now conduct ' num2str(num_reps) ' measurement sets of ' ...
    num2str(num_rep_samples) ' repeatability samples. The first three' ...
    ' samples should be the three standard materials, with material 3' ...
    ' the artificial dielectric constructed using material 2. Following' ...
    ' a first set of measurements, during which the order will be' ...
    ' prompted for material descriptors, the order is randomised for the' ...
    ' remaining ' num2str(num_reps-1) ' sets.']);
disp('-----');
for n = 1:num_reps
    % loop for number of rep. measurements in each cycle
    disp('-----');
    disp(['Repeatability measurements sequence no. ' num2str(n) ...
        ' of ' num2str(num_reps) '']);
    disp('-----');
    for a = 1:num_rep_samples
        if a == 1
            if n == 1 | 2 | 3
                disp(['This should be repeatability sample no. ' num2str(a)]);
            end
            eval(['mstr' num2str(n) ' = input(''Enter descriptor for' ...
                ' repeatability sample no. ' num2str(n) ' ');']);
            % get core diameter
            eval(['R_core_' num2str(n) ' = input(''Enter diameter of sample [mm]: ' ');']);
            % convert to m
            eval(['R_core_' num2str(n) ' = R_core_' num2str(n) ' / 2e3;']);
        else
            eval(['disp(''Please insert ' ...
                ' ' num2str(rep_order(n)) ' sample.' ');']);
            end
            % conduct measurement
            [Cp, D] = LCR_measure(lcr, 'meas_rep', 'multir', 'num_meas', 1);
            Z = cpd2z(Cp, D, freq);
            eval(['Cp_mstr' num2str(rep_order(n)) ...
                ' (:,m) = Cp; D_mstr' num2str(rep_order(n)) ' (:,m) = D;']);
            eval(['Z_mstr' num2str(rep_order(n)) ' (:,m) = Z;']);
        end
        % randomize order of next series of samples
        rep_order_old = rep_order;
        rep_order = randperm(num_rep_samples);
        % next set 1st sample must not = last of previous
        if rep_order(1) == rep_order_old(num_rep_samples)
            rep_order = randperm(num_rep_samples);
        end
        clear rep_order_old;
    end
end

% -----
% Close the link to the LCR meter:
closelcr(lcr);

% -----
% Save the data

clear Cp D Z;
if exist('save_fname_rep', 'file')
    save_fname_rep = input('File ' save_fname_rep ...
        ' already exists, please enter alternative file name: ');
else
    eval(['save ' save_fname_rep ' Cp* D* Z* mat* num_rep* samples* geometry']);
end

% -----
% Plot the results to give an immediate idea of how the test went.
plotstyle = ['brkqcm'];
mstr = '';
figure;
subplot(2,1,1); hold on; grid on;
for n = 1:num_rep_samples
    eval(['h' num2str(n) ' = errorbar(freq/1e6, mean(Cp_mstr' num2str(n) ...
        ' ' num2str(n) ' ' ' ' min(Cp_mstr' num2str(n) ...
        ' ' num2str(n) ' ' ' ' max(Cp_mstr' num2str(n) ...
        ' ' num2str(n) ' ' ' ' -mean(Cp_mstr' num2str(n) ...
        ' ' num2str(n) ' ' ' ' ');']);
    eval(['h(n) = h' num2str(n) ' (1);']);
    eval(['mstr = strvcat(mstr, mstr' num2str(n) ' ');']);
end
ylabel('Cp');
title(['repeatability of ' num2str(num_rep_samples) ' samples, measured ' ...
    num2str(num_reps) ' times']);
subplot(2,1,2); hold on; grid on;
for n = 1:num_rep_samples
    eval(['errorbar(freq/1e6, mean(D_mstr' num2str(n) ' ' ' ' mean(D_mstr' ...
        num2str(n) ' ' ' ' -min(D_mstr' num2str(n) ' ' ' ' max(D_mstr' ...
        num2str(n) ' ' ' ' -mean(D_mstr' num2str(n) ' ' ' ' '); plotstyle(n);']);
end
xlabel('frequency [MHz]'); ylabel('D');
legend(h, mstr);

end

% -----
% ----- Sample Measurement -----
% -----
if do_measurement

% This section performs the measurement along a single sample. The
% sample should always be passed through the cylinder gently, without
% exerting any unnecessary pressure on the device. Measurement should
% commence and cease while an unbroken section of the sample completely
% covers the centre electrode. Data is saved in the specified filename.

% -----
% First, open LCR meter link and adjust its settings if required.
lcr = openlcr; % opens link
if ~exist('settings_done')
    LCR_setup(lcr); % performs setup - consult 'LCR_setup.m' for options
    settings_done = 1;
end

% -----
% Commence measurement.
disp('-----');
disp('Measuring along a single sample. ');
mat_str = input('Please enter material descriptor: ');
geometry.R_core = input('Please enter diameter of core [mm]: ');
eval(['geometry.R_core_' mat_str ' = geometry.R_core/1e3;']);
% perform repeated measurement
[Cp, D] = LCR_measure(lcr, 'meas_rep', 'multip');
Z = cpd2z(Cp, D, freq);
% save data
if eval(['exist('Cp_' mat_str ' ' ' ')] == 1
    eval(['Cp_' mat_str ' = [Cp_' mat_str ' , Cp;']);
    eval(['D_' mat_str ' = [D_' mat_str ' , D;']);
    eval(['Z_' mat_str ' = [Z_' mat_str ' , Z;']);
else
    eval(['Cp_' mat_str ' = Cp; D_' mat_str ' = D; Z_' mat_str ' = Z;']);
end

% -----
% Close the link to the LCR meter:
closelcr(lcr);

% -----
% Save the data.
eval(['save ' cyl_save_fname ' Z* Cp* D* -append;']);

end

% -----
% ----- Post-characterisation -----
% -----
if do_post_characterisation

% This section performs the post-characterisation measurement of the
% cylindrical probe. This involves the measurement of the three
% reference samples, consisting of the two materials measured by the
% parallel plate and an artificial dielectric constructed from the 2nd
% reference material, and a specifiable number of rock samples.
% Measurements are conducted using 'LCR_measure.m', and the
% post-characterisation data is saved in the specified file so that it
% can be loaded later when the calibration is done. The geometry has
% already been saved in the pre-characterisation data file.

num_rock_samples = 1; % number of rock samples used as repeatability tests -
% must be same as for pre-characterisation
num_reps = 5; % default number of repetitions - again, don't use less

% Check that filename is correct - it must contain 'after':
if isempty(findstr(save_fname_rep, 'after'))
    save_fname_rep = strrep(save_fname_rep, 'before', 'after');
end

```

```

% For display purposes:
if num_reps > 1
    meas_str = 'measurements'; else meas_str = 'measurement';
end

% ----- %
% First, open LCR meter link and adjust its settings if required.
lcr = openlcr; % opens link
if ~exist('settings_done')
    LCR_setup(lcr); % performs setup - consult 'LCR_setup.m' for options
    settings_done = 1;
end

% ----- %
% Perform the pre-characterisation measurements. The first set is done
% in order, first using the 3 reference materials, then the rock
% samples. For the remaining sets, the measurement order is randomised.

% add the three references to the rock samples
num_rep_samples = num_rock_samples + 3;

rep_order = 1:num_rep_samples;
% loop for cycles of rep. measurements
disp('-----');
disp(['Will now conduct ' num2str(num_reps) ' measurement sets of ' ...
    num2str(num_rep_samples) ' repeatability samples. The first three' ...
    ' samples should be the three standard materials, with material 3' ...
    ' the artificial dielectric constructed using material 2. Following' ...
    ' a first set of measurements, during which the user will be' ...
    ' prompted for material descriptors, the order is randomised for the' ...
    ' remaining ' num2str(num_reps-1) ' sets.']);
disp('-----');
for m = 1:num_reps
    % loop for number of rep. measurements in each cycle
    disp('-----');
    disp(['Repeatability measurements sequence no. ' num2str(m) ...
        ' of ' num2str(num_reps) ' sets.']);
    disp('-----');
    for n = 1:num_rep_samples
        if m == 1
            if n == 1 | 2 | 3
                disp(['This should be repeatability sample no. ' num2str(n)]);
                eval(['mstr' num2str(n) ' = input('Enter descriptor' ...
                    ' for repeatability sample no. ' num2str(n) ': ');']);
                % get core diameter
                eval(['R_core_' num2str(n) ' = input('Enter diameter of sample [mm]: ');']);
                % convert to m
                eval(['R_core_' num2str(n) ' = R_core_' num2str(n) ' / 2e3;']);
            else
                eval(['disp('Please insert ' ...
                    ' 'mstr' num2str(rep_order(n)) ' sample. ');']);
            end
            % conduct measurement
            [Cp, D] = LCR_measure(lcr, 'meas_rep', 'multir', 'num_meas', 1);
            Z = cpd2z(Cp, D, freq);
            eval(['Cp_mstr' num2str(rep_order(n)) '(:,m) = Cp; D_mstr' ...
                num2str(rep_order(n)) '(:,m) = D;']);
            eval(['Z_mstr' num2str(rep_order(n)) '(:,m) = Z;']);
        end
        % randomize order of next series of samples
        rep_order_old = rep_order;
        rep_order = randperm(num_rep_samples);
        % next set 1st sample must not = last of previous
        if rep_order(1) == rep_order_old(num_rep_samples)
            rep_order = randperm(num_rep_samples);
        end
        clear rep_order_old;
    end
end

% ----- %
% Close the link to the LCR meter:
closelcr(lcr);

% ----- %
% Save the data
clear Cp D Z;
if exist('save_fname_rep', 'file')
    save_fname_rep = input(['File ' save_fname_rep ...
        ' already exists, please enter alternative file name: ']);
    eval(['save ' save_fname_rep ' Cp* D* Z* mstr' num_rep_samples']);
else
    eval(['save ' save_fname_rep ' Cp* D* Z* mstr' num_rep_samples']);
end

% ----- %
% Plot the results to give an immediate idea of how the test went.
plotstyle = ['brkgcm'];
mstr = '';
figure;
subplot(2,1,1); hold on; grid on;
for n = 1:num_rep_samples
    eval(['h' num2str(n) ' = errorbar(freq/ie6, mean(Cp_mstr' ...
        num2str(n) '),'', mean(Cp_mstr' num2str(n) ...
        '),'', min(Cp_mstr' num2str(n) '),'', max(Cp_mstr' ...
        num2str(n) '),'', mean(D_mstr' num2str(n) ...
        '),'', plotstyle(n));']);
    eval(['h(n) = h' num2str(n) '(1);']);
    eval(['mstr = strvc(mstr, mstr' num2str(n) ' ');']);
end
ylabel('Cp');
title(['Repeatability of ' num2str(num_rep_samples) ' samples, measured ' ...
    num2str(num_reps) ' times']);
subplot(2,1,2); hold on; grid on;
for n = 1:num_rep_samples
    eval(['errorbar(freq/ie6, mean(D_mstr' num2str(n) '),'', mean(D_mstr' ...
        num2str(n) '),'', min(D_mstr' num2str(n) '),'', max(D_mstr' ...
        num2str(n) '),'', mean(D_mstr' num2str(n) '),'', plotstyle(n));']);
end
xlabel('frequency [MHz]'); ylabel('D');
legend(h, mstr);

end

% ----- %
% ----- % Calibration ----- %
% ----- %

if do_calibration

    % Now the calibration is performed. It is important that this is the
    % final step in the process. All the data from the previous sections
    % must be available, contained in the various filenames mentioned
    % above.

    % ----- %
    % First calculate the means and uncertainties of the reference
    % standards' impedance values. Loading the 'before' repeatability data
    % also loads the geometry structure.

    % Which file exists - we want to load the data from both the 'before'
    % and 'after' files.
    if isempty(findstr(save_fname_rep, 'after')) % is it the 'before' file?
        % do both files exist?
        if exist(strrep(save_fname_rep, 'before', 'after'), 'file')
            % if yes, load both
            eval(['load ' save_fname_rep]);
            for n = 1:num_rep_samples
                eval(['Zref' num2str(n) ' = Z_mstr' num2str(n) ' ;']);
            end
            % load second file, then add measurements
            eval(['load ' strrep(save_fname_rep, 'before', 'after')]);
            for n = 1:num_rep_samples
                eval(['Zref' num2str(n) ' = [Zref' num2str(n) ' , Z_mstr' ...
                    num2str(n) ' ] ;']);
            end
        else % load only the before file
            disp('Problem: only a ''before'' repeatability test conducted. ');
            disp('It is recommended to do both a ''before'' and ''after'' test. ');
            eval(['load ' save_fname_rep]);
            for n = 1:num_rep_samples
                eval(['Zref' num2str(n) ' = Z_mstr' num2str(n) ' ;']);
            end
        end
    else % it is the 'after' file, in which case both must be present
        % if yes, load both
        eval(['load ' eval('save_fname_rep')]);
        for n = 1:num_rep_samples
            eval(['Zref' num2str(n) ' = Z_mstr' num2str(n) ' ;']);
        end
        % load second file, then add measurements
        eval(['load ' strrep(eval('save_fname_rep'), 'before', 'after')]);
        for n = 1:num_rep_samples
            eval(['Zref' num2str(n) ' = [Zref' num2str(n) ' , Z_mstr' ...
                num2str(n) ' ] ;']);
        end
    end

    % Now we have Zref1, 2 and 3. Get the means and spreads.
    Zor1 = mean(Zref1.' ');
    Zor2 = mean(Zref2.' ');
    Zor3 = mean(Zref3.' ');

    % Calculate the uncertainty in each reference value as the complex
    % standard deviation - must separate into real and imag parts - can use
    % function cstd.m
    %
    % The uncertainty evaluation is of type A by default, but should be of
    % type B if too few measurements are available.
    if size(Zref1,2) >= 10
        dZor1 = cstd(Zref1,2)/sqrt(size(Zref1,2));
        dZor2 = cstd(Zref2,2)/sqrt(size(Zref2,2));
        dZor3 = cstd(Zref3,2)/sqrt(size(Zref3,2));
    else
        dZor1 = (1/12)*(max(Zref1.'') - min(Zref1.'')).^2;
        dZor2 = (1/12)*(max(Zref2.'') - min(Zref2.'')).^2;
        dZor3 = (1/12)*(max(Zref3.'') - min(Zref3.'')).^2;
    end

    % Also need the mean and spread of the rock measurements.
    eval(['Z_dut = Z_ mat_str ']);
    dZor = []; % initialize
    for n = 4:num_rep_samples
        if size(Zref1,2) >= 10 % Type A uncertainty evaluation
            eval(['dZor' num2str(n) ' = cstd(Zref' num2str(n) ...
                ' ,2)/sqrt(size(Zref' num2str(n) ' ,2));']);
        else % Type B uncertainty evaluation
            eval(['dZor' num2str(n) ' = (1/12)*(max(Zref' num2str(n) ...
                ' ,)' - min(Zref' num2str(n) ' ,)').^2;']);
        end
        eval(['dZor = [dZor, dZor' num2str(n) ' ] ;']);
    end

    if num_rep_samples > 4
        % estimated repeatability of rocks taken as maximum of those measured
        dZ_dut = max([dZor]');
    else
        dZ_dut = dZor; % if only 1 rock repeatability sample used
    end

    % ----- %
    % Now calculate the means and uncertainties of the standard material
    % properties. This should also contain the substrate properties.

    eval(['load ' eval('ref_save_fname')]);
    % We now have epsr1,2 and deper1,2, tand1,2 and dtand1,2, and the
    % substrate properties.

    % Artificial Dielectric - dimensions defined and saved during
    % pre-characterisation.
    a = geometry.a_artdiel; b = geometry.b_artdiel;

    % separate at each freq. point
    eps2 = [epsr2, tand2];
    for m = 1:length(eps2)
        eps_eff(m) = eps_multilayer([eps2(m,:); [0 0]], ...
            [b; a], geometry.l, geometry.phio/2, 4.6, 100);
    end
end

```

```

epsr3 = real(eps_eff);
tand3 = (-imag(eps_eff)./real(eps_eff));

% must calculate error in epsr and tand of artid1
% only need to do epsr up and down; tand error will be same
% hi
eps2_hi = [epsr2+depr2, tand2];
for m = 1:length(eps2)
    eps_eff_hi(m) = eps_multilayer([eps2_hi(m,:); [0 0]], ...
    [b; a], 20e-3, 50, 4.5, 100);
end
epsr3_hi = real(eps_eff_hi);
% lo
eps2_lo = [epsr2-depr2, tand2];
for m = 1:length(eps2)
    eps_eff_lo(m) = eps_multilayer([eps2_lo(m,:); [0 0]], ...
    [b; a], 20e-3, 50, 4.6, 100);
end
epsr3_lo = real(eps_eff_lo);

% sensitivity
c_epsr3_eps2 = (epsr3_hi-epsr3_lo)/(2*depr2);

% uncertainty in epsr3 and tand3
depr3 = c_epsr3_eps2 .* depr2;
dtand3 = dtand2;

% ----- %
% Save all the data into the correct file - the variables required are
% listed in 'Cyl_calibrate.m'.
save caldata Zor1 Zor2 Zor3 dZor1 dZor2 dZor3 dZ_dut ...
    epsr1 epsr2 epsr3 tand1 tand2 tand3 depr1 depr2 depr3 ...
    dtand1 dtand2 dtand3 ...
    geometry epsr_subs tand_subs depr_subs dtand_subs;

% ----- %
% Do the calibration.
[epsr, tand, epsr_err, tand_err, W] = ...
    Cyl_calibrate(Z_dut, 'caldata.mat', geometry, freq);

% ----- %
% Calculate the attenuation factor and propagation velocity - want
% means and uncertainties here as well.
eps0 = 8.854e-12; mu0 = 4e-7*pi;
for n = 1:length(freq)
    % means
    alpha(n,:) = 2*pi*sqrt(eps0*mu0*freq(n)^2) * (epsr(n,:)/2 .* ...
    (sqrt(1+tand(n,:).^2)-1)).^(1/2);

    v(n,:) = (eps0*mu0)^(-1/2)*(epsr(n,:)/2 .* (sqrt(1+tand(n,:).^2)+1)).^(-1/2);

    % uncertainties
    alpha_epsr_hi(n,:) = 2*pi*sqrt(eps0*mu0*freq(n)^2) * ...
    ((epsr(n,:)+epsr_err(n,:))/2 .* (sqrt(1+tand(n,:).^2)+1)).^(1/2);
    alpha_epsr_lo(n,:) = 2*pi*sqrt(eps0*mu0*freq(n)^2) * ...
    ((epsr(n,:)-epsr_err(n,:))/2 .* (sqrt(1+tand(n,:).^2)+1)).^(1/2);
    alpha_tand_hi(n,:) = 2*pi*sqrt(eps0*mu0*freq(n)^2) * ...
    ((epsr(n,:)/2 .* (sqrt(1+tand(n,:)+tand_err(n,:).^2)-1)).^(1/2);
    alpha_tand_lo(n,:) = 2*pi*sqrt(eps0*mu0*freq(n)^2) * ...
    ((epsr(n,:)/2 .* (sqrt(1+tand(n,:)-tand_err(n,:).^2)-1)).^(1/2);
    v_epsr_hi(n,:) = (eps0*mu0)^(-1/2) * ...
    ((epsr(n,:)+epsr_err(n,:))/2 .* (sqrt(1+tand(n,:).^2)+1)).^(-1/2);
    v_epsr_lo(n,:) = (eps0*mu0)^(-1/2) * ...
    ((epsr(n,:)-epsr_err(n,:))/2 .* (sqrt(1+tand(n,:).^2)+1)).^(-1/2);
    v_tand_hi(n,:) = (eps0*mu0)^(-1/2) * ...
    ((epsr(n,:)/2 .* (sqrt(1+tand(n,:)+tand_err(n,:).^2)+1)).^(-1/2);
    v_tand_lo(n,:) = (eps0*mu0)^(-1/2) * ...
    ((epsr(n,:)/2 .* (sqrt(1+tand(n,:)-tand_err(n,:).^2)+1)).^(-1/2);

end

% sensitivities
c_alpha_epsr = (alpha_epsr_hi - alpha_epsr_lo)/(2*epsr_err);
c_alpha_tand = (alpha_tand_hi - alpha_tand_lo)/(2*tand_err);
c_v_epsr = (v_epsr_hi - v_epsr_lo)/(2*epsr_err);
c_v_tand = (v_tand_hi - v_tand_lo)/(2*tand_err);

% total uncertainty in alpha and v
alpha_err = abs(sqrt((c_alpha_epsr.*epsr_err).^2 + (c_alpha_tand.*tand_err).^2));
v_err = abs(sqrt((c_v_epsr.*epsr_err).^2 + (c_v_tand.*tand_err).^2));

% ----- %
% Save calibrated data.
eval(['epsr.' cal_mat_str ' = epsr;']);
eval(['tand.' cal_mat_str ' = tand;']);
eval(['alpha.' cal_mat_str ' = alpha;']);
eval(['v.' cal_mat_str ' = v;']);
eval(['epsr_err.' cal_mat_str ' = epsr_err;']);
eval(['tand_err.' cal_mat_str ' = tand_err;']);
eval(['alpha_err.' cal_mat_str ' = alpha_err;']);
eval(['v_err.' cal_mat_str ' = v_err;']);

eval(['save' cal_matprop_fname ' epsr.' cal_mat_str, ' tand.' cal_mat_str, ...
    ' alpha.' cal_mat_str, ' v.' cal_mat_str, ' epsr_err.' cal_mat_str, ...
    ' tand_err.' cal_mat_str, ' alpha_err.' cal_mat_str, ...
    ' v_err.' cal_mat_str;']);

end

```

D.2 *cyl_calibrate.m*

```

function [epsr,tand,epsr_err,tand_err,W] = ...
    Cyl_calibrate(Z_dut, fname, geometry, freq)

% function [epsr, tand, epsr_err, tand_err] = ...
%     Cyl_calibrate(Z_dut, fname, R_core, freq)
%
% This function performs the calibration of cylindrical capacitor measurements
% performed with the LCR meter. The measured DUT impedance is passed as an
% argument - data is arranged in columns, with each row corresponding to a
% frequency. Each column corresponds to a geometric point.
%
% The material properties and measured impedances of the standard materials
% are loaded from a file 'fname', containing the data in following format:
%
%   Zor1, Zor2, Zor3 - the three measured impedances, same format
%                     as Z_dut
%   dZor1, dZor2, dZor3 - the uncertainties in each of these
%   dZ_dut - estimate of the repeatability of rock
%             measurements
%   epsr1, epsr2, epsr3 - the three permittivities - the artificial
%                         is always the 3rd, constructed from material 2
%   tand1, tand2, tand3 - the three loss tangents
%   depr1, depr2, depr3 - uncertainties in all these
%   dtand1, dtand2, dtand3 - uncertainties in all these
%   epsr_subs, depr_subs - the permittivity of the substrate
%   tand_subs, dtand_subs - the loss tangent of the substrate
%
% The effect of the substrate is taken into account based on the actual core
% diameter R_core. The geometry of the electrode set as well as the
% substrate are passed to this function in the structure 'geometry'.
%
% The values returned are the nominal epsr and tand, and the errors if they
% were calculated.
%
% Marc Ruetschlin, 2 Feb. 2004.

do_error_breakdown = 0; % whether to report the individual contributors to uncertainty

% turn frequency into a column vector
if size(freq,2) > 1
    freq = freq';
end

% file containing standard values
eval(['load ' fname]);

% convert geometry and substrate properties into correct format
epsr_subs = epsr_subs.*(1-j*tand_subs);

% do this for each point in the measured impedance vector
for n = 1:size(Z_dut,2)

    % use mean values for all these parameters
    [epsr(:,n), tand(:,n), W] = cal( ...
        [epsr1, epsr2, epsr3], ...
        [tand1, tand2, tand3], ...
        Z_dut(:,n), [Zor1, Zor2, Zor3], freq, geometry, eps_subs);

    % now for the uncertainty analysis %
    % effect of epsr1
    [epsr_epsr1_hi, tand_epsr1_hi] = cal( ...
        [epsr1+depr1, epsr2, epsr3], ...
        [tand1, tand2, tand3], ...
        Z_dut(:,n), [Zor1, Zor2, Zor3], freq, geometry, eps_subs);
    [epsr_epsr1_lo, tand_epsr1_lo] = cal( ...
        [epsr1-depr1, epsr2, epsr3], ...
        [tand1, tand2, tand3], ...
        Z_dut(:,n), [Zor1, Zor2, Zor3], freq, geometry, eps_subs);
    % uncertainty
    c_epsr_epsr1 = (epsr_epsr1_hi - epsr_epsr1_lo)/(2*depr1);
    c_tand_epsr1 = (tand_epsr1_hi - tand_epsr1_lo)/(2*depr1);
    d_epsr_epsr1(:,n) = c_epsr_epsr1 .* depr1;
    d_tand_epsr1(:,n) = c_tand_epsr1 .* depr1;

    % effect of tand1
    [epsr_tand1_hi, tand_tand1_hi] = cal( ...
        [epsr1, epsr2, epsr3], ...
        [tand1+dtand1, tand2, tand3], ...
        Z_dut(:,n), [Zor1, Zor2, Zor3], freq, geometry, eps_subs);
    [epsr_tand1_lo, tand_tand1_lo] = cal( ...
        [epsr1, epsr2, epsr3], ...
        [tand1-dtand1, tand2, tand3], ...
        Z_dut(:,n), [Zor1, Zor2, Zor3], freq, geometry, eps_subs);
    % uncertainty
    c_epsr_tand1 = (epsr_tand1_hi - epsr_tand1_lo)/(2*dtand1);
    c_tand_tand1 = (tand_tand1_hi - tand_tand1_lo)/(2*dtand1);
    d_epsr_tand1(:,n) = c_epsr_tand1 .* dtand1;
    d_tand_tand1(:,n) = c_tand_tand1 .* dtand1;

    % effect of epsr2
    [epsr_epsr2_hi, tand_epsr2_hi] = cal( ...
        [epsr1, epsr2+depr2, epsr3], ...
        [tand1, tand2, tand3], ...
        Z_dut(:,n), [Zor1, Zor2, Zor3], freq, geometry, eps_subs);
    [epsr_epsr2_lo, tand_epsr2_lo] = cal( ...
        [epsr1, epsr2-depr2, epsr3], ...
        [tand1, tand2, tand3], ...
        Z_dut(:,n), [Zor1, Zor2, Zor3], freq, geometry, eps_subs);
    % uncertainty
    c_epsr_epsr2 = (epsr_epsr2_hi - epsr_epsr2_lo)/(2*depr2);
    c_tand_epsr2 = (tand_epsr2_hi - tand_epsr2_lo)/(2*depr2);
    d_epsr_epsr2(:,n) = c_epsr_epsr2 .* depr2;
    d_tand_epsr2(:,n) = c_tand_epsr2 .* depr2;

    % first nominal values %

```



```

% effect of tand2
[epsr_tand2_hi, tand_tand2_hi] = cal( ...
    [epsr1, epsr2, epsr3], ...
    [tand1, tand2+dtand2, tand3], ...
    Z_dut(:,n), [Zor1, Zor2, Zor3], freq, geometry, eps_subs);
[epsr_tand2_lo, tand_tand2_lo] = cal( ...
    [epsr1, epsr2, epsr3], ...
    [tand1, tand2-dtand2, tand3], ...
    Z_dut(:,n), [Zor1, Zor2, Zor3], freq, geometry, eps_subs);
% uncertainty
c_epsr_tand2 = (epsr_tand2_hi - epsr_tand2_lo)/(2*dtand2);
c_tand_tand2 = (tand_tand2_hi - tand_tand2_lo)/(2*dtand2);
d_epsr_tand2(:,n) = c_epsr_tand2 .* dtand2;
d_tand_tand2(:,n) = c_tand_tand2 .* dtand2;

% effect of epsr3
[epsr_epsr3_hi, tand_epsr3_hi] = cal( ...
    [epsr1, epsr2, epsr3+depsr3], ...
    [tand1, tand2, tand3], ...
    Z_dut(:,n), [Zor1, Zor2, Zor3], freq, geometry, eps_subs);
[epsr_epsr3_lo, tand_epsr3_lo] = cal( ...
    [epsr1, epsr2, epsr3-depsr3], ...
    [tand1, tand2, tand3], ...
    Z_dut(:,n), [Zor1, Zor2, Zor3], freq, geometry, eps_subs);
% uncertainty
c_epsr_epsr3 = (epsr_epsr3_hi - epsr_epsr3_lo)/(2*depsr3);
c_tand_epsr3 = (tand_epsr3_hi - tand_epsr3_lo)/(2*depsr3);
d_epsr_epsr3(:,n) = c_epsr_epsr3 .* depsr3;
d_tand_epsr3(:,n) = c_tand_epsr3 .* depsr3;

% effect of tand3
[epsr_tand3_hi, tand_tand3_hi] = cal( ...
    [epsr1, epsr2, epsr3], ...
    [tand1, tand2, tand3+dtand3], ...
    Z_dut(:,n), [Zor1, Zor2, Zor3], freq, geometry, eps_subs);
[epsr_tand3_lo, tand_tand3_lo] = cal( ...
    [epsr1, epsr2, epsr3], ...
    [tand1, tand2, tand3-dtand3], ...
    Z_dut(:,n), [Zor1, Zor2, Zor3], freq, geometry, eps_subs);
% uncertainty
c_epsr_tand3 = (epsr_tand3_hi - epsr_tand3_lo)/(2*dtand3);
c_tand_tand3 = (tand_tand3_hi - tand_tand3_lo)/(2*dtand3);
d_epsr_tand3(:,n) = c_epsr_tand3 .* dtand3;
d_tand_tand3(:,n) = c_tand_tand3 .* dtand3;

% effect of Zor1
[epsr_Zor1_hi, tand_Zor1_hi] = cal( ...
    [epsr1, epsr2, epsr3], ...
    [tand1, tand2, tand3], ...
    Z_dut(:,n), [Zor1+dzor1, Zor2, Zor3], freq, geometry, eps_subs);
[epsr_Zor1_lo, tand_Zor1_lo] = cal( ...
    [epsr1, epsr2, epsr3], ...
    [tand1, tand2, tand3], ...
    Z_dut(:,n), [Zor1-dzor1, Zor2, Zor3], freq, geometry, eps_subs);
% uncertainty
c_epsr_Zor1 = (epsr_Zor1_hi - epsr_Zor1_lo)/(2*dzor1);
c_tand_Zor1 = (tand_Zor1_hi - tand_Zor1_lo)/(2*dzor1);
d_epsr_Zor1(:,n) = c_epsr_Zor1 .* dzor1;
d_tand_Zor1(:,n) = c_tand_Zor1 .* dzor1;

% effect of Zor2
[epsr_Zor2_hi, tand_Zor2_hi] = cal( ...
    [epsr1, epsr2, epsr3], ...
    [tand1, tand2, tand3], ...
    Z_dut(:,n), [Zor1, Zor2+dzor2, Zor3], freq, geometry, eps_subs);
[epsr_Zor2_lo, tand_Zor2_lo] = cal( ...
    [epsr1, epsr2, epsr3], ...
    [tand1, tand2, tand3], ...
    Z_dut(:,n), [Zor1, Zor2-dzor2, Zor3], freq, geometry, eps_subs);
% uncertainty
c_epsr_Zor2 = (epsr_Zor2_hi - epsr_Zor2_lo)/(2*dzor2);
c_tand_Zor2 = (tand_Zor2_hi - tand_Zor2_lo)/(2*dzor2);
d_epsr_Zor2(:,n) = c_epsr_Zor2 .* dzor2;
d_tand_Zor2(:,n) = c_tand_Zor2 .* dzor2;

% effect of Zor3
[epsr_Zor3_hi, tand_Zor3_hi] = cal( ...
    [epsr1, epsr2, epsr3], ...
    [tand1, tand2, tand3], ...
    Z_dut(:,n), [Zor1, Zor2, Zor3+dzor3], freq, geometry, eps_subs);
[epsr_Zor3_lo, tand_Zor3_lo] = cal( ...
    [epsr1, epsr2, epsr3], ...
    [tand1, tand2, tand3], ...
    Z_dut(:,n), [Zor1, Zor2, Zor3-dzor3], freq, geometry, eps_subs);
% uncertainty
c_epsr_Zor3 = (epsr_Zor3_hi - epsr_Zor3_lo)/(2*dzor3);
c_tand_Zor3 = (tand_Zor3_hi - tand_Zor3_lo)/(2*dzor3);
d_epsr_Zor3(:,n) = c_epsr_Zor3 .* dzor3;
d_tand_Zor3(:,n) = c_tand_Zor3 .* dzor3;

% effect of Z_dut (based on max repeatability of rocks)
[epsr_Z_dut_hi, tand_Z_dut_hi] = cal( ...
    [epsr1, epsr2, epsr3], ...
    [tand1, tand2, tand3], ...
    Z_dut(:,n)+dZ_dut, [Zor1, Zor2, Zor3], freq, geometry, eps_subs);
[epsr_Z_dut_lo, tand_Z_dut_lo] = cal( ...
    [epsr1, epsr2, epsr3], ...
    [tand1, tand2, tand3], ...
    Z_dut(:,n)-dZ_dut, [Zor1, Zor2, Zor3], freq, geometry, eps_subs);
% uncertainty
c_epsr_Z_dut = (epsr_Z_dut_hi - epsr_Z_dut_lo)/(2*dZ_dut);
c_tand_Z_dut = (tand_Z_dut_hi - tand_Z_dut_lo)/(2*dZ_dut);
d_epsr_Z_dut(:,n) = c_epsr_Z_dut .* dZ_dut;
d_tand_Z_dut(:,n) = c_tand_Z_dut .* dZ_dut;

% effect of epsr_subs
[epsr_epsr_subs_hi, tand_epsr_subs_hi] = cal( ...
    [epsr1, epsr2, epsr3], ...
    [tand1, tand2, tand3], ...
    Z_dut(:,n), [Zor1, Zor2, Zor3], freq, geometry, ...
    (epsr_subs+depsr_subs)*(1-j*tand_subs));
[epsr_epsr_subs_lo, tand_epsr_subs_lo] = cal( ...
    [epsr1, epsr2, epsr3], ...
    [tand1, tand2, tand3], ...
    Z_dut(:,n), [Zor1, Zor2, Zor3], freq, geometry, ...
    (epsr_subs-depsr_subs)*(1-j*tand_subs));
end

% Totals
epsr_err = sqrt(d_epsr_epsr1.^2 + d_epsr_tand1.^2 + ...
    d_epsr_epsr2.^2 + d_epsr_tand2.^2 + ...
    d_epsr_epsr3.^2 + d_epsr_tand3.^2 + ...
    d_epsr_Zor1.^2 + d_epsr_Zor2.^2 + d_epsr_Zor3.^2 + ...
    d_epsr_Z_dut.^2 + ...
    d_epsr_epsr_subs.^2 + d_epsr_tand_subs.^2);

tand_err = sqrt(d_tand_epsr1.^2 + d_tand_tand1.^2 + ...
    d_tand_epsr2.^2 + d_tand_tand2.^2 + ...
    d_tand_epsr3.^2 + d_tand_tand3.^2 + ...
    d_tand_Zor1.^2 + d_tand_Zor2.^2 + d_tand_Zor3.^2 + ...
    d_tand_Z_dut.^2 + ...
    d_tand_epsr_subs.^2 + d_tand_tand_subs.^2);

% Error breakdown:
if do_error_breakdown
    disp('Uncertainty contribution breakdown:');
    disp('-----');
    disp('max. uncertainty in epsr due to:');
    disp(['ref. mat. prop. epsr1 - ' num2str(max(abs(d_epsr_epsr1)))]);
    disp(['ref. mat. prop. epsr2 - ' num2str(max(abs(d_epsr_epsr2)))]);
    disp(['ref. mat. prop. epsr3 - ' num2str(max(abs(d_epsr_epsr3)))]);
    disp(['ref. mat. prop. tand1 - ' num2str(max(abs(d_epsr_tand1)))]);
    disp(['ref. mat. prop. tand2 - ' num2str(max(abs(d_epsr_tand2)))]);
    disp(['ref. mat. prop. tand3 - ' num2str(max(abs(d_epsr_tand3)))]);
    disp(['subs. mat. prop. epsr - ' num2str(max(abs(d_epsr_epsr_subs)))]);
    disp(['subs. mat. prop. tand - ' num2str(max(abs(d_epsr_tand_subs)))]);
    disp(['measured Z_std1 - ' num2str(max(abs(d_epsr_Zor1)))]);
    disp(['measured Z_std2 - ' num2str(max(abs(d_epsr_Zor2)))]);
    disp(['measured Z_std3 - ' num2str(max(abs(d_epsr_Zor3)))]);
    disp(['measured Z_dut - ' num2str(max(abs(d_epsr_Z_dut)))]);
    disp(['Total - ' num2str(max(abs(epsr_err)))]);
    disp('-----');
    disp('max. uncertainty in tand due to:');
    disp(['ref. mat. prop. epsr1 - ' num2str(max(abs(d_tand_epsr1)))]);
    disp(['ref. mat. prop. epsr2 - ' num2str(max(abs(d_tand_epsr2)))]);
    disp(['ref. mat. prop. epsr3 - ' num2str(max(abs(d_tand_epsr3)))]);
    disp(['ref. mat. prop. tand1 - ' num2str(max(abs(d_tand_tand1)))]);
    disp(['ref. mat. prop. tand2 - ' num2str(max(abs(d_tand_tand2)))]);
    disp(['ref. mat. prop. tand3 - ' num2str(max(abs(d_tand_tand3)))]);
    disp(['subs. mat. prop. epsr - ' num2str(max(abs(d_tand_epsr_subs)))]);
    disp(['subs. mat. prop. tand - ' num2str(max(abs(d_tand_tand_subs)))]);
    disp(['measured Z_std1 - ' num2str(max(abs(d_tand_Zor1)))]);
    disp(['measured Z_std2 - ' num2str(max(abs(d_tand_Zor2)))]);
    disp(['measured Z_std3 - ' num2str(max(abs(d_tand_Zor3)))]);
    disp(['measured Z_dut - ' num2str(max(abs(d_tand_Z_dut)))]);
    disp(['Total - ' num2str(max(abs(tand_err)))]);
    disp('-----');
end

epsr_err = abs(epsr_err);
tand_err = abs(tand_err);

% This function returns nominal values for epsr(:,n) and tand(:,n) only - the
% function can be used to calculate uncertainty by calling it with, e.g.
% [epsr1,depsr1.

function [epsr, tand, W] = cal(epsr, tand, Z_dut, Zor, freq, geometry, eps_subs)

% The inputs epsr(:,n) = [epsr1, epsr2, epsr3],
% tand(:,n) = [tand1, tand2, tand3],
% Zor = [Zor1, Zor2, Zor3]
%
% The inputs all have the same no. of rows as freq (column vector).
%
% If the substrate arguments are not specified, its effect is not removed.
% The argument geometry consists of [1, geometry, R_core, d_subs]. All
% dimensions are in metres and degrees.

Z_subs = 0.5 * 1./(j*2*pi*freq*8.854e-12 .* eps_subs .* ...
    20e-3*(100*pi/180)*18.4e-3 / 50e-6);

% first create reference standard impedances from epsr(:,n) and tand
Zr1 = cpd2z(epsr(:,1), tand(:,1), freq);
Zr2 = cpd2z(epsr(:,2), tand(:,2), freq);
Zr3 = cpd2z(epsr(:,3), tand(:,3), freq);
Zor1 = Zor(:,1) - Z_subs;
Zor2 = Zor(:,2) - Z_subs;
Zor3 = Zor(:,3) - Z_subs;
Z_dut = Z_dut - Z_subs;

do_Zreim_interp = 0;
do_Yreim_interp = 1;

if do_Zreim_interp
    % quadratic compensation factors
    W.W123r = (real(Z_dut)-real(Zor2)).*(real(Z_dut)-real(Zor3))./(...
        (real(Zor1)-real(Zor2)).*(real(Zor1)-real(Zor3)));
    W.W231r = (real(Z_dut)-real(Zor3)).*(real(Z_dut)-real(Zor1))./(...
        (real(Zor2)-real(Zor3)).*(real(Zor2)-real(Zor1)));
    W.W312r = (real(Z_dut)-real(Zor1)).*(real(Z_dut)-real(Zor2))./(...

```

```

((real(Zor3)-real(Zor1)).*(real(Zor3)-real(Zor2)));
% calibrated effective impedance
Zxr = W.W123r.*real(Zr1) + W.W231r.*real(Zr2) + W.W312r.*real(Zr3);
% quadratic compensation factors
W.W123i = (imag(Z_dut)-imag(Zor2)).*(imag(Z_dut)-imag(Zor3))./...
((imag(Zor1)-imag(Zor2)).*(imag(Zor1)-imag(Zor3)));
W.W231i = (imag(Z_dut)-imag(Zor3)).*(imag(Z_dut)-imag(Zor1))./...
((imag(Zor2)-imag(Zor3)).*(imag(Zor2)-imag(Zor1)));
W.W312i = (imag(Z_dut)-imag(Zor1)).*(imag(Z_dut)-imag(Zor2))./...
((imag(Zor3)-imag(Zor1)).*(imag(Zor3)-imag(Zor2)));
% calibrated effective impedance
Zxi = W.W123i.*imag(Zr1) + W.W231i.*imag(Zr2) + W.W312i.*imag(Zr3);

Zx = Zxr + j.*Zxi;
end

if do_Yreim_interp
Yr1 = 1./Zr1; Yr2 = 1./Zr2; Yr3 = 1./Zr3;
Yor1 = 1./Zor1; Yor2 = 1./Zor2; Yor3 = 1./Zor3;
Y_dut = 1./Z_dut;

% quadratic compensation factors
W.W123r = (real(Y_dut)-real(Yor2)).*(real(Y_dut)-real(Yor3))./...
((real(Yor1)-real(Yor2)).*(real(Yor1)-real(Yor3)));
W.W231r = (real(Y_dut)-real(Yor3)).*(real(Y_dut)-real(Yor1))./...
((real(Yor2)-real(Yor3)).*(real(Yor2)-real(Yor1)));
W.W312r = (real(Y_dut)-real(Yor1)).*(real(Y_dut)-real(Yor2))./...
((real(Yor3)-real(Yor1)).*(real(Yor3)-real(Yor2)));
% calibrated effective impedance
Yxr = W.W123r.*real(Yr1) + W.W231r.*real(Yr2) + W.W312r.*real(Yr3);
% quadratic compensation factors
W.W123i = (imag(Y_dut)-imag(Yor2)).*(imag(Y_dut)-imag(Yor3))./...
((imag(Yor1)-imag(Yor2)).*(imag(Yor1)-imag(Yor3)));
W.W231i = (imag(Y_dut)-imag(Yor3)).*(imag(Y_dut)-imag(Yor1))./...
((imag(Yor2)-imag(Yor3)).*(imag(Yor2)-imag(Yor1)));
W.W312i = (imag(Y_dut)-imag(Yor1)).*(imag(Y_dut)-imag(Yor2))./...
((imag(Yor3)-imag(Yor1)).*(imag(Yor3)-imag(Yor2)));

% calibrated effective impedance
Yxi = W.W123i.*imag(Yr1) + W.W231i.*imag(Yr2) + W.W312i.*imag(Yr3);
Yx = Yxr + j.*Yxi;
Zx = 1./Yx;
end

% Effective complex dielectric constant.
eps_eff = (1./Zx)./(j.*2*pi*f*freq);

% Still add effect of changing core radius.

% A larger core radius has the effect of reducing the effective arc
% coverage and thus measuring a smaller capacitance. Thus, if a larger
% core's properties are to be calibrated for correctly by the standards of
% a certain diameter, the measured capacitance (complex) must be adjusted
% by the ratio of R_dut:R_std.
%
% The vacuum capacitance should be calculated for the nominal arc (i.e. of the
% standards), and for the arc corresponding to the changed core radius. We
% should in principle use the most exact equation, although the rough
% approximation will give a very similar ratio. For now we'll just use
% gapcap instead of cylcap.
%
[C0_nom, Cg_nom] = gapcap(geometry.1, geometry.phi0, geometry.g); C_nom = ...
C0_nom + Cg_nom;
phi_core = geometry.phi0 * geometry.R_nom / geometry.R_core; % effective arc coverage
[C0_core, Cg_core] = gapcap(geometry.1, phi_core, geometry.g); C_core = ...
C0_core + Cg_core;
eps_eff = eps_eff * C_nom/C_core;

% Assign output variables.
eper = real(eps_eff); tand = abs(imag(eps_eff)./real(eps_eff));

```

D.3 PP_calibrate.m

```

function [eper, tand, eper_err, tand_err] = PP_calibrate(Z_open, Z_short, ...
Z_dut, Z_air, d_dut, freq)

% function [eper, eper_err, tand, tand_err] = PP_calibrate(matsetr)
%
% This function performs the calibration of parallel plate measurements
% performed with the LCR meter. Four measured impedances are passed as
% arguments - data is arranged in columns, with each row corresponding to a
% frequency. If more than one column is present, an error analysis is
% performed.
%
% The air gap error is calculated based on d_dut = [d_max d_min]. The
% dimensions of the parallel plate capacitor's centre electrode must be
% changed manually in this file.
%
% The values returned are the nominal eper and tand, and the errors if they
% were calculated.
%
% Marc Ruetschlin, 1 Feb. 2004.

% whether to report the individual contributors to uncertainty
do_error_breakdown = 1;

% Type by which the uncertainty of the input arguments is evaluated. 'A'
% results in a statistical evaluation in which the measurement distribution
% is assumed to be normal (Gaussian) and uses the mean and standard deviation,
% 'B' uses the upper and lower measured values and assumes a rectangular
% (constant) distribution.
uncertainty_type = 'A';

% electrode geometry
R = 19.9e-3/2; g = 0.15e-3;

% turn frequency into a column vector
if size(freq,2) > 1
    freq = freq';
end

%XXXXXXXXXX first nominal values XXXXXXXXXXXX
Zstd = cpd2z(1, 0, freq); % using air as the standard
% for n = 1:size(Z_open,2)-1 % same size as other matrices
% Zstd = cat(2,Zstd,cpd2z(1, 0, freq)); % using air as the standard
% end
Zs = mean(Z_short.'');
Zo = mean(Z_open.'');
Zsm = mean(Z_air.'');
Zxm = mean(Z_dut.'');

% calibration
Z_cal = Zstd.*(Zo-Zsm).*(Zxm-Zs)./((Zsm-Zs).*(Zo-Zxm));
[Cp_dut, D_dut] = z2cpd(Z_cal, freq);
eper = Cp_dut;
tand = D_dut;

%XXXXXXXXXX air gap analysis XXXXXXXXXXXX
[C0,Cg] = pp_gapcap(R, mean(d_dut), g);
for n = 1:length(freq)
    ag_diff = PP_aggap_effect(Z_cal(n)/(C0+Cg), freq(n), R, g, d_dut);
    % These values represent the difference between outputs for no air gap
    % and a total air gap of half the measured range of sample thicknesses.
    % We will see this as a Type B uncertainty with a rectangular
    % distribution, and thus take the uncertainty to be [a*sqrt(3)] u =
    % (1/3)*a^2, where a is the difference between the maximum and minimum
    % values.
    d_eper_ag(n,1) = sqrt((1/3)*abs(ag_diff(1))^2);
    d_tand_ag(n,1) = sqrt((1/3)*abs(ag_diff(2))^2);

    eper_err(n,1) = abs(ag_diff(1));
    tand_err(n,1) = abs(ag_diff(2));
end

%XXXXXXXXXX repeatability error analysis XXXXXXXXXXXX
if size(Z_dut,2) > 1
    % calculate maximum differences
    if uncertainty_type == 'A'
        dZopen = cstd(Z_open,2)/sqrt(size(Z_open,2));
        dZshort = cstd(Z_short,2)/sqrt(size(Z_short,2));
        dZair = cstd(Z_air,2)/sqrt(size(Z_air,2));
        dZdut = cstd(Z_dut,2)/sqrt(size(Z_dut,2));
    elseif uncertainty_type == 'B'
        dZopen = sqrt((1/3)*((max(Z_open.')-min(Z_open.')).')^2)./2).^2;
        dZshort = sqrt((1/3)*((max(Z_short.')-min(Z_short.')).')^2)./2).^2;
        dZair = sqrt((1/3)*((max(Z_air.')-min(Z_air.')).')^2)./2).^2;
        dZdut = sqrt((1/3)*((max(Z_dut.')-min(Z_dut.')).')^2)./2).^2;
    end

    %XXXXXXXXXX vary Zo XXXXXXXXXXXX
    % effect of changes in Zopen on calculated eper and tand

    % eper = imag(Y)
    eper_dut_dZo_hi = imag(1./((Zstd.*(Zo+dZopen)-Zsm).*(Zxm-Zs)./((Zsm-Zs)...
    .*(Zo+dZopen)-Zxm)))./(2*pi*freq);
    eper_dut_dZo_lo = imag(1./((Zstd.*(Zo-dZopen)-Zsm).*(Zxm-Zs)./((Zsm-Zs)...
    .*(Zo-dZopen)-Zxm)))./(2*pi*freq);
    c_eper_dut_dZo = (eper_dut_dZo_hi - eper_dut_dZo_lo)./(2*dZopen);
    % tand = real(Y)/imag(Y)
    tand_dut_dZo_hi = real(1./((Zstd.*(Zo+dZopen)-Zsm).*(Zxm-Zs)./((Zsm-Zs)...
    .*(Zo+dZopen)-Zxm)))./imag(1./((Zstd.*(Zo+dZopen)-Zsm).*(Zxm-Zs)...
    ./(Zsm-Zs).*(Zo+dZopen)-Zxm)));
    tand_dut_dZo_lo = real(1./((Zstd.*(Zo-dZopen)-Zsm).*(Zxm-Zs)./((Zsm-Zs)...
    .*(Zo-dZopen)-Zxm)))./imag(1./((Zstd.*(Zo-dZopen)-Zsm).*(Zxm-Zs)...
    ./(Zsm-Zs).*(Zo-dZopen)-Zxm)));
    c_tand_dut_dZo = (tand_dut_dZo_hi - tand_dut_dZo_lo)./(2*dZopen);

    % worst case
    d_eper_dut_dZo = c_eper_dut_dZo * dZopen;
    d_tand_dut_dZo = c_tand_dut_dZo * dZopen;

    %XXXXXXXXXX vary Zs XXXXXXXXXXXX
    % effect of changes in Zshort on calculated eper and tand

    % eper = imag(Y)
    eper_dut_dZs_hi = imag(1./((Zstd.*(Zo-Zsm).*(Zxm-(Zs+dZshort))./...
    .*(Zsm-(Zs+dZshort)).*(Zo-Zxm)))./(2*pi*freq);
    eper_dut_dZs_lo = imag(1./((Zstd.*(Zo-Zsm).*(Zxm-(Zs-dZshort))./...
    .*(Zsm-(Zs-dZshort)).*(Zo-Zxm)))./(2*pi*freq);
    c_eper_dut_dZs = (eper_dut_dZs_hi - eper_dut_dZs_lo)./(2*dZopen);
    % tand = real(Y)/imag(Y)
    tand_dut_dZs_hi = real(1./((Zstd.*(Zo-Zsm).*(Zxm-(Zs+dZshort))./...
    .*(Zsm-(Zs+dZshort)).*(Zo-Zxm)))./imag(1./((Zstd.*(Zo-Zsm).*(Zxm-(Zs+dZshort))./...
    .*(Zsm-(Zs+dZshort)).*(Zo-Zxm)))./(2*pi*freq);
    tand_dut_dZs_lo = real(1./((Zstd.*(Zo-Zsm).*(Zxm-(Zs-dZshort))./...
    .*(Zsm-(Zs-dZshort)).*(Zo-Zxm)))./imag(1./((Zstd.*(Zo-Zsm).*(Zxm-(Zs-dZshort))./...
    .*(Zsm-(Zs-dZshort)).*(Zo-Zxm)))./(2*pi*freq);
    c_tand_dut_dZs = (tand_dut_dZs_hi - tand_dut_dZs_lo)./(2*dZopen);

    % worst case
    d_eper_dut_dZs = c_eper_dut_dZs * dZshort;
    d_tand_dut_dZs = c_tand_dut_dZs * dZshort;

    %XXXXXXXXXX vary Zxm XXXXXXXXXXXX
    % effect of changes in Zair on calculated eper and tand

```

```

% eper = imag(Y)
eper_dut_dZm_hi = imag(1./((Zstd.*(Zo-(Zsm+dZair)).*(Zxm-Zs))./...
    (((Zsm+dZair)-Zs).*(Zo-Zxm)))))./(2*pi*freq);
eper_dut_dZm_lo = imag(1./((Zstd.*(Zo-(Zsm-dZair)).*(Zxm-Zs))./...
    (((Zsm-dZair)-Zs).*(Zo-Zxm)))))./(2*pi*freq);
c_eper_dut_dZm = (eper_dut_dZm_hi - eper_dut_dZm_lo)./(2*dZair);
% tand = real(Y)/imag(Y)
tand_dut_dZm_hi = real(1./((Zstd.*(Zo-(Zsm+dZair)).*(Zxm-Zs))./...
    (((Zsm+dZair)-Zs).*(Zo-Zxm)))))./imag(1./((Zstd.*(Zo-(Zsm+dZair)).*...
    (Zxm-Zs))./(((Zsm+dZair)-Zs).*(Zo-Zxm)))));
tand_dut_dZm_lo = real(1./((Zstd.*(Zo-(Zsm-dZair)).*(Zxm-Zs))./...
    (((Zsm-dZair)-Zs).*(Zo-Zxm)))))./imag(1./((Zstd.*(Zo-(Zsm-dZair)).*...
    (Zxm-Zs))./(((Zsm-dZair)-Zs).*(Zo-Zxm)))));
c_tand_dut_dZm = (tand_dut_dZm_hi - tand_dut_dZm_lo)./(2*dZair);

% worst case
d_eper_dut_dZm = c_eper_dut_dZm .* dZair;
d_tand_dut_dZm = c_tand_dut_dZm .* dZair;

%%%%%%%%%%%%%%%%%%%%%%%%%%%%%%%%%%%%%%%%%%%%%%%%%%%%%%%%%%%%%%%%%%%%%%%%
% effect of changes in Zdut on calculated eper and tand

% eper = imag(Y)
eper_dut_dZxm_hi = imag(1./((Zstd.*(Zo-Zsm).*((Zxm+dZdut)-Zs))./...
    ((Zsm-Zs).*(Zo-(Zxm+dZdut)))))./(2*pi*freq);
eper_dut_dZxm_lo = imag(1./((Zstd.*(Zo-Zsm).*((Zxm-dZdut)-Zs))./...
    ((Zsm-Zs).*(Zo-(Zxm-dZdut)))))./(2*pi*freq);
c_eper_dut_dZxm = (eper_dut_dZxm_hi - eper_dut_dZxm_lo)./(2*dZdut);
% tand = real(Y)/imag(Y)
tand_dut_dZxm_hi = real(1./((Zstd.*(Zo-Zsm).*((Zxm+dZdut)-Zs))./...
    ((Zsm-Zs).*(Zo-(Zxm+dZdut)))))./imag(1./((Zstd.*(Zo-Zsm).*...
    (Zxm+dZdut)-Zs))./((Zsm-Zs).*(Zo-(Zxm+dZdut)))));
tand_dut_dZxm_lo = real(1./((Zstd.*(Zo-Zsm).*((Zxm-dZdut)-Zs))./...
    ((Zsm-Zs).*(Zo-(Zxm-dZdut)))))./imag(1./((Zstd.*(Zo-Zsm).*...
    (Zxm-dZdut)-Zs))./((Zsm-Zs).*(Zo-(Zxm-dZdut)))));
c_tand_dut_dZxm = (tand_dut_dZxm_hi - tand_dut_dZxm_lo)./(2*dZdut);

% worst case
d_eper_dut_dZxm = c_eper_dut_dZxm .* dZdut;
d_tand_dut_dZxm = c_tand_dut_dZxm .* dZdut;

%%%%%%%%%%%%%%%%%%%%%%%%%%%%%%%%%%%%%%%%%%%%%%%%%%%%%%%%%%%%%%%%%%%%%%%% Totals %%%%%%%%%
d_eper_dut = sqrt(d_eper_dut_dZm.^2 + d_eper_dut_dZs.^2 + ...
    d_eper_dut_dZsm.^2 + d_eper_dut_dZxm.^2 + d_eper_ag.^2);
d_tand_dut = sqrt(d_tand_dut_dZm.^2 + d_tand_dut_dZs.^2 + ...
    d_tand_dut_dZsm.^2 + d_tand_dut_dZxm.^2 + d_tand_ag.^2);

end

% Error breakdown:
if do_error_breakdown
disp('Uncertainty contribution breakdown:');
disp('-----');
disp('max. uncertainty in eper due to:');
disp(['Z_open - ' num2str(max(abs(d_eper_dut_dZm)))]);
disp(['Z_short - ' num2str(max(abs(d_eper_dut_dZs)))]);
disp(['Z_air - ' num2str(max(abs(d_eper_dut_dZsm)))]);
disp(['Z_dut - ' num2str(max(abs(d_eper_dut_dZxm)))]);
disp(['air gap - ' num2str(max(abs(d_eper_ag)))]);
disp(['Total - ' num2str(max(abs(d_eper_dut)))]);
disp('-----');
disp('max. uncertainty in tand due to:');
disp(['Z_open - ' num2str(max(abs(d_tand_dut_dZm)))]);
disp(['Z_short - ' num2str(max(abs(d_tand_dut_dZs)))]);
disp(['Z_air - ' num2str(max(abs(d_tand_dut_dZsm)))]);
disp(['Z_dut - ' num2str(max(abs(d_tand_dut_dZxm)))]);
disp(['air gap - ' num2str(max(abs(d_tand_ag)))]);
disp(['Total - ' num2str(max(abs(d_tand_dut)))]);
disp('-----');

eper_err = abs(d_eper_dut);
tand_err = abs(d_tand_dut);
end

```

D.4 *process_cyl_data.m*

```

% This function is intended to analyse and plot the data from measured
% samples. Capabilities must include being able to take either a single
% series or combine the four orientations, different no. of sample points,
% plotting results but also tabulating them numerically.
%
% The statistical parameters of interest must be calculated: Cv (-SMS),
% with perhaps some guidelines on what an acceptable range of Cv is for
% meaningfully describing a sample with it. E.g., if Cv = 0.5, then the
% sample's material properties are clearly not constant, but change a lot
% over its length. This is something worth pointing out in the analysis
% code. Other hints will appear as the case studies are completed.
%
% NB: In all cases, measure.m is used to perform the calibration - it must be
% ensured that the settings in that file are correct.

get_jonscher_parameters = 0;

% filenames
% Reference material properties for calibration.
ref_save_fname = 'ref_measdata.mat';

% Repeatability data for cylinder characterisation.
save_fname_rep = 'repdata_before.mat';

% Cylindrical measured data
cyl_save_fname = 'cyldata.mat';

% plotting factor: e.g. if measured every 2 mm,
% then gfactor set to 0.2 for correct plotting
gfactor = 0.2;
doffset = 6; % [points] subtracted from d in plotting

eval(['load ' cyl_save_fname]);

sample_str = 'samplestr';
disp(['Working with sample ' sample_str '.']);

% if this is greater than 1, then the two, three or four orientations are
% combined and the average is calculated --- the algorithm will append
% '0deg', '90deg', etc. to mat_str in its quest for the correct variables
num_orientations = 4;

cal_single = 1; % only perform the calibration of a single sample
cal_4orientations = 0; % take all four orientations into account

if cal_single
    if exist(['Z_' sample_str])
        mat_str = sample_str;
        eval(['d = 1:size(Z_' mat_str ',2)']);
        measure;
        eval(['eper_tot = eper_' mat_str '; tand_tot = tand_' mat_str ';']);
        eval(['alpha_tot = alpha_' mat_str '; v_tot = v_' mat_str ';']);
        eval(['eper_tot_err = eper_err_' mat_str ...
            '; tand_tot_err = tand_err_' mat_str ';']);
        eval(['alpha_tot_err = alpha_err_' mat_str ...
            '; v_tot_err = v_err_' mat_str ';']);
    else
        disp(['Error: no sample with name Z_' mat_str ' present.']);
    end
end

if cal_4orientations
    % 0 degrees
    if exist(['Z_' sample_str, '_0deg'])
        mat_str = [sample_str, '_0deg'];
        measure;
        eval(['eper_tot = cat(3,eper_tot,eper_' mat_str ...
            '); tand_tot = cat(3,tand_tot,tand_' mat_str ');']);
        eval(['alpha_tot = cat(3,alpha_tot,alpha_' mat_str ...
            '); v_tot = cat(3,v_tot,v_' mat_str ');']);
        eval(['eper_tot_err = cat(3,eper_tot_err,eper_err_' mat_str ...
            '); tand_tot_err = cat(3,tand_tot_err,tand_err_' mat_str ');']);
        eval(['alpha_tot_err = cat(3,alpha_tot_err,alpha_err_' mat_str ...
            '); v_tot_err = cat(3,v_tot_err,v_err_' mat_str ');']);
    end

    % 90 degrees
    if exist(['Z_' sample_str, '_90deg'])
        mat_str = [sample_str, '_90deg'];
        measure;
        eval(['eper_tot = cat(3,eper_tot,eper_' mat_str ...
            '); tand_tot = cat(3,tand_tot,tand_' mat_str ');']);
        eval(['alpha_tot = cat(3,alpha_tot,alpha_' mat_str ...
            '); v_tot = cat(3,v_tot,v_' mat_str ');']);
        eval(['eper_tot_err = cat(3,eper_tot_err,eper_err_' mat_str ...
            '); tand_tot_err = cat(3,tand_tot_err,tand_err_' mat_str ');']);
        eval(['alpha_tot_err = cat(3,alpha_tot_err,alpha_err_' mat_str ...
            '); v_tot_err = cat(3,v_tot_err,v_err_' mat_str ');']);
    end

    % 180 degrees
    if exist(['Z_' sample_str, '_180deg'])
        mat_str = [sample_str, '_180deg'];
        measure;
        eval(['eper_tot = cat(3,eper_tot,eper_' mat_str ...
            '); tand_tot = cat(3,tand_tot,tand_' mat_str ');']);
        eval(['alpha_tot = cat(3,alpha_tot,alpha_' mat_str ...
            '); v_tot = cat(3,v_tot,v_' mat_str ');']);
        eval(['eper_tot_err = cat(3,eper_tot_err,eper_err_' mat_str ...
            '); tand_tot_err = cat(3,tand_tot_err,tand_err_' mat_str ');']);
        eval(['alpha_tot_err = cat(3,alpha_tot_err,alpha_err_' mat_str ...
            '); v_tot_err = cat(3,v_tot_err,v_err_' mat_str ');']);
    end

    % 270 degrees
    if exist(['Z_' sample_str, '_270deg'])
        mat_str = [sample_str, '_270deg'];
        measure;
        eval(['eper_tot = cat(3,eper_tot,eper_' mat_str ...
            '); tand_tot = cat(3,tand_tot,tand_' mat_str ');']);
        eval(['alpha_tot = cat(3,alpha_tot,alpha_' mat_str ...
            '); v_tot = cat(3,v_tot,v_' mat_str ');']);
        eval(['eper_tot_err = cat(3,eper_tot_err,eper_err_' mat_str ...
            '); tand_tot_err = cat(3,tand_tot_err,tand_err_' mat_str ');']);
        eval(['alpha_tot_err = cat(3,alpha_tot_err,alpha_err_' mat_str ...
            '); v_tot_err = cat(3,v_tot_err,v_err_' mat_str ');']);
    end

    % So now we have eper_tot, tand_tot, eper_tot_err and tand_tot_err, as well
    % as alpha_tot, v_tot and their uncertainties.

    % Must calculate the total mean of all four orientations. Also, the
    % standard deviation of all the measurements should be calculated. This is
    % not an additional uncertainty, but rather only a measure of how the
    % material properties may vary in a sample. How to represent the
    % uncertainty then? Maybe the best way would be to take the mean (or max.)
    % of all the uncertainties?

    % Want to calculate the parameters of interest for the analysis of the rock

```



```

% properties: the coefficient of variance (Cv). The larger this is, the
% poorer the translation to bulk propagation properties the measurement is
% deemed to be.

% What we're actually doing here is calculating the variation of properties
% along the rock. We are only going to look at the expected values (mean)
% and see how they vary. The standard deviation here is not an uncertainty
% measure, but only an analysis tool.

% coverage factor
k = 1;
epsr_properties = variance_tests(epsr_tot, k*epsr_tot_err);
tand_properties = variance_tests(tand_tot, k*tand_tot_err);
alpha_properties = variance_tests(alpha_tot, k*alpha_tot_err);
v_properties = variance_tests(v_tot, k*v_tot_err);

%-----X
%--- plotting ---X
%-----X

dataset = [1:7]; % which frequency points
plotstyle = 'brkcyk';
legendstring = ''; % initialise legend string
k = 1; % coverage factor

figure;
subplot(2,1,1); grid on; hold on;
for n = 1:length(dataset)
    h(:,n) = errorbar(gfactor*(d-doffset), epsr_properties.RG_mean(dataset(n,:),...
        epsr_properties.GU_rot(dataset(n,:),...
        epsr_properties.GU_rot(dataset(n,:), plotstyle(n)));
    plot(gfactor*(d-doffset), epsr_tot(dataset(n,:),1), [plotstyle(n) ':']);
    if cal_4orientations
        if exist(['Z.' sample_str, '_90deg'])
            plot(gfactor*(d-doffset), epsr_tot(dataset(n,:),2), [plotstyle(n) ':']);
        end
        if exist(['Z.' sample_str, '_180deg'])
            plot(gfactor*(d-doffset), epsr_tot(dataset(n,:),3), [plotstyle(n) ':']);
        end
        if exist(['Z.' sample_str, '_270deg'])
            plot(gfactor*(d-doffset), epsr_tot(dataset(n,:),4), [plotstyle(n) ':']);
        end
        legendstring = strvcat(legendstring, [num2str(freq(dataset(n))/1e6) ' MHz']);
    end
end
end
ylabel('epsilon_r');
title(['measured results of ' sample_str]);
subplot(2,1,2); grid on; hold on;
for n = 1:length(dataset)
    errorbar(gfactor*(d-doffset), tand_properties.RG_mean(dataset(n,:),...
        tand_properties.GU_rot(dataset(n,:),...
        tand_properties.GU_rot(dataset(n,:), plotstyle(n)));
    plot(gfactor*(d-doffset), tand_tot(dataset(n,:),1), [plotstyle(n) ':']);
    if cal_4orientations
        if exist(['Z.' sample_str, '_90deg'])
            plot(gfactor*(d-doffset), tand_tot(dataset(n,:),2), [plotstyle(n) ':']);
        end
        if exist(['Z.' sample_str, '_180deg'])
            plot(gfactor*(d-doffset), tand_tot(dataset(n,:),3), [plotstyle(n) ':']);
        end
        if exist(['Z.' sample_str, '_270deg'])
            plot(gfactor*(d-doffset), tand_tot(dataset(n,:),4), [plotstyle(n) ':']);
        end
    end
end
end
ylabel('tan/delta'); xlabel('x [cm]');
legend(h(2,:), legendstring);

%%%%%%%%%%%%%%%%%%%%%%%%%%%%%%%%%%%%%%%%%%%%%%%%%%%%%%%%%%%%%%%%%%%%%%%%
% plot alpha and v results
figure;
subplot(2,1,1); hold on; grid on;
for n = 1:length(dataset)
    h(:,n) = errorbar(gfactor*(d-doffset),...
        abs(20*log10(exp(-alpha_properties.RG_mean(dataset(n,:),...
        abs(20*log10(exp(-k*alpha_properties.GU_rot(dataset(n,:),...
        abs(20*log10(exp(-k*alpha_properties.GU_rot(dataset(n,:),...
        plotstyle(n)));
    plot(gfactor*(d-doffset), abs(20*log10(exp(-alpha_tot(dataset(n,:),1))),...
        [plotstyle(n) ':']);
    if cal_4orientations
        if exist(['Z.' sample_str, '_90deg'])
            plot(gfactor*(d-doffset), ...
                abs(20*log10(exp(-alpha_tot(dataset(n,:),2))), [plotstyle(n) ':']);
        end
        if exist(['Z.' sample_str, '_180deg'])
            plot(gfactor*(d-doffset), ...
                abs(20*log10(exp(-alpha_tot(dataset(n,:),3))), [plotstyle(n) ':']);
        end
        if exist(['Z.' sample_str, '_270deg'])
            plot(gfactor*(d-doffset), ...
                abs(20*log10(exp(-alpha_tot(dataset(n,:),4))), [plotstyle(n) ':']);
        end
    end
end
end
%%%%%%%%%%%%%%%%%%%%%%%%%%%%%%%%%%%%%%%%%%%%%%%%%%%%%%%%%%%%%%%%%%%%%%%%

abs(20*log10(exp(-alpha_tot(dataset(n,:),4))), [plotstyle(n) ':']);
end
end
ylabel('alpha [dB/m]');
title(['attenuation and propagation velocity in ' sample_str]);
subplot(2,1,2); hold on; grid on;
for n = 1:length(dataset)
    errorbar(gfactor*(d-doffset), v_properties.RG_mean(dataset(n,:),...
        v_properties.GU_rot(dataset(n,:),...
        v_properties.GU_rot(dataset(n,:),...
        plotstyle(n)));
    plot(gfactor*(d-doffset), v_tot(dataset(n,:),1), [plotstyle(n) ':']);
    if cal_4orientations
        if exist(['Z.' sample_str, '_90deg'])
            plot(gfactor*(d-doffset), v_tot(dataset(n,:),2), [plotstyle(n) ':']);
        end
        if exist(['Z.' sample_str, '_180deg'])
            plot(gfactor*(d-doffset), v_tot(dataset(n,:),3), [plotstyle(n) ':']);
        end
        if exist(['Z.' sample_str, '_270deg'])
            plot(gfactor*(d-doffset), v_tot(dataset(n,:),4), [plotstyle(n) ':']);
        end
    end
end
end
ylabel('v [m/ms]');
xlabel('x [cm]');
legend(h(2,:), legendstring);

% Calculate the Jonscher parameters of the material's mean properties.
if get_jonscher_parameters
    %--- Jonscher parameter extraction. ---X
    eps_mean = epsr_properties.tot_mean*(1-j*tand_properties.tot_mean);
    % first attempt
    [coeff err output_c] = ...
        lsq(8*rand(3,1), 'jonscher_erfunc', 20, [], eps_mean, 'freq', 100);
    err_s = err(end);
    coefficients = coeff;
    output_curve = output_c;

    % try a number of starting points to see if different result better
    % (avoids local minima)
    for x = 1:10
        [coeff err output_c] = ...
            lsq(8*rand(3,1), 'jonscher_erfunc', 20, [], eps_mean, 'freq', 100);
        err = err(end);
        if err < err_s
            coefficients = coeff;
            output_curve = output_c;
            err_s = err;
        end
    end

    % output Jonscher coefficients to workspace
    nj = coefficients(1);
    chi_r = coefficients(2);
    eps_inf = coefficients(3);
    w_r = 20; % specified in jonscher_erfunc.m
    err_min = err_s; % minimum error

    % plot results
    figure;
    plot(freq/1e6, real(eps_mean), 'r');
    hold on;
    plot(linspace(min(freq/1e6), max(freq/1e6), 100), real(output_curve), 'r');
    plot(freq/1e6, -imag(eps_mean), 'b');
    plot(linspace(min(freq/1e6), max(freq/1e6), 100), -imag(output_curve), 'b');
    title(['Jonscher model fitted to measured data of sample ' sample_str '']);
    legend(['Desired Points to fit', 'Best fitted curve']);
    ylabel(['epsilon_s/epsilon_0']: xlabel('frequency [MHz]');
    v = axis;
    n = coefficients(1); chi_r = coefficients(2); eps_inf = coefficients(3);
    text(v(1)+5, 0.2, ['n = ', num2str(round(n*100)/100), ', \chi_r = ', ...
        num2str(round(chi_r*100)/100), ', \epsilon_\infty = ', ...
        num2str(round(eps_inf*100)/100), '']);
    grid;

    epsj = (freq./(w_r/1e6)).^(nj-1)*chi_r*(1-j*cot(nj*pi/2)) + eps_inf;
    epsrj = real(epsj); tandj = -imag(epsj)/real(epsj);

    epsr_mean = real(eps_mean);
    tand_mean = -imag(eps_mean)/real(eps_mean);
    [epsr_deviation, epsr_max] = max(epsr_mean./epsrj);
    [epsr_deviation] = abs(100-100*epsr_deviation);
    [tand_deviation, tand_max] = max(abs(tand_mean-tandj));
end

```

D.5 geometry.m

```

% this script generates geometry design for guarded
% cylindrical capacitor

% measured core diameter (add a little bit)
%
% options used thus far:
%   axt - 32.5 mm
%   bq - 36.4 mm

core_diameter = 41.7e-3;

% choose centre electrode length
l = 20e-3;
% choose arc coverage [degrees]
phi0 = 100;

% pcb parameters
d_pcb = 0.05e-3; % thickness [mm]

%%% gaps XXX
% side gap [deg] (must be kept below 8 deg for phi0 = 120 deg
side_gap = 4; %

```

```

% guard-centre gap [mm] (error expression available - keep small)
gap_gc = 0.2e-3;

% radius
R = core_diameter/2;
% guard electrode length
L = l + 2*gap_gc + 4*R;

%%% electrode dimensions [mm] %%%
disp('-----');
% core geometry
disp(['core diameter = ' num2str(2*R*1000) ' mm']);

disp('-----');
% pcb parameters
disp(['pcb thickness = ' num2str(d_pcb*1000) ' mm']);

% centre electrode length
disp('-----');
disp('-----');
disp('pcb electrode design parameters:');
disp('-----');
disp(['electrode length: l = ' num2str(l*1000) ' mm']);
% centre electrode width

u = (R+d_pcb)*pi/180;
disp(['arc coverage: phi0 = ' num2str(phi0) ' deg --> u = '...
      num2str(u*1000) ' mm']);
% guard-centred gap
g = gap_gc;
disp(['guard-centre gap: g = ' num2str(g*1000) ' mm']);
% side gap
sg = (R+d_pcb)*side_gap*pi/180;
disp(['side gap of ' num2str(side_gap) ' deg --> sg = '...
      num2str(sg*1000) ' mm']);
% guard length
disp(['total guard length: L = ' num2str(L*1000) ' mm']);
% guard width
W = (R+d_pcb)*(180-side_gap)*pi/180;
disp(['total guard width: W = ' num2str(W*1000) ' mm']);
disp('-----');

%%% errors %%%
[CO, Cg] = gapcap(l, phi0, g);
disp(['vacuum capacitance: CO = ' num2str(CO*1e12) ' pF']);
disp(['gap capacitance correction: Cg = ' num2str(Cg*1e12)...
      ' pF (' num2str(100*Cg/CO) '% of CO)']);
disp('-----');

```

Bibliography

- [1] M. K. Roberts and J. K. Schweitzer, "Geotechnical Areas Associated with the Ventersdorp Contact Reef, Witwatersrand Basin, South Africa," *J. S. Afr. Inst. Mining and Mineralogy*, pp. 157–166, May 1999.
- [2] K. G. Lomborg, E. S. Martin, M. A. Patterson, and J. E. Venter, "The Morphology of Potholes in the UG2 Chromitite Layer and Merensky Reef (Pothole Reef Facies) at Union Section, Rustenburg Platinum Mines," *S. Afr. J. Geol.*, Vol. 102, No. 3, pp. 209–220, Sept. 1999.
- [3] B. R. Spies, "Electrical and Electromagnetic Borehole Measurements: A Review," *Surveys in Geophysics*, Vol. 17, pp. 517–556, 1996.
- [4] D. M. Claassen, *Electromagnetic Characterisation of a Wideband Borehole Radar Imaging System*, Ph.D. thesis, University of Oxford, 1995.
- [5] C. M. Simmat, N. Osman, M. R. Levinson, J. E. Hargreaves, and I. M. Mason, "Application of Borehole Radar to VCR Gold Mines in the Witwatersrand Basin, South Africa," in *Proc. of the Workshop on Remote Sensing by Low-Frequency Radars*, Naples, Italy, Sept. 2001.
- [6] I. M. Mason, Q. Liu, N. Osman, C. Simmat, and L. Min, "Broadband Synthetic Borehole Radar Interferometry," in *Proc. 8th Int. Conf. GPR*, pp. 132–137, May 2000.
- [7] A. R. von Hippel, Ed., *Dielectric Materials and Applications*, Artech House, Boston, 1954.
- [8] J. Baker-Jarvis, C. Jones, B. Riddle, M. Janezic, R. G. Geyer, J. J. Grosvenor, Jr., and C. Weil, "Dielectric and Magnetic Measurements: A Survey of Nondestructive, Quasi-Nondestructive, and Process-Control Techniques," *Res. Nondestr. Eval.*, Vol. 7, pp. 117–136, 1995.
- [9] M. N. Afsar, J. R. Birch, R. N. Clarke, and G. W. Chantry, (ed.), "The Measurement of the Properties of Materials," *Proc. IEEE*, Vol. 74, No. 1, pp. 183–199, Jan. 1986.
- [10] H. E. Bussey, "Measurement of RF Properties of Materials A Survey," *Proc. IEEE*, Vol. 55, No. 6, pp. 1046–1053, June 1967.
- [11] G. Roussy and J. A. Pearce, *Foundations and Industrial Applications of Microwave and Radio Frequency Fields: Physical and Chemical Processes*, John Wiley & Sons, New York, 1995.
- [12] M. R. Taherian, W. E. Kenton, and K. A. Safinya, "Measurement of Dielectric Response of Water-Saturated Rocks," *Geophysics*, Vol. 55, No. 12, pp. 1530–1541, Dec. 1990.
- [13] M. J. Campbell and J. Ulrichs, "Electrical Properties of Rocks and Their Significance for Lunar Radar Observations," *J. Geophys. Res.*, Vol. 74, No. 25, pp. 5867–5881, Nov. 1969.
- [14] R. J. Knight and A. Nur, "The Dielectric Constant of Sandstones, 60 kHz to 4 MHz," *Geophysics*, Vol. 52, No. 5, pp. 644–654, May 1987.

- [15] R. Alvarez, "Complex Dielectric Permittivity in Rocks: A Method for its Measurement and Analysis," *Geophysics*, Vol. 38, No. 5, pp. 920–940, Oct. 1973.
- [16] A. Kyritsis, M. Siakantari, A. Vassilikou-Dova, P. Sissis, and P. Varotsos, "Dielectric and Electrical Properties of Polycrystalline Rocks at Various Hydration Levels," *IEEE Trans. Dielec. and Elec. Insul.*, Vol. 7, No. 4, pp. 493–497, Aug. 2000.
- [17] J. H. Scott, R. D. Carroll, and D. R. Cunningham, "Dielectric Constant and Electrical Conductivity Measurements of Moist Rock: A New Laboratory Method," *J. Geophys. Res.*, Vol. 72, No. 20, pp. 5101–5115, Oct. 1967.
- [18] M. Saint-Amant and D. W. Strangway, "Dielectric Properties of Dry, Geologic Materials," *Geophysics*, Vol. 35, No. 4, pp. 624–645, Aug. 1970.
- [19] F. T. Ulaby, T. H. Bengal, M. C. Dobson, J. R. East, J. B. Garvin, and D. L. Evans, "Microwave Dielectric Properties of Dry Rocks," Vol. 28, No. 3, pp. 325–336, May 1990.
- [20] X. Wang, H. Guo, C. Wang, P. Chen, and Y. Shi, "Relative Dielectric Constant from Dry Rocks," *Chinese Science Bulletin*, Vol. 44, No. 24, pp. 2286–2293, Dec. 1999.
- [21] Q. J. Tian, P. Gong, B. Xu, X. Wang, H. Guo, and Q. Tong, "Reflectance, Dielectric Constant and Chemical Content of Selected Sedimentary Rocks," *Int. J. Remote Sensing*, Vol. 23, No. 23, pp. 5123–5128, 2002.
- [22] J. P. Grant, R. N. Clarke, G. T. Symm, and N. M. Spyrou, "A Critical Study of the Open-Ended Coaxial Line Sensor for RF and Microwave Complex Permittivity Measurements," *J. Phys. E: Sci. Instrum.*, Vol. 22, pp. 757–770, 1989.
- [23] J. R. Mosig, J.-C. E. Besson, M. Gex-Fabry, and F. E. Gardiol, "Reflection of an Open-Ended Coaxial Line and Application to Nondestructive Measurement of Materials," *IEEE Trans. Instrum. Meas.*, Vol. 30, No. 1, pp. 46–51, Mar. 1981.
- [24] D. L. Gershon, J. P. Calame, Y. Carmel, T. M. Antonsen, Jr., and R. M. Hutcheon, "Open-Ended Coaxial Probe for High-Temperature and Broad-Band Dielectric Measurements," *IEEE Trans. Microwave Theory Tech.*, Vol. 47, No. 9, pp. 1640–1648, Sept. 1999.
- [25] J. Baker-Jarvis, M. D. Janezic, P. D. Domich, and R. G. Geyer, "Analysis of an Open-Ended Coaxial Probe for Nondestructive Testing," *IEEE Trans. Instrum. Meas.*, Vol. 43, No. 5, pp. 711–717, Oct. 1994.
- [26] C. Karpuz, M. Duyar, and A. Gorur, "Analysis of Coplanar-Coupled Lines on a Cylindrical Substrate," *Microwave and Opt. Technol. Lett.*, Vol. 27, No. 3, pp. 187–190, Nov. 2000.
- [27] J. C. Moore and J. G. Paren, "A New Technique for Dielectric Logging of Antarctic Ice Cores," *J. Phys. (Paris)*, Vol. 48, *Colloq. C1*, pp. 155–160, 1987.
- [28] F. Wilhelms, "Messung dielektrischer Eigenschaften polarer Eiskerne," *Berichte zur Polarforschung*, Vol. 367, 2000.
- [29] J. Moore and N. Maeno, "Application of the Dielectric Profiling Technique to Ice Core Studies," in *Proc. NIPR Symp. Polar Meteorol. Glaciol.*, Vol. 4, pp. 81–92, 1991.
- [30] J. C. Moore, "High-Resolution Dielectric Profiling of Ice Cores," *Journal of Glaciology*, Vol. 39, No. 132, pp. 245–248, 1993.

- [31] F. Wilhelms, "Leitfähigkeits- und Dichtemessung an Eisbohrkernen," *Ber. Polarforsch.*, Vol. 191, 1996.
- [32] F. Wilhelms, J. Kipfstuhl, H. Miller, K. Heinloth, and J. Firestone, "Precise Dielectric Profiling of Ice Cores: A New Device with Improved Guarding and its History," *Journal of Glaciology*, Vol. 44, No. 146, pp. 171–174, 1998.
- [33] Hewlett-Packard, "Effective Impedance Measurement Using OPEN/SHORT/LOAD Correction," Application Note 346-3, June 1998.
- [34] De Beers, "Layered Cr-Pt Mafic-Ultramafic Complexes," Document published on <http://geology.csupomona.edu/drjessey/class/GSC433/Layered.htm>.
- [35] A. R. von Hippel, Ed., *Dielectrics and Waves*, Artech House, Boston, 1954.
- [36] W. C. Chew, *Waves and Fields in Inhomogeneous Media*, Van Nostrand Reinhold, New York, 1990.
- [37] J. R. James and G. Andrasic, "Assessing the Accuracy of Wideband Electrical Data Using Hilbert Transforms," *Proc. IEEE - H*, Vol. 137, No. 3, pp. 184–188, June 1990.
- [38] F. Hollender and S. Tillard, "Modeling Ground-Penetrating Radar Wave Propagation and Reflection with the Jonscher Parameterization," *Geophysics*, Vol. 63, No. 6, pp. 1933–1942, Nov. 1998.
- [39] P. Debye, *Polar Molecules*, Dover Publications, New York, 1929.
- [40] K. S. Cole and R. H. Cole, "Dispersion and Absorption in Dielectrics," *J. Chem. Phys.*, Vol. 9, pp. 341–351, Apr. 1941.
- [41] R. Feynman, R. B. Leighton, and M. L. Sands, *The Feynman Lectures on Physics*, Addison-Wesley, Reading, Massachusetts, 1963.
- [42] S. Ramo, J. R. Whinnery, and T. van Duzer, *Fields and Waves in Communication Electronics*, John Wiley & Sons, New York, 3rd edition, 1994.
- [43] A. K. Jonscher, "Physical Basis for Dielectric Loss," *Nature*, Vol. 253, pp. 717–719, Feb. 1975.
- [44] A. K. Jonscher, "Dielectric Relaxation in Solids," *J. Phys. D: Appl. Phys.*, Vol. 32, pp. R57–R70, 1999.
- [45] A. K. Jonscher, "The 'Universal' Dielectric Response," *Nature*, Vol. 267, pp. 673–679, June 1977.
- [46] R. E. Díaz and N. G. Alexopoulos, "An Analytic Continuation Method for the Analysis and Design of Dispersive Materials," *IEEE Trans. Ant. Prop.*, Vol. 45, No. 11, pp. 1602–1610, Nov. 1997.
- [47] H. A. Haus and J. R. Melcher, *Electromagnetic Fields and Energy*, Prentice Hall, New Jersey, Englewood Cliffs, 1989.
- [48] J. C. Maxwell, *A Treatise on Electricity and Magnetism*, Clarendon Press, Oxford, 2nd edition, 1881.
- [49] H. Nishiyama and M. Nakamura, "Capacitance of Disk Capacitors," *IEEE Trans. Comp., Hybrids, Manuf. Technol.*, Vol. 16, No. 3, pp. 360–366, May 1993.
- [50] W. Thomson, *Report of the British Association*, Unknown, Dundee, 1867.

- [51] W. C. Heerens, "Application of Capacitive Techniques in Sensor Design," *J. Phy. E: Sci. Instrum.*, Vol. 19, pp. 897–906, 1986.
- [52] S. Darayan, D. P. Shattuck, L. C. Shen, and R. C. Liu, "Measurement of Dielectric Constant and Conductivity of Samples Using Guarded Electrodes," *Radio Science*, Vol. 31, No. 6, pp. 1417–1426, Nov. 1996.
- [53] European Co-operation for Accreditation, "Expression of the Uncertainty of Measurement in Calibration," EA-4/02, Dec. 1999.
- [54] B. N. Taylor and C. E. Kuyatt, "Guidelines for Evaluating and Expressing the Uncertainty of NIST Measurement Results," NIST Technical Note 1297, National Institute of Standards and Technology, Sept. 1994.
- [55] A. Papoulis, *Probability, Random Variables, and Stochastic Processes*, McGraw-Hill, Singapore, 2nd edition, 1984.
- [56] R. J. Barlow, *Statistics: A Guide to the Use of Statistical Methods in the Physical Sciences*, John Wiley & Sons, Chichester, England, 1989.
- [57] L. O. Chua, C. A. Desoer, and E. S. Kuh, *Linear and Nonlinear Circuits*, McGraw-Hill, New York, 1987.
- [58] K. L. Su, *Analog Filters*, Chapman & Hall, London, 1st edition, 1996.
- [59] H. Haruta, *Agilent Technologies Impedance Measurement Handbook*, Agilent Technologies, 2nd edition, 2000.
- [60] Agilent Technologies, Hyogo, Japan, *Agilent 4285A Precision LCR Meter Operation Manual*.
- [61] Agilent Technologies, "New Technologies For Accurate Impedance Measurement (40Hz to 110MHz)," Product Note 4294A, 2000.
- [62] K. J. Silvonen, "Calibration of Test Fixtures Using at Least Two Standards," *IEEE Trans. Microwave Theory Tech.*, Vol. 39, No. 4, pp. 624–630, Apr. 1991.
- [63] J.-G. Liu and U. Frühauf, "Self-Calibration Measuring Methods and Applications to Measurements of Electrical Quantities," *Measurement*, Vol. 26, pp. 129–142, 1999.
- [64] D. W. Braudaway, "The Costs of Calibration," *IEEE Trans. Instrum. Meas.*, Vol. 52, No. 3, pp. 738–741, June 2003.
- [65] J.-G. Liu, U. Frühauf, and A. Schönecker, "Accuracy Improvement of Impedance Measurements by Using the Self-Calibration," *Measurement*, Vol. 25, pp. 213–225, 1999.
- [66] Agilent Technologies, Hyogo, Japan, *Agilent 16451B Dielectric Test Fixture Operation and Service Manual*.
- [67] E. du Pont de Nemours and Company, "DuPont Teflon(R) and Tefzel(R) Films," <http://www.dupont.com/teflon/films/>, 2003.
- [68] D. G. W. Goad and H. J. Wintle, "Capacitance Corrections for Guard Gaps," *Meas. Sci. Technol.*, Vol. 1, pp. 965–969, 1990.
- [69] W. C. Heerens, E. M. Boogh, and G. Keizer, "Gap Influences in Guarded Capacitor," *Delft Progress Report*, Vol. 8, No. 2, pp. 149–160, June 1983.

- [70] W. C. Heerens, “Basic Principles in Designing Highly Reliable Multi-Terminal Capacitor Sensors and Performance of Some Laboratory Test Models,” *Sensors and Actuators*, Vol. 3, pp. 137–148, 1982.
- [71] EM Software and Systems, Technopark, Stellenbosch, 7600, South Africa, *FEKO User’s Manual*.
- [72] M. A. Brown and C. E. Bulleid, “The Effect of Tilt and Surface Damage on Practical Capacitance Transducers,” *J. Phys. E: Sci. Instrum.*, Vol. 11, pp. 429–432, 1978.
- [73] Symalit, “Symalit® PVDF,” Available at <http://www.symalit.com/>, 2003.
- [74] M. Rütshlin, “Measurement of Vaal Reef and VCR Foot- and Hangingwall Dielectric Properties,” Internal Report, Dept. Electrical and Electronic Engineering, University of Stellenbosch, June 2001.
- [75] J. D. Jackson, *Classical Electrodynamics*, John Wiley & Sons, New York, 3rd edition, 1999.
- [76] C. R. Wylie and L. C. Barrett, *Advanced Engineering Mathematics*, McGraw-Hill, New York, 6th edition, 1995.
- [77] H. J. Schell, *Unendliche Reihen*, Verlag Harri Deutsch, Thun, 1978.
- [78] H. Heuser, *Lehrbuch der Analysis, Teil 1*, B.G. Teubner, Stuttgart, 8th edition, 1990.
- [79] E. W. Weisstein, “Supremum,” From MathWorld—A Wolfram Web Resource. <http://mathworld.wolfram.com/Supremum.html>.
- [80] D. M. Pozar, *Microwave Engineering*, John Wiley & Sons, New York, 2nd edition, 1998.
- [81] J. G. Proakis and D. G. Manolakis, *Digital Signal Processing — Principles, Algorithms, and Applications*, Prentice-Hall, Upper Saddle River, New Jersey, U.S.A., 3rd edition, 1996.
- [82] J. A. Kinnaird, F. J. Kruger, P. A. M. Nex, and R. Cawthorn, “Chromitite Formation — A Key to Understanding Processes of Platinum Enrichment,” *Trans. Inst. Min. Metall. (Sect. B: Appl. Earth Sci.)*, Vol. 111, No. 1, pp. B23–B35, Apr. 2002.
- [83] P. L. R. Herselman, *Borehole Radar System Analysis in Stratified Geological Systems Applied to Imaging of Platiniferous Reefs in the Bushveld Igneous Complex*, Ph.D. thesis, University of Stellenbosch, 2003.
- [84] H. R. Lindman, *Analysis of Variance in Complex Experimental Designs*, W. H. Freeman and Company, San Francisco, 1974.
- [85] S. A. Glantz and B. K. Slinker, *Primer of Applied Regression and Analysis of Variance*, McGraw-Hill, New York, 1990.
- [86] J. H. Zar, *Biostatistical Analysis*, Prentice Hall, Upper Saddle River, New Jersey, U.S.A., 4th edition, 1999.
- [87] Johnson Matthey, “Platinum Today: Production: South Africa,” Document published at <http://www.platinum.matthey.com/production/africa.php>.
- [88] F. Vos, “Bleskop Marker,” Personal communication between Mr. F. Vos, Managing Geologist, Anglo Platinum Rustenburg Section, and Prof. J.H. Cloete, University of Stellenbosch, Sept. 2002.
- [89] F. Vos, “UG2 Reef at Bleskop Shaft,” Personal communication between Mr. F. Vos, Managing Geologist, Anglo Platinum Rustenburg Section, and Prof. J.H. Cloete, University of Stellenbosch, Feb. 2003.

- [90] Anglo Platinum, "Geological Log of: Rustenberg Section - Waterval, Borehole WV171," Aug. 2003, Courtesy of Anglo Platinum Rustenberg Section.
- [91] De Beers, "Diamond Geology," Document published on <http://www.debeersgroup.com>.
- [92] M. Field and B. H. Scott Smith, "Near Surface Emplacement of Kimberlites: Contrasting Models and Why," in *7th Int. Kimberlite Conf., Extended Abstracts*, Cape Town, South Africa, pp. 211–213, Apr. 1998.
- [93] C. R. Clement and A. M. Reid, "The Origin of Kimberlite Pipes: An Interpretation Based on a Synthesis of Geological Features Displayed by Southern African Occurrences," in *4th Int. Kimberlite Conf., Extended Abstracts*, Perth, Western Australia, Geol. Soc. Australia, pp. 167–169, Aug. 1986.
- [94] J. B. Hawthorn, "Model of a Kimberlite Pipe," *Phys. Chem. Earth*, Vol. 9, pp. 1–15, 1975.
- [95] De Beers Consolidated Mines, "Geological Log of Hole PM551," Courtesy of Cullinan Mine, De Beers Consolidated Mines.
- [96] GTS Flexible Materials Ltd., "GTS7600 — Copper Polyimide Laminate," Technical Data.
- [97] P. T. Hammer, R. M. Clowes, and K. Ramachandran, "High-Resolution Seismic Reflection Imaging of Thin, Diamondiferous Kimberlite Dykes and Sills," *Eos Trans. AGU*, 84(46), Fall Meet. Suppl. S21C-07, 2003.
- [98] D. M. McBean, M. B. Kirkley, and C. R. Revering, "Structural Controls on the Morphology of the Snap Lake Kimberlite Dyke," Poster 1.P6 at the 8th Int. Kimberlite Conf., Victoria, B.C., Canada, June, 2003.
- [99] M. Kirkley, "Snap Lake BQ Core Samples," Personal Communication between Dr. Melissa Kirkley, Chief Geologist, Snap Lake, and Prof. J.H. Cloete, University of Stellenbosch, Sept. 2003.
- [100] A. M. Agashev, N. P. Pokhilenko, J. A. McDonald, E. Takazawa, M. A. Vavilov, N. V. Sobolev, and T. Watanabe, "A Unique Kimberlite-Carbonatite Primary Association in the Snap Lake Dyke System, Slave Craton: Evidence from Geochemical and Isotopic Studies," Slave-Kaapvaal Workshop, Seismology and Electromagnetism Section, Geological Survey of Canada, <http://www.cg.nrcan.gc.ca/>, 2003.
- [101] I. M. Mason, "Re: the nugget effect," Email Communication with Prof. Iain Mason, Professor of Geophysics at the University of Sydney, Nov. 2003.
- [102] Y. Kudo and H. Inoue, "Relative Dielectric Constant Characteristics of Liquid at VHF Band Using Small Cell Impedance Analysis," in *IEEE International Symposium on EMC*, Vol. 1, pp. 329–333, Aug. 1998.